SCANNING PROBE & OPTICAL TWEEZER INVESTIGATIONS OF BIOMOLECULAR INTERACTIONS

SHELLIE RIGBY-SINGLETON, BSc (Hons)

Thesis submitted to the University of Nottingham for the degree of Doctor of Philosophy, September 2002

CONTENTS

ABSTRACT

A complex array of intermolecular forces controls the interactions between and within biological molecules. The desire to empirically explore these fundamental forces has led to the development of several biophysical techniques. Of these, the atomic force microscope (AFM) and the optical tweezers have been employed throughout this thesis to monitor the intermolecular forces involved in biomolecular interactions.

The AFM is a well-established force sensing technique capable of measuring biomolecular interactions at a single molecule level. However, its versatility has not been extrapolated to the investigation of a drug-enzyme complex. The energy landscape for the force induced dissociation of the DHFR-methotrexate complex was studied. Revealing an energy barrier to dissociation located ~0.3 nm from the bound state.

Unfortunately, the AFM has a limited range of accessible loading rates and in order to profile the complete energy landscape alternative force sensing instrumentation should be considered, for example the BFP and optical tweezers. Thus, this thesis outlines the development and construction of an optical trap capable of measuring intermolecular forces between biomolecules at the single molecule level. To demonstrate the force sensing abilities of the optical set up, proof of principle measurements were performed which

investigate the interactions between proteins and polymer surfaces subjected to varying degrees of argon plasma treatment. Complementary data was gained from measurements performed independently by the AFM. Changes in polymer resistance to proteins as a response to changes in polymer surface chemistry were detected utilising both AFM and optical tweezers measurements.

Finally, the AFM and optical tweezers were employed as ultrasensitive biosensors. Single molecule investigations of the antibody-antigen interaction between the cardiac troponin I marker and its complementary antibody, reveals the impact therapeutic concentrations of heparin have up on the association and dissociation of the complex.

In the thesis the AFM and optical tweezers independently provide complementary data towards the understanding of biomolecular interactions.

TABLES

FIGURES

ABBREVIATIONS

3-APDES	3-aminopropyldimethylexthoysilane
Ab	antibody
AFM	atomic force microscopy
Ag	antigen
AMI	acute myocardial infarction
Asp	aspartate
BBSA	biotin bovine serum albumin
BFP	biomembrane force probe
BSA	bovine serum albumin
CCD	charge-coupled device
CDR	complementary determining region
CK	creatine kinase
cTnI	cardiac troponin I subunit
cTnT	cardiac troponin T subunit
cTnC	cardiac troponin C subunit
Da	dalton
DCA	dynamic contact angle
DFS	dynamic force spectroscopy
DHFR	dihydrofolate reductase
DNA	deoxyribonucleic acid
E	energy
Ec	*Escherichia coli*
EDC	N-ethyl-N'-(dimethylaminopropyl) carbodiimide
EDTA	ethylenediamine-tetra-acetic acid
ELISA	enzyme-linked immunosorbent assay
HSA	human serum albumin
Ig	immunoglobulin
IU	international units
kDa	kilo dalton

Lc	*Lactobacillus casei*
Leu	leucine
Lys	lysine
MAb	monoclonal antibody
MFP	molecular force probe
M_r	molecular weight
MTX	methotrexate
NA	numerical aperture
NADPH	nicotinamide adenine dinucleotide phosphate
NHS	N-hydroxysuccinimide
NMR	nuclear magnetic resonance
NOESY	nuclear overhauser effect spectroscopy
PBS	phosphate buffered saline
RF	radio frequency
RNA	ribonucleic acid
RNAP	ribonucleic acid polymerase
rpm	revolutions per minute
s.d.	standard deviation
SFA	surface force apparatus
SPM	scanning probe microscopy
STM	scanning tunnel microscopy
THF	tetrahydrofolate
Thr	threonine
ToF-SIMS	time of flight-secondary ion mass spectroscopy
Trp	tryptophan
VDW	van der Waals
XPS	x-ray photoelectron spectroscopy

CHAPTER 1

INTRODUCTION:

The Measurement of Force

The recent ability to empirically determine intermolecular forces using surface force apparatus (Israelachvili, 1978), atomic force microscopy (Binnig *et al*., 1986), optical force techniques (Ashkin, 1986) and the biomembrane force probe (Evans *et al*., 1995) has facilitated our understanding of the nature of these forces, and their fundamental involvement in life.

The research presented in this thesis employs the atomic force microscope (AFM) and optical tweezers to measure the intermolecular forces involved in a number of biomolecular interactions. Therefore, as a basis for this research, this introductory chapter will provide a review of the intermolecular forces governing biomolecular interactions and the current techniques available for probing these interactions. The applications of these force spectroscopy techniques are reviewed, with emphasis on single molecule and dynamic force measurements.

1.1 FORCES OF NATURE

Intermolecular forces are fundamental to existence. Essentially, intermolecular forces determine the physical properties of solids, liquids and gases, and the organisation of biological entities (Israelachvili, 1991). Structural cohesion and biomolecular interactions are dictated by a complex array of weak, non-covalent intermolecular forces (Leckband & Israelachvili, 1993). These forces are categorised by the roles in which they play in molecular recognition; forces involved in the *lock-and-key* mechanism of receptor-ligand binding are commonly referred to as specific forces and include hydrogen bonding, hydrophobic interactions and van der Waals forces. Forces involved in directing the ligand trajectories towards the binding site operate outside the binding pocket, and are typically electrostatic and van der Waals forces (Leckband & Israelachvili, 2001). It is the interplay of these two categories which mediates the biomolecular recognition process.

The focus of this thesis is on the specific forces involved in complex formation between complementary molecules, and therefore forces which operate outside the binding pocket shall not be discussed hereafter. For a comprehensive text detailing intermolecular and intersurface forces not discussed here, the reader is directed to Israelachvili, (1991) or alternatively Leckband & Israelachvili, (2001).

1.2 TECHNIQUES FOR PROBING INTERMOLECULAR FORCES

A host of biophysical techniques have emerged over the last two decades which are capable of directly measuring the intermolecular forces that control biomolecular interactions. The principle techniques include surface force apparatus (Israelachvili *et al*., 1978), the atomic force microscope (Binnig *et al*., 1986), the biomembrane force probe (Evans *et al*., 1995) and optical tweezers (Ashkin, 1987). Accumulatively, these techniques provide an accessible force window from 10^{-7} – 10^{-14} N, although individually their force and dynamic ranges vary with a degree of overlap from one technique to the next. Table 1.1 highlights the force range for the available force sensing techniques.

1.2.1 Surface Force Apparatus (SFA)

The SFA provided the first means of directly measuring intermolecular forces (Tabor & Winterton, 1969; Tabor & Israelachvili, 1972). Figure 1.1a depicts the essential components of the instrumentation. The sample surfaces are supported on two curved substrates that can be brought towards each other or separated in a controlled fashion, from millimetres to sub-ångstrom separations. Approach and separation rates can be varied over a range of eight orders of magnitude from 1 mm s^{-1} to 1 Å min^{-1}. The resulting change in the separation between the two surfaces is then measured optically and the deflection of the spring, is converted to force using Hooke's Law ($F = kd$).

Force Technique	Force Range
Surface Force Apparatus	> 10 nN
Atomic Force Microscopy	0.01 – 100 nN
Microneedles	> 0.1 pN
Biomembrane Force Probe	0.01 pN – 1 nN
Optical Tweezers	0.01 – 200 pN
Magnetic Beads	0.01 – 100 pN

Table 1.1 Typical values of the accessible force-range for the available force spectroscopy techniques (taken from references cited in the text).

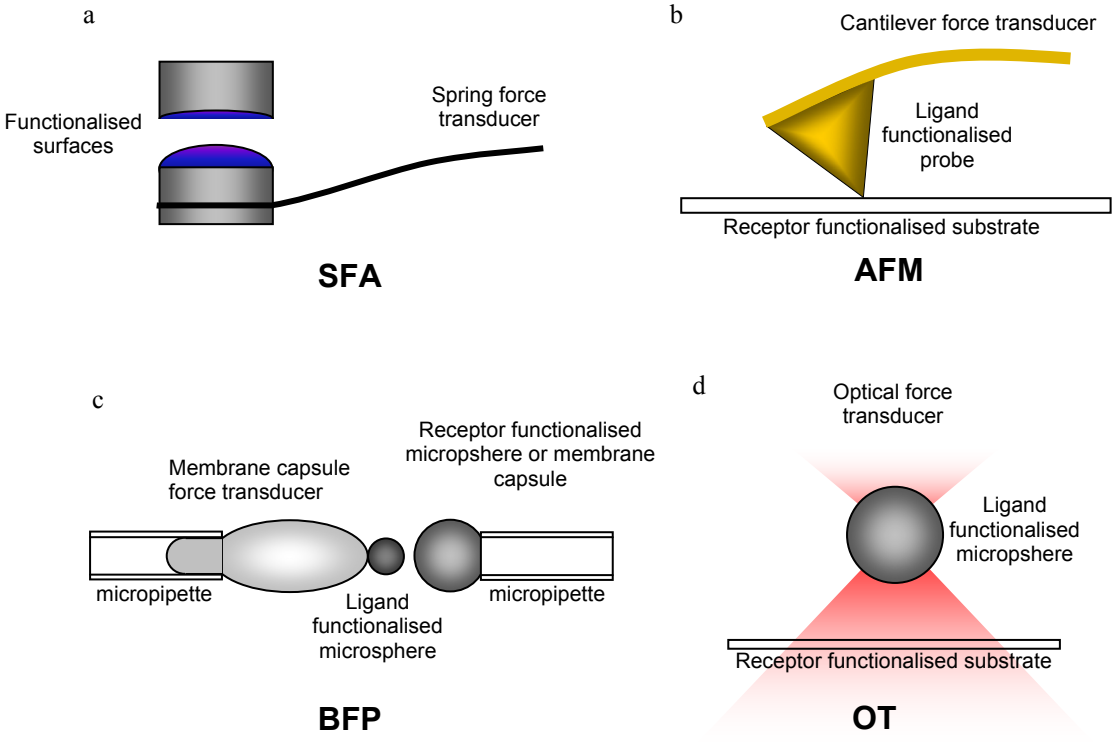

Fig. 1.1 – Force transducers employed for the measurement of intermolecular forces. a)The surface force apparatus, illustrated by a force-transducing spring; b) The atomic force microscope, demonstrating an adhesive interaction between the probe and surface; c) The biomembrane force probe, in which a membrane capsule aspirated into a pipette behaves as the force transducer; d) Optical tweezers, in which radiation pressure acts a force transducer (adapted from Leckband, 2000).

The SFA technique allows for the measurement of a very wide range of surface forces and interactions over a large axial distance regime from ångstroms to microns. These include VDW, electrostatic, hydration, hydrophobic, bio-specific, capillary, adhesion, viscous, lubrication, and charge-transfer interactions (Leckband & Israelachvili, 2001). The SFA has been employed to study the avidin-biotin interaction (Leckband *et al*., 1992; Leckband *et al*., 1994), antibody-antigen interactions (Leckband *et al*., 1995) and the interactions between complimentary DNA strands (Princet *et al*., 1996). However, the lateral surface distance of the instrumentation can be resolved only to 1-5 μm^2 equating to approximately 10,000 molecular interactions, and a force resolution of >10 nN (Leckband, 2000). Unfortunately, due to the large number of molecular interactions probed, this technique cannot be employed in dynamic force spectroscopy of bio-specific interactions (refer to section 1.3.1).

1.2.2 Atomic Force Microscopy (AFM)

The AFM, a descendent of the scanning probe microscopy family, was invented by Binnig *et al*. (1986) following the advent of the scanning tunnelling microscope in 1982 (Binnig *et al*., 1982). Since this time the AFM has become an established surface analytical technique, capable of high resolution imaging of insulating and conducting surfaces in a variety of environmental conditions, as well as submolecular imaging of biological material (Hansma *et al*., 1997). The AFM has also proved to be an invaluable tool in the determination of inter- and intra-molecular forces. The AFM has a

theoretical force resolution of 10^{-15} N (Smith, 1995), and employs probes with a tip apex radius of 10-15 nm (Thundat *et al*., 1992) providing contact regions as small as 10 nm^2 (Lee *et al*., 1994). The high force resolution and small contact area provided by the AFM, overcome the limitations of SFA, and are ideally suited for the measurement of single molecular interactions. The establishment of the AFM as a force sensing apparatus has also lead to the elucidation of additional nanomechanical properties, such as the elasticity and plasticity of molecules.

1.2.2.1 *Instrumentation*

The AFM probes the surface of a substrate with a sharp silicon nitride or silicon tip, integrated to the apex of a microfabricated cantilever of a known spring constant, k (N/m). A collimated laser beam is reflected off the back of the v-shaped cantilever onto a position sensitive quadrant photo-diode. A map of the substrate surface topography is generated by monitoring cantilever deflections (a result of forces acting between the tip and surface) as the tip is raster scanned across the surface. By monitoring the position of the laser beam through the output signals from each of the diode segments cantilever deflections as small as 0.1 Å can be detected (Rugar & Hansma 1990). The principal components of an AFM are shown schematically in fig. 1.2.

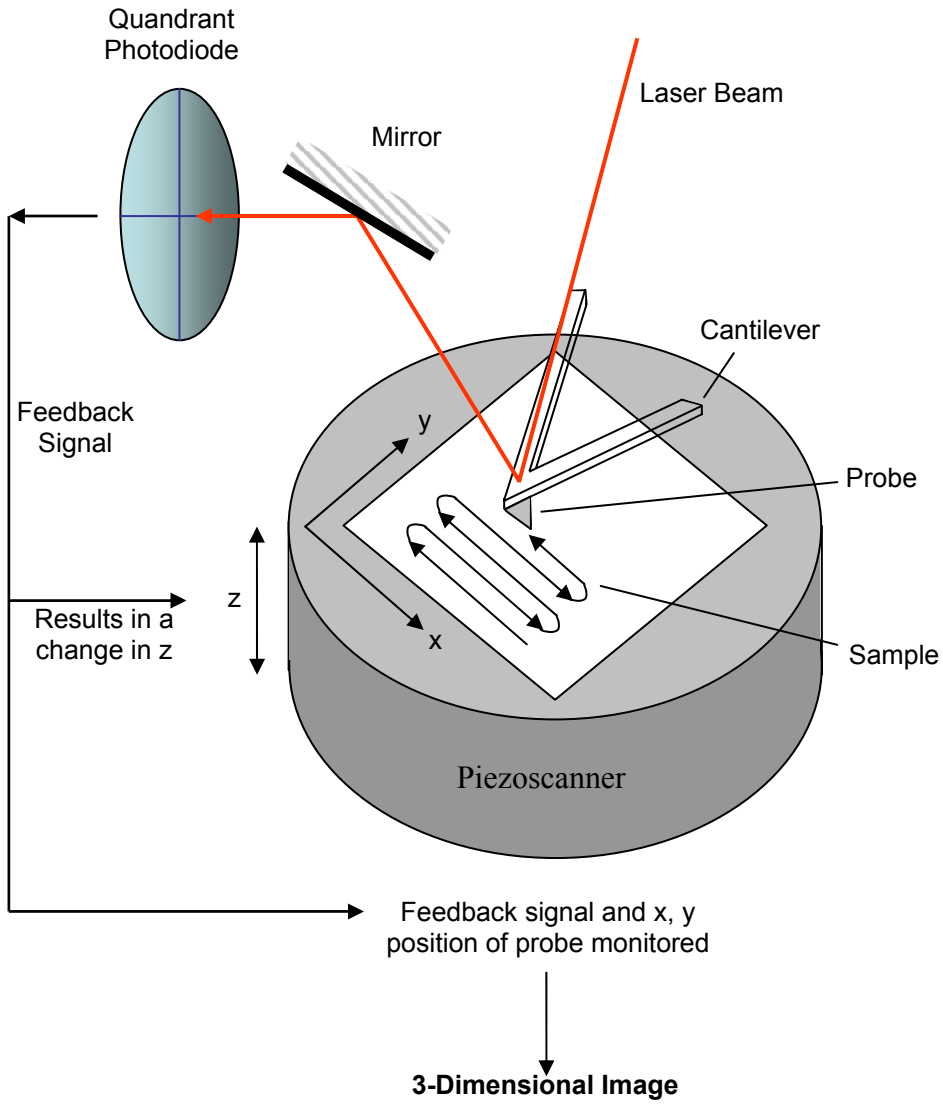

Fig. 1.2 – Contact mode imaging using an AFM (in an instrument where the piezoscanner is situated beneath the sample). Typically the probe is raster scanned while touching the sample surface. As the probe passes over a raised portion of the sample surface repulsive forces increase between the probe and sample, resulting in a change in the cantilever deflection. A feedback circuit is employed to reduce the height of the sample, restoring the cantilever deflection to its original value and maintaining a constant probe-sample force. Three dimensional images, which are representative of sample topography are therefore obtained by monitoring the feedback signal and the lateral position of the AFM probe (adapted from Allen, 1997).

1.2.2.2 *Imaging Modes of the AFM*

There are a number of imaging modes that can be employed to investigate substrate surfaces, depending upon the sensitivity of the sample. The modes available are contact mode, non-contact mode, and tapping mode.

In contact mode the tip is brought into physical contact with the substrate surface. A drawback to contact mode imaging is that it can cause deformation of sensitive biological surfaces due to large repulsive forces experienced between the probe and sample which are in the order of 10^{-9} N (Lindsay, 1993). Non-contact and tapping AFM imaging modes were thus subsequently developed to overcome these limitations.

In non-contact AFM the cantilever is oscillated at its resonant frequency with the probe situated in close proximity to, but not touching the substrate surface. Unfortunately, this technique lacks sensitivity to small changes in probe-sample separation and as a result images demonstrate lower resolution than the other imaging modes available (Magonov & Whangbo, 1996).

Tapping mode imaging combines the high-resolution and rapid image acquisition ability of contact AFM with the non-destructive approach of non-contact AFM. In this approach the cantilever probe is oscillated at its' resonant frequency and the probe gently 'taps' the sample surface. As the probe and sample come into intermittent contact, the vibrational amplitude of the

cantilever lowers. It is these changes in amplitude which are monitored to produce images of sample topography. The determination of the phase shift between the oscillations driving the probe and those produced by the probe during intermittent contact with the surface provides information on surface properties such as adhesion and viscoelasticity, which may otherwise remain undetected by other conventional imaging modes.

The AFM has been employed in the production of high resolution images of biomolecules such as proteins, DNA (Hansma *et al*., 1992), lipid membranes (Thomson *et al*., 2000; Schneider *et al*., 2000) and cells (Hoh & Schoenenberger, 1994). More recently, real time molecular resolution images of biomolecular interactions have been achieved (Martin *et al*., 2000, 2001; Neish *et al*., 2002). The application of the AFM as an imaging tool has frequently been the subject of review (Shao & Yang, 1995; Ikai *et al*., 1996; Hansma *et al*., 1997) and shall not be discussed in detail hereafter.

1.2.2.3 *Measuring Forces*

The measurement of force in biomolecular systems forms the basis of the thesis, and the AFM was employed as a force spectroscopic technique throughout the work described in chapters 2, 4 and 5.

The early years of force spectroscopy was dominated by the AFM. The ability of the AFM to measure discrete adhesive forces, of approximately 10 pN was

first highlighted by Hoh *et al*., (1992) who attributed the force to that required to rupture a single hydrogen bond. Since this time the AFM has been employed to investigate an array of receptor-ligand interactions, protein unfolding mechanics, and intramolecular forces within polymers.

In the application of the AFM as a force sensing technique the deflection of the cantilever is monitored as the probe is brought into contact with the sample surface and then separated. The data retrieved from the deflection of the cantilever is then used to create an illustration of force termed a force-distance curve (Cappella *et al.*, 1997) (Fig. 1.3). It should be noted that such force measurements are performed in liquid environments in order to eliminate capillary forces which would otherwise mask the biomolecular interactions of interest (Weisenhorn *et al*., 1989).

In the approach trace of the force *versus* distance curve the piezo translates the probe in an axial direction towards the surface until a pre-determined maximum load is reached (C). As the probe and sample are brought into close proximity the cantilever is deflected from its equilibrium position (A) in response to attractive forces (the attractive force gradient exceeds the spring constant of the cantilever) causing the probe jump into contact with the sample (B). The forces responsible for this strong attraction are predominantly due to van der Waals forces.

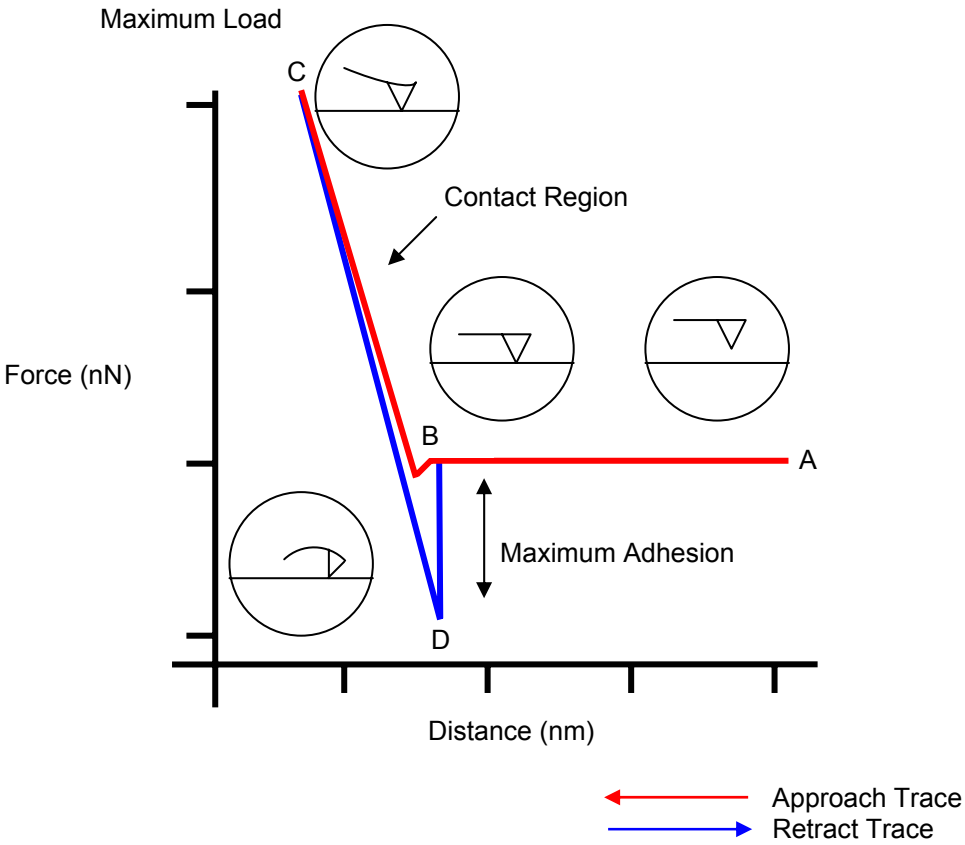

Fig. 1.3 - A schematic of a force distance curve. At the start of a force measurement (A) the cantilever is at its' equilibrium position (resting state). As the probe and sample are brought closer in proximity (approach trace) the probe reaches a distance (B) where the probe 'jumps' into contact with the sample. This 'jump to contact' is a result of the attractive force gradient exceeding the spring constant of the cantilever. The cantilever is continued in a forward motion until a predetermined point of maximum load (C).The probe is then retracted from the sample surface (retract trace), however the probe may adhere to the sample surface due to specific intermolecular interactions (D). Throughout the force measurement cycle cantilever deflection is monitored by a laser beam being reflected off the cantilever to a quadrant photo-diode detector (adapted from Allen, *et al*., 1997).

Once contact is made any continuing forward motion results in repulsive forces acting upon the probe and cantilever, as the electron orbital of the atoms of the probe and sample overlap (Born repulsion). The profile of the contact region can provide detailed information on the nanomechanical properties of the sample as the load is increased, for example, elastic and plastic deformation of the tip/sample (Tao *et al*., 1992; Radmacher *et al*., 1994, 1996).

Once the maximum load is reached the direction of motion is reversed and the probe and sample are separated. Upon retraction, the probe may become adhered to the surface due to either non-specific interactions (capillary forces, electrostatic forces) or by specific interactions between complementary molecules on the probe and the sample surface (D), for example a receptor-ligand pair. As the probe and sample are further separated the probe detaches rupturing bonds formed between the probe and surface, and the cantilever returns to its resting state.

Raw force measurement data was typically obtained in plots where cantilever deflection signal (nA or v) versus distance of z-piezo movement (nm). The cantilever deflection signal can be converted into the force experienced by the probe as follows: initially the deflection signal is converted to the deflection distance (nm) using the gradient (nA nm^{-1} or v nm^{-1}) of the contact region of the force curve. Hooke's Law ($F = -kd$) is then used to convert the deflection distance to force, F (nN), where d, is the distance the cantilever is deflected from its resting state, and k, is the empirically determined spring constant of

the cantilever (discussed in detail below). The actual probe-sample distance is determined by subtracting the deflection distance (nm) from the distance moved by the z-piezo (nm) for the individual data points of the force cycle.

It has been established that for accurate measurement of piconewton scale forces it is essential to experimentally calibrate the cantilever spring constant. The spring constants of commercially available AFM cantilevers can range from 0.01 – 1.0 Nm^{-1}. However, the estimated manufacturer's spring constants can vary significantly from experimentally derived stiffness (Cleveland *et al*., 1993), highlighting the necessity for accurate calibration. The experimental methods available include the measurement of the change in resonant frequency due to the addition of increasing known masses (typically tungsten spheres, 10^{-12} Kg) to the end of the cantilever (Cleveland *et al*., 1993), the measurement of cantilever deflection when pressed against a reference cantilever of known spring constant (Butt *et al*., 1993), or alternatively the measurement of the thermal excitation spectrum of the cantilever (Hutter & Bechhoefer, 1993). Florin *et al*., (1995) experimentally reviewed the above described calibration methods and concluded that the thermal excitation method was the most accurate method for cantilevers with small *k* values, which are commonly employed in biological experiments.

In the thermal excitation technique the probe is positioned a distance away from the sample (where the probe is not affected by long-range forces) so that the motion experienced is purely due to thermal fluctuations. Application of the

equipartition theorem means it is possible to determine the spring force constant, k, from a measurement of the mean-square spring displacement,

$$k = k_B T / \langle q \rangle^2 \qquad (1\text{-}1)$$

where k_B is Boltzmann's constant, T is the temperature (K) and q is the displacement of the oscillator (spring) (m) (Hutter & Bechhoefer, 1993).

1.2.3 Biomembrane Force Probe (BFP)

The BFP employs soft membrane capsules (for example, mammalian red blood cells and synthetic lipid bilayer vesicles) as the force transducer rather than mechanical springs (fig. 1.1c). A functionalised microsphere is commonly attached to the membrane capsule (via biospecific bonds) in order to diversify the type of biomolecular interactions available for studied using this technique (Evans *et al*., 1995). The biomolecular functionalised microsphere is brought into contact with a complementary surface (a functionlised microsphere, a cell, or a lipid bilayer vesicle). Using reflectance interference contrast microscopy, the distances between the microsphere and the substrate can be determined, with a resolution of 5nm (Evans *et al*., 1995). The adhesion force between surfaces is determined from micromechanical analyses of the global deformations of the membrane capsule. As the micropipette is retracted the spherical shape of the membrane capsule will extend by a small displacement proportional to force, and upon bond rupture the membrane recoils back to its undistorted, spherical shape (Evans *et al*., 1995).

The stiffness of the force transducer is determined by membrane tension, which is controlled via the pressurisation of the membrane capsule using micropipette suction. This allows the tension to be varied over a wide range of values to yield effective spring constants between 10^{-6} – 10^{-12} N m^{-1} (Evans *et al*., 1995), providing rates of loading over seven orders of magnitude from 0.1 to 10^{6} pN s^{-1} (Evans *et al*., 1995; Merkel *et al*., 1999). The BFP can assess the widest dynamic range, and thus, can be employed to map intermolecular potentials for dissociation.

1.2.4 Optical Tweezers

The introduction of optical tweezers into the scientific field of biophysics over a decade ago has enabled the measurement of intermolecular forces from 0.01 – 200 pN. The non-destructive trait and the versatility of the technique has provided a means of studying molecular mechanical properties (Yin *et al*., 1995; Wang *et al*., 1998; Tskhovrebova *et al*., 1997; Smith *et al*., 1996; Arai *et al*., 1999), cellular functions (Mammen, *et al*., 1997) and receptor-ligand interactions (Helmerson *et al*., 1997; Stout, 2001).

Optical tweezers exploit radiation pressure for the manipulation of micron and submicron particles (see fig. 1.1d). This trapping force arises due to a transfer in photon momentum as the light is absorbed, scattered, emitted or reradiated upon contact with a refractile particle (see chapter 3 for more detail). The

forces imparted on matter can be broken down into the gradient force and the scattering force. The gradient force, proportional to the gradient of light intensity, acts in the direction of the light intensity. The scattering force, proportional to the light intensity, acts in the direction of light propagation. For stable trapping the gradient force must exceed that of the scattering force, otherwise the particle will be propelled away from the light source along the optical path (Ashkin, 1987).

Calibration of trapping forces must be determined empirically and there are a number of methods available. The escape force method measures the minimal force required for a trapped particle to escape from the optical trap; the drag force method measures the displacement from the optical trap when a known viscous drag force is applied; the equipartition method measures the thermal fluctuations of a trapped particle; and the power spectrum method determines the power spectrum of the position of a trapped particle (for a review the reader is referred to Visscher *et al*., 1996).

A distinct advantage of optical trapping techniques is the degree of control over the applied force. The spring constant of the system can be readily increased or decreased by altering the laser power at the optical focus, providing access to a wide range of loading. Wang *et al*. (1998) and Visscher *et al*. (1999) determined the stalling force for RNA polymerase and kinesin motion, respectively, by gradually increasing the load on the molecules. This ability to rapidly increase, decrease, or terminate the load gives the tweezers the best

time-dependent control of forces applied to single molecules (Leckband & Israelachvili, 2001).

1.3 BIOLOGICAL APPLICATIONS OF FORCE SPECTROSCOPY

To perform force measurements between individual receptor-ligand complexes, be it with the AFM, BFP or optical tweezers, the force transducer and the substrate are functionalised with the receptor and the complementary ligand, respectively (fig. 1.4). The receptor and ligand molecules are then brought into contact allowing the formation of the receptor-ligand complex. These biomolecules are then separated by the retraction of the force transducer.

In order to achieve single molecular interactions between complementary biomolecules a number of approaches can be employed. The binding site availability can be minimised, by the addition of free ligand into the surrounding environment (Florin *et al*., 1994), by controlling surface densities through the addition of lateral spacer molecules (Lee *et al*., 1994a; Hinterdorfer *et al*., 1996), and by the random orientation of molecules on the surface (Allen *et al*., 1999). Alternatively, single molecule can be achieved by the addition of flexible polymer molecules to the probe (Hinterdorfer *et al*., 1996; Schmidt *et al*., 1999; Li *et al*., 1999; Hinterdorfer *et al*., 2000; Janshoff *et al*., 2000) and/or sample architecture (Stevens *et al*., 2000). Theoretically, Poisson statistical analysis of experimental data can provide a method of estimating the quantity of single and multiple interactions (Han *et al*., 1995).

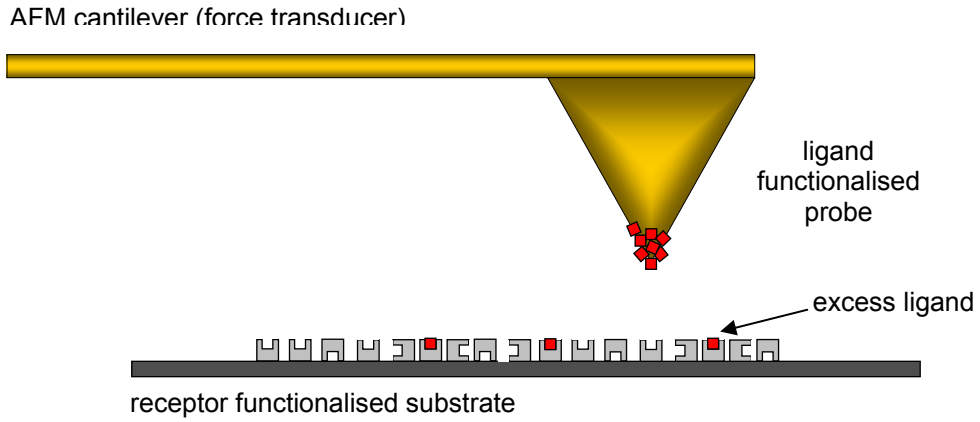

Fig. 1.4 - A schematic of the experimental procedure employed for the measurement of intermolecular forces between receptor-ligand interactions. The example illustrated is for the AFM instrumentation, where the AFM probe is typically functionalised with a biomolecule of interest (i.e. ligand) and the substrate is functionalised with the complementary molecule (i.e. the receptor). The majority of the binding sites are inaccessible due to molecule orientation and blocking by the addition of excess ligand, to achieve single molecule interactions. This basic experimental principle also applies to the alternative force sensing techniques, for example optical tweezers and BFP.

The presence of a flexible crosslinker is advantageous not only for the measurement of single molecule interactions, but it also reduces steric hindrance and provides a means of distinguishing between specific and non-specific intermolecular interactions; all of which are discussed below, and represented schematically in figure 1.5. A crosslinker spaces the biomolecule from the surface of the probe, and in doing so it allows the attached biomolecule to move without restriction in the identification of its binding site. This also allows the molecule to assume the correct orientation and conformation for binding (Hinterdorfer *et al*., 1996). Ordinarily, when biomolecules are directly attached to the probe it is difficult to distinguish between intermolecular interactions specific to complex formation between complementary biomolecules, and the non-specific interactions attributable to probe-substrate interactions. In an AFM approach-retract cycle, non-specific interactions are illustrated by a linear extension of the contact region (see fig. 1.5c). However, the addition of a flexible polymer in the probe/sample architecture demonstrates a nonlinear, parabolic-like stretch characteristic (due to the viscoelastic properties of the crosslinker) to the point of bond rupture under applied force (fig. 1.5b). Figure 1.5a inset illustrates this stretching characteristic when an amylose crosslinker is employed in a receptor-ligand interaction performed with the AFM.

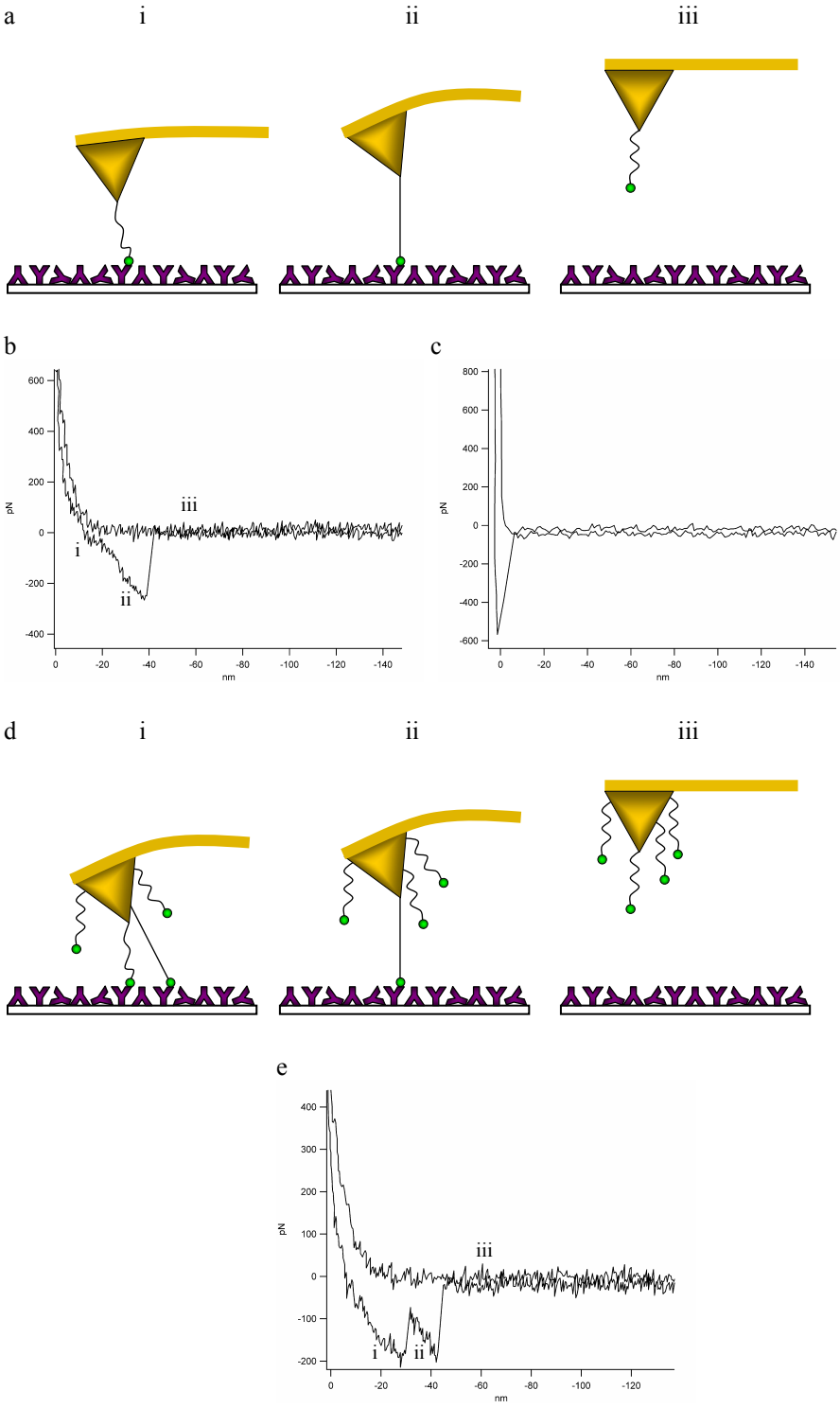

Fig. 1.5 – The application of polymer tethers, a) schematic of force-extension model of the AFM, b) illustrates a typical force-extension profile of the model proposed in (a). c) A typical force-distance profile illustrating a non-specific interaction. d) Model of the sequential rupture of multiple interactions when a polymer tether of fixed known length is employed, e) a typical force-extension profile of the model proposed in (d).

Furthermore, if a crosslinker of a known fixed length is employed then upon the formation of multiple complexes it is probable that the final rupture event to occur under an external force is due to the rupture of a single molecular interaction (fig 1.5d-e) (Janshoff *et al*., 2000).

1.3.1 Intermolecular Interactions

The streptavidin-biotin system was the first receptor-ligand interaction studied using the AFM. The high specificity and affinity (Wilchek & Bayer, 1990) of the complex, and the availability of structural (Weber *et al*., 1989) and thermodynamic (Chilkoti *et al*., 1995; Grubmüller *et al*., 1996; Izrailev *et al*., 1997) data makes it an ideal model system. The unbinding forces for the streptavidin-biotin complex have varied greatly over the years, yielding force estimates from 83 to 410 pN (Florin *et al*., 1994; Lee *et al*., 1994; Moy *et al*., 1994; Chilkoti *et al*., 1995; Allen *et al*., 1996). Such deviations in rupture force have since been attributed to variances in the rate of applied load, where the most probable rupture force is a function of the rate of loading (Evans & Richtie, 1997).

This relationship between the forces required to induce bond failure and the lifetime and energy of the bond was first proposed by Bell (1978). Here, he predicted that the application of an external force to a bond would increase the dissociation rate of that bond, and that the strength of the bond is dependent on the gradient of the binding free energy (Bell, 1978). Evans & Ritchie (1997)

expanded on Bell's predictions, and employing Kramers' rate theory (Kramer, 1940) produced a theoretical model of induced bond failure.

Bonds formed between complementary biomolecules have limited lifetimes and will spontaneously dissociate under zero force upon expiry of that lifetime (Williams & Evans, 2002). Spontaneous dissociation at equilibrium occurs when the bond acquires sufficient energy (through Brownian excitation) to overcome the intermolecular potential of the dissociation landscape (Evans, 1998).

However, if the bond is ruptured at a faster rate than the natural lifetime of the bond, then the bond will demonstrate dynamic strength, and force will be required for dissociation of the complex (Williams & Evans, 2001). Thus, over time the strength of the bond is reduced by thermal activation. The off-rate under applied force, $k_{off}(f)$, for a simple bond confined by a single potential can be described as

$$k_{off}(f) = k_{off} \exp\left[\frac{f}{f_\beta}\right] \qquad (1\text{-}2)$$

where f is force, k_{off} is the natural dissociation rate of the interaction, f_β is the force scale and is defined by

$$f_\beta = k_B T / x_\beta \qquad (1\text{-}3)$$

where, k_B is the Boltzmann constant, T is temperature and x_β is the distance to the energy barrier to rupture.

Figure 1.6 illustrates the effect of a mechanical potential (applied force) on an intermolecular potential (Evans, 1998). The application of an external mechanical potential ($-(f\cos\theta)x$) to a bond confined by a single energy barrier (fig. 1.6a) tilts the energy landscape and lowers the energy barrier relative to k_BT (thermal energy) at the transition state (x_β), and the thermal force scale (f_β) emerges. This distortion of the intermolecular potential exponentially increases the probability that the barrier will be overcome, and hence the probability that the bond will survive decreases exponentially. A combination of the two phenomena provides the probability that a bond will rupture at a given force, where r_f is the rate of loading.

$$p(f) = \frac{1}{r_f} k_{off} \exp\left(\frac{f}{f_\beta}\right) \exp\left\{-\frac{1}{r_f} f_\beta \cdot k_{off}\left[\exp\left(\frac{f}{f_\beta}\right) - 1\right]\right\} \qquad (1\text{-}4)$$

Figure 1.6b illustrates the effect of applied force on the net potential of a dissociation landscape with two energy barriers defining a primary bound state and a secondary metastable state. The prominent barriers encountered along a single dissociation pathway are predicted to emerge and dominate kinetics in succession under increasing force.

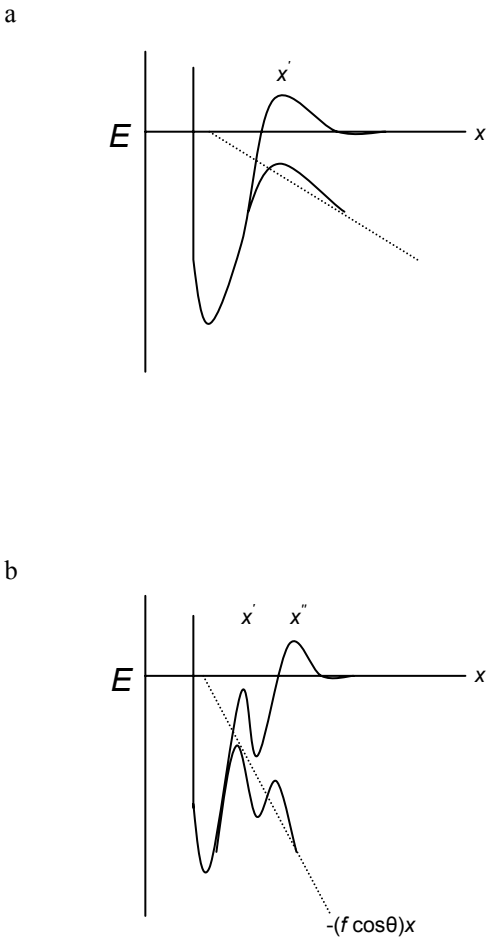

Fig. 1.6 – The effect of an applied mechanical force on an intermolecular potential mapping receptor–ligand unbinding. a) The application of a mechanical potential $-(f\cos\theta)x$ to a bond confined by a single energy barrier; b) a bond confined by two energy barriers (adapted from Merkel *et al*., 1999).

The inner barrier becomes exposed when the outer barrier is driven below it by $\geq k_B T$, where the applied force is greater than the thermal force scale of the outer barrier. Thus, a cascade of barriers over a single unbinding pathway leads to different levels of strength on different time scales (Evans, 1998).

Once again, the streptavidin/avidin-biotin complex provided an ideal system with which to demonstrate Evans & Ritchie (1997) theoretical predictions (Merkel *et al*., 1999; De Paris *et al*., 2000; Williams *et al*., 2000; Yuan *et al*., 2000; Lo *et al*., 2001). Merkel *et al*. (1999) provided the first empirical evidence of the Evans & Ritchie predictions, by elucidating the dynamic strength spectrum for the unbinding of streptavidin/avidin and biotin over six orders of magnitude in loading rate (fig. 1.7). From these investigations it is evident that at least two energy potentials (each characterised by a linear regime) exist in a single forced dissociation landscape of the streptavidin-biotin complex and three energy potentials for the avidin-biotin complex.

To overcome a single energy barrier along the unbinding coordinate a linear decrease in applied force is required with a logarithmic decrease in the rate of loading,

$$F^* = f_\beta \ln\left(\frac{r_f}{f_\beta \cdot k_{off}}\right) \qquad (1\text{-}5)$$

where, F^* is the most probable rupture force (this equation is derived by maximising Eqn 1-4).

A cascade of barriers along the unbinding pathway, as depicted for a single streptavidin/avidin-biotin interaction (fig. 1.7), follows a piece-wise continuous sequence of linear regimes with ascending force scales (Merkel *et al*., 1999). The decrease in force scale from 34 pN (streptavidin/avidin-biotin complex) for one regime to 8 pN, and 13-14 pN for the next regime (streptavidin and avidin, respectively) signifies that the inner barrier (34 pN) has been overcome through thermal activation alone and thus, each successive barrier (8pN for streptavidin, and 13-14 pN followed by 1.4 pN for avidin) along the time coordinate of dissociation then becomes the dominant kinetic impedance.

Since $f_\beta = k_B T / x_\beta$, then the location of the barriers relative to the bound state can be determined. Thus, the force scales determined for the streptavidin-biotin interaction corresponds to barriers situated 0.12 nm and 0.5 nm from the bound state, and 0.12 nm, 0.3 nm and 3 nm for the avidin and biotin complex. The thermal off-rate of each barrier can also be elucidated through the extrapolation of the force scale to intercept the x-axis at zero force.

Subsequent groups have also demonstrated that two energy potentials exist in a single forced dissociation landscape of the streptavidin-biotin complex, suggesting that the dissociation of the complex proceeds via an

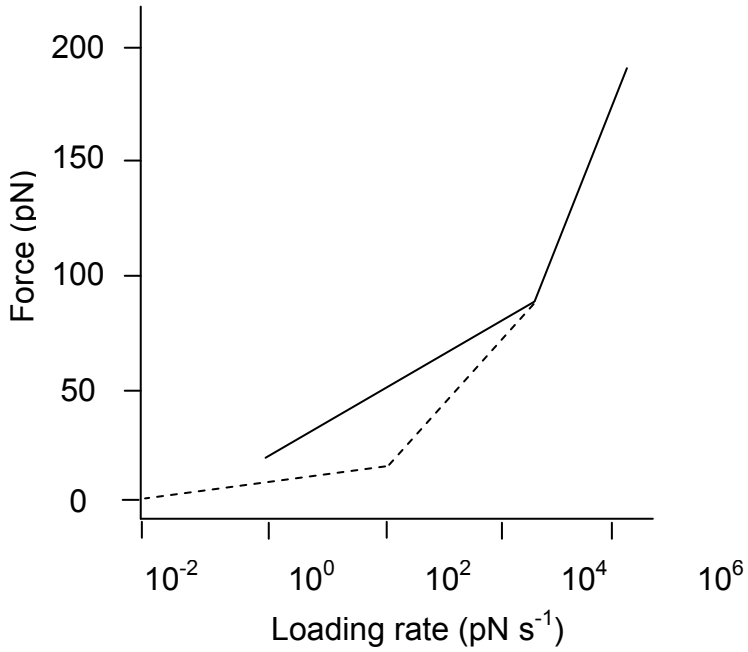

Fig. 1.7 – Dependence of bond strength on the loading rate for streptavidin-biotin and avidin-biotin. The streptavidin-biotin bond exhibits two distinct regimes mapping the position of two different energy barriers along the dissociation pathway (*solid*). The avidin-biotin bond exhibits three such regimes (*dash*). Adapted from Merkel *et al*., 1999.

intermediate state (Merkel *et al*., 1999; Williams *et al*., 2000; Yuan *et al*., 2000; Lo *et al*., 2001).

The specificity of an immunological antibody response to antigens has also inspired the employment of the AFM, BFP and optical tweezers for their study. Dammer *et al*., (1996) successfully measured interactions between polyclonal anti-biotin and biotinylated bovine serum albumin. Since this time antibody-antigen interactions for HSA-antiHSA (Hinterdorfer *et al*., 1996), ferritin and antiferritin (Allen *et al*., 1997; 1999), SpA and IgG (Stout, 2001) and fluorescein and anti-fluorescein single chain fragment (scFv) (Ros *et al*., 1998) have been quantified. More recently, the intermolecular potential of the fluorescein and anti-fluorescein (scFv) complex has been investigated (Schwesinger *et al*., 2000). An energy barrier located 0.4 ± 0.1 nm from a stable minimum with a relative thermal off-rate of 0.003 ± 0.002 s^{-1} demonstrated close agreement with thermal off-rates measured in solution (k_{off} = 0.004 s^{-1}). These similarities suggest that the antibody-antigen bonds studied are confined by a single barrier to dissociation (Schwesinger *et al*., 2000). Similar experiments have reported on the energy landscape of the protein A-IgG interaction (Simson *et al*., 1999; Strigl *et al*., 1999). Theoretical studies have also reported on the effect of dynamic loading on bond rupture through the simulation of antibody-haptene interactions (Heymann & Grubmüller, 1999).

1.3.2 Intramolecular Interactions

The use of force spectroscopy to determine the intramolecular forces fundamental to the formation and consequent stability of secondary and higher order protein conformations is also well established. The first mechanically induced protein unfolding experiments were performed on the modular protein titin (Rief *et al*., 1997; Kellermayer *et al*., 1997; Tskhovrebova *et al*., 1997). Titin is comprised of multiple tandem repeats of Ig and fibronectin III domains, each possessing a β-sandwich structure. AFM measurements of individual titin molecules exhibited periodic rupture events (illustrated by a "sawtooth" pattern) that were attributed to the reversible unfolding transition of the individual domains (Rief *et al*., 1997). Similar findings were reported in optical tweezer force-extension experiments of the muscle protein (Kellermayer *et al*., 1997; Tskhovrebova *et al*., 1997). Moreover, molecular dynamics simulations suggested that the rupture of hydrogen bonds between two anti-parallel strands of the β-sheets of the Ig domains generates the force to induce domain unfolding, as illustrated by the rupture peaks in the AFM force-extension profiles (Lu *et al*., 1998a, b). However, despite the high homology between domains in titin they are not identical. Therefore, it was not surprising that domain-domain variations in stability and unfolding were found to exist (Rief *et al*., 1997; Oberhauser *et al*., 1998). As a result the assignment of individual rupture events to specific domains in the protein is not possible. In order to overcome this predicament, polypeptides comprising of identical domains have been engineered (Carrion-Vazquez *et al*., 1999; Marszalek *et al*., 1999; Lenne

et al., 2000; Li *et al*., 2002). The uniformity of these engineered proteins allows for a defined investigation of protein folding mechanisms based on the identical size, structure and stability of each individual domain (Clausen-Schaumann *et al*., 2000).

Combining high resolution imaging and single molecule force spectroscopy measurements, individual molecules of the membrane protein bacteriorhodopsin have been localised, unfolded and extracted from a lipid bilayer (Oesterhelt *et al*., 2000). Bacteriorhodopsin is structurally comprised of seven closely packed α-helices (named A-G) which upon applied force demonstrated paired unfolding (G and F; E and D) due to interhelical interactions stabilizing secondary structure, except for helices B and C which were shown to unfold sequentially (Oesterhelt *et al*., 2000). The mechanical manipulation of selected molecules, as demonstrated by Oesterhelt *et al*., (2000), should facilitate the elucidation of the unfolding pathways of a broad range of membrane proteins. However, it should be noted that as with receptor-ligand bonding, force induced protein unfolding is also dependent on rate of loading (Rief *et al*., 1997, 1999; Oberhauser *et al*., 1998; Merkel, 2001).

The first polymer studied using single molecule force spectroscopy was DNA (Lee *et al*., 1994; Smith *et al*., 1997). Lee *et al*., (1994) identified intra- and interchain forces between complementary DNA strands associated with sequence specific base pairing. In later years, the unbinding forces for G-C and A-T base pairs were determined, 20 ± 3 pN and 9 ± 3 pN, respectively, by

unzipping synthetic DNA sequences (Rief *et al*., 1999). Employing dynamic force spectroscopy Strunz et al., (1999) extrapolated on Lee's (1994) early work, elucidating a single energy barrier along the unbinding pathway of duplex DNA. Furthermore, the thermal off-rate and distance (from a stable minimum) of this barrier was found to be dependent on the number of base pairs, decreasing exponentially with the number of base pairs in the duplex (Strunz *et al*., 1999; Grange *et al*., 2001).

Double stranded DNA has also demonstrated a melting transition upon applied load (Rief *et al*., 1999), in which the helical double strand splits into two single strands. The degree of applied load necessary to induce this melting transition was found to vary with counter ion concentration, temperature, and sequence (Clausen-Schaumann *et al*., 2000). The effect of proteins (Wang *et al*., 1997; Léger *et al*., 1998; Hegner *et al*., 1999; Bennink *et al*., 1999; Maier *et al*., 2000) and drugs (Krautbauer *et al*., 2000, 2001, 2002) on DNA mechanics is also an exciting topic under current investigation.

1.3.3 Molecular Motors

Molecular motors have also been subject to study using force spectroscopy. Individual rotary motors, for example bacterial flagella, have demonstrated the capacity to generate a torque of up to ~4500 pN nm (Berry & Berg, 1997). Although perhaps the more extensively studied type of molecular motor are linear motors, such as actin-based myosin (Finer *et al*., 1994; Molloy *et al*.,

1995; Veigel *et al*., 1998), microtubule-based kinesin (Svoboda *et al*., 1993; Svoboda & Block, 1994; Kojima *et al*., 1997) and RNA polymerase (Wang *et al*., 1998), all of which are discussed in greater detail in chapter 3.

During the timescale of this research project, critical advances have been made in the empirical determination of the intermolecular forces governing biomolecular interactions (Evans & Ritchie, 1997; Merkel *et al*., 1999). Theory predicts that the force required to induce bond failure is defined by the rate of loading (Evans & Ritchie, 1997). Therefore by performing force measurements over many orders of magnitude of loading rate a profile of the intermolecular potentials governing the dissociation landscape may be elucidated (Merkel *et al*., 1999). The transition from fixed rate force spectroscopy to dynamic force spectroscopy has provided a mechanical means of exploring the energy landscape of molecular recognition processes (Merkel *et al*., 1999) and protein unfolding pathways (Carrion-Vazquez *et al*., 1999). Therefore, such significant advances should not be overlooked when understanding biomolecular interactions.

1.4 SPECIFIC AIMS OF THE RESEARCH PROJECT

The main objective of this research project was to investigate the intermolecular forces that govern receptor-ligand interactions. To achieve this, the complementary force sensing techniques of AFM and optical tweezers were employed. The AFM instrumentation used was either commercially available

or previously constructed in-house. However, optical tweezers are not, at this time, commercially available and thus a significant part of this research project was the construction of the optical tweezer instrumentation.

The AFM is a well-established force sensing technique, and has previously demonstrated its versatility in measuring biomolecular interactions (Lee *et al*., 1994a, b; Dammer *et al*., 1996; Hinterdorfer *et al*., 1996; Rief *et al*., 1997, 1999; Oeserhalt *et al*., 2000). However, to date the AFM has not been utilized to investigate receptor-ligand interactions between pharmaceuticals and their target enzymes. Chapter 2 of this thesis, demonstrates for the first time, the potential of the AFM as a dynamic force sensing instrument to explore the energy landscape of a model drug-enzyme complex. The intermolecular forces governing the dissociation landscape of receptor-ligand complexes are critically dependent on the immediate environment, (for example, pH and salt concentration), protein conformation and steric fit of the interacting sites (van Oss, 1994; Cserháti & Szögyi, 1995). The effect of such influential factors (pH and protein conformation) on the intermolecular forces experienced between a model drug-enzyme complex are also subject to investigation.

Optical tweezers is an alternative force sensing technique, which employs radiation pressure to apply load to interacting molecules. The basis of chapter 3 was to develop and construct an optical trap capable of manipulating biological entities and biologically functionalised microspheres (in the size order of microns) without causing functional denaturation. Chapter 4 provides proof of

principle optical tweezers measurements to demonstrate utility. The chapter investigates the effect argon plasma has upon polymer surface chemistry and protein adsorption. Complementary data to the optical tweezers was obtained from measurements performed by AFM and contact angle analysis.

The AFM and optical tweezers have also been employed as ultrasensitive immunoassay techniques (Dammer *et al*., 1996; Hinterdorfer *et al*., 1996; Allen *et al*., 1997; Helmerson *et al*., 1997). In chapter 5, these two force sensing techniques are utilised to investigate the effect of therapeutic quantities of the anticoagulant heparin on acute myocardial infarction immunoassays. Specifically, the sensitivity of the optical tweezers is explored, as well as, the intermolecular potential governing the antibody-antigen interaction.

CHAPTER 2

The Investigation of Drug-Enzyme Interactions

This chapter describes the employment of the AFM, for the first time, to explore the intermolecular forces that govern the energy landscape of a single unbinding trajectory for the model drug-enzyme complex, dihydrofolate reductase and methotrexate.

2.1 INTRODUCTION

The speed of technical advancements over the last half century has facilitated exploration into biological processes at a molecular level. Molecular recognition involved in drug-receptor complexes have been extensively studied in the hope that an understanding of the molecular origins of binding specificity will provide a foundation for rational drug design. One of the most extensively studied systems is the interaction of the anticancer drug, methotrexate with the enzyme dihydrofolate reductase (DHFR). It is this particular drug-enzyme complex which will form the basis of study within this chapter. The chapter discusses the employment of the AFM to explore the dissociation pathway of the drug-enzyme complex.

Dihydrofolate reductase (DHFR) is a biologically ubiquitous enzyme, which catalyses the NADPH-dependent reduction of folate and dihydrofolate to tetrahydrofolate (eqn.2-1 and 2-2 respectively).

$$\text{Folate} + \text{NADPH} + H^+ \rightleftharpoons \text{7,8-dihydrofolate} + NADP^+ \qquad (2\text{-}1)$$

$$\text{7,8-Dihydrofolate} + \text{NADPH} + H^+ \rightleftharpoons \text{5,6,7,8-tretrahydrofolate} + NADP^+ \qquad (2\text{-}2)$$

Tetrahydrofolate is an important precursor in biosynthetic processes involved in the production of purines, pyrimidines, and several amino acids (Blakely, 1969). Due to the fundamental involvement of DHFR in DNA biosynthesis, the enzyme has been exploited as a target for various antifolate therapies, including anticancer (methotrexate), antibacterials (trimethoprim), and antimalarials (pyrimethamine) (Blakely, 1969) since its discovery by Futterman in 1957.

DHFR is a globular protein with a M_r of 16-21 kDa and to date more than 60 3-dimensional structures of various species of DHFR complexes have been determined. Using NMR spectroscopy and X-ray crystallography extensive structural information has been obtained for the free enzyme (Bystroff & Kraut, 1991), the binary (natural ligand, folate; or antifolate drugs) (Bolin *et al*., 1982; Kuyper *et al*., 1982; Matthews *et al*., 1985a,b; Reyes *et al*., 1995; Sawaya & Kraut, 1997; Polshakov *et al*., 1999) and ternary complexes (cofactor, NADPH) (Bolin *et al*., 1982 (Fig.2.1); Sawaya & Kraut, 1997). More recently, NMR has been used to determine the solution structure of complexed

DHFR (Gargaro *et al*., 1998). As yet, the conformational behaviour of the enzyme throughout the catalytic reaction cycle is unknown. However, five intermediate states over the kinetic pathway have been identified: holoenzyme, Michaelis complex, ternary product complex, THF binary complex, and THF.NADPH complex for *Escherichia coli* (Fierke *et al*., 1987), *Lactobacillus casei* (Andrews *et al*., 1989), *Pneumocystis carinii* (Margosiak *et al*., 1993), mouse (Thillet *et al*., 1990), and human DHFR (Appleman *et al*., 1990). Stopped-flow fluorescence and absorbance spectroscopy have provided the association and dissociation rate constants for such steady-state intermediates (Fierke *et al*., 1987; Andrews *et al*., 1989; Margosiak *et al*., 1993; Thillet *et al*., 1990; Appleman *et al*., 1990). The conformation and motion of the DHFR molecule at these five detectable kinetic intermediates have been elucidated by x-ray crystallography (Sawaya & Kraut, 1997).

Due to the extensive amount of available information on the *Lactobacillus casei* species of the DHFR molecule, the AFM work which constitutes this chapter was performed using this bacterial species, which was generously supplied by Dr. James Feeney, Molecular Structure Division, National Institute of Medical Research, London, UK. As such all DHFR references made beyond this point, unless specified, refer to *Lactobacillus casei* DHFR.

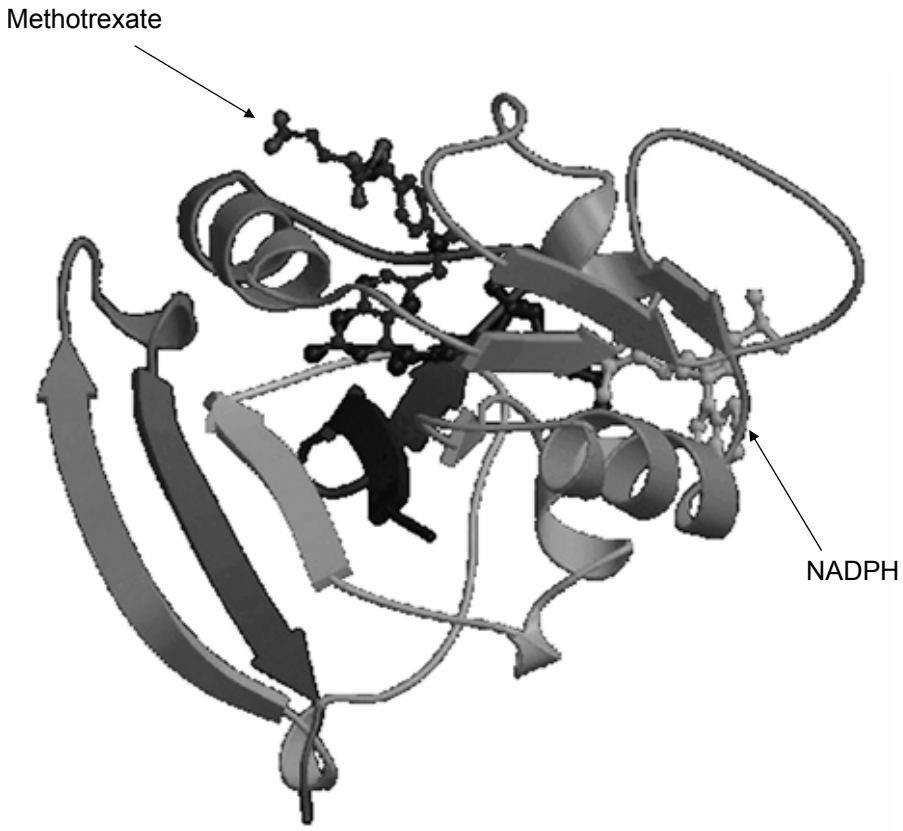

Fig. 2.1 – Crystal structure of *Lactobacillus casei* dihydrofolate reductase complexed with methotrexate and NADPH (Bolin *et al*., 1982).

2.1.1 Structure of the Binary Complex; DHFR-MTX

High-resolution crystal structures of the enzyme-inhibitor complex have also been elucidated (Bolin *et al*., 1982; Kuyper *et al*., 1982; Matthews *et al*., 1985a,b; Sawaya & Kraut, 1997; Gargaro *et al*., 1998; Polshakov *et al*., 1999). In particular, the inhibitor methotrexate has been extensively studied over the last half century as the prevalence of cancer rises, and shall provide the target of study within this chapter. Methotrexate upon binding to DHFR inhabits the same hydrophobic binding site as folate. Demonstrating a higher binding affinity for DHFR than folate, methotrexate acts as an affective competitive inhibitor of DHFR. Figure 2.2 displays the chemical formulae of methotrexate and folate, demonstrating structural similarities. When bound, it is evident that methotrexate adopts an inverse orientation compared to that of folate, but retains the same hydrogen bonding geometry as the enzyme-substrate complex (Bolin *et al*., 1982). The binding site is configured of an αB helix (residues 24-32,), a loop (49-57, which forms a part of the active site) connecting the αC helix (43-48) to the βC sheet (58-62), and a 9 to 23 residue loop (connecting the βA sheet and the αB helix) (Bolin *et al*., 1982; Gargaro *et al*., 1998). The 9 to 23 loop can exist in various conformations in different complexes, namely in an “open”, “closed”, “occluded” or “disordered” state with respect to the active site (Sawaya & Kraut, 1997). X-ray crystallography suggests that the loop adopts a disordered state (a time-average interconversion between the closed and occluded conformations) in the presence of methotrexate, and forms a closed conformation in the ternary complex

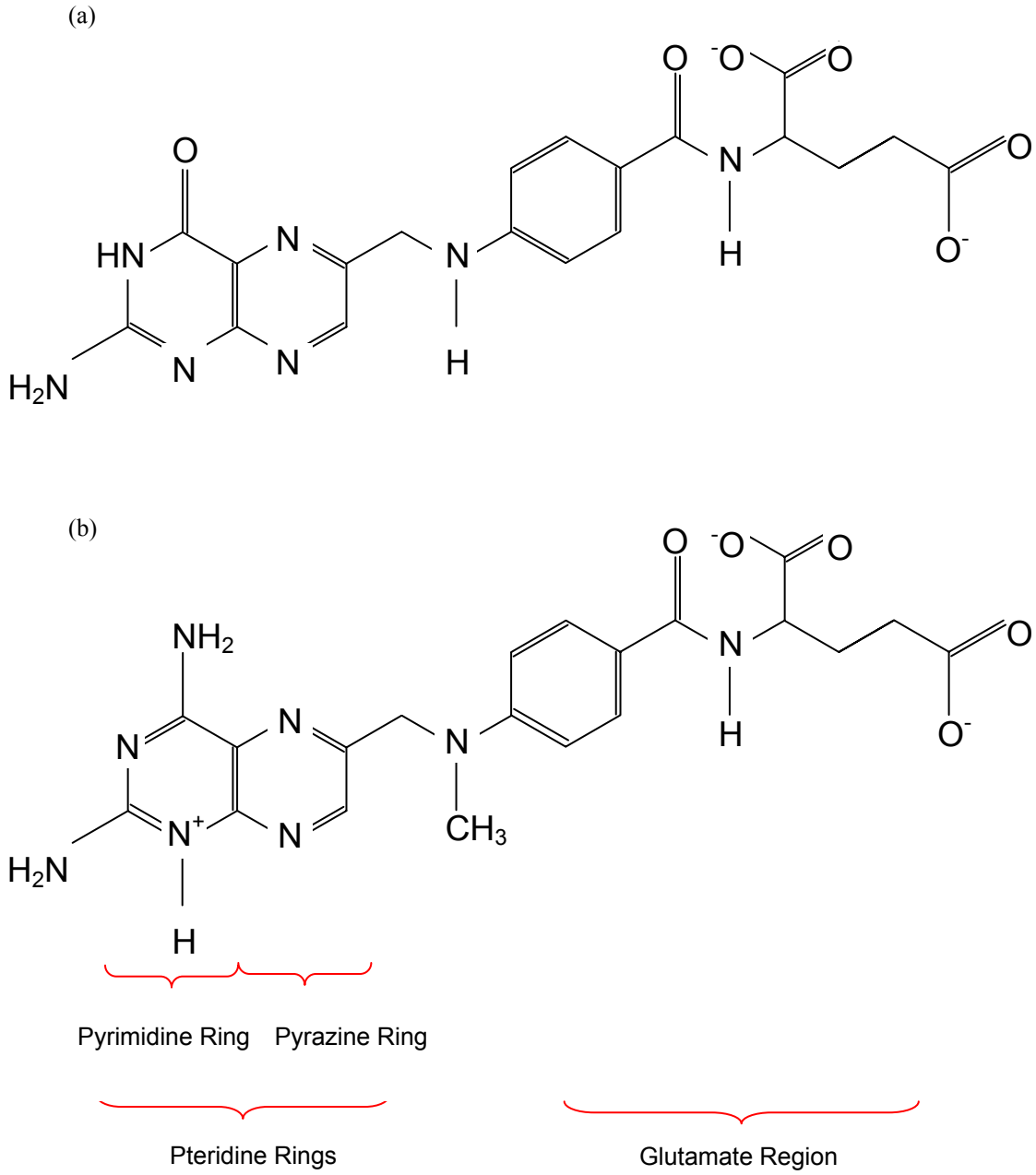

Fig. 2.2 - (a) Chemical formulae of folate; (b) chemical formulae of methotrexate

(MTX-NADPH) (Sawaya & Kraut, 1997). However, recent NMR spectroscopy of the solution structure of the DHFR-methotrexate complex, indicates that the 9-23 loop is present in a closed conformation (Gargaro *et al*., 1998). In the closed conformation the 9-23 loop extends across the active site forming a short antiparallel β-sheet and a type III′ hairpin turn. Hydrogen bonding occurs between the hairpin and the β-sheet, Gly14 to Asp125 and Asp16 to Asp125 adding support to the conformation (Gargaro *et al*., 1998). In *E. coli* an additional hydrogen bond is formed between Asn18 in the hairpin and His45 in the αC helix which effectively seals the active site (Sawaya & Kraut, 1997). The corresponding residues in *L. casei*, Gly17 and Arg44, respectively, cannot hydrogen bond, however the solution structure suggests that despite the lack of hydrogen bonding between the hairpin and the αC helix the 9-23 loop shows no desire to enter the nicotinamide binding site and take the occluded conformation (Gargaro *et al*., 1998).

A number of intermolecular bonds are formed upon the association of methotrexate to DHFR. The bond formations involved in the binary complex are described in detail in the text below, to assist comprehension they are also summarised in tables 2.1 and 2.2, and are depicted schematically in Fig. 2.3. The 2,4-diaminopteridine ring of methotrexate forms a number of hydrogen bonds both directly and indirectly with the enzyme. A portion of the pteridine binding site consists of a triad of residues, Asp26, Thr116, and wat201, that form a tightly constrained polar pocket, displaying complementary geometry and charge distribution to the three protons positioned on the N1 and the

Constituent of Methotrexate	Bond formed with *Lactobacillus casei* DHFR		Reference
	DHFR	Details	
Pyrimidine Ring			
4 – amino grp	Leu 4 – carbonyl grp Ala 97 – carbonyl grp		Bolin *et al*., 1982
2 – amino grp	Asp 26 – Oδ1carboxylate Wat-201 (structurally conserved water molecule)	→Thr 116 →Thr 116 (γ-hydroxyl Proton) →Asp 26 Oδ1 →Leu 114	Bolin *et al*., 1982 Bolin *et al*., 1982 Gargaro *et al*., 1998
N1	Asp 26 – Oδ2carboxylate		
Pyrazine Ring			
N8	Wat-253	→Oδ2 Asp 26 →Wat-217 →Leu 23 (amide N) →N∈ Trp 21	Bolin *et al*., 1982
Glutamate			
α-carboxylate	Arg 57 – guanidinium		Bolin *et al*., 1982 Sawaya *et al*., 1997 Gargaro *et al*., 1998 Feeney *et al*., 2000
γ-carboxylate	His 28 – imidazole		

Table 2.1 Hydrogen bonding interactions between *Lactobacillus casei* DHFR and MTX (adapted from Bolin *et al*., 1982). Arrow indicates further hydrogen bonding.

Constituent of methotrexate	**Contact formed with *Lactobacillus casei* DHFR**
6-Me-Pteridine	Leu4 side chain Trp5 main chain Ala6 N Cα Cβ Leu19 side chain Leu27 side chain Phe30 side chain Ala97 Cα Cβ Nicotinamide ring
N10-methyl	Leu19 side chain Ser48 side chain Wat439
P-aminobenzamide	Leu27 side chain Phe30 side chain Phe49 side chain Pro50 side chain Leu54 side chain
L-Glutamate	Leu27 side chain Phe30 side chain Arg31 Cβ Cγ Cδ Leu54 side chain

Table 2.2 Hydrophobic and van der Waals interactions between *Lactobacillus casei* DHFR and methotrexate (Bolin *et al*., 1982)

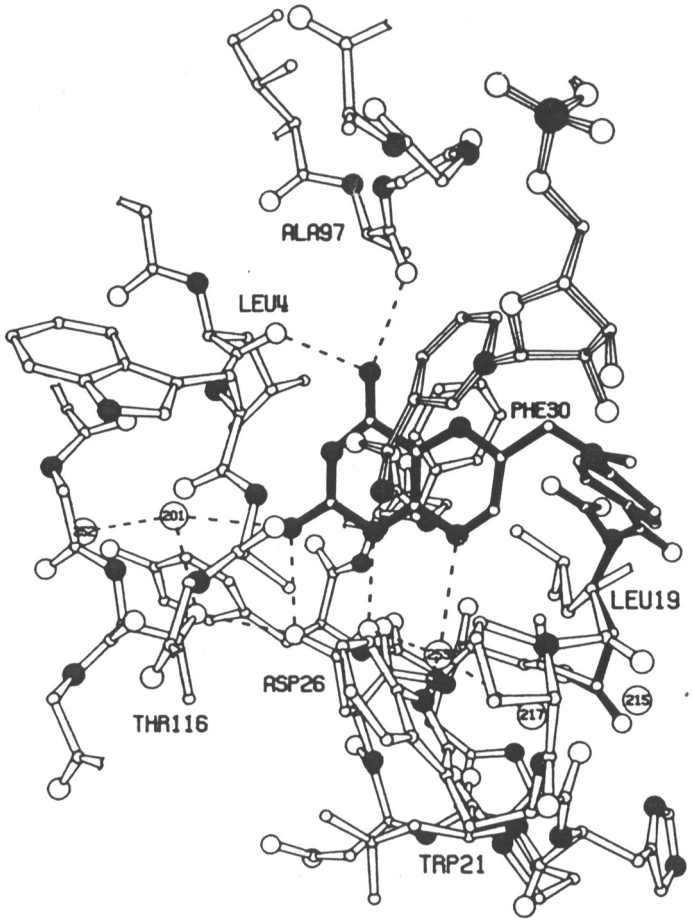

Fig 2.3 – A structural bond map of the pteridine-binding site of *Lactobacillus casei* DHFR complexed with methotrexate (Bolin *et al*., 1982). DHFR is illustrated by *open bars*, the *solid bars* represent methotrexate, and the *striped bars* indicate a portion of the NADPH molecule. *Small open circles* represent carbon atoms, *large open circles* the oxygen atoms, and the *black circles* are the nitrogen atoms. Fixed solvent molecules are indicated by the *large numbered circles*. The formation of hydrogen bonds between DHFR and methotrexate are demonstrated by the *dashed lines*.

2-amino group of methotrexate (Bolin *et al*., 1982). Hence, N1 hydrogen bonds to Asp26(Oδ2), and the 2-amino group form hydrogen bonds with Asp26(Oδ1) and wat201 (structurally conserved water molecule), both of which, in turn hydrogen bond to Thr116 (Gargaro *et al*., 1998). The 4-amino group of the pteridine ring hydrogen bonds to the carbonyl oxygen of Leu4 and Ala97. The pyrazine portion of the pteridine ring does not directly hydrogen bond with the enzyme. Instead, N8 forms a weak hydrogen bond with the structurally conserved water molecule wat253, facilitating Wat253 to form a number of intermolecular bonds. This structurally conserved water molecule hydrogen bonds to Asp26(Oδ2) and to wat217. In turn the wat217 is hydrogen bonded to the 9-23 loop via the backbone amide nitrogen of Leu23 (Bolin *et al*., 1982; Gargaro *et al*., 1998). Previously it had been suggested that N8 is also hydrogen bonded directly with Asp26 (Matthews *et al*., 1979), but more in depth x-ray crystallographic studies of the binary complex have shown that this is not the case (Bolin *et al*., 1982; Gargaro *et al*., 1998).

The benzoyl ring of methotrexate does not form any bonds with DHFR, but exhibits ring-flipping behaviour (Clore *et al*., 1984; Verma *et al*., 1996), demonstrating a ring-flipping rate of 7×10^3 s^{-1} at 298 K for the binary complex and 2×10^4 s^{-1} at 298 K for the ternary complex (Clore *et al*., 1984). The α- and γ-carboxylates of the glutamate region ("tail end") of methotrexate hydrogen bonds to the guanidine group of Arg57 and the imidazole group of His28, respectively (Bolin *et al*., 1982; Gargaro *et al*., 1998). Correlated rotation of these bonds has been demonstrated (Feeney, 2001). However, due

to limitations of the AFM (as discussed in chapter 1) it is not possible to probe the outer boundaries of the energetic landscape for dissociation. Thus, it is unlikely that the hydrogen bonding experienced between the glutamyl carboxylates and the enzyme, and the potential effect of the flipping motion of the benzoyl ring on dissociation will be probed in the series of AFM force studies explored in this chapter.

The availability of such detailed structural bonding maps provides an insight into the number and type of bonds involved in the association and dissociation pathways.

2.1.2 Ternary Complex; DHFR-MTX-NADPH

Structural NMR studies reveal that the conformation of the binary complex (DHFR-MTX) is comparable to the ternary complex, DHFR-MTX-NADPH, where the 9-23 loop forms a "closed" conformation in both the binary (Gargaro *et al*., 1998) and ternary complex (Sawaya & Kraut, 1997; Gargaro *et al.*, 1998), suggesting that the NADPH binding site is essentially preformed in the binary complex (Gargaro *et al*., 1998). Furthermore, bound methotrexate occupies a similar position in the binary and ternary complexes, and thus no major conformational change takes place in the protein when NADPH binds to the binary complex (Gargaro *et al*., 1998).

Despite this lack of conformational change between the binary to the ternary complex a cooperative relationship between the coenzyme and

substrate/inhibitor exists (Perkins & Bertino, 1966; Otting & Heunnekins, 1972; Williams *et al*., 1978a,b; Birdsall *et al*., 1978, 1980a,b; Roberts *et al*., 1974). This type of cooperative relationship is not unique to DHFR, and has been documented in other dehydrogenases (Theorell & Yonetani, 1963; Woronick, 1963; Kolb & Weber, 1975; Holbrook *et al*., 1975).

Birdsall *et al*., 1980a demonstrated through fluorescence quenching studies that there was variation in the binding constants among the reduced and the oxidised forms of the coenzyme. Reduction of the nicotinamide ring results in a much tighter binding of the coenzyme to the free enzyme and to substrate/inhibitor complexes compared to its oxidised counterparts. The study went on to show that the coenzyme binds significantly tighter to the enzyme-substrate and enzyme-inhibitor complexes than to the enzyme alone. In particular methotrexate increased NADPH binding by a factor of 675 (6.8 x 10^{10} M^{-1}), and to a lesser extent trimethoprim which increases NADPH binding by a factor of 135 (1.35 x 10^{10} M^{-1}) (Birdsall *et al*., 1978, 1980a). Since cooperativity of ligand binding is reciprocal then the coenzyme increases inhibitor binding by an equivalent extent (Williams, *et al*., 1979; Birdsall, *et al*., 1980a). Baccanari *et al*., 1982 demonstrated that NADPH, in turn, increases the affinity of bacterial DHFR for diaminobenzylpyrimidine inhibitors, and that this affinity varied with degree of methoxy substitution of the inhibitor. Moreover, NADPH increases the binding of the ρ-aminobenzoyl-L-glutamate fragment of methotrexate, with a larger effect on the binding of the 2,4-diaminopyrimidine fragment (Birdsall *et al*., 1980b). Such variations in

cooperativity between different forms of coenzyme and various inhibitors suggests that the binding constant of the coenzyme is dependent upon the structure of both ligands (Birdsall *et al*., 1978, 1980a,b; Baccanari *et al*., 1982), and thus some form of interaction occurs between the two. Earlier studies also suggested that the nicotinamide of NADPH makes contact with the pyrazine portion of the pteridine ring of methotrexate in the ternary complex of *Lactobacillus casei* (Matthews *et al*., 1978a). Moreover, in the ternary complex, residues in the M20 loop of *E.coli* (9-23 loop of *L.casei*) interact with the nicotinamide-ribose moiety of the coenzyme in the crystal structures of DHFR complexes containing $NADP^+$ (Sawaya & Kraut, 1997), potentially contributing to cooperativity.

However in light of all this information, the source of cooperativity remains elusive.

2.1.3 The Role of Asp26 in Inhibitor Binding

The presence of the ionizable carboxyl Asp residue in the active site (Bolin *et al*., 1982) has generated considerable interest in the role of the residue in enzyme catalysis (Williams & Morrison, 1981; Stone & Morrison, 1984, 1988). In the natural ternary complex, it is suggested that the protonation of Asp27 (*E.coli*) results in a transfer of protonation to the N5 of dihydrofolate facilitating hydride transfer leading to the production of tetrahydrofolate (Stone & Morrison, 1984).

Conformational changes in the DHFR molecule that correspond with changes in pH have been reported (Birdsall *et al*., 1982; Stone & Morrison, 1984). Using ^{1}H and ^{13}C NMR techniques three interconverting conformational states of the DHFR-folate-$NADP^{+}$ complex have been identified, and the relative proportions of these states are pH dependent (Birdsall *et al*., 1982). This dependency of conformation on pH has been linked to the protonation of the Asp26 residue (Birdsall *et al*., 1982; Stone & Morrison *et al*., 1984). The carboxylate group of Asp26 is the only group available for protonation in the substrate binding site, producing a charged donor in the substrate binding site, leading to a disruption in bond formation in the ternary complex (Birdsall *et al*., 1982; Stone & Morrison *et al*., 1984).

The interaction between the carboxyl group of Asp26 and the N1 nitrogen of 2,4-diaminopteridine inhibitors was made aware by Cocco *et al*. in 1981. Studies around the same time also showed that the N1 of methotrexate is protonated when bound to DHFR, producing a charged donator (Subramanian & Kaufman, 1978; Gready, 1980; Cocco *et al*., 1981; Cheug *et al*., 1983). X-ray crystallographic studies showed that Asp26 demonstrates a complementary charge distribution to the proton on N1 (Bolin *et al*., 1982), implying that an interaction between Asp26 and N1 would be ionic in nature (Bolin *et al*., 1982). NMR spectroscopy and NOESY analysis of the solution crystal structure of the enzyme-inhibitor complex also implicates the N1 proton in a hydrogen bonding interaction with the carboxyl group of Asp26. Asp26 being

the nearest charged group acceptor (a distance of less than 4 Å) to the protonated N1, the next closest being 8 Å away (Gargaro *et al*., 1998). The length of a hydrogen bond is ~ 2-3 Å (Israelachvili, 1991; Khan, 2000), therefore Asp26 is the only available group. Thus, the protonation of the Asp26 residue is likely to result in a disruption in bond formation between Asp26 and the N1 group of methotrexate.

In this chapter the AFM is employed to investigate the rupture forces of the drug-enzyme complex, DHFR-methotrexate, in their binary and ternary conformations. A dependency of force required to rupture the DHFR-methotrexate complex on the rate of dissociation is demonstrated. In summary, the association and dissociation processes exhibited by receptor-ligand complexes occur at a state of equilibrium where zero force is applied (Evans, 1998). If detachment occurs prior to diffusive relaxation then the bond will demonstrate dynamic strength, and force will be required for dissociation of the complex. Thus, the required force is dependent upon the timeframe of the dissociation event. Inducing dissociation through the application of force over wide time scales produces detailed maps of the energy landscapes which contour the dissociation pathway (Evans, 1998). Since dissociation rate is exponentiated under force a wide range of loading rates are required to explore the whole dissociation pathway. For a more detailed discussion on the theory of dissociation kinetics for receptor-ligand complexes the reader is directed to chapter 1.

Previous studies on the complex (DHFR-methotrexate) describe the structural conformations, and the association and dissociation constants for such conformational states of the enzyme. However, the dissociation kinetics over the unbinding pathway for the complex remains poorly understood. Through the combination of dynamic force spectroscopy, molecular modelling and the structural data it is possible to elucidate the energy landscape of unbinding process, providing thermodynamic and dissociation rate details over the complete dissociation landscape. However, due to the wide range of loading rates required, the application of AFM for dynamic force spectroscopy is restricted to a limited region of the force spectrum. This chapter identifies a barrier in the energy landscape for the dissociation pathway of DHFR-methotrexate. The effect the cooperative relationship between coenzyme and inhibitor has upon barrier, as well as the effect of pH on the unbinding process are also discussed.

2.2. MATERIALS & METHODS

All materials were purchased from Sigma, Poole, UK, unless stated otherwise.

In studying the rupture forces between the binary and ternary complex, silicon nitride AFM probes were functionalised by the attachment of a methotrexate-modified agarose bead. The methotrexate was bound covalently to the agarose bead via an 8-atom carbon linker. Rupture forces were recorded between the probe and a *Lactobacillus casei* DHFR monolayer covalently attached to

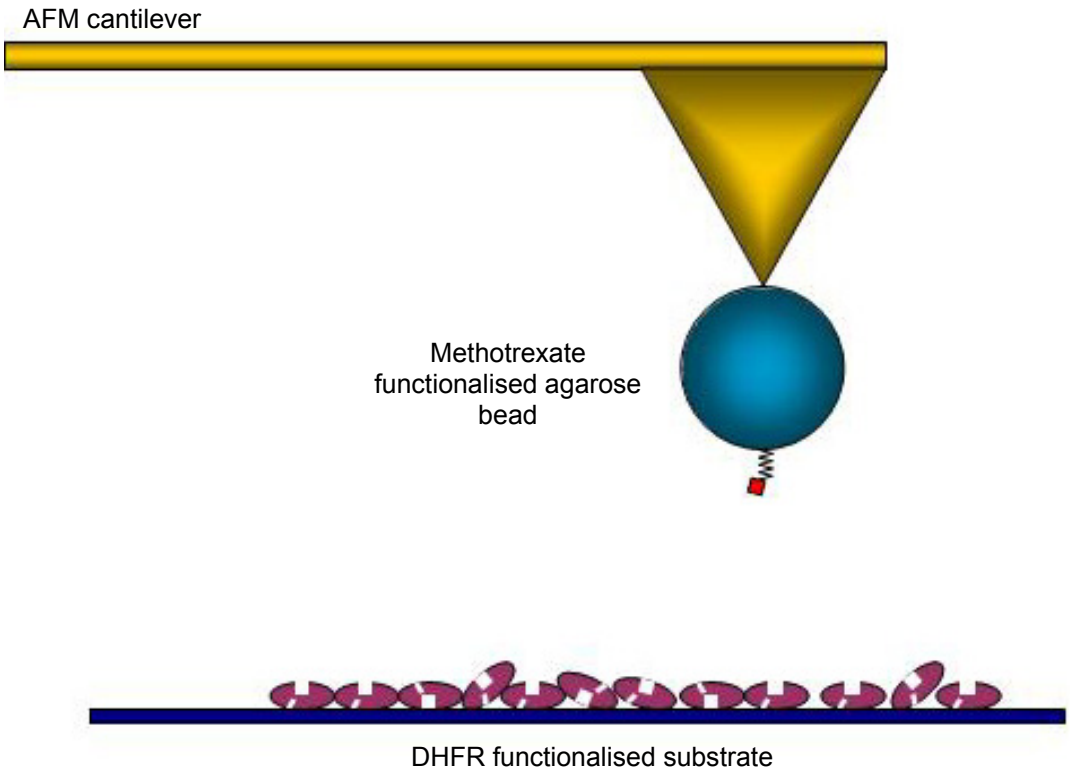

Fig 2.4 – Schematic illustrating basic experimental protocol. The *red square* represents methotrexate, which is attached to an agarose bead (*blue* circle) via an 8-atom carbon linker illustrated by a *zig-zag structure*. The modified agarose bead is affixed to the apex of a cantilever probe. DHFR represented by the *burgundy ovals*, is covalently immobilised to a silicon substrate.

polished silicon wafers via the ε-amino groups of the lysine residues available on the surface of the protein (Fig. 2.4).

2.2.1 Probe Functionalisation

Silicon nitride (Si_3N_4) cantilevers (Digital Instruments, Santa Barbara, CA, USA) were functionalised with methotrexate via the attachment of an individual methotrexate-modified agarose bead to the apex of the cantilever. Methotrexate was non-selectively covalently bound by either the α- or γ-carboxylate group of the glutamate region to the agarose bead (cross-linked 4%) via an 8-atom carbon linker (Sigma, Poole, UK). Individual drug-modified agarose beads were attached to the cantilever with Araldite-Rapid™ epoxyadhesive (Bostik Ltd, Leicester, UK), and positioned using a micromanipulator (Research Instruments Ltd., Cornwall, UK) viewed under an optical microscope. The bead radius was obtained using an eye-piece micrometer as part of the optical microscope, and measured 40 ± 6 μm. This functionalisation strategy reduces steric hindrance due to the freedom of movement of the agarose polymer and the carbon linker. The addition of the agarose bead and carbon linker also provides an extension to the cantilever tip acting as a "molecular fishing rod" promoting single molecular interactions.

2.2.2 Sample Immobilisation Chemistry

Utilising a preparation method modified from Vinckier *et al.,* 1995 (as previously described by Allen *et al.,* 1997), a concentration of 0.03 mg mL^{-1} *Lactobacillus casei* DHFR (gratefully received from James Feeney, Molecular Structure Division, National Institute of Medical Research, London, UK) was covalently immobilised onto polished silicon wafers (Rockwood, Riddings, UK). In preparation for protein immobilisation silicon wafers were cleaned by immersion in a 30 % v/v solution of hydrogen peroxide and sulphuric acid (piranha solution) for 15 min at room temperature. The silicon wafers were rinsed thoroughly in high-purity deionised water (purified using an ELGA water system - resistivity 15 MΩ cm) and dried under a flow of nitrogen. Following cleaning the silicon substrates were oxidised in 20 Pa oxygen plasma for 1 min at 100W using a RF Plasma Barrel Etcher PT7100 (BIO-RAD Polaron Division). The silicon wafers were incubated in 4 % v/v 3-aminopropyldimethylethoxysilane (3-APDES) and toluene for a period of 2h at room temperature, producing NH_2 groups at the substrate surface. The silanised substrates were rinsed in propanol, methanol and high-purity deionised water by sonication (Decon FS Minor, Decon Ultrasonics Ltd., Hove Sussex, UK) for 1 min, respectively, to remove any loosely bound silane. The amine functionalised substrates were then activated via incubation in a 10 % v/v solution of glutaraldehyde (Grade II, 25 % aqueous solution) in sodium phosphate buffer (100 mM, pH 7.4) for 1 h at 2-8 ºC (schematic representation of protocol in fig. 2.5). The residual groups are activated and are able to covalently couple to the side chain ε-amino groups of lysine residues of the protein.

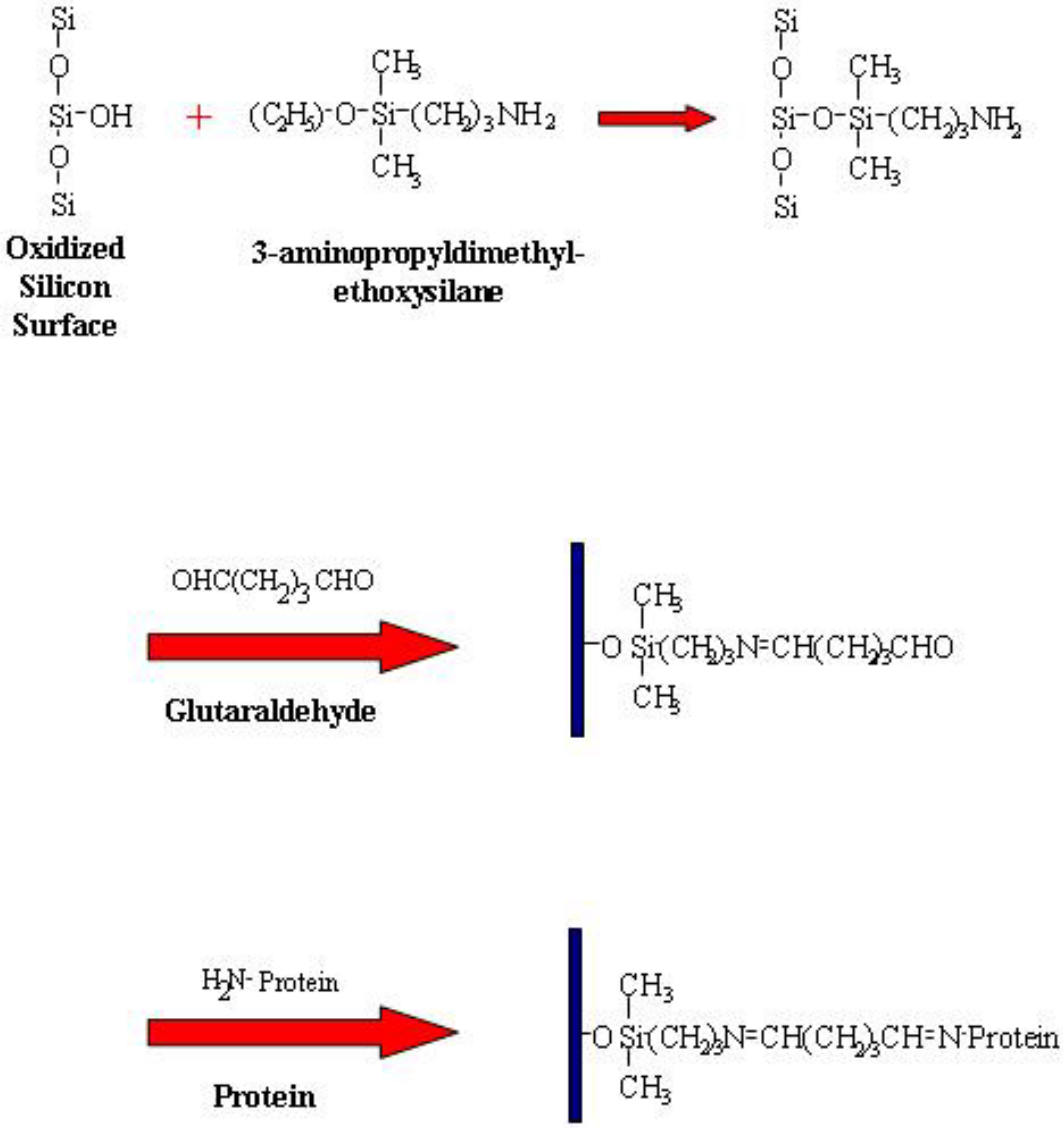

Fig 2.5 – Scheme of chemical modification of silicon substrate for covalent attachment of protein (modified from Vinckier *et al*., 1995).

Following a high-purity deionised water wash, the chemically modified silicon substrates were incubated in 0.03 mg mL^{-1} DHFR. Prior to AFM analysis the DHFR samples were rinsed thoroughly in high-purity deionised water to remove any non-covalently bound protein.

2.2.3 AFM Imaging

Tapping mode AFM was employed to assess the surface coverage of the covalently immobilised DHFR to silicon substrates. Topographical images were obtained in a liquid environment of 100 mM sodium phosphate buffer, pH 7.4, at a scan rate of 2 Hz using a multimode AFM with a Nanoscope IIIa Controller (Digital Instruments, Veeco Metrology Group, Santa Barbara, CA, USA). Unfunctionalised V-shaped silicon nitride cantilevers with integrated pyramidal oxide-sharpened probes were employed. The manufacturer's estimated spring constant for the cantilevers employed is 0.06 Nm^{-1} (Digital Instruments, Veeco Metrology Group, Santa Barbara, CA, USA). Topographical images are displayed as greyscale representations, where the higher features appear lighter in colour.

2.2.4 AFM Force Measurements

AFM force measurements were obtained in 100 mM sodium phosphate buffer, pH 7.4, unless otherwise stated.

2.2.4.1 *Rate Studies*

Force measurements were obtained between a methotrexate functionalised AFM probe and a DHFR monolayer, at piezo-retract rates of 1.0 μm s^{-1}, 0.5 μm s^{-1} and 0.1 μm s^{-1}. AFM force measurements were performed using instrumentation built and developed in the Laboratory of Biophysics and Surface Analysis (Lomas, 2000; PhD Thesis, University of Nottingham, UK).

2.2.4.2 *Cofactor Studies*

Force measurements were obtained between methotrexate and DHFR (as previously described), in the presence and absence of 1.2 μg mL^{-1} NADPH (Sigma, Poole, UK). Measurements were recorded at a retract rate of 0.5 μm s^{-1}, using a commercial AFM instrument, Molecular Force Probe (Asylum Research, California, USA).

2.2.4.3 *pH Studies*

Force measurements were recorded between methotrexate and a DHFR, at different environmental pH, pH 7.4 and pH 5.6, 100 mM sodium phosphate buffer. Measurements were acquired at a retraction rate of 1.0 μm s^{-1}, using an AFM instrument built and developed in the Laboratory of Biophysics and Surface Analysis (Lomas, 2000).

2.2.4.4 *Control Studies*

For each investigation a control system was performed to ensure that the adhesive interactions observed were specific in nature, and that the DHFR was present in an active form. The methotrexate binding sites on the DHFR molecules were blocked through the addition of free methotrexate (Sigma, Poole). DHFR samples were incubated in 0.64 μg mL^{-1} methotrexate (100 mM sodium phosphate buffer, pH 8.0) for a period of 1 h at room temperature. Measurements were re-recorded.

In addition force measurements were performed between an unmodified 4% cross-linked agarose beaded probe (XC Corporation, Agarose Bead Technologies, Lowell, MA, USA) and a DHFR monolayer to verify that the forces recorded in the experimental systems are due to the interaction between the drug and enzyme. Measurements were acquired at a retract velocity of 1.0 μm s^{-1} in a 100 mM sodium phosphate buffer environment, pH 7.4, using the AFM instrumentation constructed in the Laboratory of Biophysics and Surface Analysis (Lomas, 2000)

All force measurements were repeatable at the same point on the sample surface, indicating that the functionalised methotrexate bead probe remained intact during measurements and that the DHFR molecules were not being pulled off the silicon wafer during the experimental studies. The same functionalised probe was used to acquire all force data throughout both the

experimental and control systems. It was necessary to utilise the same probe in order to prevent the introduction of unnecessary errors due to variations in spring constant of the cantilever probe and methotrexate bead size.

2.2.4.5 *Force Analysis*

Raw force data retrieved displayed the cantilever deflection signal (nA) versus distance of z-piezo movement (nm). Plots were converted to force (nN) versus probe-sample distance (nm) (conversion method previously described in chapter 1). The cantilever spring constants were calibrated with the methotrexate-modified agarose bead attached using the thermal resonance method proposed by Hutter *et al*., 1993. For a detail discussion of the thermal resonance calibration method the reader is directed to chapter 1. The calibration of spring constants following the attachment of the bead encompasses the potential affects the presence of the bead and glue may have on the compliance of the cantilever. The diameter of the hydrated MTX-modified agarose beads were 40 ± 6 μm and contributed marginally to the hydrodynamic force present in the system. The hydrodynamic drag applied to a 40 μm bead over the velocities studies was estimated using Stokes Law, where η is the viscosity of the suspension media (water is 0.001002 N m^{-2} s at a temperature of 293 K), r is the sphere radius (m) and v is the velocity (m s^{-1}).

$$F = 6\pi\eta r v \qquad (2\text{-}1)$$

At 1.0 μm s^{-1} a hydrodynamic force of 0.38 pN is exerted on a 40 μm bead, at 0.5 μm s^{-1} a force of 0.19 pN is exerted, and at 0.1 μm s^{-1} a force of 0.038 pN. Such forces are well within the instrumental noise (~10 pN), and therefore will have negligible affect upon the rupture forces observed. It should be noted that the affect of cantilever hydrodynamics upon rupture force values is at present poorly understood and is currently a subject of debate.

Rupture forces indicative of specific interactions (refer to 2.3.2) were plotted as force *versus* frequency histograms. The histogram peak values were plotted as a function of logarithm of the retract rate, and initial approximations for k_{off} and f_β, were derived from this using equation 1-3 ($f_\beta = k_\beta T / x_\beta$). The probability that a complex will dissociate at a given force is expressed in terms of loading rate (r_f) (in our case velocity), k_{off} and f_β values. Employing approximations of these values and utilising Eqn. 1-4 a model force distribution was derived (Evans, 1999) and overlaid onto each histogram, producing the most probable rupture force for the histograms. A distribution of dissociation forces is expected at any given loading rate as a result of kinetics. However, the distribution of forces will also be broadened due to error. A precise quantification of the experimental error is currently not possible. Although there are several potential sources of error, the thermal fluctuation method for the determination of the cantilever spring constant (Hutter *et al*., 1993) has probably the most significant impact upon error, with an absolute uncertainty at ~10% (Florin *et al*., 1995).

2.3 RESULTS AND DISCUSSION

2.3.1 AFM Imaging

DHFR was covalently immobilised to silicon substrates and imaged using tapping mode AFM. Imaging was performed using unfunctionalised sharpened silicon nitride probes, scanned across the surface at a rate of 2 Hz in a liquid environment of 100 mM Sodium Phosphate buffer, pH 7.4. 1μm^2 and 500 nm^2 topographical images were taken to verify protein deposition and determine surface coverage. The images are displayed as grey scale representations of the sample topography.

Fig. 2.6a and b display topographical images of silicon substrates following chemical modification and subsequent protein attachment. Fig. 2.6a presents a 1 μm^2 image of the sample surface. Fig. 2.6b displays a reduced scan size to 500 nm^2 producing enhanced spatial resolution of the sample topography. The uniformity of the globular features displayed in the topographical images (fig. 2.6a and b) suggests that monolayer coverage is achieved. The approximate diameter of the globular features observed is 10 ± 2 nm. The precise dimensions of the DHFR molecule, 4.39nm x 3.46nm, was determined using X-ray crystallography data (Davies, *et al*., 1990), thus when probe geometry responsible for broadening effects and probe compliance has been taken into consideration, the features illustrated may be attributed to individual DHFR molecules.

a

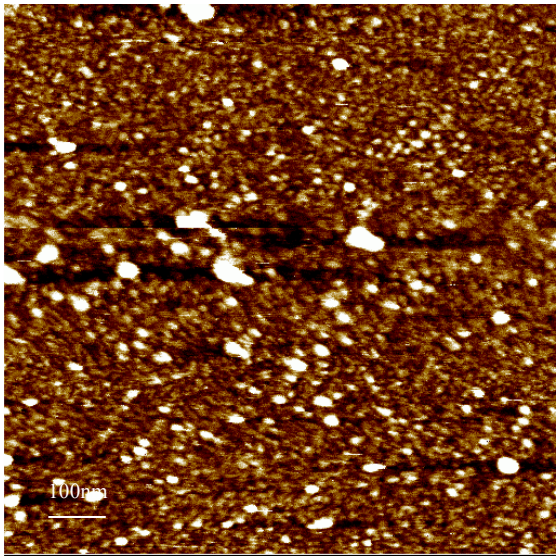

b

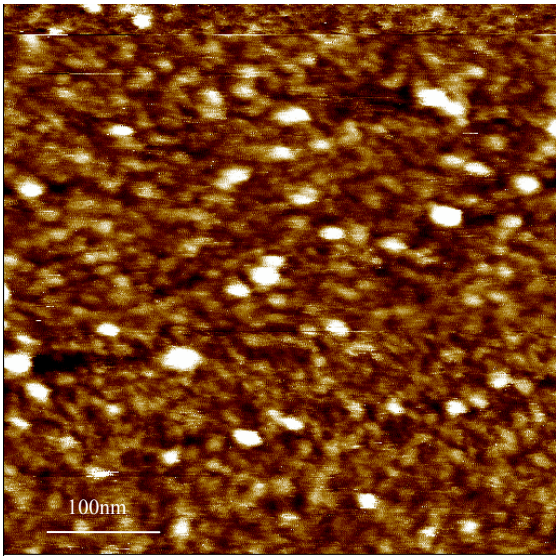

Fig 2.6 – Typical AFM images of surface topography of silicon substrates functionalised with *Lactobacillus casei* DHFR. (a) size 1 µm x 1 µm, z-scale 6 nm; (b) image size 500 nm x 500nm, z-scale 6 nm.

Thus, the surface topography illustrated in fig. 2.6a and b suggests the presence of a monolayer of DHFR.

2.3.2. AFM Force Measurements

Rupture force measurements were performed between the binary (DHFR-MTX) and ternary (DHFR-MTX-NADPH) complexes. Silicon nitride AFM probes were functionalised by the direct attachment of a methotrexate-modified agarose bead. Rupture forces were recorded between the probe and a DHFR monolayer covalently attached to a silicon substrate.

A typical force versus distance curve for a measurement performed between DHFR and methotrexate in 100mM sodium phosphate buffer, pH 7.4 at a retract velocity of 0.5 μm s^{-1}, is displayed in Fig. 2.7a. The specificity of interaction is characterised by the non-linear stretch prior to detachment. In contrast, non-specific adhesion on the other hand, as illustrated in fig. 2.7b, is characterised by a continuation of the gradient of the contact region upon retraction, prior to a sharp pull off (Willemsen, *et al*., 1999).

2.3.2.1 *Piezo-Retraction Rates*

Analysis of force measurements recorded for the DHFR-methotrexate complex over a range of mechanical dissociation rates produced a logarithmic relationship between rupture force and dissociation rate.

(a)

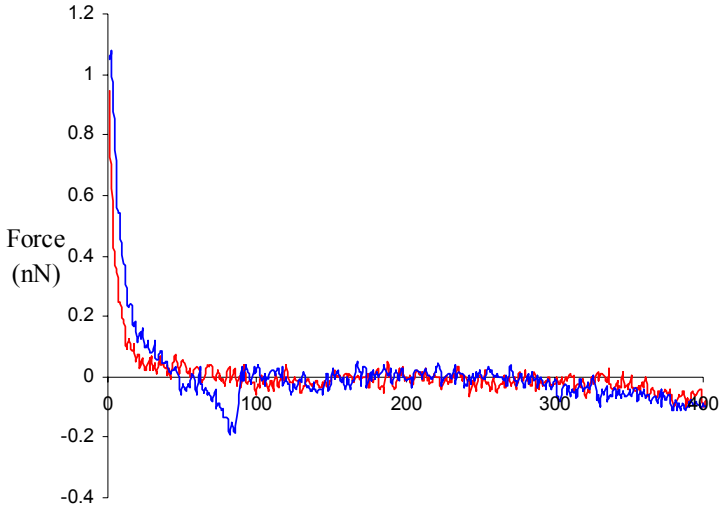

(b)

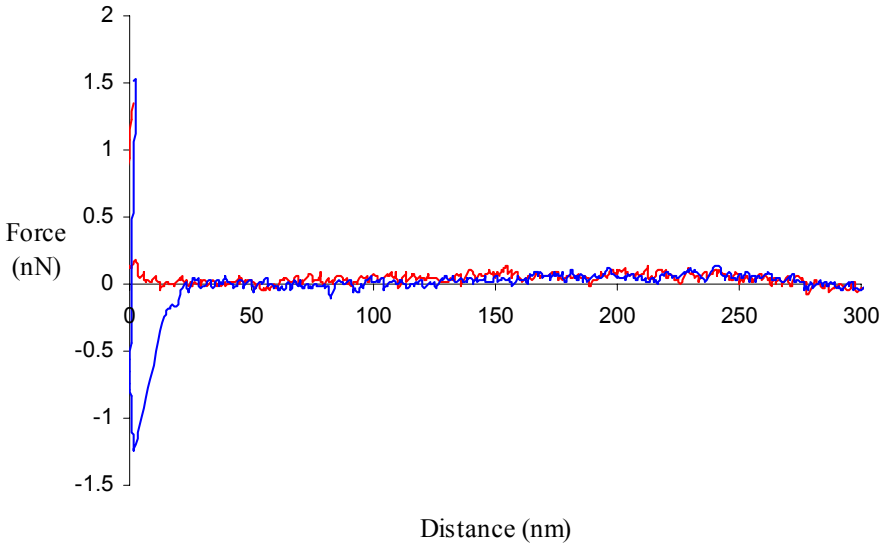

Fig. 2.7 – a) A typical force *versus* distance curve performed between to complementary molecules, illustrating a characteristic parabolic stretch prior to detachment; b) A typical force *versus* distance curve demonstrating a non-specific interaction. The approach trace is shown in *red*, the retract trace is shown in *blue*.

This relationship concurs with previous studies performed between other receptor-ligand complexes, such as streptavidin-biotin (Merkel *et al*., 1999). The dependency of rupture force upon rate is not restricted to receptor-ligand interactions, a variety of other biological systems have displayed similar characteristics, for example, the unfolding of titin domains (Rief *et al*., 1997), unbinding of VE cadherin dimers (Baumgartner *et al*., 2000), extraction of diC lipid from lipid:cholesterol vesicles (Ludwig & Evans 2000) and the fracture of DNA duplexes (Strunz *et al*., 1999), all of which have been discussed in detail in chapter 1.

A peak rupture force of 91 s.d. 25 pN was obtained for the unbinding of the binary complex at a retract velocity of 1.0 μm s^{-1} (Fig. 2.8a, *white histogram*). A decrease in force was experienced with a decrease in velocity. At 0.5 μm s^{-1} a force of 88 s.d. 16 pN was required for rupture (Fig. 2.8b), and a further decrease in velocity to 0.1 μm s^{-1} lead to a decrease in peak rupture force to 64 s.d. 14 pN, as depicted in figure 2.8c. Figures 2.8a (*white histogram*) and 2.8c exhibit a wide distribution of rupture forces with long tails to high force, which are suggestive of multiple interactions and/or multiple transition states (Williams & Evans, 2002). In both cases a high probability of adhesion was observed implying that the long tails of the distributions are features of multiple interactions rather than multiple transitions (Evans, 1998). However, reproducibility of the primary peak rupture force, particularly at 1.0 μm s^{-1}, in the pH and control studies suggests that these forces are attributable to single molecular interactions.

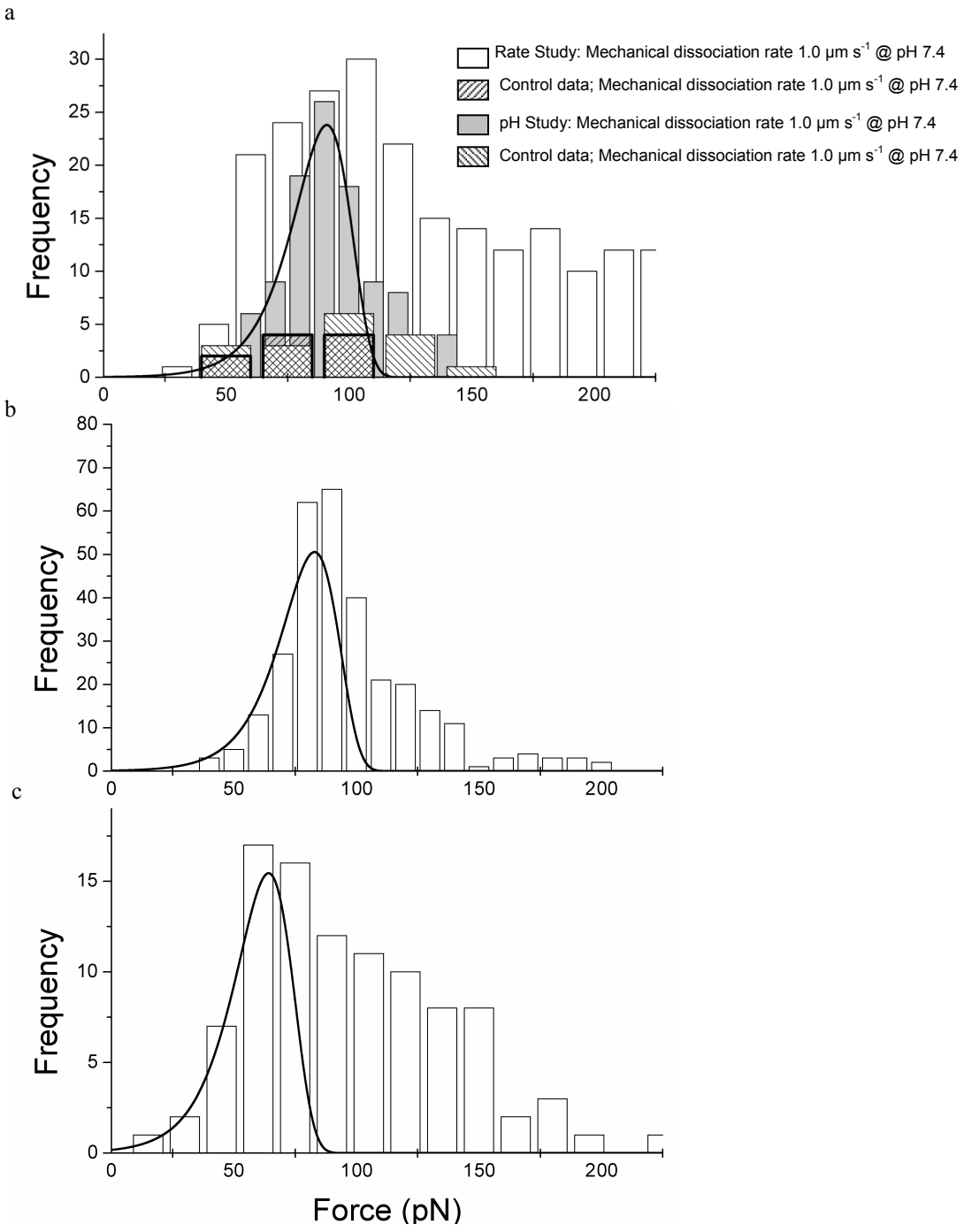

Fig. 2.8 - Frequency distribution histograms for the binary complex performed in a 100 mM sodium phosphate, pH 7.4 environment at various retract velocities; (*a*) 1.0 µm s^{-1} yielding rupture forces of 91 s.d. 25 pN and 90 s.d. 16 pN (*white and grey* histograms, respectively), the *back slash* histogram represents the control block force measurements for the *white histogram* data, and the *forward slash* histogram for the control measurements for the *grey histogram* data; (*b*) 0.5 µm s^{-1} yielding rupture forces of 88 s.d. 16 pN; (*c*) 0.1 µm s^{-1} displaying rupture forces of 64 s.d. 14 pN. Superimposed upon the force histograms is a model distribution derived from the experimental force scale of 12 pN.

(a)

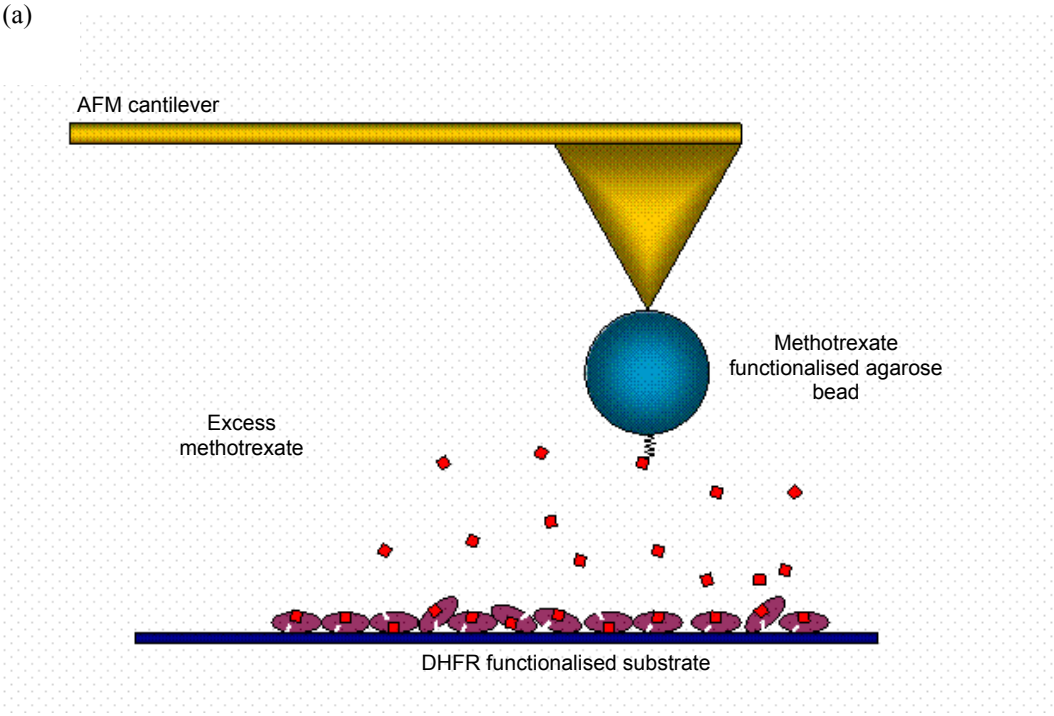

(b)

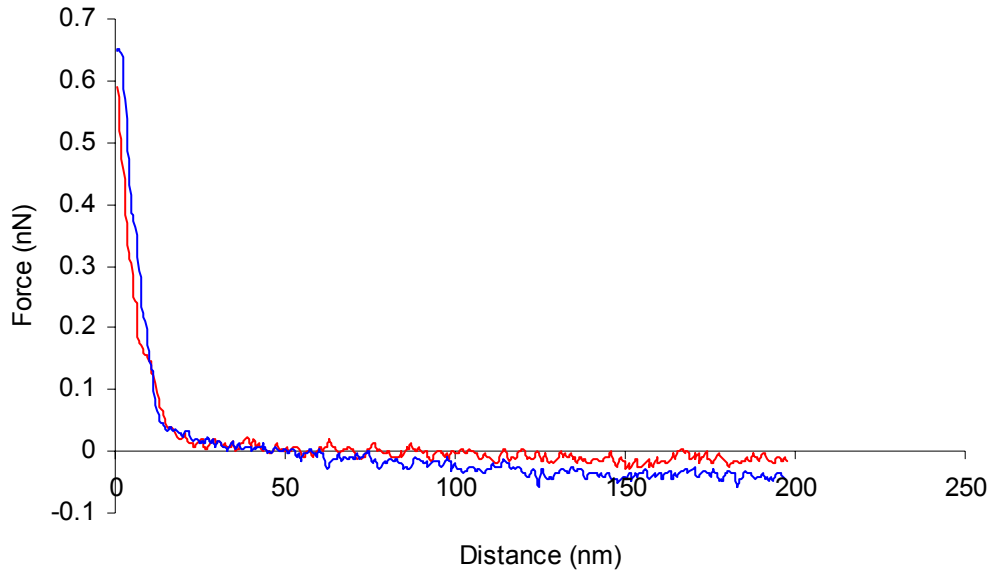

Fig 2.9 – (a) Schematic illustrating the experimental procedure for the control system where the methotrexate binding sites are blocked with free methotrexate. The *red squares* represent methotrexate, the agarose bead is displayed as the *blue* circle, the 8-atom carbon linker is illustrated by a *zig-zag structure*. The modified agarose bead is affixed to the apex of a cantilever probe. DHFR represented by the *burgundy ovals*, is covalently immobilised to a silicon substrate; (b) A typical force *versus* distance curve performed in the control system.

Furthermore, the probability of specific rupture events for the control studies (see later) are consistent with Poisson analysis for single molecular interactions, which suggests that when the probability of observing a rupture event is below 10 %, then 95 % of the rupture events observed are attributable to single molecule unbinding (Evans, 1998).

To confirm that the DHFR molecule is in an active form and that forces recorded were specific to the interaction of DHFR and methotrexate, the methotrexate binding sites on the DHFR molecules were blocked through the addition of free methotrexate, represented as a schematic in fig. 2.9a. A typical force *versus* extension curve of the control system is displayed in fig. 2.9b where there is a significant lack of a rupture event. The blockage of the binding sites resulted in a decrease in probability of a rupture event occurring, and 92 % of force measurements lacked any specific binding event. This low percentage adhesion, a peak force of 93 pN and the narrow force distribution (Fig. 2.8a, *back slash histogram*) also suggests that the forces experienced are single molecular. Furthermore, the decrease in the probability of adhesion with a decrease in available binding sites highlights the specificity of the rupture forces experienced in the experimental system.

The observed decrease in rupture force of the binary complex with retract velocity concurs with Evans theorem on bond dissociation dynamics (described in detail in chapter 1), where force of rupture is a function of time. Thus, if forced dissociation occurs over wide time scales it will provide an energetic landscape for the dissociation pathway.

A plot of peak rupture force versus the logarithm of retract velocity produced a linear regime in which the gradient is comparable to the standard deviations of the force distributions (Fig. 2.10). Furthermore, the standard deviations remained constant over this linear regime. Dictated by thermal actuation, forces measured for a single interaction are broadened by kinetics and therefore the standard deviation of forces equals the thermal force scale (gradient of the slope). The maintenance of standard deviations over the linear regime and the comparable values for the thermal force scale and the standard deviations are indicative of a single energy barrier of the dissociation pathway (Evans, 1998). A change in force scale and gradient indicates the exploration of a new energy barrier (Evans, 1998).

Ordinarily, velocity is expressed in the rate of loading (rate x spring constant of the system) to provide an accurate profile of the energy landscape for dissociation. However, in this case the dynamic and mechanical properties of the polymer (agarose bead) and carbon linker employed are unknown, thus the precise rate of loading cannot be identified. If we assume that at the retract velocities employed the polymeric linker is stretched to its asymptotic regime, where it becomes stiff, then the loading rate should be linear with the retract velocity. Thus, the calculated gradient of the linear regime (force scale) of 12 pN, the comparable standard deviations, and maintenance of the standard deviations over this linear regime (Fig. 2.10) suggest that the calculated force scale value is a reasonable estimate for the force scale of the barrier measured in these studies.

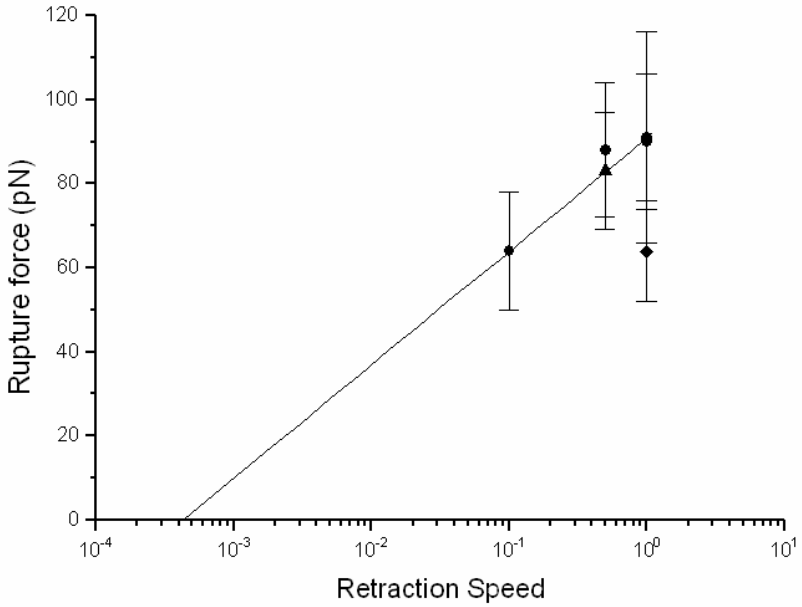

Fig. 2.10 - Representation of rupture forces *versus* logarithm of velocity. *Circle*, binary complex studied at various retract velocities at pH 7.4; *triangle*, ternary complex performed at pH 7.4; *diamond*, binary complex at pH 5.6.

The distance of the probed barrier from the bound state can be calculated if f_β of the energy barrier is known, where, $f_\beta = k_\beta T / x_\beta$ (Eqn. 1-3), k_β is the Boltzmann constant, T is temperature, x_β is the distance between the energy barrier to rupture and a stable minimum (Evans & Ritchie, 1997). The force scale calculated for a DHFR-methotrexate interaction over the rates studied infers the presence of an energy barrier positioned approximately 3.49 Å from the bound state.

However, to reveal the natural lifetime of the interaction requires knowledge of the loading dynamics. Where flexible polymers, such as those employed here, are used to attach the molecular complex to the force transducer, a second timescale is added to that of the interaction. This is a characteristic time to extend the polymer and apply force, and is dependent on the contour and persistence lengths of the attachment (Williams & Evans, 2002). Here these lengths, and hence this time scale, are unknown and therefore the dissociation rate for the probed energy barrier cannot be estimated from the force data.

In order to map the complete dissociation pathway it is necessary to perform studies of applied force over many orders of loading rates (Evans, 1998). The AFM is unable to achieve such a vast range of measurements, which limits its sensitivity to the energy barriers of unbinding which are situated close to the bound state. To accomplish the wide spectrum of rates necessary to build a profile of the dissociation pathway, the recently developed biomembrane force probe (Evans *et al*., 1995) may be employed.

2.3.2.2 *Intermolecular Interactions of MTX in the Ternary Complex*

A cooperative relationship has been observed between the substrate/inhibitor and the coenzyme of DHFR using various analytical techniques (Birdsall *et al*., 1978, 1980a; Matthew *et al*., 1978; Baccanari *et al*., 1982). However, the source of cooperativity remains elusive. Here the AFM has been employed to provide an additional technique towards the understanding of the origins of this cooperativity.

Rupture forces were measured for the forced dissociation of methotrexate from both the binary and ternary complex. In order to execute such experiments, it is necessary to covalently immobilise the enzyme, DHFR, to a substrate surface. However, the location of the methotrexate and NADPH binding sites in the DHFR molecule, would imply that in order to generate the ternary complex flexibility of the enzyme is paramount. As previously described, DHFR was coupled to amine functional groups on the substrate via the ε-amino groups of the lysine residues on the surface of the protein. Figure 2.11 highlights the positions of the lys residues in relation to both the methotrexate and NADPH binding sites. The lys residues appear distributed throughout the protein and are not clustered around either the methotrexate or the NADPH binding site, suggesting that both methotrexate and NADPH are free to bind. It is therefore feasible to conclude that NADPH is bound in the ternary complex studies.

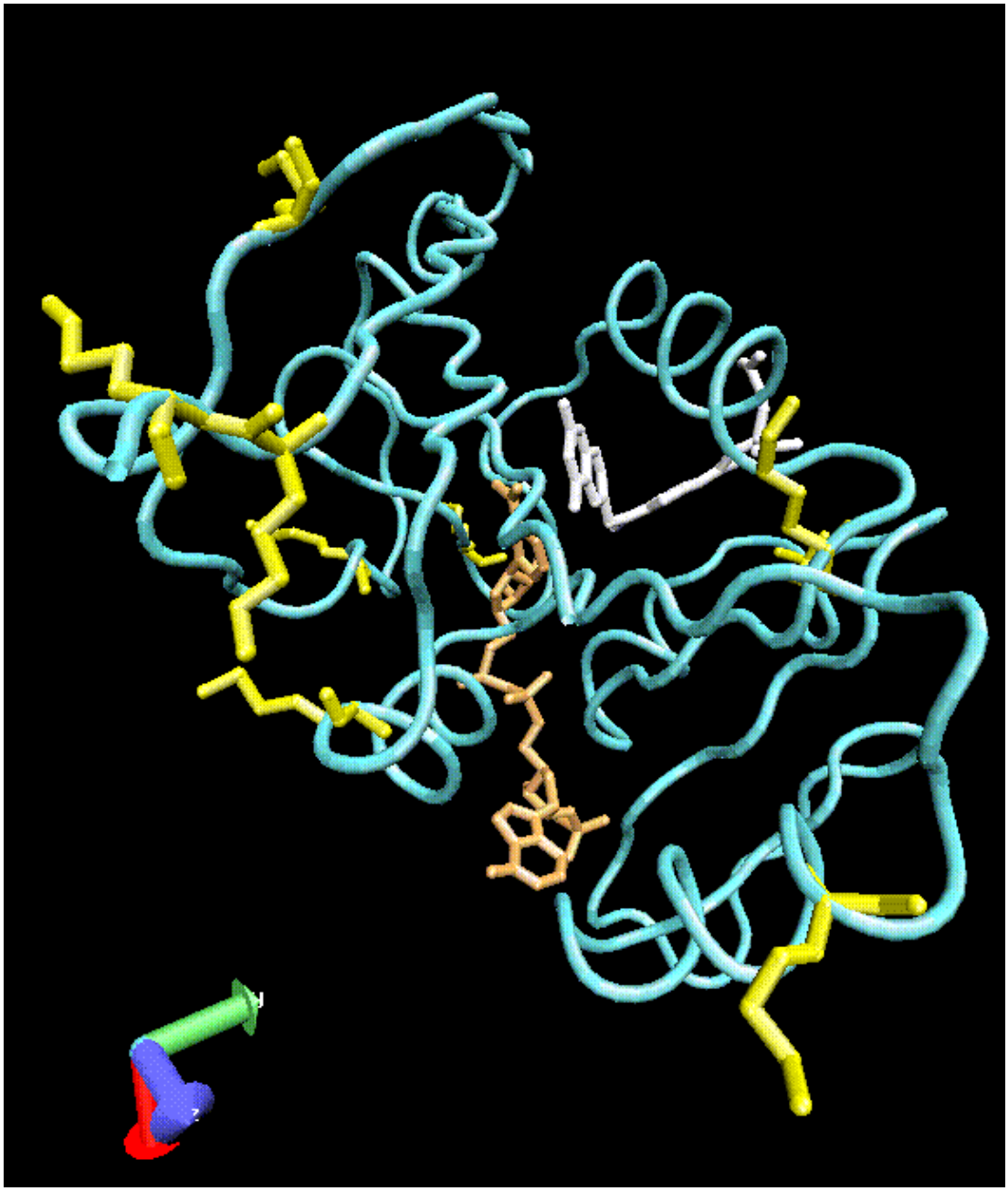

Fig. 2.11 – The crystal structure of dihydrofolate reductase, the lysine residues are highlighted in *yellow* indicating the positioning of the residues in relation to the methotrexate, *white*, and NADPH, *orange*, binding sites.

AFM force analysis for measurements recorded for the binary and ternary complexes demonstrated equivalent rupture forces for the forced dissociation of methotrexate. A force of 88 s.d. 16 pN was observed between DHFR and methotrexate (binary complex) (Fig. 2.12a), and for the ternary complex a rupture force of 83 s.d. 14 pN was obtained (Fig. 2.12b). The rupture forces and force scale measured for the ternary complex fall within the linear regime probed during the rate study for the binary complex. This suggests that the energy barrier positioned at 3.49 Å in the dissociation landscape of the binary complex is also present in the energy landscape of the ternary complex.[b]

The probability of adhesion demonstrated in the experimental system was 20 %. The subsequent addition of free methotrexate to the surrounding environment resulted in a decrease in the probability of adhesion to 8 %. A comparable peak rupture force, 89 pN, and force distribution was recorded with control system (Fig. 2.12b, *grey histogram*), emphasising that forces experienced are characteristic of single molecular interactions.

Recent solution NMR studies have demonstrated that no major conformation change occurs between the binary (DHFR-MTX) and ternary complex (DHFR-MTX-NADPH) of *L.casei* (Gargaro, *et al*., 1998). Both complexes assume a "closed" conformation, in which the 9-23 loop extends across the active site, hydrogen bonding with the β-sheet of DHFR. Despite the absence of NADPH in the binary complex, the 9-23 loop does not protrude into the nicotinamide binding site to form an "occluded" conformation (Gargaro *et al*., 1998).

(a)

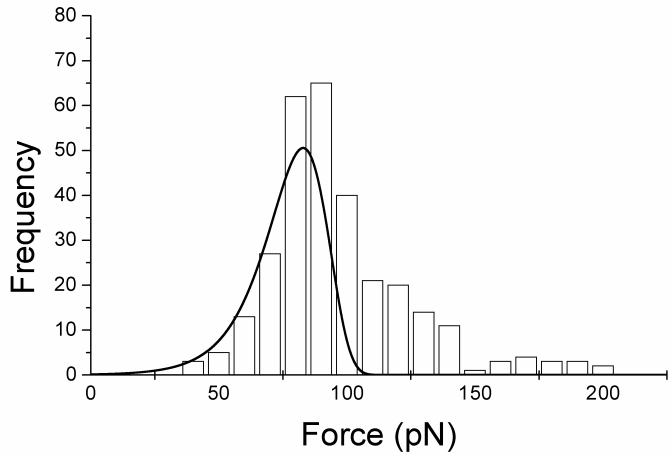

(b)

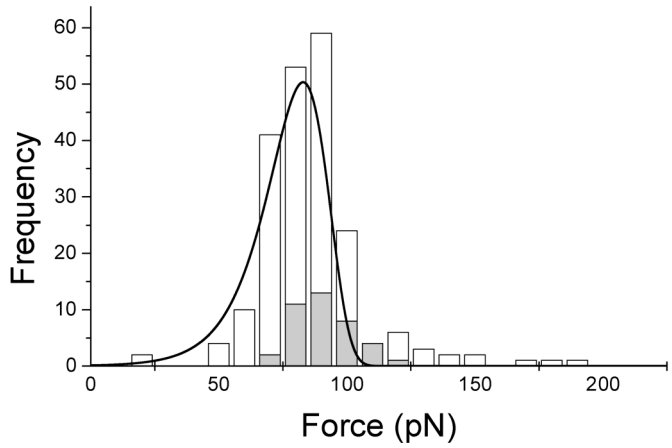

Fig. 2.12 – Frequency distribution histograms of rupture forces performed between the binary and ternary complexes, in 100 mM sodium phosphate buffer at a retract velocity of 0.5 μm s^{-1} . a) Forced dissociation of the binary complex (DHFR-MTX) yielded a peak rupture force of 88 s.d. 16 pN; b) Forced dissociation of the ternary complex (DHFR-MTX-NADPH) produced a peak rupture force of 83 ± 14 pN (*white* histogram). The *grey* histogram represents the control block force measurements. Superimposed upon the force histograms is the model distribution derived from the experimental force scale of 12 pN.

Consequently, the NADPH binding site is preformed in the binary complex. Furthermore, methotrexate occupies a similar position in the binary and ternary complex, thus no major conformational change occurs in relation to bound methotrexate (Gargaro et al, 1998). The similarity of the rupture forces and force scale for both the binary and ternary complexes also infers that no significant changes in conformation occurs, which would impede unbinding of methotrexate over the region of the dissociation pathway studied. Thus, NADPH does not facilitate cooperativity in this probed region.

Interactions between the two ligands, cofactor and inhibitor, have been demonstrated, which may contribute to the cooperativity of ligand binding. The binding constant of the cofactor has shown to be dependent upon the structure of the cofactor, as well as the presence and structure of the substrate/inhibitor (Birdsall, *et al*., 1978, 1980a,b; Baccanari, *et al*., 1982), suggesting cooperativity is related to hydrophobic and van der Waals interactions between the two ligands (Baccanari, *et al*., 1982). Moreover, Matthews, *et al*., 1979 has shown that direct contact occurs between the nicotinamide ring of NADPH and the pyrazine ring of methotrexate. However, the extent of inhibitor-cofactor interactions accountable for cooperativity was questioned by Birdsall *et al*., 1980a. The overlap of the two rings is not extensive and their planes are not parallel, Birdsall went on to speculate that it is unlikely that ligand-ligand interactions could account for the additional binding energy of the ternary complex, and the degree of the cooperativity between NADPH and methotrexate arises from conformational change (Birdsall, *et al*., 1980a), or

through the preparation of the binding site by removal of the water molecules (Feeney, 2001).

Early studies speculated that a conformational change occurs upon the binding of NADPH, where the 'teen loop' (residues 13-22,*lc*) moves substantially translating the side chain of leu19 to a position where van der Waals contact is made with the pyrazine ring of methotrexate (Matthews, *et al*., 1978). However, it would appear from more recent NMR studies that this is not the case and no major conformational change occurs (Gargaro, *et al*., 1998) (as previously discussed).

X-ray crystallographic data has demonstrated that residues in the M20 loop of *E.coli* interact with the nicotinamide-ribose moiety of the $NADP^+$ (Sawaya & Kraut, 1997), contributing to cooperativity. However it is not known whether the corresponding loop in *L.casei* (9-23 loop) interacts with $NADP^+$, or with the reduced form of the coenzyme.

Such interactions between methotrexate and NADPH are not evident in the rupture forces for the ternary complex at the dissociation rates studied. It is apparent from the results that NADPH does not affect the force of unbinding at a retract velocity of 0.5 μm s^{-1}. This suggests that the proposed increase in binding affinity of methotrexate in the presence of the cofactor, as demonstrated by NMR, fluorometry, and x-ray crystallography occurs outside the transition probed in this series of studies (Fig. 2.10). Although the inferred

increase in methotrexate binding is not mirrored in AFM experiments, it is important to note that rupture forces are a measure of dissociation.

The origins of the cooperativity still remain unclear, but it is evident that cooperative binding is not a result of a single event, rather a complex combination of events. Although it is apparent that such events do not impede unbinding of methotrexate over the region of the dissociation pathway studied. However, in order to elucidate cooperativity between the ligand and cofactor, more NMR, fluorometry, AFM and maybe other alternative techniques will have to be employed.

2.3.2.3 *The Influence of pH on Interactions between the Binary, Dug-Enzyme Complex*

The Asp26 residue of DHFR plays an invaluable role in enzyme catalysis (Williams & Morrison, 1981; Stone & Morisson, 1984, 1988) and in the binding of inhibitors (Cocco *et al*., 1981). A number of research groups have implicated Asp26 in a hydrogen bonding interaction with the N1 nitrogen of 2,4-diaminopteridine inhibitors (Subramanian & Kaufman, 1978; Gready, 1980; Cocco *et al*., 1981; Bolin *et al*., 1982; Cheug *et al*., 1983; Gargaro *et al*., 1998). The protonation of the residue has also been related to pH dependent conformational changes of the enzyme (Birdsall *et al*., 1982; Stone & Morrison, 1984).

Here the AFM is employed to investigate the affect of pH upon the dissociation of methotrexate from the binary complex. The carboxylic acid side chain of the Asp26 residue of the free enzyme has a pKa of 6.3 (Dunn & King, 1980; Stone & Morrison, 1984; Fierke *et al*., 1987; Thillet *et al*., 1990), and a reduction of the pH below the pKa results in the protonation of the residue. Rupture force measurements were obtained for the forced dissociation of methotrexate from the binary complex in an environmental pH of 7.4 and 5.6. The decrease in pH resulted in a decrease in the force required for dissociation. At pH 7.4 and a retract velocity of 1.0 μm s^{-1} a force of 90 s.d. 16 pN was observed (Fig. 2.8a, *grey histogram*). The rupture force decreased to 64 s.d. 12 pN at pH 5.6 (Fig. 2.13). The addition of free methotrexate resulted in a reduction in the percentage adhesion from 16 % to 6%, yielding a peak rupture force and force distribution comparable to the experimental system (Fig. 2.8a, *forward slash histogram*).

The interaction between the carboxyl group of Asp26 and the N1 nitrogen of methotrexate is ionic in nature (Bolin, *et al*., 1982). The N1 of methotrexate is protonated when bound to DHFR, producing a charged donator (Subramanian & Kaufman, 1978; Gready, 1980; Cocco *et al*., 1981; Cheug *et al*., 1983). Furthermore, X-ray crystallographic studies have shown that Asp26 demonstrates a complementary charge distribution to the protonated N1, where Asp26, Thr116 and Wat201 form a highly constrained binding pocket with complementary geometry and charge to the N1 and 2-amino group of the pyrimidine ring of methotrexate (Bolin *et al*., 1982).

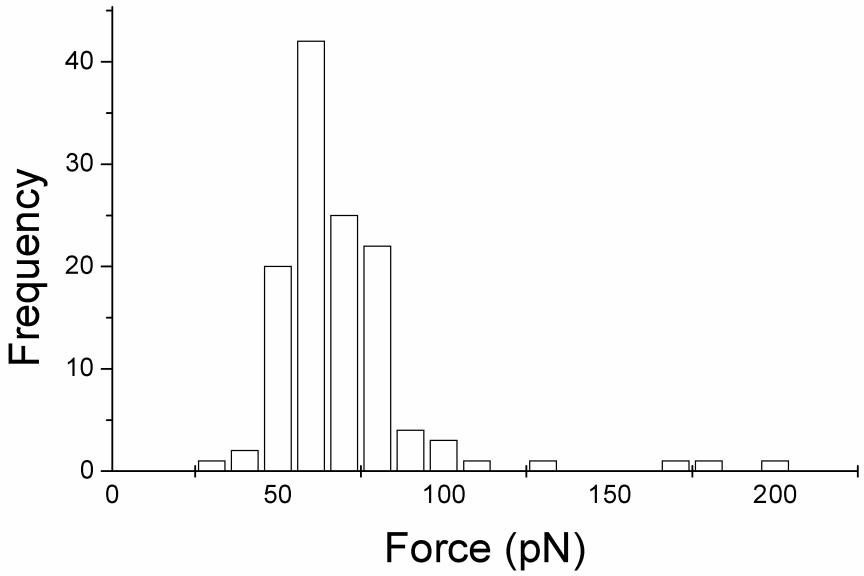

Fig. 2.13 – Frequency distribution histogram of rupture forces of 64 ± 12 pN demonstrated between DHFR-methotrexate, at pH 5.6, 100 mM sodium phosphate. Performed at a retract velocity of 1.0 μm s^{-1}.

Asp26 is the closest available charged group acceptor (a distance of less than 4 Å) to the protonated N1, enabling hydrogen bonding to occur between the two. Thus, protonation of Asp26 would lead to disruption in this bond formation. Therefore, the observed decrease in force with protonation of Asp26 is suggestive of this perturbation.

The maintenance of a comparable force scale over the pH range implies that the same energy barrier to dissociation is as in the previous studies (fig 2.10). If this is the case then the decrease in rupture force is indicative of a decrease in the number of bonds ruptured upon dissociation, which concurs with x-ray crystallographic and NMR data. A decrease in bonds ruptured would be accompanied by a decrease in the barrier height and an amplification of the dissociation kinetics for the barrier probed. However, from the force data it is not conclusive that the energy barrier (3.49 Å) to dissociation probed in the rate and cofactor studies is the same barrier probed in this study.

2.3.2.4 *Control Force Measurements*

As an experimental control to confirm that the DHFR molecule was in an active form and that forces recorded were specific to the interaction of DHFR and methotrexate, the number of available methotrexate binding sites were reduced through the addition of free methotrexate. The decrease in observed specific rupture events in the control systems highlights the specificity of the rupture forces experienced in the experimental systems. Moreover, the

probability of specific rupture events in the control studies are consistent with Poisson analysis for single molecular interactions, which suggests that when the probability of observing a rupture event is below 10 %, then 95 % of the rupture events observed are attributable to single molecule unbinding (Evans, 1998). Thus, the reproducibility of the peak rupture forces in the experimental and control systems, suggests that rupture forces experienced in both systems are characteristic of single molecule unbinding.

Additional, force measurements were recorded between and agarose bead and a DHFR monolayer (fig.2.14a), to verify that rupture forces measured are specific to the forced dissociation of the MTX-DHFR complex and are not due to an interaction between the agarose bead and the DHFR monolayer. Figure 2.14b illustrates a typical force *versus* extension curve of an interaction between an unmodified 4% cross-linked agarose bead and a DHFR monolayer. Frequency *versus* rupture force histogram (fig. 2.15) yields a peak rupture force of 300 pN s.d. 50 pN. The dissimilarity of the peak forces and force scales experienced between the agarose control (300 s.d.50 pN) and the experimental systems suggests that the rupture forces described throughout the chapter are a result of the forced dissociation of methotrexate from DHFR.

(a)

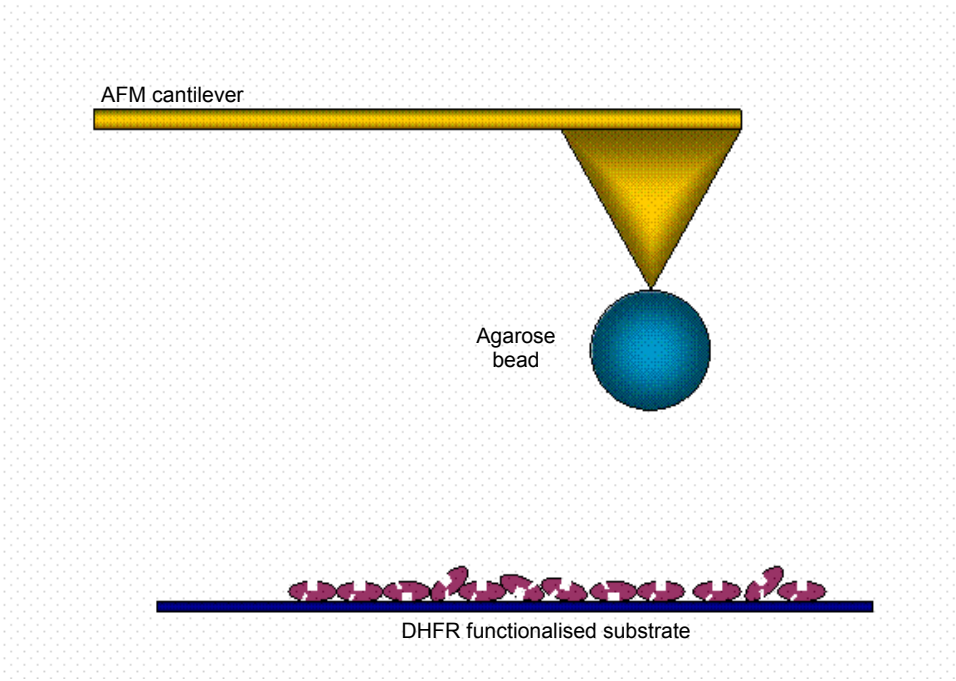

(b)

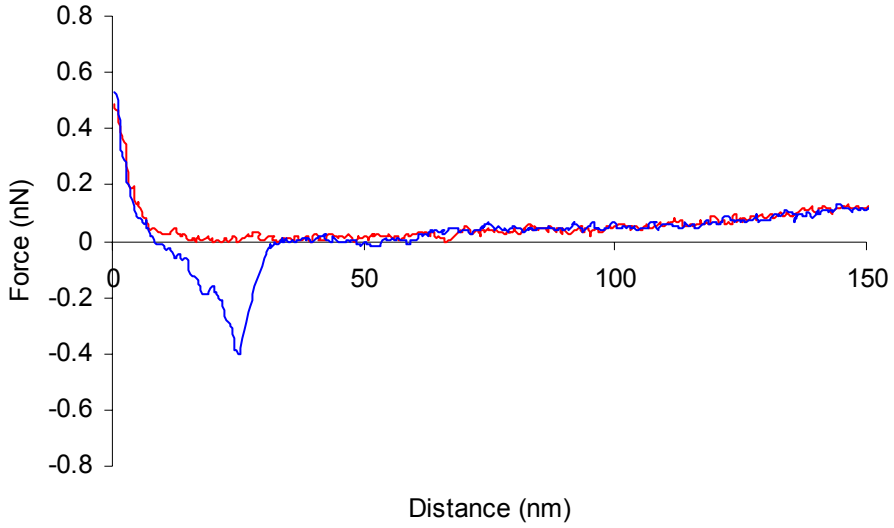

Fig. 2.14 – a) Schematic illustrating the experimental procedure for the agarose control system, where the agarose bead is displayed as the *blue* circle attached to the apex of a cantilever probe. DHFR represented by the *burgundy ovals*, is covalently immobilised to a silicon substrate; b) A typical force *versus* distance curve performed between the two surfaces. The approach trace is shown in *red*, the retract in *blue*.

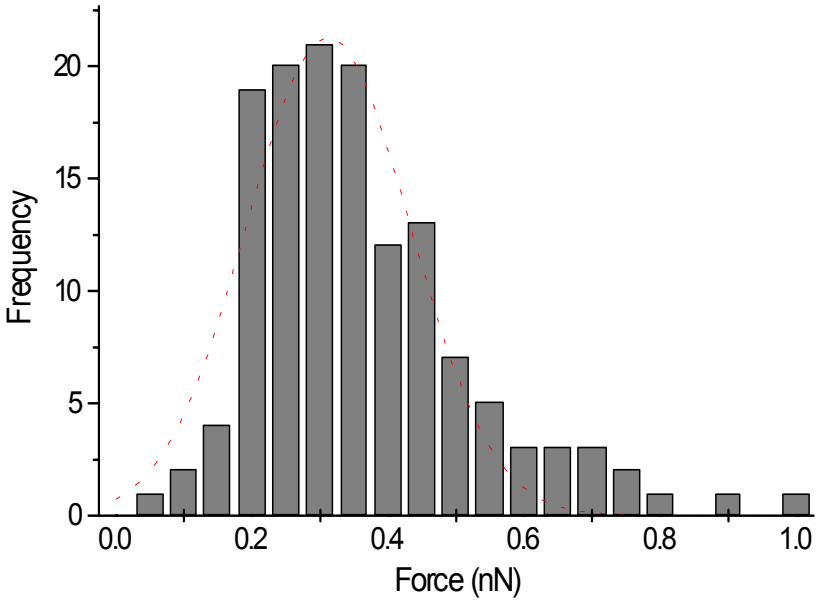

Fig. 2.15 - Force histogram for force measurements performed between a 4% cross-linked agarose bead and a DHFR monolayer, at a retract velocity of 1.0 μm s^{-1}, in an environment of 100 mM sodium phosphate buffer pH 7.4. A Gaussian curve fit is superimposed on the force histogram to estimate the most frequent rupture force

2.4. CONCLUSIONS

Over the last 8 years the AFM has been employed as a high resolution instrument for the investigation of the universal forces which govern receptor-ligand interactions. However, the AFM has been limited to dynamic force spectroscopy of complimentary biomolecules, such as antibody-antigen (Stuart & Hlady, 1995; Hinterdorfer *et* al., 1996; Dammer *et al*., 1996; Allen *et al*., 1997; Ros *et al*., 1998; Schwesinger *et al*., 2000) and protein-protein (Lee *et al*., 1994; Florin *et al*., 1994; Moy *et al*., 1994) complexes. In this chapter, the AFM has been employed for the first time (to my knowledge) to investigate the forced dissociation of a drug-enzyme complex, diversifying the biological and pharmaceutical applications of the instrument.

A dependency of force required to rupture the DHFR-methotrexate complex on the rate of dissociation is demonstrated, giving rise to a single energy barrier to dissociation of the binary and ternary complexes positioned 3.49 Å from the bound state. The cooperativity experience in the association of the ternary complex (Williams *et al*., 1979; Birdsall *et al*., 1978, 1980a,b; Baccanari *et al*., 1982; Matthews *et al*., 1978, 1979; Feeney, 2001) was not mirrored in the dissociation of the complex for the region studied. In addition, the protonation of the Asp26 residue is known to cause a disruption in bond formation between DHFR and methotrexate (Bolin *et al*., 1982), thus the decrease in force observed with a decrease in pH is suggestive of this perturbation.

CHAPTER 3

The Development and Construction of Optical Tweezers

This chapter describes the design, construction and application of the force sensing technique, optical tweezers. The theory behind the instrumentation is discussed, followed by a detailed description of the instrumentation employed and its construction. The optical trap is calibrated, in order to determine the force applied to trapped particles. Finally, the ability of the optical tweezers to manipulate biological particles within a micron range is demonstrated.

3.1 INTRODUCTION

Light is a powerful tool! The stimulating use of light as a "*tractor beam*" in popular science fiction has become a reality on a microscopic scale. The optical manipulation of micron and submicron dielectric particles and even individual atoms has been achievable since the early 1970's (Ashkin, 1970), but it wasn't until mid-1980's that the technique was applied to biological particles (Ashkin, 1987). Since then, optical forces have been used to trap and manipulate bacteria and viruses (Ashkin & Dziedzic, 1987), living cells (Ashkin *et al*., 1987; Ashkin & Dziedzic, 1987), organelles (Block *et al*., 1989;

Berns *et al*., 1989; Ashkin & Dziedzic, 1989) and DNA (Chu 1991; Wang *et al*., 1994; Smith *et al*., 1996; Arai *et al*., 1999). In addition to manipulation, its exploits encompass the measurement of force (Kuo & Sheetz, 1993; Finer *et al*., 1994; Yin *et al*., 1995; Mammen *et al*., 1996; Helmerson *et al*., 1997; Wang *et al*., 1998; Stout, 2001), elasticity (Wang *et al*., 1994; Smith *et al*., 1996; Kellermayer et al., 1997; Tskhovrebova *et al*., 1997; Cui & Bustamante, 2000), surface structure (Svoboda & Block, 1994), and microsurgery (Steubing *et al*., 1991; Buer *et al*., 1998).

The advent of optical tweezers has enabled biomechanical studies of single molecule motors. The study of rotary motors, such as those responsible for the propulsion of motile bacteria, was one of the first quantitative applications of the optical tweezers technique (Block *et al*., 1989). However, attention has become focussed on linear motor proteins, which move along polymer tracks. RNA polymerase (RNAP) is a molecular motor transcribing a DNA template into messenger RNA, advancing a distance of 1bp along the DNA helix per nucleotide added to the transcript (Erie *et al*., 1992). Yin *et al*., (1995) and Wang *et al*., (1998) measured the force required to stall the RNAP motor by tethering a single DNA strand between an optically trapped bead and an immobilised RNAP (depicted in fig 3.1a). RNAP was shown to stall against applied loads of ~21-27 pN.

Analogous studies of the kinesin motor have also reported stalling forces, but in the range of 5-7 pN (Svoboda *et al*., 1993; Svoboda & Block, 1994;

a

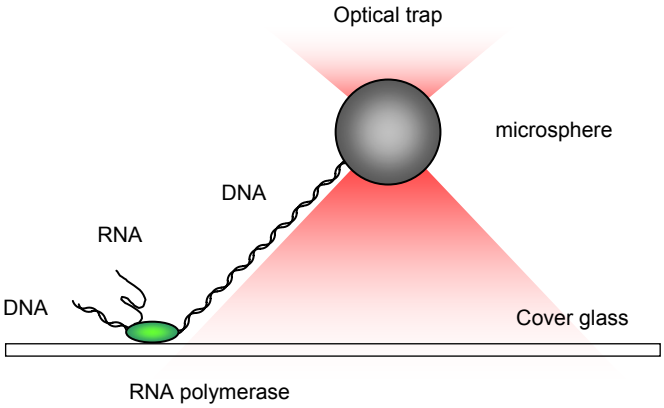

b

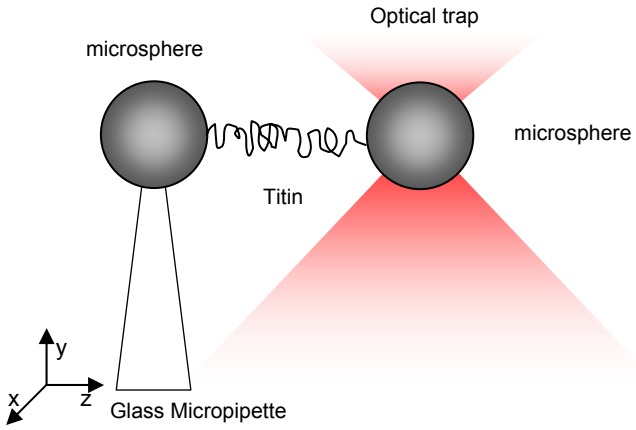

c

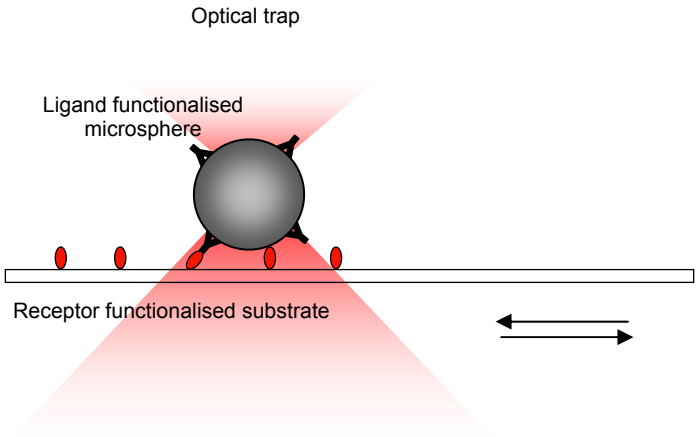

Fig. 3.1 – a) Schematic of the experimental procedure employed by Yin et al., (1995) to investigate the molecular motor, RNAP; b) Experimental setup employed to study titin unfolding (Kellermayer et al., 1997); c) The experimental setup employed by Stout (2001), to detect and characterise individual intermolecular bonds between IgG and SpA.

Kojima *et al*., 1997), with a step movement of 8 nm (Svoboda *et al*., 1993). The higher forces required for stalling RNAP maybe reflective of the forceful disentanglement of the DNA secondary structure (Mehta *et al*., 1999). The muscle motor myosin has also been extensively studied, demonstrating a step movement of 4-15 nm (Finer *et al*., 1994; Molloy *et al*., 1995; Veigel *et al*., 1998).

The dynamics of biopolymer elasticity and unfolding have been also studied using optical tweezers, AFM, and other mechanical probes. The elastic properties of DNA (Smith *et al*., 1996; Wang *et al*., 1997; Baumann *et al*., 2000) and the effect of binding proteins on this elasticity have been readily investigated using optical tweezers (Leger *et al*., 1998; Sakata-Sogawa *et al*., 1998). The persistence lengths and stretch moduli of chromatin fibres have also been determined (Cui & Bustamante, 2000). The unfolding of the giant filamentous muscle protein titin, as examined by optical tweezers (experimental setup illustrated in fig. 3.1b) (Kellermayer *et al*., 1997; Tskhovrebova *et al*., 1997) and AFM (Rief *et al*., 1997), have both demonstrated a reversible, sequential unfolding of the Ig and Fn3 domains of the polypeptide (Tskhovrebova *et al*., 1997; Rief *et al*., 1997).

It is also possible to determine the forces which govern receptor-ligand interactions using optical tweezers (Stout, 2001). However, the range of possible receptor-ligand complexes available for study is limited to the maximum force the optical trap can apply. Rupture forces of 25-44 pN for

single molecular interactions between IgG and SpA have been determined, by trapping an IgG microsphere and scanning the SpA-coated substrate beneath the trapped spheres (Stout, 2001) (fig. 3.1c). Optical tweezers have also shown to be an effective and accurate bioassay detection system (Mammen *et al*., 1996), capable of detecting femtomolar concentrations of biomolecules (Helmerson *et al*., 1997).

3.1.1 Theory of Optical Tweezers

The fundamental principle of optical tweezers lies in the radiation pressure exerted by a beam of light on a dielectric particle. Radiation pressure was first acknowledged in the early 17th C by the astronomer Johannes Kelper, who proposed that the radiation of the sun forced comet tails to always point in the opposite direction (Hecht, 1987). In 1873 James Clerk Maxwell showed in his theory of electromagnetism that light can exert force (Hecht, 1987). However, experimentally this was not demonstrated until the 1970's following the advent of the laser (Ashkin, 1970).

The optical forces (F), such as radiation pressure, exerted on a dielectric particle in a light focus are defined by the incident light power (P), the speed of light (c) (2.998 x 10^8 m s^{-1}), the refractive index of the surrounding medium (n_m) and a dimensionless efficiency factor (Q), where,

$$F = Q\frac{n_m P}{c} \qquad (3\text{-}1)$$

The dimensionless efficiency factor, Q, is a representation of the fraction of power utilised to exert force and is dependent upon numerical aperture of the objective employed to focus the laser, the light wavelength (λ) and polarization state, the laser mode structure, the relative refractive index, and the geometry of the trapped particle (Svoboda & Block, 1994). This dimensionless efficiency factor can be determined by a number of different means, for example, the escape force, drag force, equipartition, and power spectral density methods (all of which are discussed in detail in 3.3.1).

The radiation pressure exerted upon a dielectric particle can be divided into two principle forces, namely, the gradient force and the scattering force (Ashkin, 1970). Although, other optical forces exist, for example, the optical binding force and the radiometric force, the role in which they play in optical trapping is currently poorly understood (Svoboda & Block, 1994). The gradient force is proportional to the spatial gradient of the light intensity, and acts in the direction of the gradient of light intensity. As a counteractive force, the scattering force is proportional to the light intensity, and acts in the direction of the propagation of the light. Optical tweezers owe their trapping ability to the gradient force, which attracts the particle towards the focus of a laser beam, whereas the scattering force drives the particle along the z-axis of beam propagation (Ashkin, 1970). To achieve stability of the optical trap, the radiation pressure must create a three-dimensional equilibrium, in which the

gradient force is dominant over the scattering force. To accomplish this it is necessary to produce a steep gradient of light intensity (Ashkin, 1992).

The current theoretical models which describe the forces involved in optical tweezers are based upon spherical dielectric particles, such as polystyrene microspheres (Ashkin, 1992; Svoboda & Block, 1994). However, it should be noted that optical forces are sensitive to small perturbations in the geometry of trapped particles, and as such theoretical computation will probably be unable to accurately predict the forces of biological systems, for example, cells. Therefore, in order to determine forces which govern biological interactions it is necessary to perform empirical measurements. Nevertheless, theoretical models are invaluable for highlighting improvements in experimental geometry (Svoboda & Block, 1994).

The theoretical models available are particle size dependent. The Rayleigh regime accounts for particles whose diameter (d) is less than the wavelength of the laser light. In contrast, the Mie or ray-optics regime is applicable to particles with a diameter greater than the wavelength. However, there is a degree of overlap between the two models when $d = \lambda$, this is commonly the case in biological applications, in which cells and other biological components are directly manipulated (Ashkin, 1992).

Light exhibits both wave and particle characteristics (Grant & Phillips, 2001). The Rayleigh model considers the wave-like properties of light, whereas the

fundamental basis of the Mie model is quantum physics, in which a beam of light is made up of stream of particles.

3.1.1.1 *Rayleigh Regime* ($d < \lambda$)

Light travels in the form of waves, consisting of a time-varying electric field accompanied by a time-varying magnetic field (Muncaster, 1988). In the Rayleigh regime, the uniformity of an electromagnetic field produced across a dielectric, enables the particle to behave as simple dipole (Svoboda & Block, 1994). Thus, the application of force to the dipole, results in the natural division of the force into two counteractive components, the gradient force and the scattering force (Svoboda & Block, 1994).

The application of the optical tweezers in this thesis employs particles whose diameter is greater than the wave length of the laser light, and thus this regime is not further considered. For a more detailed text on the Rayleigh regime refer to Svoboda & Block (1994).

3.1.1.2 *Mie Regime* ($d > \lambda$)

The Mie regime, commonly known as the ray-optics regime, is applicable to dielectric particles larger than the laser wavelength and can be explained using a simple ray optics diagram. The fundamental principle is the derivation of optical force from momentum transfer.

Quantum mechanics infer that a beam of light consists of a stream of photons (Corpuscular theory of light; Newton) (Hecht, 1987). A photon is described as a quantum of energy, and as such carry momentum in the direction of light propagation. The energy (E) and momentum (p) of the photons present in the light are determined by the frequency of the light (the time period for an electron to go from a ground state to an excited state and return to a ground state) (Hecht, 1987).

$$\mathrm{E} = h\upsilon \tag{3-2}$$

$$p = \frac{h\upsilon}{c} = \frac{\mathrm{E}}{c} \tag{3-3}$$

where, h is Planck's constant (6.6256 ± 0.0005 × 10^{-34} J s), and υ is frequency (Hz).

A change in photon momentum is incurred upon the reflection and refraction of light at a dielectric interface with a greater index of refraction than the surrounding media. Conservation of momentum requires that the rate of change in photon momentum conveys an equal and opposite rate of change in momentum to the dielectric. Newton's second law maintains that the rate of change of momentum equals force, thus the resulting force from the refracted ray acts in the direction of light intensity, and reflection produces a force acting in the direction of light propagation (Fig. 3.2) (Ashkin, 1992; Svoboda & Block, 1994).

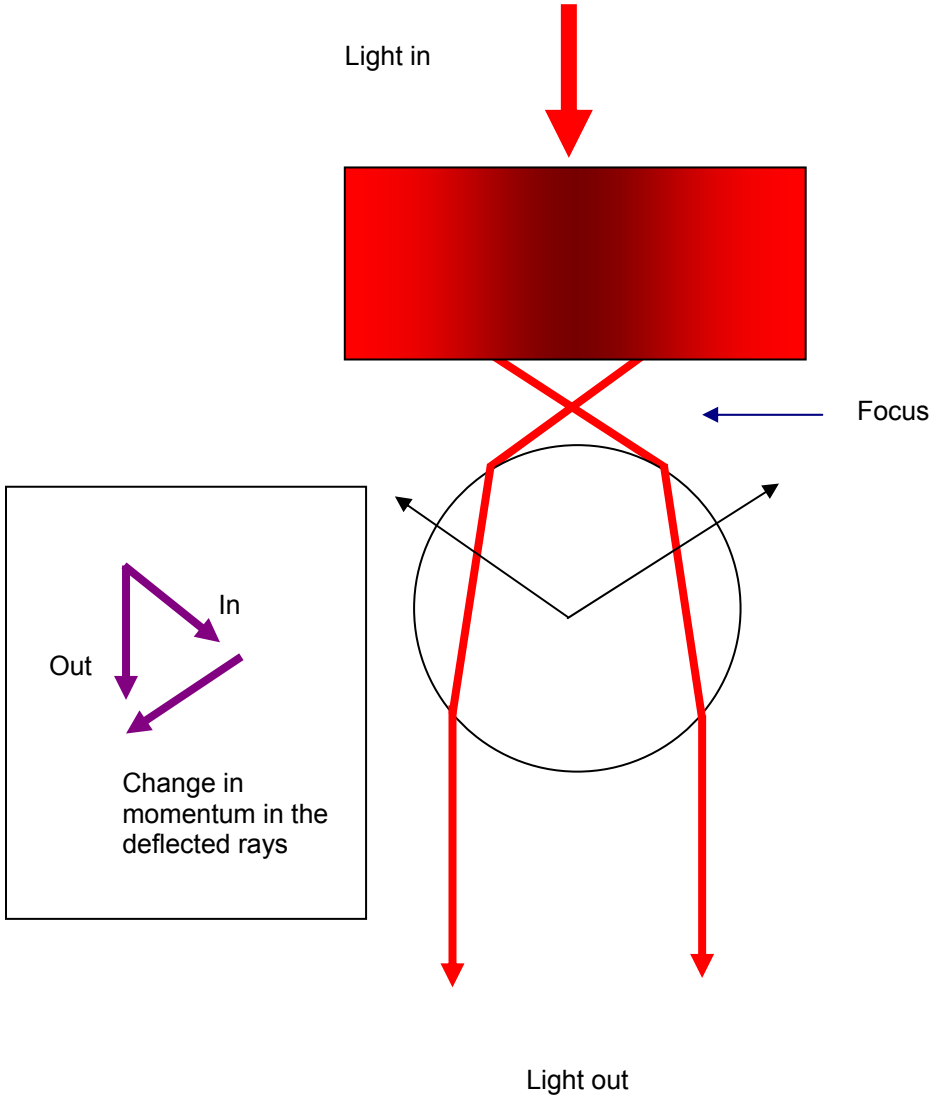

Fig. 3.2 – A ray-optic schematic of the gradient force acting upon a sphere. The laser light is brought to a focus (its beam profile has an intensity gradient). The rays (red arrows) are refracted as they pass through a spherical object (with a refractive index higher than the surrounding environment), located beyond the focus. Resulting reaction forces pull the sphere towards the focus of the laser beam. In the momentum diagram (illustrated within the box) the rate of change in momentum by the deflected rays produces an equal and opposite reaction in the sphere. The force (described by Newton's second law) produced by this change in momentum drags the sphere towards the focus (adapted from Svoboda and Block, 1994).

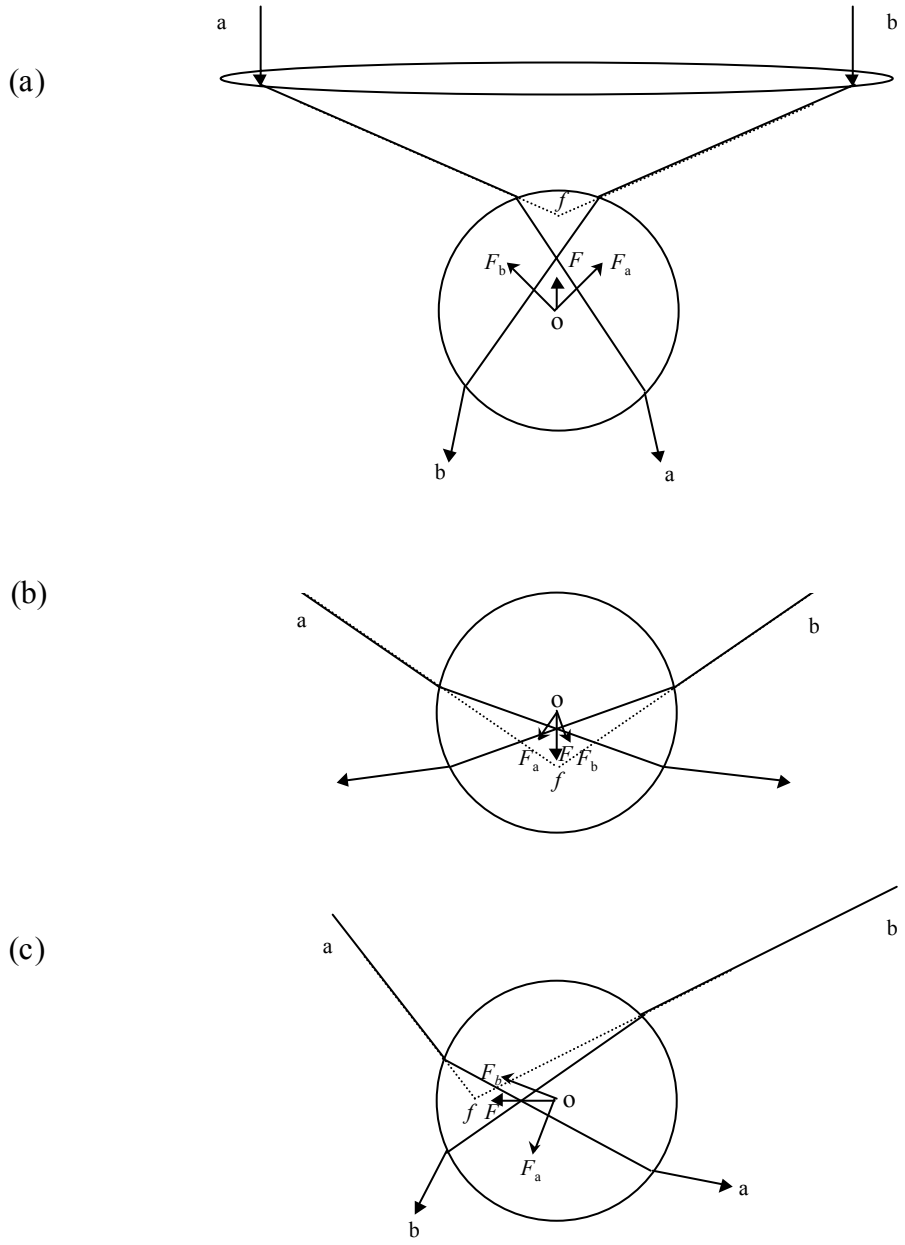

Fig. 3.3 – Qualitative view of the gradient force applied to a dielectric sphere due to the refraction of a typical pair of rays a and b. The refraction of the two rays gives rise to forces F_a and F_b, whose vector sum F is the restoring force for axial and transverse displacements of the sphere from the trap focus *f*. a) and b) represent axial displacements; c) represents transverse displacements (adapted from Ashkin, 1992).

If we consider a beam of light as an accumulation of individual rays, and that an optical trap is generated by focusing the beam ray-by-ray to a dimensionless focal point, *f*, then the vector sum of the refracted rays gives a net restoring force (F), for axial and transverse displacements of the origin of the dielectric sphere (O), directing it back to the focus. Figure 3.3 depicts the total force acting upon a dielectric sphere due to a typical pair of rays (*a* and *b*) of a converging beam. The change in photon momentum due to refraction alone, gives rise to forces F_a and F_b, shown in the direction of momentum change. The net restoring force of the two rays acts in the direction of the light intensity, thus translating the sphere origin to the laser focus.

To quantify such optical forces, the force due to a single ray of power *P*, contacting a dielectric sphere at an angle of incidence θ, with incident momentum per second of $n_m P/c$, can be considered (Fig. 3.4, adapted from Ashkin, 1992). The total optical force acting upon the sphere is the sum of contributions due to the reflected ray *PR*, and the infinite number of emergent refracted rays of successively decreasing power PT^2, PT^2R, . . . PT^2R^n, . . . The values of *R* and *T* are the Fresnel reflection and refraction coefficients of the surface at θ. The net force acting through the origin can be broken into F_{scatt} (due to the reflected ray) and F_{grad} (product of the refracted ray), equations 3-4 and 3-5, respectively (Ashkin, 1992).

$$F_{scatt} = \frac{n_m P}{c}\left\{1 + R\cos 2\theta - \frac{T^2\left[\cos(2\theta - 2\in) + R\cos 2\theta\right]}{1 + R^2 + 2R\cos 2\in}\right\} \quad (3\text{-}4)$$

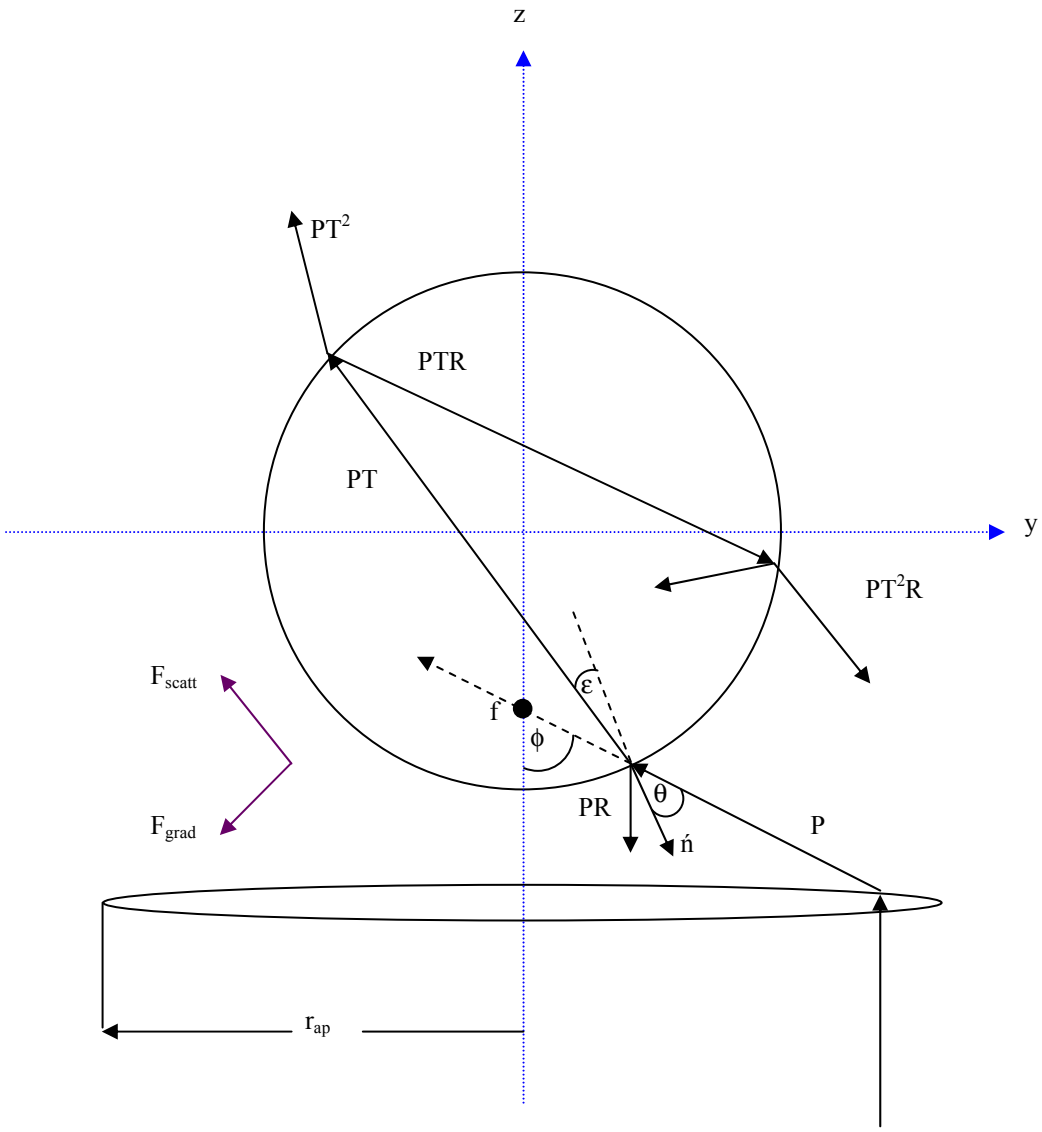

Fig. 3.4 – The quantification of optical forces due to a single ray of power, P, contacting a dielectric sphere at an angle of incidence, θ. R and T are the Fresnel reflection and transmission coefficients, respectively (adapted from Ashkin (1992)).

$$F_{grad} = \frac{n_m P}{c}\left\{R\sin 2\theta \frac{T^2\left[\sin(2\theta - 2r) + R\sin 2\theta\right]}{1 + R^2 + 2R\cos 2\in}\right\} \qquad (3\text{-}5)$$

Where, θ is the angle of incidence, $\in$ is the angle of refraction, R is the reflection coefficient defined as the ratio of the reflected power to the incident power, and T is the refraction coefficient defined as the ratio of the refracted power to the incident power.

The absolute magnitude of the total force acting upon the dielectric sphere is given by

$$F_{mag} = \left(F_{scatt}{}^2 + F_{grad}{}^2\right)^{1/2} \qquad (3\text{-}6)$$

The overall force exerted by a beam of light is simply the vector sum of the forces resulting from the assembly of rays that comprise the beam (Ashkin, 1992).

3.2 INSTRUMENTATION

In this section, the design of the optical tweezer system employed, its optical components and the alignment procedure are discussed in detail.

3.2.1 Optical Tweezers Design

There are a number of different optical configurations to be considered in an optical tweezers design. The configuration employed is dependent upon the sophistication of the desired applications, and perhaps more importantly the availability of financial funds. However, the single beam model (Ashkin, 1986) is the foundation for any optical tweezers system, and can be readily adapted to produce more sophisticated system. For example, the incorporation of an electric-piezo stage would provide accurate trap manipulation in the *x, y,* and *z* axes, and a position-sensitive detector capable of nanometer resolution would allow the determination of the displacement of particles from the centre of the optical trap. There is also an escalating desire to produce multiple optical traps as the possible applications become increasingly diverse and infinitely more complex.

There are a variety of ways of producing multiple optical traps. The most trivial is to increase the number of light sources, a simple yet costly approach. Alternatively, a single light source can be divided using a polarizing beam-splitting cube to produce a dual optical trap capable of movement in all three dimensions (Fällman & Axner, 1997). Acousto-optic modulators have also been employed to produce multiple traps from a single light source (Visscher *et al*., 1996; Molloy *et al*., 1999). In this approach, the light source is time-shared between a number of positions in the specimen plane. The light must be scanned rapidly among the positions to generate individual traps. This rapid 'blinking' at each position mimics the effect of steady illumination (Visscher *et*

al., 1996). Optical tweezers system have also been adapted and combined with other instrumental techniques, for example, fluorescence microscopy (Funatsu *et al*., 1996; Ishii *et al*., 1998), AFM (Shivashankar & Libchaber, 1997), a pulsed UV laser microbeam (Steubing *et al*., 1991), and an optical stretcher (Guck *et al*., 2001).

Due to the financial implications in the design and development of an optical trap, the single beam model was chosen as the basis for our system. Although, perhaps not as sophisticated as the multi-beam systems, the single beam has been employed to study motor proteins (Yin *et al*., 1997), cells and organelles (Ashkin *et al*., 1987; Ashkin & Dziedzic, 1987; Block *et al*., 1989; Berns *et al*., 1989; Ashkin & Dziedzic, 1989), DNA (Chu, 1991; Wang *et al*., 1994; Smith *et al*., 1996; Arai *et al*., 1999), and receptor-ligand interactions (Mammen *et al*., 1996; Helmerson *et al*., 1997; Stout, 2000).

The requirements of any single beam optical trap is a tightly focused laser beam, and the ability to translate this optical focus in the *x*, *y*, and *z* axes. In order to generate a strong stable three-dimensional trap it is necessary to produce the steepest intensity gradient possible. By producing a steep intensity gradient, the gradient force becomes dominant over the counteractive scattering force. This is achieved using of a microscope objective with a high numerical aperture (NA), in the range of 1.00-1.40 (corresponding to angles up to 140°). An additional requirement for strong optical trapping is the *overfilling* of the rear pupil of the objective rather than simply filling the pupil. These highly

converging rays contribute disproportionately to the axial intensity gradient (Ashkin, 1992).

The design of the optical tweezers employed in this thesis, was based upon the designs of Ghislain *et al*. (1994) and the Visscher *et al*. (1996), as depicted in figures 3.5a and 3.5b, respectively. In the Ghislain system a telescope lens element was employed to generate expansion of the laser beam to ensure *overfilling* of the objective rear pupil. Translation of the optical focus in the specimen plane was achieved using an *x*-*y*-*z* piezo-electric scanning stage (fig 3.5a). Alternatively, Visscher expanded the beam diameter three fold using a microscope objective, and employed a 1:1 telescope to allow translation of the trap in *x*, *y* and *z* (fig. 3.5b). Incorporated into this design were two polarising beam splitters to produce a steerable dual-beam trap. Our design, depicted schematically in figure 3.5c, incorporates both the microscope objective and the telescope lens element in order to generate the required expansion of the laser beam. The telescope was also employed for manual *x*, *y*, and *z* translation of the trap.

The configuration of our single beam design is represented photographically and schematically in figure 3.6a and b, respectively, and is outlined in the text below, in sequential order. Optical elements were purchased from Melles Griot (Cambridge, UK), unless specified otherwise, and all lenses were grade BK-7 glass. Starting with a Nd:YAG diode laser (λ=1064 nm, max. power 1 W)

a

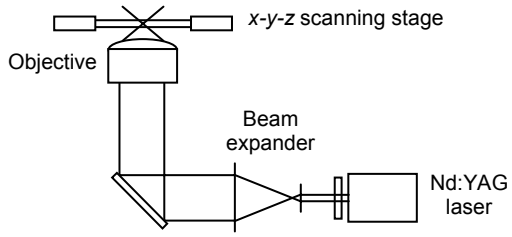

b

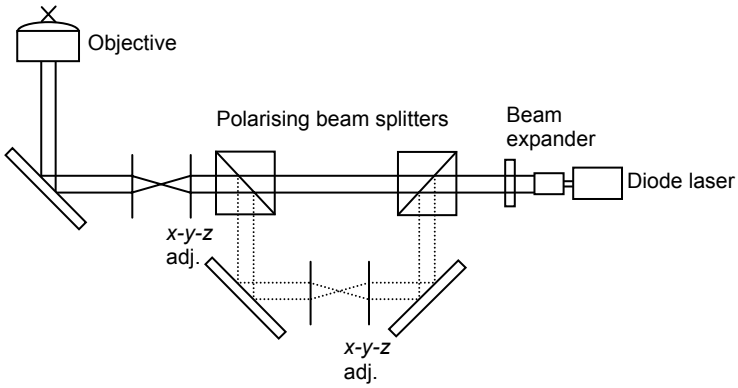

c

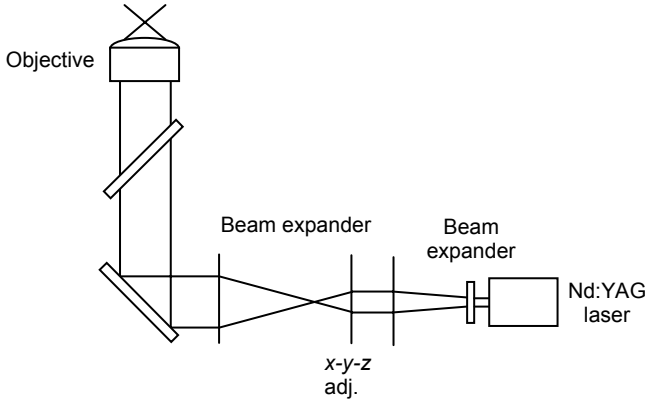

Fig. 3.5 – Optical tweezers designs; (a) Ghislian *et al*., (1994); (b) Visscher *et al*., (1996); and (c) the basic optical design employed in this thesis.

a

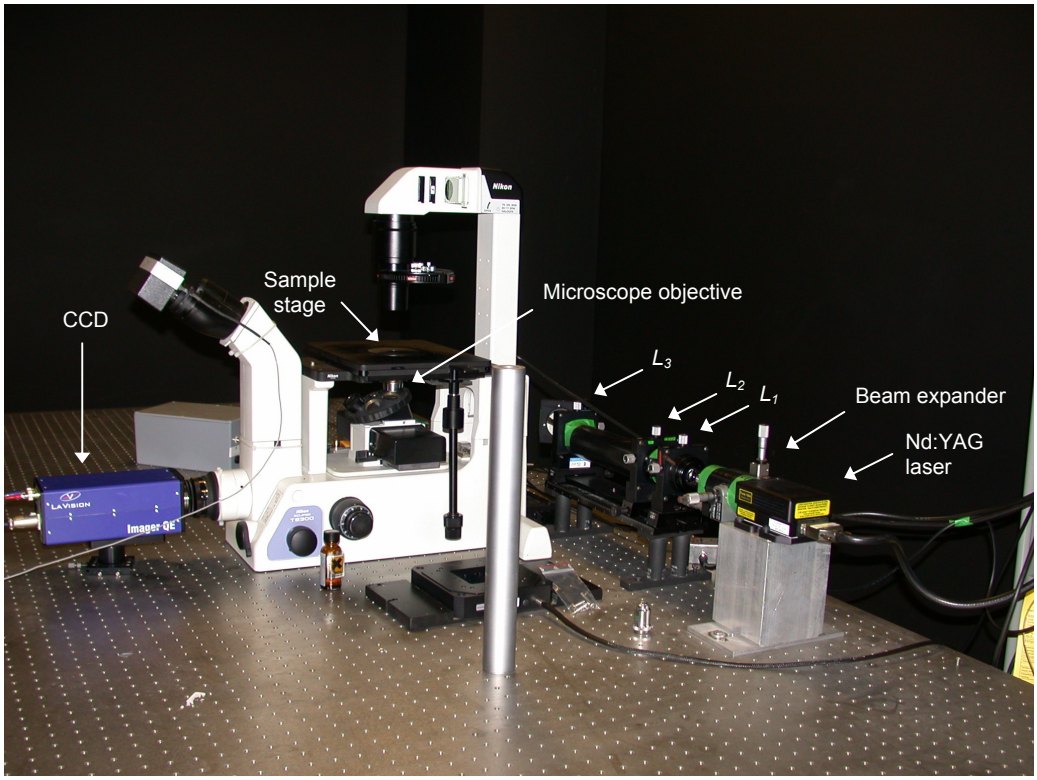

b

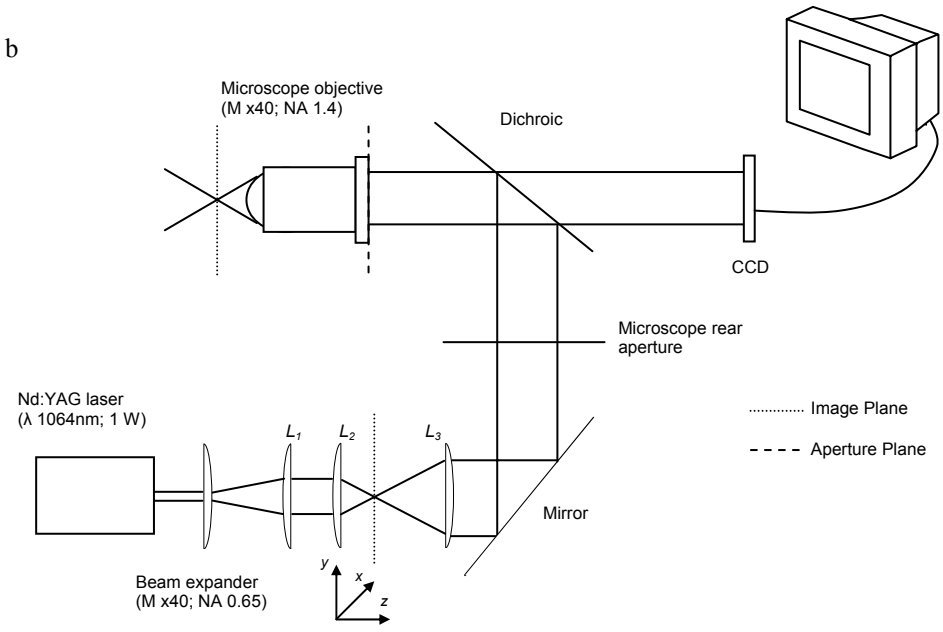

Fig. 3.6 – A schematic of the optical path employed in the construction of a single beam optical tweezers. The microscope objective was positioned directly at the laser source providing expansion of the laser beam. L_1 was positioned its focal length (35 mm) from the beam expander, resulting in collimation of the expanded beam. The telescope lens system, consisting of consecutive lenses L_2 and L_3, were positioned a distance of the sum of their focal lengths apart ($d=f_2+f_3$). The telescope provides a method of trap manipulation in x,y,z. L_3 is located a distance of $2f_3$ from the rear pupil of the final microscope objective. A kinematic mount mirror directs the beam into the rear entrance of the microscope, and a dichroic mirror positioned 25 mm inside the rear aperture plane of the microscope reflects only the infrared beam up vertically through the microscope objective.

(Forte 1060 series, Laser Quantum Ltd., Laser Support Services, Manchester, UK); a microscope eyepiece with a NA of 0.65, and a magnification of x40, (Nikon, Surrey, UK) mounted on an *x-y-z* micrometer stage; a planoconvex lens (L_1), focal length (f_1) 35 mm; a telescope lens system comprising of two further planoconvex lens, L_2 and L_3. L_2 of the telescope has a focal length (f_2) of 50 mm, L_3 has a focal length (f_3) of 200 mm, both lens have a diameter of 30 mm, and all lens were mount on *x-y-z* translation stages; a mirror also mount on an *x-y-z* translation stage; an inverted microscope (Eclipse TE300, Nikon, Surrey, UK); a dichroic mirror with a reflective wave length of 1064 nm (Chroma Technology, Battleborough, VT, USA); a microscope objective with a NA of 1.4, a magnification of x40 and a working distance of 220 μm; and a CCD camera (Nikon, Surrey, UK) which relays the video signal to an image processor (JCV television), and the output is recorded by a VCR.

3.2.2 Construction and Alignment

The single beam optical apparatus was built directly onto a compressed air table (Newport Ltd, Newbury, Berkshire, UK) to minimise vibrations.

3.2.2.1 *The Laser*

There are a number of important laser characteristics to be considered when building an optical trap. The wavelength of the laser is the primary consideration, particularly if the proposed application is biological. Biological

pigments, such as haemoglobin, readily absorb light in the visible region. Absorbance becomes increasingly less with progression along the spectrum towards the near infrared up to 800 nm. Beyond 800 nm the light is absorbed by water rather than biological material (Svoboda & Block, 1994). The lesser of the two evils is the heating of the surrounding environment, and if the power levels and employment periods are kept to a minimum, then light absorption in the infrared region should not result in a detrimental effect upon biological material (Svoboda & Block, 1994). At a power of 80 mW, assuming an absorption coefficient of ~0.1 cm^{-1}, the temperature rise is estimated to be several degrees centigrade (Ashkin, 1987). Therefore, an infrared light source is probably the most beneficial compromise, when trapping biological material. Thus, the laser employed in this and in a large proportion of optical traps (Veigel *et al*., 1998; Zahn *et al*., 1999; Lenormand *et al*., 2001) is the Nd:YAG (neodynium:yttrium aluminium garnet) diode-pumped solid state laser, with a wavelength (λ) of 1064 nm, and a maximum source power of 1 W (Forte 1060 series, Laser Quantum Ltd., Laser Support Services, Manchester, UK).

The shape of the output beam (the beam astigmatism) is also crucial in effective trapping. The beam shape determines the precision of the microscope objective to focus the laser. Therefore, a clean, spherical and uniform beam is necessary to produce a strong intensity gradient and an efficient trapping focus.

Laser safety is always an important consideration when operating lasers. It is necessary to wear safety goggles, which filter out the appropriate wavelengths,

when the laser is in operation. The laser beam must be maintained below eye level and parallel to the optical bench. The minimum laser power necessary to image the beam should be used during the alignment procedure. A laser interlock system connecting laboratory entrances, exits and shields covering the microscope eyepieces, to the laser power supply should also be in place to prevent accidental beam exposure.

The laser was positioned parallel to the optical bench, at a height of 150 mm, corresponding to the height of the centre of the rear microscope entrance. All optical elements thereafter were positioned perpendicular to the laser beam and optical bench, at a lens centre height of 150 mm.

3.2.2.2 *Trapping Optics*

To assist with comprehension of the text to follow, which discusses each element within the optical path, the reader is referred to figure 3.6. The first optical element, the microscope eye-piece was positioned directly at the laser source providing expansion of the laser beam. L_1 was positioned f_1 (35 mm) from the beam expander, resulting in collimation of the expanded beam. The telescope lens system, consisting of consecutive lenses L_2 and L_3, provided a method of trap manipulation in x, y and z, as well as further expansion of the beam. By orientating these planoconvex lenses so that the flat surface of the lenses are facing, divides the degree of deviation equally between each lens

surface, minimising potential spherical aberrations (distortions) (Muncaster, 1988).

L_2 was positioned 25 mm from L_1, although the distance is not of significance due to beam collimation. L_2 and L_3 were positioned a distance of the sum of their focal lengths apart ($d = f_2 + f_3$). The focal lengths of the lenses employed in this telescope system provides further expansion of the laser beam, necessary to overfill the rear aperture of the final microscope objective. The ratio of f_2 to f_3 determines the degree of magnification of the beam diameter, where $M = f_2 / f_3$. Figure 3.7a illustrates the beam magnification provided by the telescope lens system. L_2 and L_3 have focal lengths of 50 mm and 200 mm, respectively, producing a 4:1 telescope arrangement, corresponding to a magnification of the beam diameter by a factor of 4.

It was also necessary to ensure that L_3 was located a distance of $2f_3$ from the rear pupil of the final microscope objective. This is related to the maintenance of the optically conjugate planes of the microscope, namely the image and aperture plane. The image plane comprises of the camera focus, the intermediate image, the specimen plane, the telescope focus, and the field diaphragm. Conversely, the aperture plane consists of the eye point of the eyepiece, the condenser aperture, and the objective rear pupil. These two planes hold a special relationship, where the translation of an image along an axis in one plane produces rotation of the beam about its axis in the other (Block, 1999).

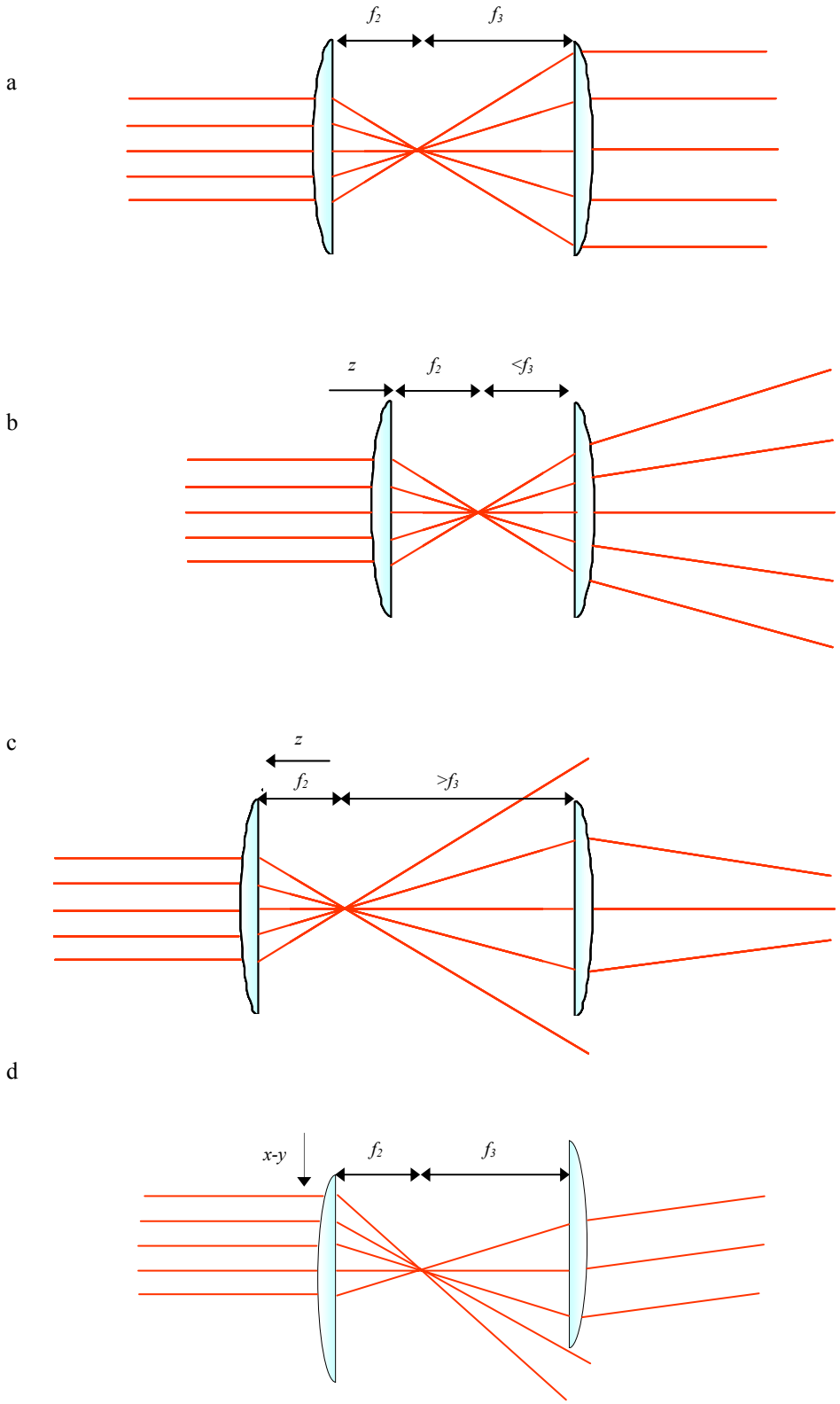

Fig. 3.7 - Ray diagrams of the telescope element of the optical tweezers system; a) Illustration of beam expansion; b) Axial translation of the optical trap deeper into the sample chamber; c) Axial translation of the optical trap towards the chamber surface; d) Transverse translation of the optical trap (based on Block, 1999).

This feature forms the basis of trap steering, when employing the telescope system. The relevant planes are highlight in the optical pathway, figure 3.6b.

Axial and lateral translation of the optical trap in the specimen plane was achieved by manipulating only L_2 of the telescope, and maintaining a fixed position for all other optical elements. The predetermined distance between L_2 and L_3 is the sum of their focal length ($d = \Sigma f$), this arrangement results in collimation of the laser light exiting L_3. The collimated light entering a lens specifies the focal point of that lens, thus if the light received by that lens is focused at the focal point of the lens then the light exiting the lens is collimated (fig. 3.7a). Thus, if the focus of the light received by the lens is after the focal point of the lens (where light is converging) then the resulting beam is divergent (fig. 3.7b). Conversely, if the focus of the light received is before the focal point of the lens (where light is diverging) then the resulting beam is convergent (fig. 3.7c). The degree of divergence and convergence is dependent on the distance of the light focus from the lens focus. This is the principle behind the axial translation of the optical trap. Positive movement of the trap along the *z*-axis in the specimen plane occurs when the distance between L_2 and L_3 is reduced, where $d < \Sigma f$. The translation of telescope focal point towards L_3 produces divergence of the beam after the telescope (fig. 3.7b). Due to the divergence of the beam entering the microscope objective, the focal point of the objective lens is translated deeper into the sample chamber (Block, 1999). Negative movement in the *z*-axis, where the focal point of the objective lens is brought closer to the objective, was achieved by creating a convergent

beam after L_3, where $d > \Sigma f$ (Block, 1999) (fig. 3.7c). If the image focal plane is maintained, then such axial translations of the trap can be identified (on a CCD) by a uniformly circular laser spot coming in and out of focus as it is translated along the *z*-axis (Block, 1999).

Lateral translation of the trap was produced by translating L_2 in the *x*, *y*-axis, perpendicular to the optical path. As previously mentioned, the focal point of the telescope and the specimen plane are conjugate to each other, thus translation of the beam in the telescope results in translation of the beam in the specimen plane. Whereby, translation of focus in the telescope image plane produces rotation of the beam about its axis through the objective rear pupil aperture plane, which then results in translation of the focus in the specimen image plane (fig. 3.7d). To maintain these conjugate planes, L_3 must be imaged at the rear pupil objective plane, to achieve this L_3 was positioned a distance of $2f_3$ from the rear pupil objective.

Following the telescope lens system, a polished circular mirror was mounted on an *x*-*y*-*z* translation stage and positioned at approximately a 45º angle to the laser beam, to direct the beam into the rear of the inverted microscope. 25 mm inside the rear aperture plane of the microscope was a dichroic mirror, again positioned at a 45º angle to reflect the laser beam up vertically through the microscope objective. The dichroic mirror reflects only infrared light and allows visible light to pass through, thus allowing only the laser light to be focused by the objective.

The final optical element in the optical tweezer system is the x40, 1.4 NA microscope objective which produces the trap by focusing the beam in the specimen plane. This particular microscope objective was chosen due to its infrared properties (produces less aberrations in the infrared region of the spectrum, as stated by the manufacturer) and its high numerical aperture, which (as previously discussed) is one of the factors necessary to produce a steep intensity gradient, invaluable for stable trapping.

3.2.2.3 *Laser Alignment*

The laser alignment procedure employed was adapted from Block (1999).

In order to visualise the infrared beam an IR detection card (Scientific Imaging Systems, Eastman Kodak Company, Rochester, NY, USA) was used. To minimise any risk from laser exposure, the minimum laser power required to image the beam was used during the alignment procedure. Before carrying out the laser alignment procedure it was necessary to ensure that the microscope is accurately aligned, for example, alignment of the microscope condenser to the microscope objective. This was achieved using a treated coverslip (of a thickness corresponding to the focal distance of the microscope objective) in which only a pin prick of visible light (from the condenser) can pass through. The microscope objective was focused upon the pinhole light and the condenser was aligned and centred to the objective.

Initially the optical path of the laser to the microscope was chosen, taking into consideration the dimensions and specifications of all optical elements. Due to spatial constraints a 90º angle change in the optical path was required. This was achieved using a kinematic mirror mount and metallic mirror positioned at approximately 45º to the rear entrance aperture of the microscope.

The laser, mirror, microscope and dichroic mirror provided the foundation with which to build. Initially, the dichroic mirror was optically mounted in the microscope filter cube to allow the horizontal infrared laser light entering from the rear of the microscope to be reflected up vertically through the open objective turret. The laser was then turned on to the minimum power to visualise the beam, and the metallic mirror was coarsely positioned at a 45º to the rear entrance of the microscope to direct the laser beam in through the centre of this entry point. The microscope objective was then positioned and fine adjustment of the angle of the kinematic mounted mirror was undertaken to ensure that the emission of the laser light from the microscope objective was vertical. During this process the accuracy of the alignment of infrared laser light maybe compromised due to obvious visualisation problems. Therefore, it is beneficial to retrace the optical path in reverse, from the microscope illuminator to the laser source, using visible light (Molloy, 1999). This was performed after the addition of each optical element.

The microscope eyepiece (x40, NA 0.65), providing expansion of the beam (as previously described), was the next element added. al distance away from the

laser source and parallel to the optical bench. The beam expander position was then adjusted in the *x,y*-axis to enable the beam to pass directly through the centre. Unfortunately, due to divergence of the beam upon exit it was not possible to determine whether the expander was positioned accurately. Therefore, fine adjustment was achieved again by tracing the visible light from the microscope illuminator through the expander back to the laser source.

L_1 was then positioned its focal distance from the beam expander producing a collimated beam. This collimating lens was manipulated in *x-y* axis until the laser light emitted from the final microscope objective was perpendicular to the optical bench. It is important to note that the beam of light should enter and exit the centre of the lenses, and not be skewed (Hecht, 1987).

The telescope lens system was the final optical component added. Starting with the second lens of the telescope, L_3 was positioned prior to the kinematic mount mirror at a distance of $2f_3$ from the rear pupil of the microscope objective (for reasons previously described in section 3.2.2.2). The lens was coarsely adjusted in the *x-y* axis so that the laser beam passed vertically through the centre of the open microscope objective turret. At this stage the laser beam was focused at the rear aperture of the microscope. The microscope objective was then replaced and the emerging beam was centralised by fine adjustment of L_3. L_2 was then positioned the sum of the focal lengths of L_2 and L_3 ($d = \Sigma f$) away from L_3. This resulted in collimation of the laser beam exiting the telescope system. Once again, coarse adjustment was followed by

fine adjustment in *x*-*y* to produce a uniform vertical beam exiting the microscope objective.

Employing a CCD camera and a glass microscope slide, it was possible at this stage of alignment, to visualise (on a video screen) a bright spot corresponding to the laser being reflected off the underside of the microscope slide. As well as the laser spot, interference fringes were commonly seen. The laser spot was centred in the field of view by adjusting L_2 in *x*-*y*. Focusing the laser beam in the specimen plane was achieved by translating the telescope focal point in the *z* axis. This was accomplished by translating L_2 in the *z*-axis (to and from L_3) until the diameter of the visualised spot was at its minimum.

Fine laser alignment was achieved by "*walking the beam*" through a series of beam rotations (by L_2) and translations (by the mirror) until it was precisely coaxial with the optical axis of the objective to produce a diffraction-limited spot. The spot was moved off centre in the *x*-axis using either L_2 or the mirror and restored to the centre using the alternative optical component, the mirror or L_2. The procedure was repeated in the *y*-axis. The aim of this final alignment step was to cause the laser light to form a uniformly circular set of rings that collapsed to a single point of focus and expanded back into a uniform circular set of rings beyond it. The laser was then aligned and optimised for effective stable trapping.

3.2.2.4 *Laser Power*

The accuracy of laser alignment and the effectiveness of the optical elements employed were determined by performing a laser power assessment over the optical pathway. This provides a detailed profile of laser power, drawing attention to areas of significant losses. The laser power was measured using a silicon cell power meter (spectral response range 400-1064 nm (Edmund Scientific, Barrington, NJ, USA)). Readings were performed at positions in the optical pathway, where the total laser intensity could be measured (i.e. not at points where the diameter of the laser beam is so great that it overfills the meter diode). Figure 3.8 illustrates the points at which power readings were taken.

The manufactures power supply estimates were initially assessed, to determine whether the power displayed on the LED screen was equivalent to the output laser power. The LED screen displayed the laser power in the unit Amps, for comparability (with power meter readings (mW)) Amps were converted to the SI unit W via a graph supplied by the manufacture (fig. 3.9). The manufactures power estimates from 10 – 440 mW were found to differ from those measured at the laser output (fig. 3.10). For manufacture power estimates below 100 mW the output power meter measurements were as little as 2 % of the power estimates.

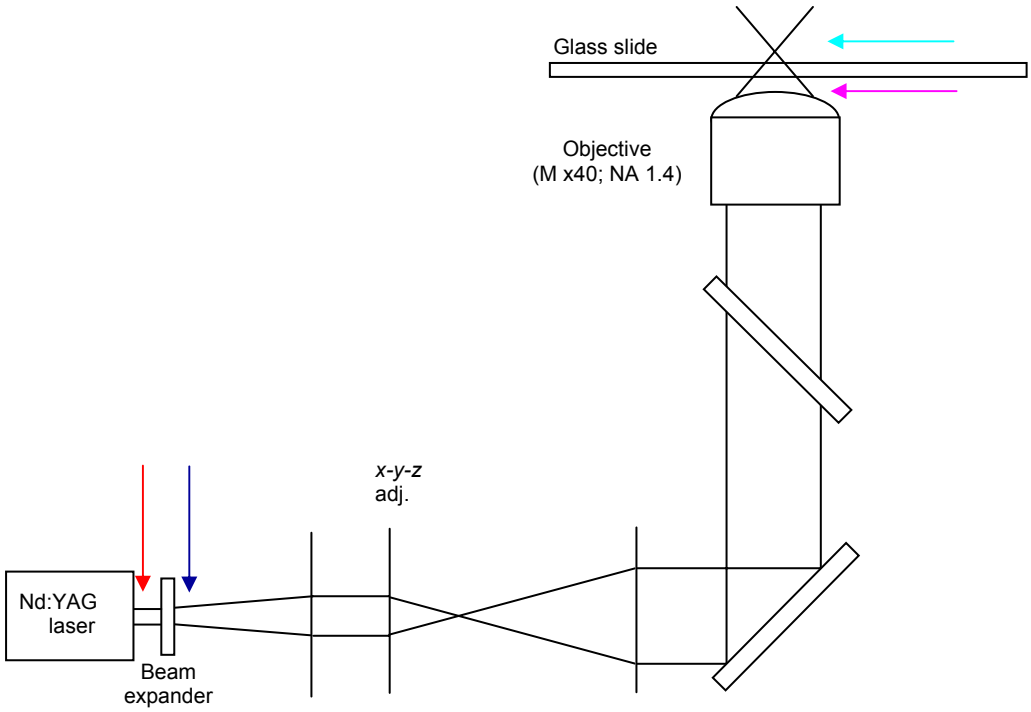

Fig. 3.8 – Indicates the points at which power meter readings were taken in the optical pathway. The *red arrow* relates to the power source, the *navy arrow* relates to the meter reading after the first stage of beam expansion, the *pink arrow* relates to the laser power upon emission from the final microscope objective, and the *turquoise arrow* relates to the laser power following diffraction through a glass coverslip with a thickness of 170 µm.

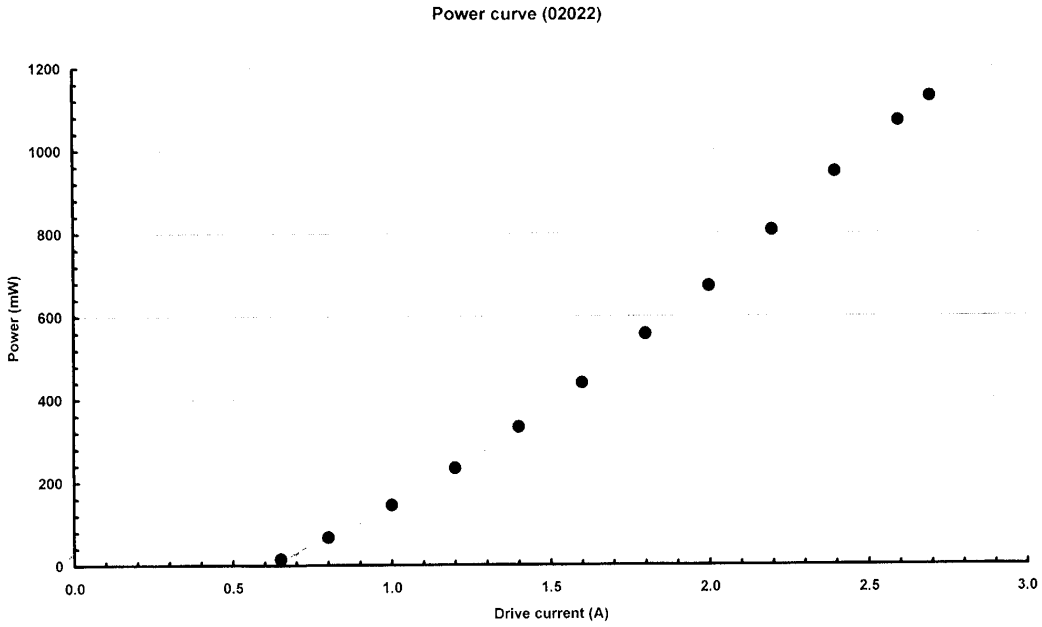

Fig. 3.9 - Manufacturers laser output power estimates for the 1064 nm Nd:YAG diode-pumped solid state laser (Forte 1060 series, Laser Quantum Ltd.).

a

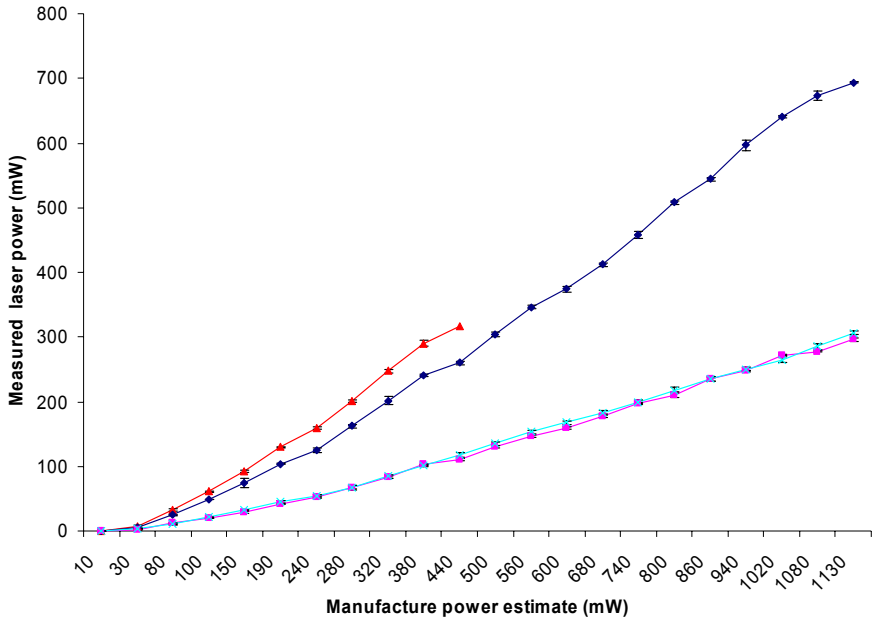

b

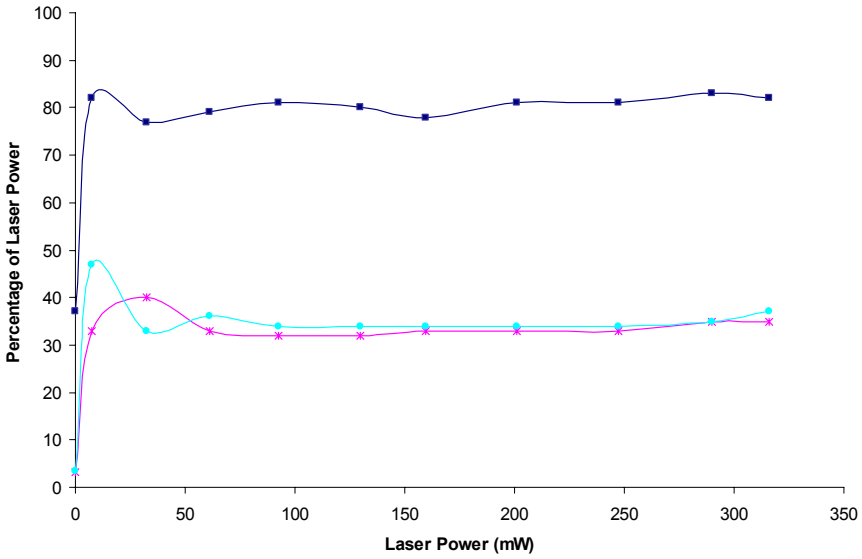

Fig. 3.10 – A profile of the laser power throughout the optical pathway. a) Compares measured laser power (mW) to the manufactures power estimates (mW); b) Displays the percentages of the laser power over the optical path, the measured laser output being 100%.

Although, this improved to a steady 69 % at manufacture estimates greater than 100 mW, as depicted in figure 3.10a (*red* data set). The power losses encountered over the optical pathway will be discussed, hereafter, in relation to the measured power at the laser output using the silicon cell power meter and not the manufactures estimates. Thus, laser power measured at the laser output is considered to be 100% power. There is a degree of inherent power loss in the system with the addition of each optical component (fig. 3.10a, b). The microscope objective required for early beam expansion was found to be responsible for a 20 % loss in laser power (*navy* data sets in figures 3.10a and b). Losses incurred due to L_1, the telescope element (L_2 and L_3), the kinematic mounted mirror, the dichroic mirror, and the microscope objective could not be determined individually due to expansion of the beam beyond the limits of the power meter. Collectively, these optical elements were responsible for a decrease in laser power by 45 % (*pink* data set fig. 3.10a-b). There were however, no noticeable power losses due to the presence of the objective immersion oil and a 170 μm thick glass coverslip (which provides the lower boundary in the sample chambers employed) (*turquoise* data set fig. 3.10a-b). Thus, the resulting optical trap power was approximately 35 ± 5 % of the power measured at the laser output. These measured power losses remained constant above an output power greater than approximately 25 mW. The maximum laser power recorded at the optical trap position was 300 mW.

The power losses recorded over our optical pathway concur with previously reported values (Svoboda & Block, 1994, Felgner *et al*., 1995). Therefore, we

can conclude that the alignment of the laser has been performed to a standard where effective trapping can occur. Also, the ability to achieve a wide power range provides access to a wide force range imposable by the optical trap. The power losses experienced are most likely due to the optical components employed and not poor laser alignment. Such power losses can be reduced by coating optical components in an anti-infrared reflectivity coating (Block, 1999), however, this can be costly, and due to the maintenance of relatively standard power losses it was not deemed necessary for the presented studies.

3.2.2.5 *Imaging system*

The optical trap was viewed through a CCD camera (at x40 magnification) attached to the front port of the inverted microscope. The CCD camera was encapsulated within a custom built cylindrical sliding mechanism, which allowed axial movement of the CCD array. This freedom of movement permitted the visualisation of the trap focus over a range of *z*-positions within the sample cell. The CCD array relayed the video signal to a television and the output was recorded on a VCR. This imaging system was employed for the studies outlined in chapters 4 and 5.

A later addition to the imaging system was a imager QE CCD camera (LaVision UK, Oxon, UK) which relayed the video signal to a computer. Unfortunately, the camera maintained a fixed axial focus position which was not in the same focal plane as the laser focus. This system was employed to

demonstrate the utility of the instrumentation to trap and manipulate a range of particles (see section 3.4).

3.3 CALIBRATION

The difficulty which surrounds the theoretical computation of trapping forces (discussed in 3.1) means that forces must be determined empirically. There are two principal approaches for the determination of trapping forces; namely, the calibration of force and the calibration of trap stiffness (Ashkin, 1991). Encompassed within the individual approaches are numerous well-established calibration methods (discussed in the following sections), each with their own advantages and disadvantages.

3.3.1 Force Calibration

This method of calibration ascertains the maximal force imposed by the optical trap on a particle, and is measured as a function of particle size, refractive index, laser power, wave length, and proximity of a chamber surface.

3.3.1.1 *Escape Force Method*

The most commonly employed method of force calibration is the determination of the escape force. This method determines the transverse and axial strength of the optical trap by measuring the minimal force required to pull an object

free from an optical trap (Ashkin *et al*., 1986; Svoboda & Block, 1994; Felgner *et al*., 1995; Visscher *et al*., 1996). The transverse trapping forces are calibrated against the viscous drag exerted by fluid flow using Stokes' Law,

$$f_{la} = 6\pi\eta r v \tag{3-7}$$

where f_{la} is the lateral force, η is fluid viscosity, *r* is the sphere radius, and *v* is velocity. Conversely, the axial trapping forces are calibrated against the gravitational minus the buoyant force (Felgner *et al*., 1995), and are given by

$$f_{ax} = \frac{\pi}{6}(\rho_s - \rho_m)d^3 g \tag{3-8}$$

where f_{ax} is the axial force, ρ_s is sphere density, ρ_m is the density of the suspending medium, *d* is the sphere diameter and *g* is the gravitational force. This method is only applicable for microspheres whose densities are great enough for the spheres to fall out of the optical trap as a result of insufficient power. This only appears to be the case for larger spheres within the Mie regime (Felgner *et al*., 1995). However, smaller polystyrene spheres may appear to fall out of the trap at reduced powers, as a result of thermal energy driving the sphere over the potential energy barrier in the weakest direction of the optical trap (axially). Thus, the axial trapping force can be expressed in the terms of a harmonic trap potential, where the force required for escape is equal

to the thermal energy (Felgner *et al*., 1995). In this case the calibration force is given by

$$f_{ax} = \frac{2k_B T}{d} \tag{3-9}$$

where, k_B is the Boltzmann constant, T is the absolute temperature, d is the diameter of the sphere. It should be noted that when calibrating axial forces for larger, denser particles it is necessary to consider thermal energy, by simply adding the thermal and gravitational contributions together (Felgner *et al*., 1995).

3.3.2 Calibration of Trap Stiffness

Alternatively, the trap stiffness can be calibrated. Optical traps behave as Hookian springs, where the restoring force for small particle displacements from the centre of the optical trap is directly proportional to the displacement (Visscher *et al*., 1996). Thus, optical traps are characterised by a fixed stiffness. Once trap stiffness is known optical force can be calculated using Hookes' law ($F = kd$).

There are a number of efficient methods available for the determination of trap stiffness, only two of which are outlined below.

3.3.2.1 *Drag Force Method*

This technique determines trap stiffness through the application of a known viscous drag force to a trapped particle and measuring its displacement from the trap centre.

$$\alpha = f/x \tag{3-10}$$

where α is the trap stiffness, f is the viscous drag force and x is the position of the particle relative to the trap centre.

3.3.2.2 *Equipartition Method*

Alternatively, trap stiffness can be determined by studying the Brownian motion displayed by a trapped sphere at a particular laser power. The degree of particle diffusion is measured relative to the stationary point at the trap centre. The displacement of the particle is proportional to the trapping force. By applying the Equipartition theorem for a particle bound in a harmonic potential, where,

$$\tfrac{1}{2}k_B T = \tfrac{1}{2}\alpha\langle x^2\rangle \tag{3-11}$$

then the trap stiffness can be calculated.

For an in depth review of trap calibration the reader is directed to Svoboda & Block (1994) or Visscher *et al*. (1996).

3.3.3 Calibration of the Optical Trap

The described methods of calibration which require the determination of trap stiffness all require a position detector with nanometer resolution. Unfortunately, due to limited funds a position detector was not within budget. Therefore, the only form of calibration achievable was the calibration of force via the "escape force method". This method of calibration has previously been employed by a number of groups (Ashkin *et al*., 1986; Ghislain *et al*., 1994; Felgner *et al*., 1995; Smith *et al*., 1999), and was employed to calibrate the trapping forces for force measurements performed in chapters 4 and 5 of this thesis.

3.3.3.1 *Transverse Trapping Force*

The calibration of transverse trapping forces was achieved by determining the minimum force required for a trapped microsphere to escape from the optical focus when a known viscous drag force is applied. A flow chamber (designed and constructed within our laboratory) with a surface thickness of 170 μm and a chamber depth of 85 μm was employed. An aqueous solution containing monodispersed 2 μm polystyrene microspheres (Sigma, Poole, UK) was flowed perpendicular to the laser beam through the chamber at a known

velocity using a syringe pump (WPI Ltd, Stevenage, Hertfordshire, UK). The velocity of fluid flow was determined by measuring the time (s) for single 2 μm polystyrene beads to travel a predetermined distance (μm). By translating L_2 towards L_3 the optical trap was translated to a depth of 15 ± 0.5 μm within the sample chamber. Once a single microsphere was trapped the power of the laser was gradually decrease to the moment of escape.

Transverse trapping forces for 2 μm polystyrene microspheres, at a trap depth of 15 ± 0.5 μm in a suspension medium of high-purity deionised water (resistivity 15 MΩ cm), were calibrated against Stokes drag, where the viscosity of the of the suspension medium, water, is 0.001025 N m^{-2} s (at a temperature of 20°C), with a refractive index of 1.33, and a fluid velocity of 71.25 ± 14.29 μm s^{-1}. Ordinarily, when calculating Stokes drag the profile of fluid flow must be taken into consideration. When the fluid is contained within a chamber, the flow of the fluid takes on a laminar profile, where the fluid in contact with the surfaces travels at a slower velocity than the fluid travelling centred in relation to the outer boundaries. Therefore, if the trap is located in close proximity to a planar surface and is greatly affected by the laminar profile, then a correction factor accounting for this must be incorporated into the stokes equation (Svoboda & Block, 1994; Felgner *et al*., 1995):

$$f_{la} = 6\pi\eta rvk \qquad (3\text{-}12)$$

where, k is the correction factor and is defined by Faxen's Law,

$$k = \frac{1}{1 - \frac{9}{32}\left(\frac{d}{T}\right) + \frac{1}{64}\left(\frac{d}{T}\right)^3 - \frac{45}{4096}\left(\frac{d}{T}\right)^4 - \frac{1}{512}\left(\frac{d}{T}\right)^5} \qquad (3\text{-}13)$$

where, d is the diameter of the sphere, T is the distance of the sphere centre from the coverslip (Felgner *et al*., 1995). Fortunately, if the distance of the trapped microsphere from the chamber boundaries is greater than 2d of the microsphere, then this correction factor need not be taken into consideration (Smith *et al*., 1998). The trap depth chosen in this calibration procedure is much greater than 2d, and therefore the correction factor is not considered.

The viscous drag force imposed upon the trapped particle was calculated to be 1.38 ± 0.28 pN. The minimum escape power of the trapped particle when a force of 1.38 ± 0.28 pN was applied, was 0.698 ± 0.033 Amp, equivalent to 2.8 mW at the optical focus. The trapping force is proportional to the laser power at the focus, and therefore force can be expressed by the dimensionless factor, Q (Eqn. 3-1) (Felgner *et al*., 1995). The transverse trapping efficiency, $Q_{la,}$ calculated was 0.11075. This Q value is in good agreement with previously published data (see table 3.1).

Sphere diameter (μm)	Q_{la}	Q_{ax}	Reference
2	0.11075	0.0025	Our data
1.0	0.08	0.07	Ghislain, *et al*., 1994
2.1	0.16	0.08	Ghislain, *et al*., 1994
1.020	0.085 ± 0.011	0.0058 ± 0.0025	Felgner, *et al*., 1995
2.967	0.21 ± 0.03		Felgner, *et al*., 1995

Table 3.1 Lateral and axial calibration of dimensionless efficiency factors employed in the determination of optical force (Eqn. 3-1).

3.3.3.2 *Axial Trapping Force*

The axial trapping force was calibrated by simply reducing the laser power until the trapped microsphere dropped out of the optical trap. Axial trapping forces for 2 μm polystyrene microspheres, at a trap depth of 8 ± 0.5 μm in a suspension medium of high-purity deionised water, were calibrated against the gravitational minus the buoyant force (Eqn. 3-8), and the thermal force (Eqn. 3-9). The gravitational and thermal contributions were then simply added to calibrate the axial trapping forces. The minimum escape power of the trapped particle when an axial force (f_{ax}) of 0.015 ± 0.001 pN was applied, was 0.64 ± 0.02 Amp, equal to 1.35 mW at the optical focus. By incorporating these figures into eqn. 3-1, an axial trapping efficiency of Q_{ax}=0.0025 was determined. This value is comparable to data published by Felgner *et al*., (1995). However, both of these Q_{ax} values (our data and Felgner *et al*., 1995) are low compared to Ghislain *et al*., (1994) (table 3.1), this maybe due to variation in calibration technique. Felgner *et al*., (1995) employed the same calibration method used in this chapter, however, Ghislain *et al*., (1994) employed the drag force method, in which a position sensitive detector is used providing a greater degree of sensitivity (previously described in section 3.3.2.1). However, due to financial constraints within the current project the Ghislain method could not be employed.

3.4 MANIPULATION OF PARTICLES

As previously discussed, an infrared optical focus is capable of trapping and manipulating micron and submicron biological particles (Ashkin *et al*., 1987; Block *et al*., 1989; Chu 1991; Mammen *et al*., 1996; Helmerson *et al*., 1997; Kellermayer et al., 1997; Tskhovrebova *et al*., 1997; Cui & Bustamante, 2000; Stout, 2001). In this section, the newly constructed optical tweezers are employed to trap and manipulate a range of dielectric microspheres from 1-12 μm in diameter. The system was also employed to demonstrate its ability to optically trap and manipulate biological cells (bacteria and neutrophils) without inducing necrosis.

3.4.1 Trapping procedure

A standard microscope slide and coverslip creates a simple but effective chamber for trapping particles suspended in an aqueous medium. The addition of vacuum grease around the outer edge of the coverslip produces a seal, preventing evaporation of the aqueous medium (fig. 3.11). The ideal preparation depth of the chamber is 50-100 μm, with an optical trap depth of <50 μm (Smith *et al*., 1999). Trapping becomes increasingly more difficult as the focus is moved deeper into the sample chamber, as a result of spherical aberrations (Wright *et al*, 1994). Fortunately, the proposed trap depth for effective axial trapping of particles is the diameter of the particle above the particle (Helmerson *et al*., 1997).

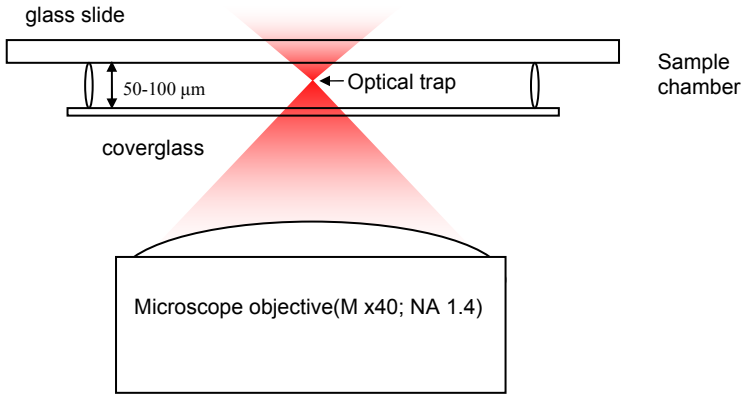

Fig. 3.11 – Schematic of the sample chamber employed when optically trapping particles.

In order to achieve trapping and manipulation, the optical focus was positioned above individual particles (for distances refer to the individual cases to follow) and a ramp of power was applied until the particle became attracted to the optical focus. The optical focus, and hence the trapped particle, was then coarsely translated in the *x*, *y* and *z* axes, in an environment of 10 mM PBS, pH 7.4, at undetermined velocities.

3.4.2 Dielectric microspheres

In a large proportion of optical tweezers applications polystyrene or silica microspheres are employed to enable the manipulation of biological molecules (For example, Wang *et al*., 1994; Helmerson *et al*., 1997; Kellermayer et al., 1997; Tskhovrebova *et al*., 1997; Stout, 2001). Owing to their availability, size, dielectric properties, and the ability to modify their surface chemistry, these "handles" are ideal tools for the manipulation of biomolecules.

Individual 1μm polystyrene microspheres were optically trapped and manipulated in the *x* and *y* axes at a sample chamber depth of approximately 6 μm, under an applied optical power of 2.8 mW. Figure 3.12 illustrates the sequential translation of a single microsphere in *x* (i-v), *y* (v-vii), and *x* again (vii-xii). The profile of the translation of the microsphere along the *x* axis is illustrated in figure 3.12b, where approximately 12.6 pixel units are equal to 1 μm. The microsphere was translated a distance of approx. 11 μm from left to right (fig. 3.12b i-v), and approx. 16 μm from right to left (fig. 3.12b vii-xii).

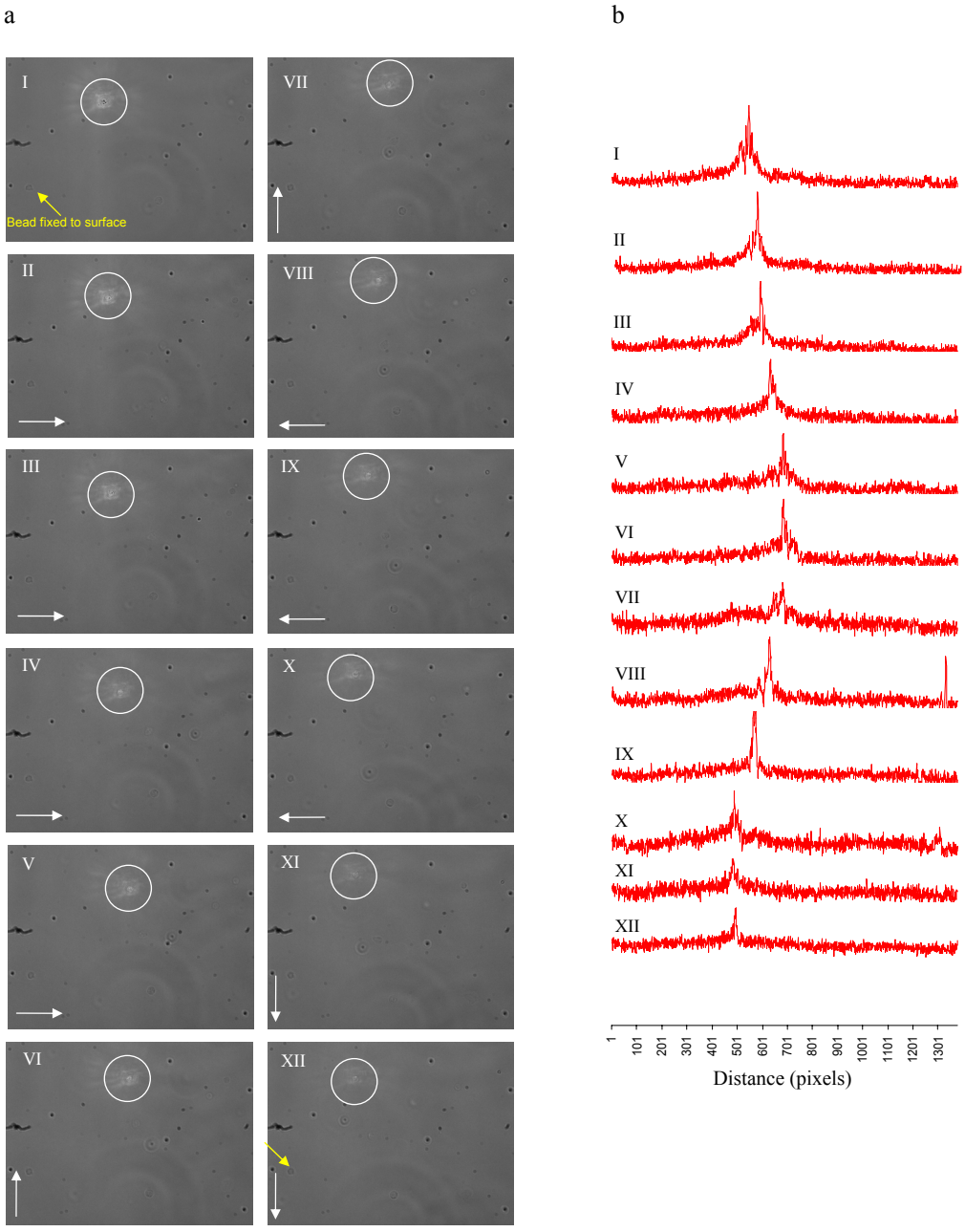

Fig. 3.12 - The optical manipulation of a 1 µm polystyrene microsphere in the *x* and *y* axes. a) The white circle highlights the trapped microsphere, the *white arrow* indicates the direction of translation (I-XII), the *yellow arrow* indicates the presence of an attached microsphere to the coverslip surface in I and remains present through to XII; b) Profiles of microsphere manipulation in the *x* axis, where 1µm equals approximately 12.5 pixels.

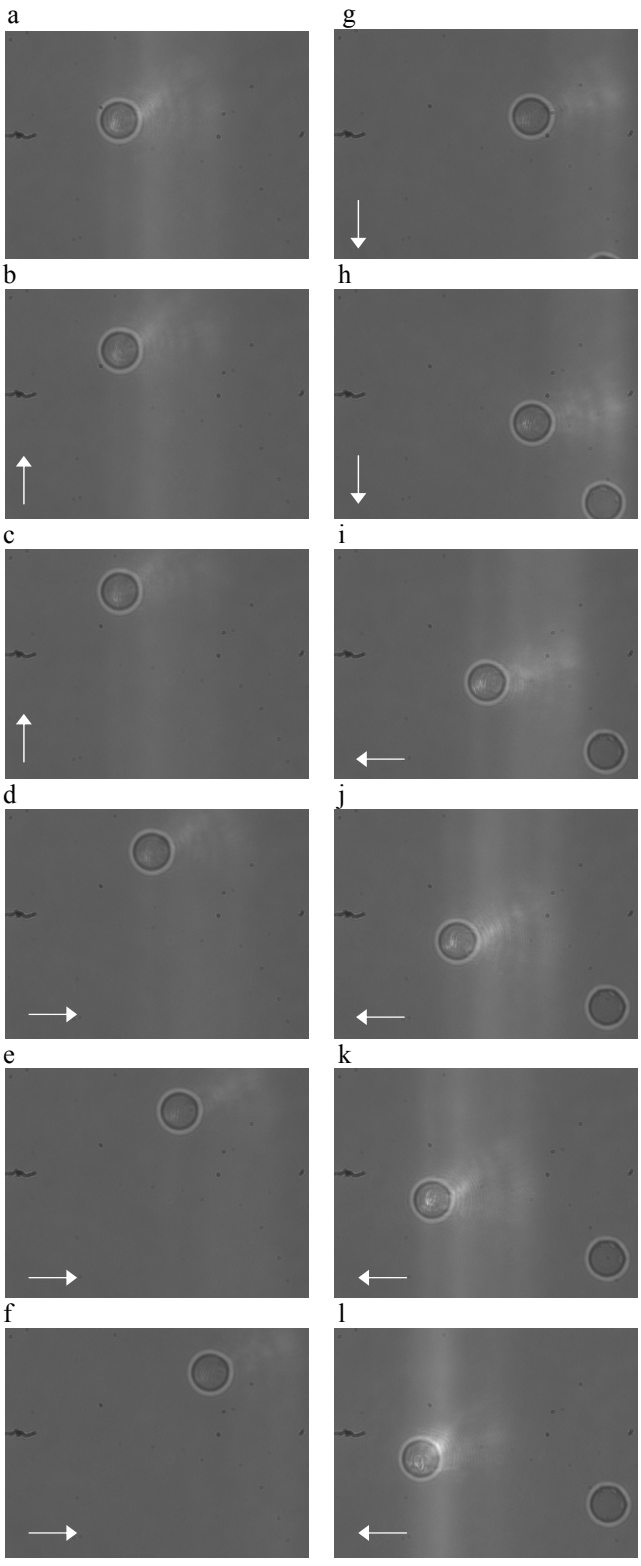

Fig. 3.13 - The optical manipulation of a 12 μm silica microsphere in the *x* and *y* axes. The *white arrow* indicates the direction of translation.

12 μm silica microspheres were also trapped and manipulated in the *x*, *y* and *z* axes, at a sample chamber depth of approximately 8 μm, under an applied power of 40 mW. Figure 3.13 illustrates the translation of an individual 12 μm silica microsphere a distance of approximately 15 μm along the *y* axis from bottom to top (a-c), 25 μm along the *x* axis from left to right (c-f), 25 μm from top to bottom (f-h), and 30 μm from right to left (h-l).

Unfortunately, the camera focus was not in the same focal plane as the laser focus, making it difficult to visualise translation of the microsphere in the *z* axis with static images.

3.4.3 Biological cells

The optical trapping of cells in the focal spot of a laser beam was first demonstrated by Ashin & Dziedzic (1987) and Ashkin *et al*., (1987). In subsequent years, cell-to-cell adhesion (Tashiro *et al*., 1993), cells shear moduli (Hénon *et al*., 1999; Lenormand *et al*., 2001), cell (dis)aggregation (Bronkhorst *et al*., 1997) and flagellar rotary motors (Berry & Berg, 1997) have all been investigated using optical tweezers.

Using the optical tweezers described in this thesis, individual white blood cells and motile bacteria were trapped and manipulated.

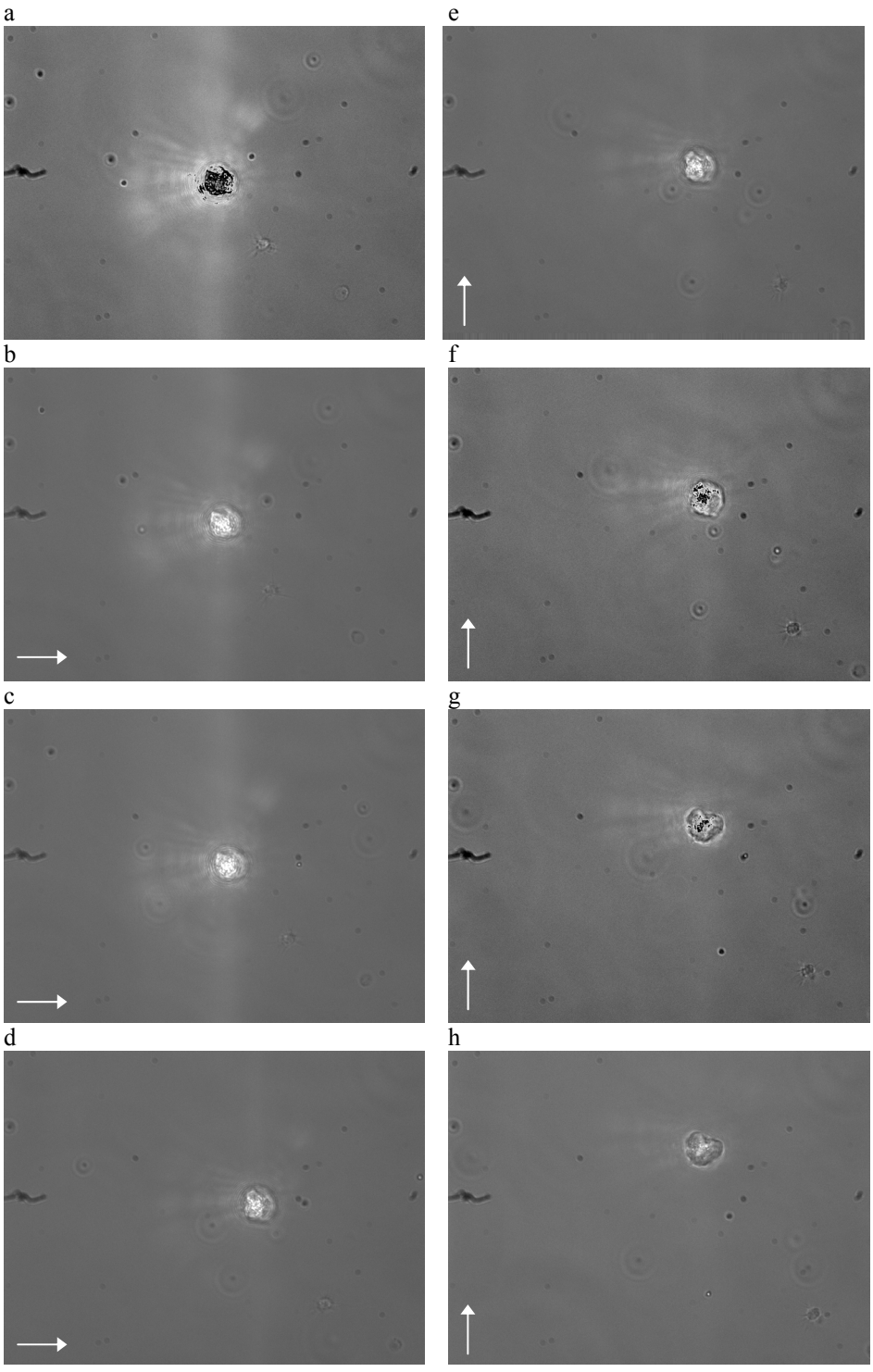

Fig. 3.14 – The optical manipulation of a 7 μm neutrophil in the *x* and *y* axes. The *white arrow* indicates the direction of translation (Tessmer, 2002).

Single neutrophils have been successfully trapped and manipulated in the *x* and *y* axes (fig. 3.14) at a depth of 6 μm, under an applied optical power of 28 mW (Tessmer, 2002), using the described optical tweezer system. The application of laser power did not appear to have a detrimental effect upon the surface functionality of the cells (Tessmer, 2002).

The application of a laser power of 43 mW was found to be suffice to halt and manipulate motile bacteria in *x* and *y* (fig. 3.15a-f), at an approximate chamber depth of 6 μm. The conversion of optical power to applied force (Eqn. 3-1) showed that a force of ~22 pN was required to stall bacterial motion. Single organisms were trapped for a period of <10 min. Following the termination of applied force the organism resumed a swimming motion, seemingly unaffected by the laser power. However, the physiology of the cell before and after laser trapping was not monitored. Previous studies have demonstrated trap-induced biological effects, in which sperm cell motility was altered (Tadir *et al*., 1989, 1990; Colon *et al*., 1992).

These basic experiments demonstrate the ability and versatility of the described optical tweezer apparatus to trap and manipulate a range of particle diameters from 1 μm to 12 μm, as well as a variety of particle compositions; from light weight synthetic polymer microspheres to heavy weight silica microspheres to biological cells.

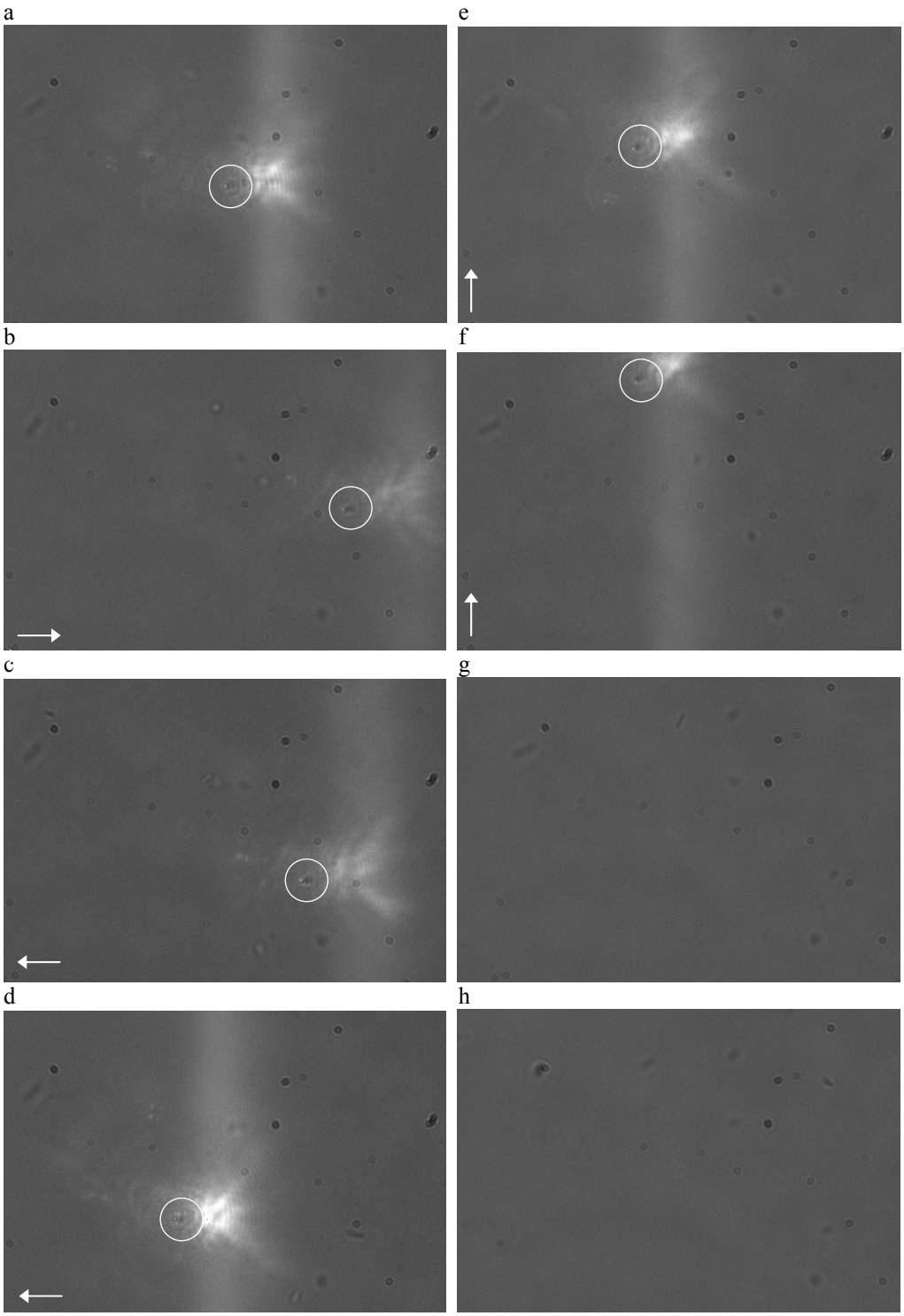

Fig. 3.15 – The optical manipulation of motile bacteria in the *x* and *y* axes (a-f). The *white circles* highlight a single trapped organism; the *white arrows* indicate the direction of translation; g-h crudely displays the motion of the bacteria in the 10 mM PBS pH 7.4 environment.

3.5 CONCLUSIONS

This chapter described the design, construction, calibration and the employment of a single beam optical tweezers. The design employed was an amalgamation of Ghislian's *et al*., (1994) and Visscher's *et al*., (1996) optical apparatus. In which an eyepiece objective and a telescope lens system were used to generate expansion of the laser beam diameter, in order to create a strong stable three-dimensional trap. The telescope element also provided *x*-*y*-*z* manipulation of the optical trap in the specimen plane. The maximum translation range of the optical trap in the *x* and *y* axes were recorded at approximately 30 μm, as illustrated in section 3.4.

Calibration of the optical trap was performed using the escape force method. This gave comparable dimensionless efficiency factors (*Q* values) to previously published data employing similar calibration methods (Ghislain *et al*., 1994; Felgner *et al*., 1995). However, in this method forces are determined by the optical properties at the edges of the trap and not the centre of the trap, and therefore the trap stiffness cannot be determined (Visscher *et al*., 1996). The addition of a position sensitive photodetector to the optical setup would enable the determination of trap stiffness (α) (where, $\alpha = F/x$, F is a known viscous drag force, and x displacement of trapped particle from trap centre) and therefore the optical forces at the centre of the trap (Visscher *et al*., 1996).

The constructed optical tweezers are versatile in the range of particle diameters and compositions which can be optically trapped and manipulated over a translation range of 30 μm in the *x* and *y* axes. Although not visually demonstrated here, the optical focus could also be translated in the *z* axis up to ~15 μm. Furthermore, the application of laser power (where, λ = 1064 nm) to the biological samples did not appear to cause immediate cell death.

CHAPTER 4

An Investigation of Interactions between a Protein and Polymer Surface

In this chapter, the optical tweezers, AFM and contact angle analysis were employed to study the effect of plasma treatment on polystyrene surfaces, and in particular the impact that this may have on protein-surface interactions. Plasma treatment is an established technique for the chemical modification of surfaces for an array of biomedical applications and has been extensively studied using a diverse range of instrumentation, including XPS, Tof-SIMS, DCA, and STM (Davies *et al*., 2000). Such studies have provided detailed chemical characterisation of plasma treated surfaces. Thus, such an approach toward surface modification provides a well characterised system to perform proof of principle measurements with the optical tweezers. To provide a complementary technique to the optical tweezers the AFM was also employed.

4.1 INTRODUCTION

Plasma treatment is capable of manipulating surface functionality (for example, the introduction of alcohol, amine and acid groups) by the implementation of various support gases (Yuan, 1993). Plasma gas treatments are frequently

employed to induce the oxygenation of surfaces. Oxygen plasma is the primary source of introducing oxygen functionality, although it has been demonstrated that argon plasmas also have the ability to introduce oxygen (Clouet & Shi, 1992). The reactive gas plasmas (those containing oxygen) functionalise the surface during the course of the plasma process (Clark & Dilks, 1979), and functionalisation occurs in response to ablation or etching (Clouet & Shi, 1992). Conversely, in employing inert gas plasmas (for example argon) the dominant process is hydrogen abstraction (Clouet & Shi, 1992), and oxygen functionality is thought to occur upon the exposure of the surface to the atmosphere (subsequent to plasma treatment), where the surface free radicals react with atmospheric oxygen (Momose *et al*., 1992; France & Short, 1998).

Oxygen and argon plasmas produce hydroxyl groups on the surface (Clouet & Shi, 1992). OH groups are hydrophilic in nature (Israelachvili, 1985), thus the degree of oxygen functionality of the surface dictates the degree of hydrophobicity of the surface.

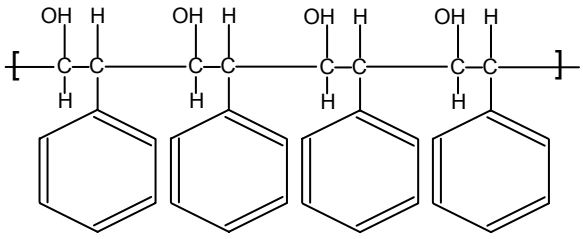

Fig. 4.1 – Oxygen/argon plasma treatment of polystyrene results in the incorporation of oxygen-containing functional groups.

A decrease in the hydrophobicity of surfaces has been associated with an increase in resistance to soluble protein and DNA adsorption (Chan *et al*., 1998; Dewez *et al*., 1998; McGurk *et al*., 1999; Gessner *et al*., 2000; Tsai *et al*., 2001; Wertz *et al*., 2001). Furthermore, a change in protein adsorption to polymer surfaces has found to be accompanied by change in the adhesive force between the protein and surface, i.e. with a decrease in protein adsorption there is a decrease in protein adhesion (McGurk, *et al*., 1999). The ability to control the adsorption of biomolecules at solid/liquid interfaces is of importance in biomedical and industrial applications.

This chapter not only provides proof of principle measurements for our optical tweezers apparatus, but also discusses the employment of argon plasma to manipulate protein adsorption in a controlled manner. Probability of adhesion and the force of adhesion between human serum albumin (HSA) functionalised polystyrene microspheres and argon plasma treated polystyrene surfaces were studied using the complementary techniques of optical tweezers and AFM. Contact angle measurements were also performed to provide a measure of surface hydrophobicity.

4.2 MATERIALS & METHODS

All materials were purchased from Sigma (Poole, UK), unless stated otherwise.

4.2.1 Sample Preparation

Glass coverslips (Agar, UK), thickness 130 ± 10 μm, were coated with 500 μL of a 10% w/v solution of polystyrene in toluene, using a spin caster at 1200 rpm. The polystyrene coated coverslips were subjected to argon plasma (20 Pa, 10 W) over various time periods ranging from 1 to 5 seconds utilising a RF (radio frequency) Plasma Barrel Etcher (PT7100 BIO-RAD Polaron Division). The modified coverslips were subjected to experimental analysis immediately following plasma etching.

4.2.1 Contact Angle Analysis

Contact angle analysis was employed to study the hydrophobicity/hydrophilicity of the polystyrene surfaces. The occurrence of a three-phase equilibria at the point of contact at a liquid/solid/vapour interface provides a quantitative measure of the hydrophobicity/hydrophilicity of a solid surface (Good, 1992). A contact angle, θ, is defined geometrically as the angle formed by a liquid at this three phase boundary (Good, 1992). Figure 4.2 is a schematic of this three-phase equilibria which exists when a drop of a liquid is placed upon a solid surface.

This three-phase equilibria is considered in terms of surface tensions, γ, or surface free energies (Good, 1992). The relationship between the surface tensions and the contact angle are given by Young's equation of interfacial tension,

$$\gamma_{sv} = \gamma_{sl} + \gamma_{lv}\cos\theta \qquad (4\text{-}1)$$

where γ_{sv} is the solid/vapour surface tension, γ_{sl} is the solid/liquid surface tension, γ_{lv} is the liquid/vapour surface tension and θ is the contact angle (Good, 1992).

Low free energy surfaces are typically hydrophobic in nature and give rise to large contact angles when water is employed as the sample media. Conversely, high free energy surfaces are usually hydrophilic and lead to low contact angles. Surfaces which exhibit contact angles of >85º are considered extremely hydrophobic, whereas, contact angles <15^{o} are considered extremely hydrophilic. Between these two points the contact angle marks a transition of surfaces from hydrophobic to hydrophilic. For a critical review of contact angles the reader is referred to Good (1992).

Sessile drop contact angle measurements were performed using a Vickers Ealing Contact Angle Goniometer (Ealing-ElectroOptics, Watford, Hertfordshire, UK). High-purity (resistivity 15 MΩ cm) deionised water was employed as the model solvent, and a 2 μL drop was placed onto the argon plasma modified polystyrene surface. Measurements were performed in air at ambient temperature, immediately following plasma treatment. Angles for both sides of the drop were determined, and repeated for a minimum of six drops.

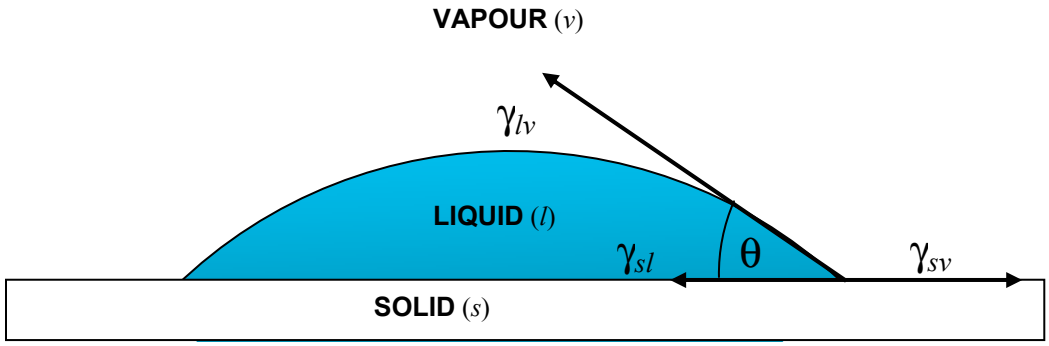

Fig. 4.2 - Schematic representation of the three-phase interfacial equilibrium at the contact point of the solid/liquid/vapour interface, where, γ_{lv} is the liquid/vapour surface tension, γ_{sl} is the solid/liquid surface tension, γ_{sv} is the solid/vapour surface tension, and θ is the contact angle (Good, 1992).

4.2.3 Optical Tweezers Force Measurements

4.2.3.1 *Probe Preparation*

Polystyrene microspheres were functionalised with HSA through physical adsorption. 2 μm polystyrene microspheres (Sigma, Poole, UK) were incubated in 0.1mg mL^{-1} HSA (100mM PBS, pH 7.4) at a microsphere concentration of 0.05% (w/v), for 1 h at 2-8 °C. Following incubation, microspheres were rinsed in 100 mM PBS (PBS purchased in tablet form from Sigma, UK), pH 7.4, to remove any loosely bound protein.

4.2.3.2 *Force Analysis*

Force measurements were performed in 100 mM PBS, pH 7.4. A sample chamber consisting of the sample surface and a glass slide was constructed. 50 μL of 2 μm HSA polystyrene microspheres (0.05% solid w/v) were encapsulated with the chamber. The monodispersed microspheres were allowed, through gravitational pull, to settle and interact with the surface. The optical focus was positioned at a depth of 8 ± 0.5 μm from the sample surface. Starting at a minimum laser power of 0.6 Amp (equivalent to an optical focus power of approximately 2.6 mW) the power was increased to the point at which the interaction between the HSA probe and polystyrene surface was overcome and the microsphere was seen to jump into the optical focus (fig. 4.3). The power required to break the interaction between the probe and the surface was converted to force by the axial escape force calibration (proposed by Ashkin *et al*. (1986) and described in detail in 3.3.1.1).

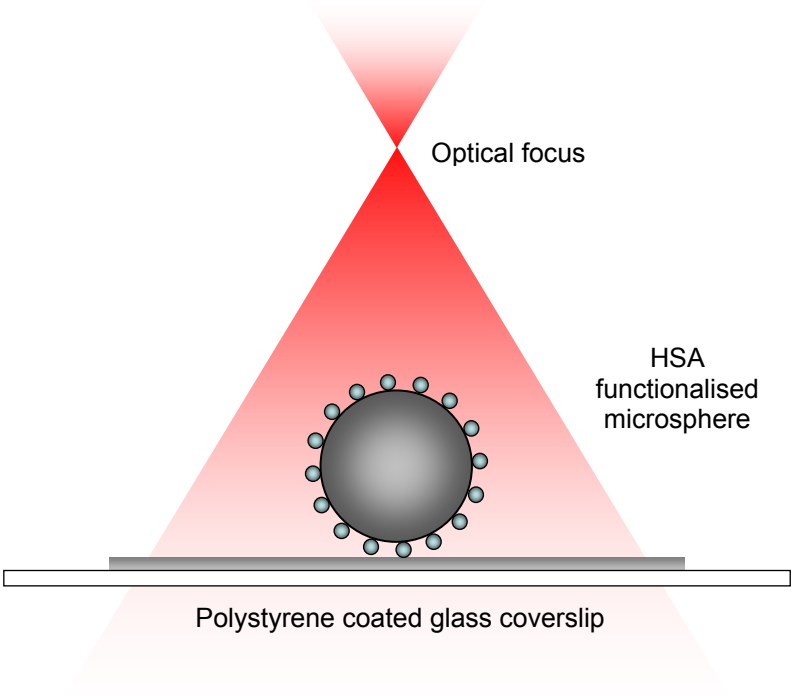

Fig. 4.3 – Schematic of the optical tweezers experimental procedure, performed in 100 mM PBS pH 7.4. The polystyrene microsphere is coated in HSA through physical absorption. The miscrosphere is rested on the plasma modified polystyrene surface, and the optical focus is positioned 8 μm from the polystyrene surface. The laser power was increased until the microsphere jumped from the surface into the optical trap, overcoming any interaction between the HSA microsphere and the plasma modified surface.

4.2.3.3 *Probability of Adhesion*

The probability that the HSA-microsphere would adhere to polystyrene surfaces was studied over argon plasma exposure times of 0-4 sec. The optical focus was positioned approximately 6 μm above individual microspheres and a ramp of laser power was applied.

Control measurements were performed in order to ascertain the minimum laser power required to trap a 2 μm microsphere ~8 μm from a surface, which demonstrates little or no interaction with the surface. To do this 2 μm polystyrene microspheres and polystyrene surfaces were both functionalised (via physical adsorption) with HSA (as previously described in 4.2.3.1). Once direct contact was made between the two surfaces a ramp of power was applied, and the power required to trap a single HSA microsphere at 8.3 ± 0.9 μm from the surface was recorded. The resulting power was 0.69 Amp, which is equivalent to an optical focus power of approximately 2.8 mW and a force of <0.02 pN (see chapter 3 for determination).

All measurements were performed in 100 mM PBS, pH 7.4. Those microspheres which required a force greater than 0.02 pN were recorded as demonstrating adhesion, those less than 0.02 pN were recorded as demonstrating no adhesion and thus no interaction.

4.2.4 AFM Force Measurements

4.2.4.1 *Probe Preparation*

Individual 2 μm polystyrene microspheres were attached to the apex of the AFM cantilever tip with Araldite-Rapid^{TM} epoxyadhesive (Bostik Ltd, Leicester, UK), and positioned using a micromanipulator (Research Instruments Ltd., Cornwall, U.K.) viewed under an optical microscope. The probes were then incubated in 0.1mg mL^{-1} HSA (100mM PBS, pH 7.4) for a period of 1 h at 2-8 °C. Following incubation microspheres were rinsed in PBS (100 mM, pH 7.4).

4.2.4.2 *Force Analysis*

AFM force measurements were recorded using instrumentation built and developed in the Laboratory of Biophysics and Surface Analysis (School of Pharmaceutical Sciences, University of Nottingham, U.K.; Lomas, 2000).

Force measurements were obtained between a HSA probe and argon plasma modified polystyrene surface (fig. 4.4a). Measurements were performed at a retract velocity of 1.0 μm s^{-1} in a liquid environment of 100 mM PBS, pH 7.4. Raw data plots displayed the cantilever deflection signal (nA) versus distance of z-piezo movement (nm). Employing Hookes' Law, plots were converted to force (nN) versus probe-sample distance (as previously described in Chapter 1). Calibration of cantilever spring constants were performed using the thermal noise / resonance method proposed by Hutter *et al*. (1993), also described in

a

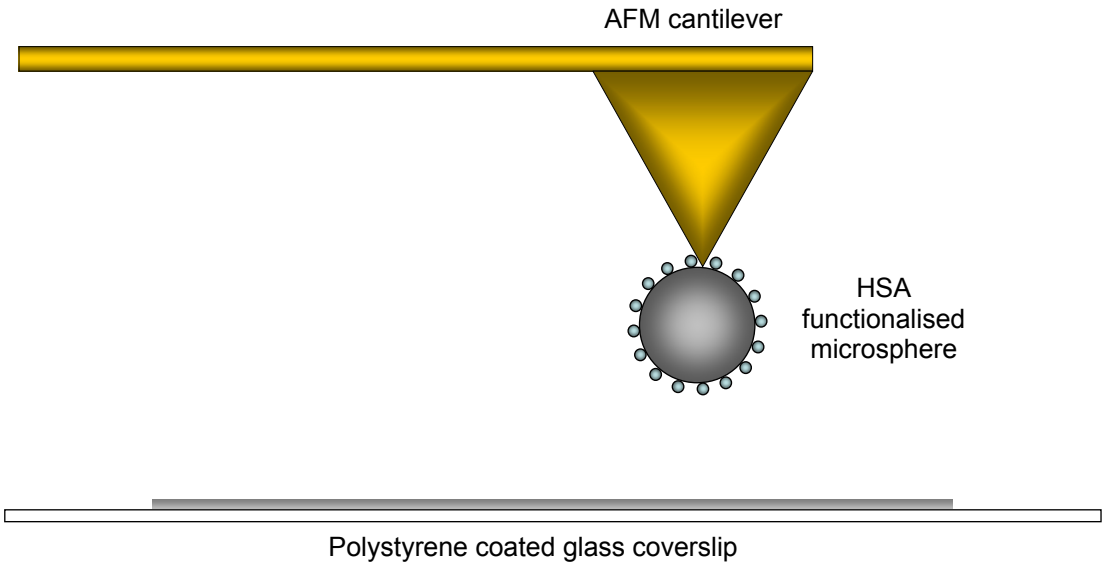

b

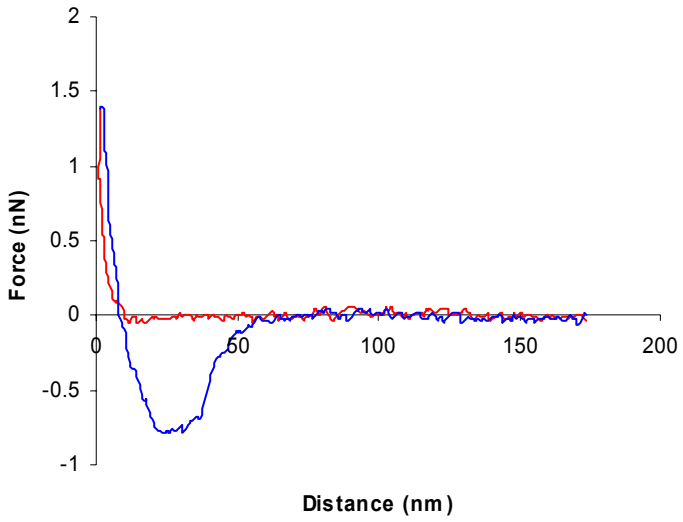

Fig. 4.4 – a) Schematic illustrating the AFM experimental setup. A HSA polystyrene microsphere was attached to the apex of the AFM probe. The probe and the plasma modified polystyrene surfaces were repeatedly brought in and out of contact; b) Displays a typical force versus distance curve recorded between a HSA polystyrene microsphere and an untreated polystyrene surface, performed in 100 mM PBS, pH 7.4, at a retract velocity of 1.0 µm s^{-1}.

chapter 1. Figure 4.4b displays a typical force versus extension trace for a measurement performed between HSA and an untreated polystyrene surface, in 100mM sodium phosphate buffer, pH 7.4 at a retract velocity of 1.0 μm s^{-1}.

4.2.4.3 *Probability of adhesion*

The probability that a rupture event occurs between the HSA functionalised probe and the modified polystyrene surfaces was recorded over argon plasma exposure times of 0-3 sec.

4.2.5 Control Studies

To ensure that measurements observed in both the AFM and optical tweezers studies, were a direct result of interaction between the HSA microsphere and the argon plasma treated polystyrene surface, control measurements were performed between a HSA probe and a HSA surface. The polystyrene coated coverslips were functionalised through physical adsorption in a solution of HSA 0.1mg mL^{-1} (100mM PBS, pH 7.4) for 1 h at 2-8 °C. Following incubation the sample surface was rinsed in PBS (100 mM, pH 7.4). Measurements were then recorded with both the AFM and optical tweezers.

4.3 RESULTS & DISCUSSION

Initially, the effect of argon plasma on surface chemistry, in particular, hydrophobicity was studied using static contact angle analysis. Leading on from this, the effect of surface hydrophobicity on protein-surface interactions was investigated, using optical tweezers and AFM via adhesion force and probability of adhesion measurements.

Employing the static contact angle approach, the drop angles measured represent those between the advancing and the receding contact angles as would be determined by dynamic contact angle analysis (DCA) (Good, 1992). The advancing angle is characterised when a drop of liquid has recently expanded on the surface. Conversely, the receding angle is when a drop of liquid has recently contracted (Good, 1992).

The untreated polystyrene surfaces displayed contact angles of 75.7º ± 6.1º, indicating that the surfaces prior to treatment were hydrophobic. These values are comparable to those (particularly the receding angles) previously recorded on untreated polystyrene surfaces (Davies *et al*., 2000). Argon plasma treatment of the polystyrene surfaces for a period of 1 sec resulted in a decrease in the contact angle measured to 40.1º ± 3.7º.

Increasing the period of argon plasma treatment to 2 sec resulted in a further decrease in the contact angle to 27.2º ± 6.4º. A further increase in argon plasma exposure up to 4 sec induced a further decrease in the measured contact angle to <15º.

Table 4.1 Contact angle measurements for polystyrene surfaces exposed to increasing times periods of argon plasma

Time period of argon plasma (sec)	Static contact angle (º)
0	75.7 ± 6.1
1	40.1 ± 3.7
2	27.2 ± 6.4
3	19.4 ± 1.5
4	<15

a

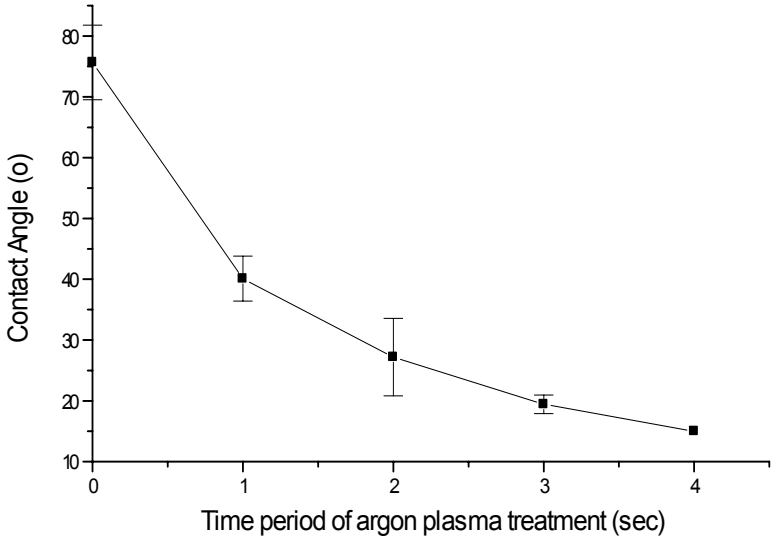

Fig. 4.5 – Static contact angle measurements. a) Contact angles represented graphically.

Table 4.1 and figure 4.5 illustrate this relationship between argon plasma treatment times and measured contact angles.

At an angle of <15º the surface is considered as extremely hydrophilic (Good, 1992). Thus, to subject a polystyrene (10% w/v) surface to 20 Pa argon plasma, at a power of 10 W for a period of 4 sec induces a change in the surface properties from hydrophobic to extremely hydrophilic.

Argon plasma treatment introduces oxygen functionality by producing hydroxyl groups on the surface upon exposure to atmospheric oxygen (Clouet *et al*., 1992). As previously discussed (section 4.1) OH groups are hydrophilic in nature, and it is therefore not surprising that an increase in argon plasma exposure time results in an increase in hydrophilicity. However, previous studies demonstrated an initial increase in hydrophobicity of polystyrene microtiter wells before a decline into hydrophilicity, when subjected to argon plasma (Davies *et al*., 2000). It was inferred that the initial effect of argon plasma treatment was to clean the surface of volatile contamination (Davies *et al*., 2000). Although this increase in hydrophobicity was not evident in our static contact angle measurements, it should be noted that in the previous studies this effect was only observed in the advancing contact angle and not the receding angle (Davies *et al*., 2000). The comparability of the static contact angles measured here to the receding contact angles previously measured (for polystyrene exposure to argon plasma) (Davies *et al*., 2000) suggests that this initial increase in hydrophobicity is overlooked in the static contact angle

technique. A much faster rate of change in hydrophobicity was also observed in these studies compared to those previously recorded (Davies *et al*., 2000). However, this may be a result of variations in plasma etching instrumentation.

Surface hydrophobicity is an important determinant in the adsorption of proteins, and therefore plays a significant role in many biomedical and industrial applications. Employing optical tweezers and AFM this relationship between surface hydrophobicity and protein adsorption was investigated.

In the optical tweezers studies HSA coated 2 μm polystyrene microspheres were allowed to interact with polystyrene surfaces subjected to varying time periods of argon plasma treatment. A ramp of optical force was applied to individual microspheres until the interaction between the HSA-microsphere and the surface was ruptured (illustrated by the microsphere being pulled from the surface into the optical focus). On untreated polystyrene surfaces, the HSA coated microspheres could not be ruptured under the application of the maximum axial force of 3.52 pN (fig. 4.6). Surfaces exposed to argon plasma for a period of 1 sec displayed few rupture events and the majority of microspheres still could not be ruptured. With increasing argon plasma times, and thus increasing hydrophilicity, a gradual decrease in required force (for rupture) from the maximum 3.52 pN to the minimum <0.02 pN (indicative of no interaction) was observed (fig. 4.6 and fig. 4.7a).

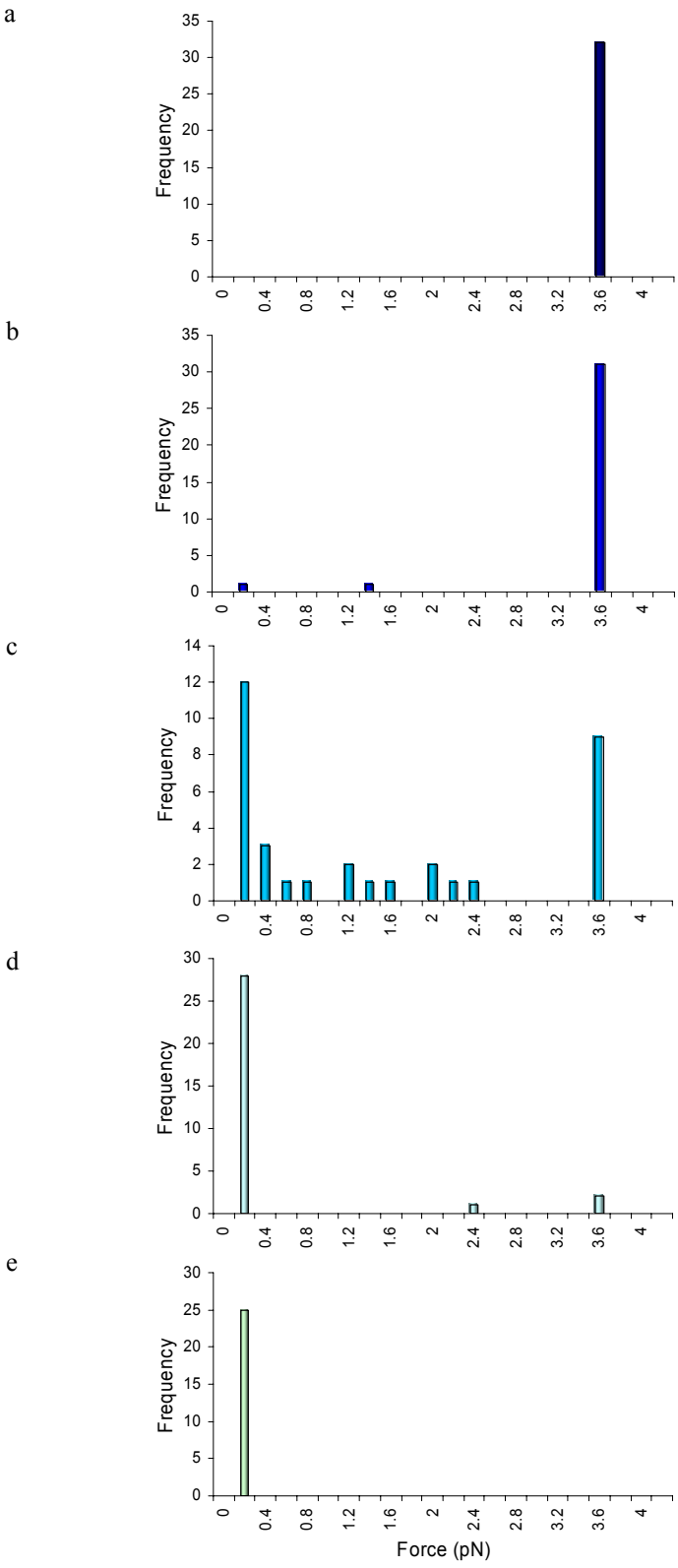

Fig. 4.6 - Force histograms for force measurements performed using optical tweezers between a HSA-functionalised polystyrene microsphere and polystyrene surfaces subjected to increasing time periods of argon plasma. Performed in an environment of 100 mM PBS pH 7.4. a) untreated polystyrene surface; b) polystyrene surface exposed to argon plasma for a period of 1 sec; c) 2sec; d) 3 sec; e) 4 sec.

a

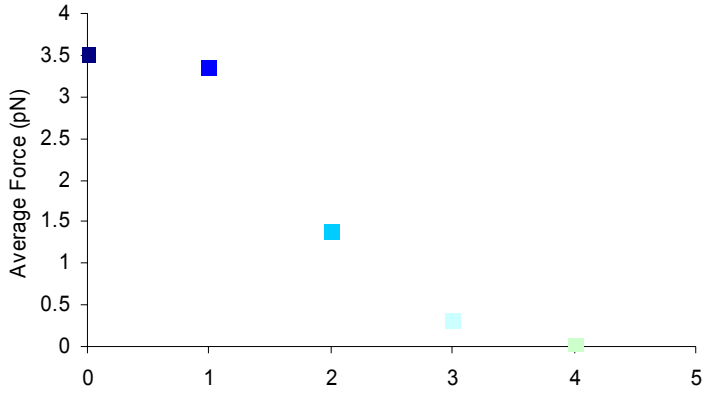

b

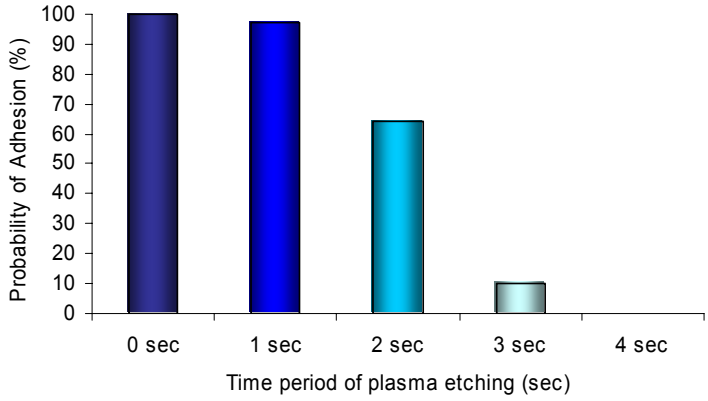

Fig. 4.7 – a) Plot of the average force observed using optical tweezers between HSA and polystyrene surfaces exposed to argon plasma; b) Probability of adhesion observed between the HSA polystyrene microspheres and the polystyrene surfaces exposed to increasing time periods of argon plasma.

It is likely that this decrease in force with an increase in hydrophilicity was result of either a decrease in the magnitude of the HSA-polystyrene interaction or a decrease in the number of interactions between the HSA microsphere and the polystyrene surface.

The probabilities of adhesion, between HSA-microspheres and treated polystyrene surfaces, were determined, where those microspheres attracted to the optical focus at an optical force of <0.02 pN are indicative of no interaction. A 100 % probability of adhesion was observed for untreated polystyrene surfaces. This decreased to 97 % when surfaces were exposed to argon plasma for a period of 1 sec, 64 % at an exposure time of 2 sec, 3 % at 3 sec, and 0 % at 4 sec (fig. 4.7b).

The decrease in probability of adhesion is also suggestive that an increase in surface hydrophilicity leads to either a decrease in the number of interactions occurring between the HSA-microsphere and the polystyrene surfaces or a decrease in the magnitude of force of interaction.

In AFM force analysis a single HSA coated 2 μm microsphere was attached to the apex of an AFM probe, and rupture force and probability of adhesion measurements were performed between the modified AFM probe and the treated polystyrene surfaces. For untreated polystyrene surfaces, a HSA-surface rupture force of 302 s.d. 109 pN was observed (fig. 4.8a). This figure is lower than previously recorded values of ~7 nN (McGurk *et al*., 1999), however this

variation in the force value is attributable to the variation in the surface contact area. A decrease in the rupture force, the force distribution width and the probability of adhesion was observed with an increase in argon plasma treatment periods (fig. 4.8-4.9). Where, the rupture force and distribution was found to decrease from 302 s.d. 109 pN to 94 s.d. 19 pN (fig. 4.8a-d and fig. 4.9a), and the probability of adhesion decreased from 69 % to 6 %, over a plasma treatment period of 3 seconds (fig. 4.9b).

To ensure that the interactions observed were between the HSA probe and the polystyrene surfaces, control measurements were performed between HSA-functionalised probes and HSA-functionalised polystyrene surfaces. In the optical tweezers studies the probability that an adhesion event was observed between a HSA-microsphere and an untreated polystyrene surface was 100 %, this decreased to 21 % for a HSA-functionalised polystyrene surface. AFM force analysis also showed a decrease in the probability of adhesion from 69 % for an unmodified polystyrene surface to 25 % for the HSA-HSA control system. Those measurements which demonstrated force are attributed to interactions between exposed polystyrene and protein. The decrease in the adhesion probabilities from the unmodified polystyrene surfaces to the HSA control surfaces obtained from both the optical tweezers and AFM, suggests that the interactions observed in the experimental systems are attributable to the adsorption of protein to polystyrene surfaces.

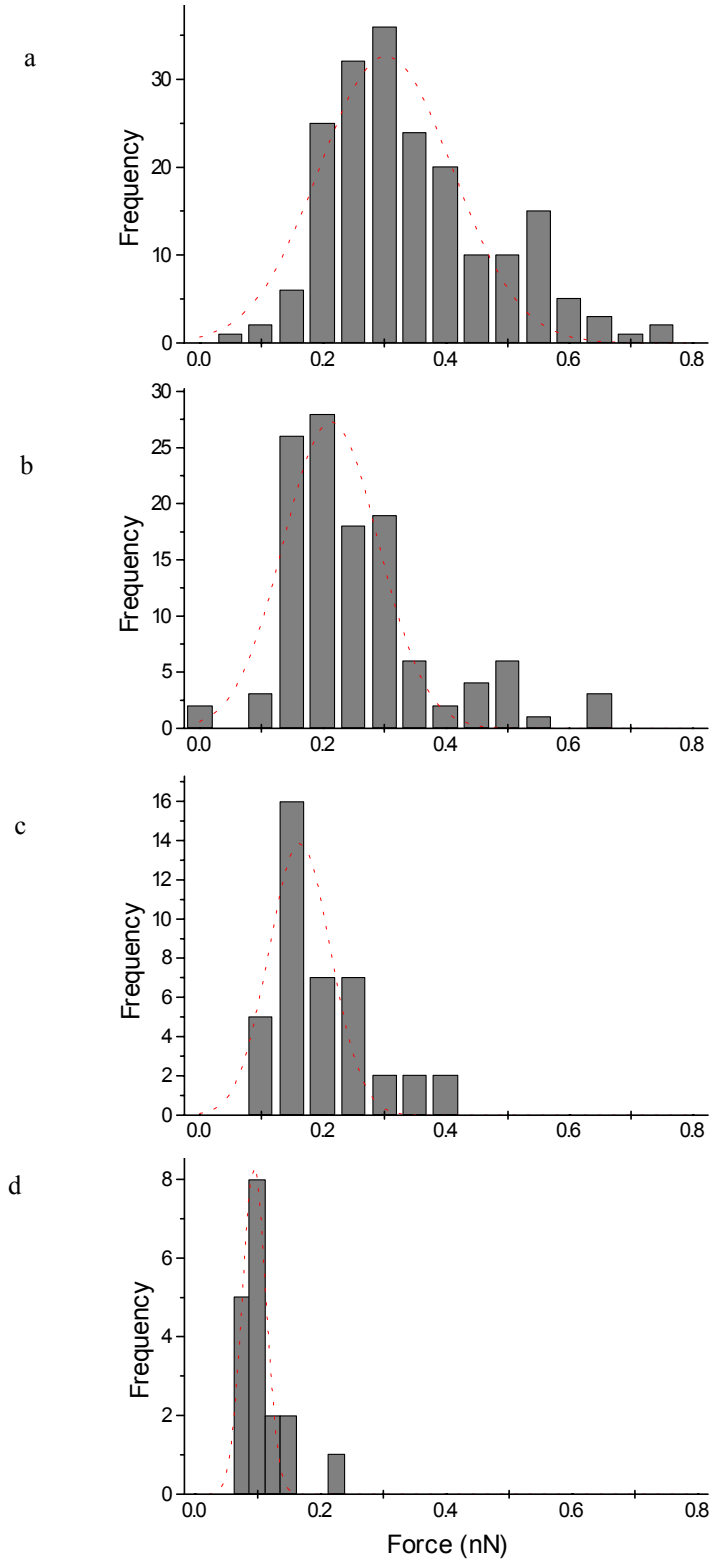

Fig. 4.8 - Force histograms for force measurements performed using the AFM between a HSA-functionalised polystyrene microsphere and polystyrene surfaces subjected to increasing time periods of argon plasma. Performed at a retract velocity of 1.0 µm s^{-1}, in an environment of 100 mM PBS buffer pH 7.4. A Gaussian curve fit is superimposed on the force histogram to estimate the most frequent rupture force. a) untreated polystyrene surface; b) polystyrene surface exposed to argon plasma for a period of 1 sec; c) 2sec; d) 3 sec.

a

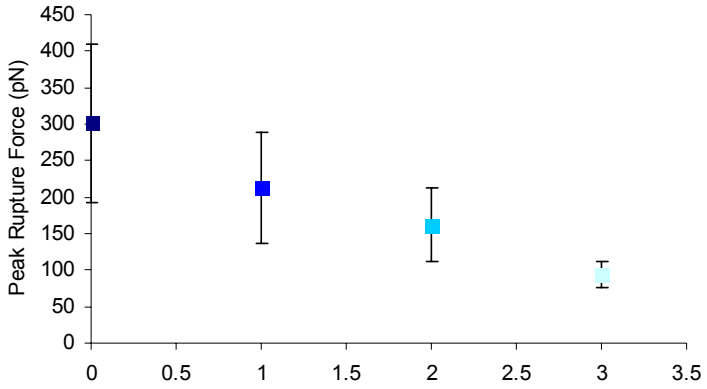

b

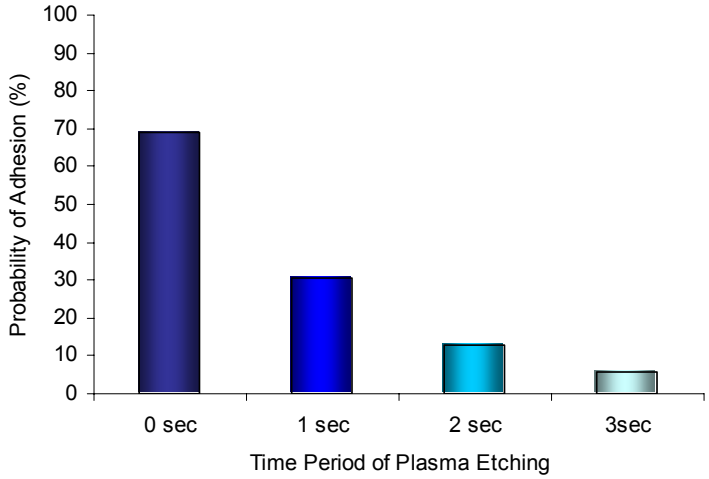

Fig. 4.9- a) AFM peak rupture forces measured for HSA interactions with polystyrene surfaces exposed to argon plasma; b) Probability of adhesion observed between the HSA polystyrene microspheres and the polystyrene surfaces exposed to increasing time periods of argon plasma.

Both the AFM and optical tweezers demonstrate a decrease in force and probability of adhesion between HSA and polystyrene with an increase in surface hydrophilicity. It should be noted however, that values obtained with the two biophysical techniques are not directly comparable. In the optical tweezer studies the interactions between surfaces are allowed to equilibrate, whilst, in the AFM studies interactions occur under an applied load. Although not comparable quantitatively, they are comparable qualitatively.

The observed decrease in protein adhesion force, and thus protein adsorption (McGurk, *et al*., 1999), with increase in surface hydrophilicity concurs with previous studies (Tabata & Ikada, 1990; Gök *et al*., 1994; Liu & Hlady, 1996; Green *et al*., 1997; Chan *et al*., 1998; Sigal *et al*., 1998; McGurk *et al*., 1999; Yang *et al*., 1999; Gessner *et al*., 2000; Wertz & Santore, 2001).

As previously discussed, treatment of a surface with argon plasma oxygenates the surface through the addition of hydroxyl groups. Hydroxyl groups possess high energies of hydration due to an electron-donor parameter that is higher than that of water and a very small residual electron acceptor (van Oss, 1997). It is the net hydration energy of the surface hydroxyl groups which dictates the degree of hydrophilic repulsion (van Oss, 1997). Because hydrophilic groups (for example, hydroxyl groups and soluble proteins such as HSA) prefer to be in contact with water rather than with each other, this leads to a strong repulsion between each other when in water (Israelachvili, 1991). The repulsion between the individual hydroxyl groups results in an increase in the

molecular mobility of the polystyrene chains (Murakami *et al*., 1998) creating a repulsive barrier to soluble protein binding. Thus, it is speculated that the underlying intermolecular force involved in HSA resistance of hydrophilic polystyrene surfaces is hydrophilic repulsion, in which the net hydration energy is greater than the net hydrophobic and van der Waals attraction energies.

4.4 CONCLUSION

The adsorption of proteins to an interface is largely determined by the surface chemistry of the substrate (Wertz & Santore, 2001), particularly surface hydrophobictiy. The potential to control and manipulate this relationship between hydrophobicity and protein adsorption has many applications, for example, biocompatible materials (Elbert & Hubbell, 1996; Green *et al*., 1997), DNA hybridization sensors (Chan *et al*., 1998), drug targeting (Gessner *et al*., 2001), biosensors and immunoassays (Benmakroha *et al*., 1995), and tissue engineering (Hubell, 1995; Dewez *et al*., 1998; Wertz & Santore, 2001).

The manipulation of the hydrophobicity of polystyrene surfaces using argon plasma demonstrated a decrease in HSA adsorption with an increase in surface hydrophilicity. An increase in argon plasma treatment time reduced the number of adsorbed HSA molecules to the polystyrene surface. Furthermore, surfaces became extremely hydrophilic within 5 seconds of exposure to argon plasma (20 Pa, 10 W), accompanied by a complete protein resistance within this time

frame. The intermolecular force governing this resistance to protein adsorption is hydrophilic repulsion.

This chapter has also provided a platform for proof of principle measurements for the constructed optical tweezers apparatus (chapter 3). The AFM and optical tweezer experiments have independently demonstrated a decrease in force and probability of adhesion between HSA and polystyrene with an increase in surface hydrophilicity. However it is unclear whether increasing surface hydrophilicity induces a decrease in the magnitude of the force of interaction, or a decrease in the number of molecules interacting with the surface, or a combination of both. In order to elucidate the direct effect of surface hydrophilicity on protein-surface interactions it is necessary to perform single molecule measurements.

In conclusion, the comparability of the AFM and optical tweezers data, demonstrates the application of the optical tweezers in the measurement of intermolecular interactions between surfaces.

CHAPTER 5

The Investigation of Antibody-Antigen Interactions by AFM and Optical Tweezers

This chapter employs the complementary force sensing techniques, AFM and optical tweezers, to investigate the sensitivity of antibody-antigen immunodetection systems. In particular, the cardiac troponin I immunoassay which is clinically employed for the detection of acute myocardial infarction, formed the basis of our studies.

5.1 INTRODUCTION

Immunoassays provide a quantitative and qualitative method for the detection and identification of biomolecules present in fluid environments. The basis of the immunoassay is the formation of specific intermolecular bonds between complementary receptor-ligand pairs. The antibody-antigen partnership, in particular, has been exploited for such immunodectection systems due to their high specificity and amenability (see table 5.1).

Antibodies are glycoproteins consisting of two identical heavy and two identical light polypeptide chains linked by disulphide bridges to form a

Table 5.1 The advantages of antibodies compared with other binding proteins

Suitable for a wide range of antigens, variable binding site composition
Available in polyclonal and monoclonal forms
Monovalent (fragments), Bivalent (IgG), or polyvalent (IgM)
Amenable to modification and systematic improvement with recombinant DNA techniques

a

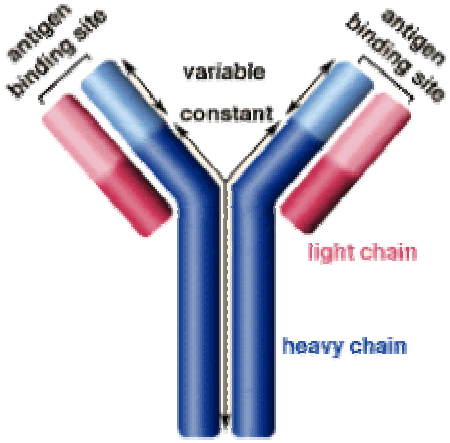

b

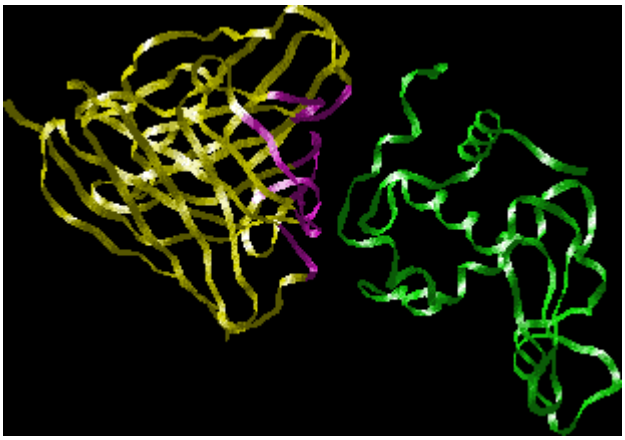

Fig. 5.1 – a) Schematic illustrating the basic structure of an antibody (Grimes *et al*., 2001); b) Ribbon structure of antibody-antigen binding. The hypervariable region of the antibody is highlighted in purple, it is these variable amino acids loops which form a direct contact with antigen (green). The FR regions of the antibody are highlighted in yellow. These regions have a more stable amino acid sequence and form a beta-sheet structure which serves as a scaffold to hold the HV regions in position to contact antigen (Grimes *et al*., 2001; Schirra *et al*., 2001).

Y-shaped molecule (fig. 5.1a). The heavy and light chains contain a constant region and a variable region. Structurally, the variable regions of the chains form beta sheets connected by amino acid loops (fig. 5.1b). These loops, referred to as the hypervariable region or complementary determining region (CDR), determine the antibodies specificity against a specific region of the antigen (epitope). It is these highly variable amino acids which form the antigen binding site.

There are two types of antibodies used as reagents in immunoassays, monoclonal and polyclonal antibodies. Monoclonal antibodies (MAb) are specific to a single epitope region of the antigen structure, whereas polyclonal antibodies are specific to a single antigen but not to a single epitope. Table 5.2 describes the advantages and disadvantages of polyclonal and monoclonal antibodies for use in immunoassays.

There are two fundamental immunoassay designs these are “non-competitive” and “competitive” binding assays, both of which rely on labelled antibody/antigen methods. Figure 5.2 illustrates these basic immunoassay formats. The non-competitive binding assay measures the quantity of occupied antibody binding sites (fig. 5.2a). Conversely, the competitive assay quantifies the unoccupied sites through the use of labelled antigens (fig. 5.2b).

The monoclonal antibody immunoassay described and investigated throughout this chapter is clinically employed to identify and assess cardiac injury. The

Table 5.2 Advantages and disadvantages of polyclonal and monoclonal antibodies for use in immunoassays

Polyclonal Antibody	Monoclonal Antibody
Higher affinity	Production of large batches
Wider reactivity	Specificity of binding
Greater stability at varying pH and salt concentrations	Homogeneity of all batches
No risk of loss of clones	Lower antigen dose for an immunoresponse
Simple production methodology	Antigen does not have to be purified
Cost to produce and purchase is lower	Antibodies to unusual and rare antigens can be produced

a

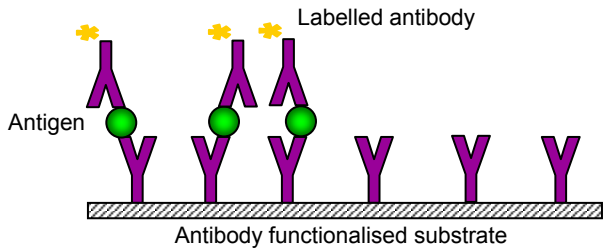

b

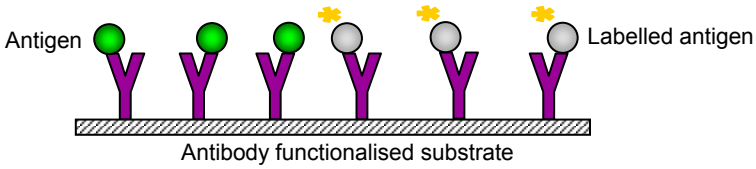

Fig. 5.2 – Basic non-competitive (a) and competitive (b) immunoassay designs. The distinction between the two designs is based upon the way in which antibody binding site occupancy is observed; Labelled antibody methods are non-competitive (a) if occupied sites of the labelled antibody are directly measured, but are competitive (b) if unoccupied sites are measured, for example via labelled antigen.

target antigen is the regulatory muscle protein troponin which is released into the bloodstream upon myocardial infarction (Katus *et al*., 1991; Bodor *et al*., 1992).

5.1.1 The immunodetection of cardiac damage

Troponin has a molecular weight of 69-77 kDa, and exists as a complex of three subunits; cardiac Troponin T (cTnT) (30-35 kDa), cardiac Troponin I (cTnI) (21-23 kDa), and cardiac Troponin C (cTnC) (18-19 kDa). Structurally, muscle is hierarchical where the muscle tissue is the pinnacle unit, comprising of myofiber cells. Each myofiber is composed of myofibrils, which are in turn composed of myofilament proteins (actin and myosin) and regulatory proteins (tropomyosin and troponin). It is these regulatory proteins which mediate the conformational changes and interactions between actin and myosin, which are responsible for muscle contraction. In a relaxed muscle state, tropomyosin inhabits the myosin binding site present on the actin filament. cTnT is the troponin binding subunit, anchoring the troponin complex to tropomyosin. cTnI is an inhibitory subunit bound to the actin filament, and cTnC is the Ca^{2+} binding receptor bridging the subunits together. Upon the binding of Ca^{2+} to the cTnC receptor a cascade of biochemical events occur resulting in the contraction of the muscle. Initially the conformation of the cTnC N-lobe changes from a “closed” to an “open” state, this induces the translation of the inhibitory region of cTnI, which in turn causes tropomyosin to translate to expose the myosin binding site on the actin molecule.

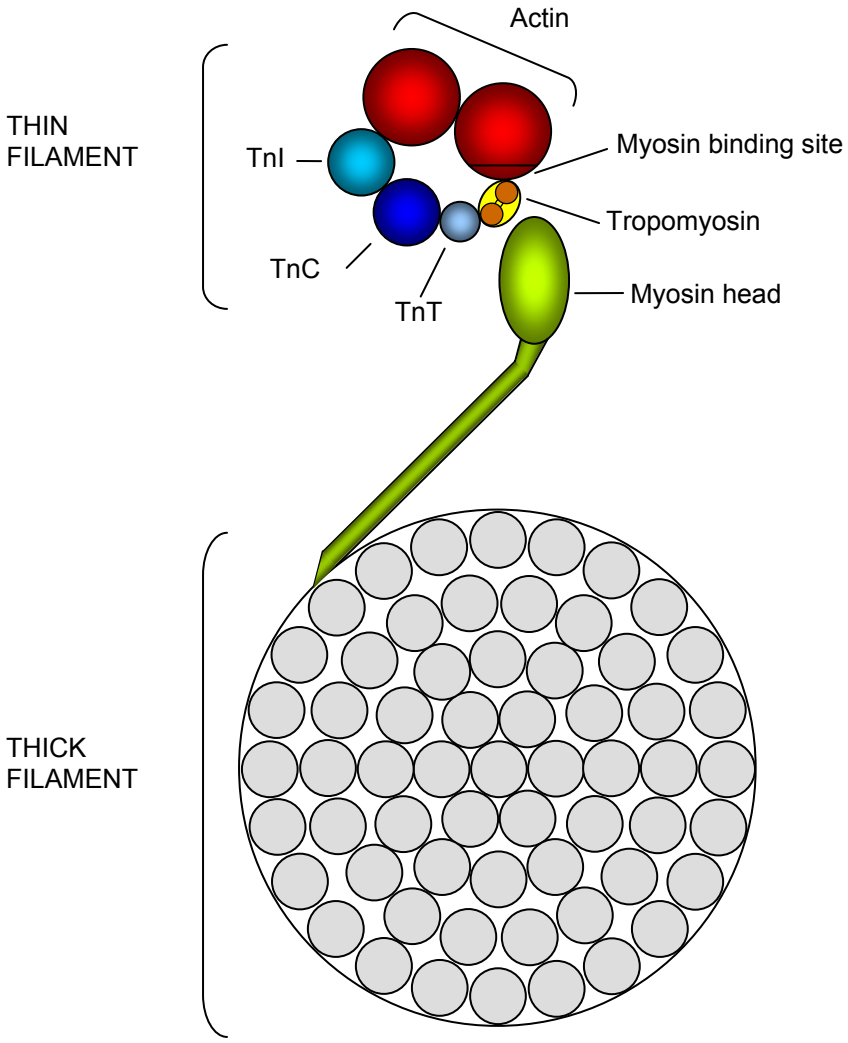

Fig. 5.3 – Schematic representation of the arrangement of tropomyosin and the troponin subunits in relaxed cardiac and skeletal muscle, where the myosin binding site is obstructed by tropomyosin inhibiting the interaction between actin and myosin. Adapted from pg 462 Molecular Biology of Muscle, edited by Alicia Haj (1992).

Myosin can then bind, consummating the actomyosin complex and inducing Mg^{2+}-ATPase activity to produce contraction of the muscle (Fig. 5.3).

As a direct result of cardiac muscle damage incurred due to myocardial infarction, troponins and a range of intracellular enzymes are released into the blood. Myocardial infarction occurs when there is a blockage of blood flow to the heart. The cells begin to suffer from severe ischemia and if circulation is not resumed the cardiac cells will ultimately die. The internal and external cell membranes begin to break down in the necrotic tissue, resulting in the leakage of the intracellular enzymes into the blood. It is therefore not surprising that these intracellular enzymes have been employed as molecular markers of cardiac damage. Immunoassays have been developed which express specificity for theses released enzymes, in particular, creatine kinase (CK), the isoenzyme of CK (CK-MB) and troponins. Such detection systems provide a method for the identification and quantification of cardiac injury.

The CK and CK-MB are the more traditional markers of cardiac damage and immunoassays specific for these intracellular enzymes have been clinically employed for over two decades. Unfortunately, they have proven to lack specificity for cardiac damage (Wilhelm *et al*., 1976; Tsung, 1981; Jaffe *et al*., 1984; Trask & Billadello, 1990). Studies have demonstrated that CK and CK-MB levels not only become elevated in response to cardiac damage, but also as a result of skeletal muscle injury (Wilhelm *et al*., 1976; Tsung, 1981; Trask & Billadello, 1990) and renal failure (Jaffe *et al*., 1984).

An alternative candidate for the role of a cardiac marker, are the cardiac troponins, particularly cTnI and cTnT. Although troponins are not specific to cardiac muscle and are present in skeletal muscle, they are coded by different genes and possess unique amino acid sequences specific for their muscle type (MacGeoch *et al*., 1991). This uniqueness has facilitated the development of highly specific immunoassays for the cardiac forms of TnT and TnI, which show no cross-reactivity with the skeletal muscle forms (Bodor *et al*., 1992). The troponin immunoassays, particularly the cTnI assays, also demonstrate a high degree of sensitivity, detecting up to 30% more cases of acute myocardial infraction than the more traditional CK and CK-MB markers (Hamm, 1998). The vast majority of studies carried out relating to cardiac markers demonstrate that cTnI is the most specific and sensitive diagnostic for detecting and quantifying cardiac damage (MacGeoch *et al*., 1991; Bodor *et al*., 1992; Abadie *et al*., 2001).

5.1.1.1 *Factors Effecting TnI assays*

The sensitivity of immunodetection assays lies in the ability of the antibody to bind to the targeted epitope. The availability of the epitope, enabling antibody recognition of the antigen, can be affected by conformational changes of the antigen, post-translational modifications, and the binding of macromolecules to the antigen (Katrukha *et al*., 1999). A well designed immunodetection system will employ antibodies which do not target epitopes vulnerable to

conformational change and biochemical processes, and those which are not positioned in close proximity to protein binding sites.

In the case of cTnI, the main factors influencing assay design, to date are; (*a*) complex formation, (*b*) molecular stability, and (*c*) the binding of macromolecules (Katrukha *et al*., 1999).

(*a*) *Complex formation*

The different conformational states of the troponin complex greatly influences the degree of recognition exhibited by a variety of cTnI specific monoclonal antibodies (Bodor *et al*., 1992; Tripet *et al*., 1997; Segura *et al*., 1999). The effect of complex formation on immunodetection is dependent upon the location of the targeted epitope. For example, Segura *et al*., (1999) employed the chelating agent EDTA (which chelates Ca^{2+} required for Tn complex formation) to determine the effectiveness of commercially available assays to the free form of cTnI. Results showed that the "*Access assay*" recognised the cTnI as a free form to a greater degree than the complexed. However, other assays have demonstrated a preference to the complex form (Bodor *et al*., 1992). Some monoclonal antibodies have been shown to recognise the free form of the antigen to a higher degree than the complex form, suggesting that the formation of the cTnI-cTnC complex may mask the cTnI epitopes making the antigen unrecognisable by the cTnI antibodies (Katrukha *et al*., 1999). In later years, studies demonstrated that cTnI released into the blood, as a direct result of myocardial infarction, exists predominantly in a binary complex with

cTnC, and as little as 5-10% of the antigen occurs in the free form (Katrukha *et al*., 1997; Wu *et al*., 1998; Guiliani *et al*., 1999). The prominence of cTnI-cTnC complex in the blood highlights the necessity to design and produce immunoassays that are sensitive to both the free form of the antigen and the complexed.

(*b*) *Molecular Stability*

cTnI is sensitive to proteolytic degradation and as a result lacks molecular stability during myocardial infarction. Prior to the release of cTnI into the bloodstream (following cardiac damage), the antigen is retained in a protease soup released from the lysosomes in the necrotic tissue. Exposure to proteases results in the cleavage of the C- and subsequently the N- terminus of the cTnI molecule (Katrukha *et al*., 1999). However, the formation of the cTnI-cTnC complex increases the molecular stability of the cTnI molecule. The TnC provides a degree of protection for the central region (residues 28-110, including the inhibitory region) of the molecule (Farah *et al.*, 1994; Moranja, 1998). Katrukha *et al.,* (1998) demonstrated that MAbs specific for epitopes located at the C- and N- terminus displayed only 2-5% immunodetection activity, whereas those targeting the central region of the molecule displayed more than 40% immunodetection activity. Moreover, the absence of the TnC complex results in a shorter half-life of the cTnI antigen in serum (Moranja *et al*., 2001). Thus, immunoassays should target epitopes located in the inhibitory region of the cTnI molecule.

The cTnI molecule has also demonstrated vulnerability to phosphorylation (Solaro, 1986). A number of structural and conformational forms of the protein can exist depending upon the extent of phosphorylation of the molecule, and theoretically all the phosphorylated forms can be released into the blood upon infarction (Hallawi *et al*., 1998). Katrukha *et al*., (1999) showed that the immunodetection activity of MAbs specific for epitopes which express sensitivity to phosphorylation was approximately 50% less than those which do not discriminate between phosphorylated and dephosphorylated forms.

The significance of oxidation and reduction of the troponin molecule, upon the immunodetection of cardiac damage is not yet known. However, the cTnI molecule possess two cysteine residues, Cys 79 and Cys 96 (Vallins *et al*., 1990), which could potentially be oxidised or reduced (Ingraham & Hodges, 1988) resulting in structural and conformational changes of the antigen. Wu *et al*., (1998) demonstrated that some commercially available assays recognise the oxidised form of the antigen to a greater degree than the reduced form. However, it is not known in what form, oxidised or reduced, cTnI is in the blood, subsequent to infarction. In light of this, the MAbs should ideally target epitopes different from those sites sensitive to oxidation-reduction.

(*c*) *Binding of macromolecules*

At physiological pH the high positive charge (pI 9.87) of cTnI (Johnson *et al*., 1980) means that it readily forms complexes with negatively charged molecules, for example, with the polysaccharide heparin (see fig. 5.4). The

formation of such complexes may interfere with the antibody-antigen recognition process (Katrukha *et al*., 1999). Indeed, the presence of heparin in the plasma samples has shown to have a significant affect on the immunodetection of cTnI (Katrukha *et al*., 1999; Gerhardt *et al*., 2000; Steigler *et al*., 2000; Wagner *et al*., 2001).

Heparin is an anionic polysaccharide consisting predominately of alternating α(1,4)-linked residues of D-glucuronate-2-sulfate and N-sulfo-D-glucosamine-6-sulfate (Voet & Voet, 1995).

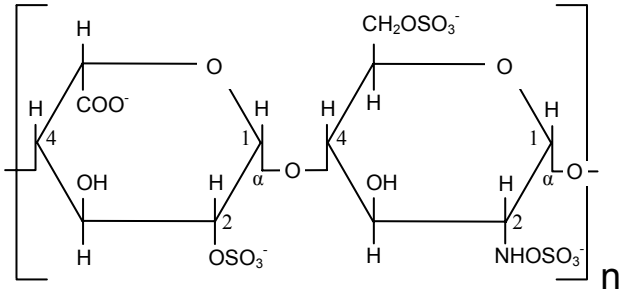

Fig. 5.4 – Molecular structure of heparin (Li, *et al*., 1999).

It possesses anticoagulant properties through the inhibition of antithrombin III, and for this reason it widely used in clinical practice. Heparinized plasma samples provide a more rapid analytical turnaround time than serum samples and also eliminates concerns of incomplete serum separations which may produce falsely increased cTnI levels (Nosanchuk, 1999; Wu *et al*., 1999). Unfortunately, heparin binds to cTnI and cTnT via a charge-charge (electrostatic) interaction, forming complexes which may result in changes in

epitope recognition, potentially reducing the effectiveness of some of the commercially available immunoassays (Katrukha *et al*., 1999).

Reduced sensitivity of commercially available cTnT and cTnI immunoassays as a direct result of heparin have previously been reported (Wu *et al*., 1998; Katrukha *et al*., 1999; Gerhardt *et al*., 2000; Stiegler *et al*., 2000). Gerhardt *et al*., (2000) reported TnT losses of up to 50 % in heparinized plasma samples compared to serum samples. At heparin concentrations of 50 IU mL^{-1} a 0-14 % reduction in the cTnT value was observed. An increase in heparin concentration to 98 IU mL^{-1} resulted in a decrease in measured cTnT to 67-99% and 450 IU mL^{-1} gave cTnT values of 51-78% (Gerhardt *et al*., 2000). This suggests that the presence of heparin can have a detrimental effect on the sensitivity of cTnT immunoassays. However, such high concentrations of heparin are not clinically employed as a therapeutic aid for cardiac damage, but are employed for rapid analytical turnaround times (Nosanchuk, 1999; Wu *et al*., 1999). A therapeutic concentration of heparin employed, as a response to cardiac damage, is commonly <1 UI mL^{-1} and surgically <5 UI mL^{-1} (Hirsh *et al*., 1995). Such low heparin concentrations (<15 IU mL^{-1}) have reportedly had no effect on two commercial cTnI assays (Wu *et al*., 1998; Katrukha *et al*., 1999), although some cTnI immunoassay manufactures have described losses of 19-30 % in concentrations <15 IU mL^{-1} (Wu *et al*., 1998). It would appear that the cTnI immunoassay resistance to heparin is epitope dependent, and varies between manufacturers.

Therefore, when employing monoclonal antibodies as a form of immunodetection for cardiac damage, it is important that they target troponin epitopes which remain accessible in the presence of heparin.

5.1.2 Force measurement techniques employed as ultrasensitive immunoassays

This chapter explores the effect of therapeutic concentrations of heparin on the association and dissociation of the cTnI-anti-cTnI complex. To achieve this, the optical tweezers and the AFM were employed as ultrasensitive immunodetection systems.

In previous years, optical tweezers have demonstrated a high degree of sensitivity, capable of detecting femtomolar concentrations of antigens (Helmerson *et al*., 1997). In the Helmerson *et al*., (1997) study, the optical power required to rupture the interaction between a bovine serum albumin (BSA) microsphere and anti-BSA surface, exposed to increasing environmental BSA concentrations was investigated. A decrease in the applied optical power with an increase in free BSA was observed at antigen concentrations as low as 1.45×10^{-15} mol L^{-1}. This form of competitive-binding assay was employed in this chapter, not only, to demonstrate the sensitivity of our constructed optical tweezer apparatus, but also to investigate the effect of therapeutic concentrations of heparin on cTnI recognition.

The AFM has also been employed for the detection of antibody-antigen binding events, for example, between biotin and anti-biotin (Dammer *et al*., 1996), human serum albumin (HSA) and anti-HSA (Hinterdorfer *et al*., 1996), ferritin and anti-ferritin (Allen *et al*., 1997), and scFv fragments FITC-E2 and 4D5-Flu (Schwesinger *et al*., 2000). In the investigation presented here, the AFM not only provides a complementary technique to the optical tweezers, but also determines the force for a single unbinding event between cTnI and anti-cTnI in the absence and presence of heparin. Furthermore, an intermolecular potential in the antibody-antigen unbinding pathway is investigated, providing details on the effect of therapeutic concentrations of heparin on the dissociation kinetics of the antibody-antigen complex.

The effect of therapeutic concentrations of heparin on cTnI MAbs has not been previously detected, using the more traditional immunodetection techniques (for example, ELISA) (Wu *et al*., 1998; Katrukha *et al*., 1999). These techniques are based upon an ensemble measurement (a cumulative response), and as such do not provide the high degree of sensitivity as demonstrated by optical tweezers and AFM, which are techniques capable of measuring individual molecular interactions.

5.2 MATERIALS & METHODS

To investigate the effect of therapeutic concentrations of heparin on the interaction between the clinically employed cTnI monoclonal antibody and

cTnI, the force spectroscopy techniques, optical tweezers and AFM were employed.

In the optical tweezer studies a competitive-binding assay method was employed, in which the force and probability of the interaction was explored in environments of increasing concentration of free antibody. The experimental optical tweezer-immunsensor system employed is illustrated in figure 5.5a. The antigen cTnI was covalently attached to 2 μm polystyrene microspheres and the complementary monoclonal antibody was bound covalently to the sample chamber surface. The optical focus was positioned at a chamber depth of 8.3 ± 0.9 μm, and measurements were recorded between individual cTnI microspheres and the anti-cTnI surface.

In the AFM studies the force of interaction was explored in greater detail, paying particular attention to the effect of heparin on the dissociation dynamics of the antibody-antigen complex. Figure 5.5b provides a schematic representation of the experimental procedure employed. Silicon nitride AFM probes were functionalised with cTnI via an amylose polymeric linker. The monoclonal antibody cTnI was bound covalently to a silicon substrate and rupture force measurements were recorded between the cTnI probe and sample surface. Figure 5.5c displays a typical force versus distance curve for a measurement performed between cTnI and anti-cTnI in 100mM PBS, pH 7.4 at a retract velocity of 1.0 μm s^{-1}. The specificity of interaction is characterised by the non-linear stretch of the carboxymethylated amylose linker prior to the

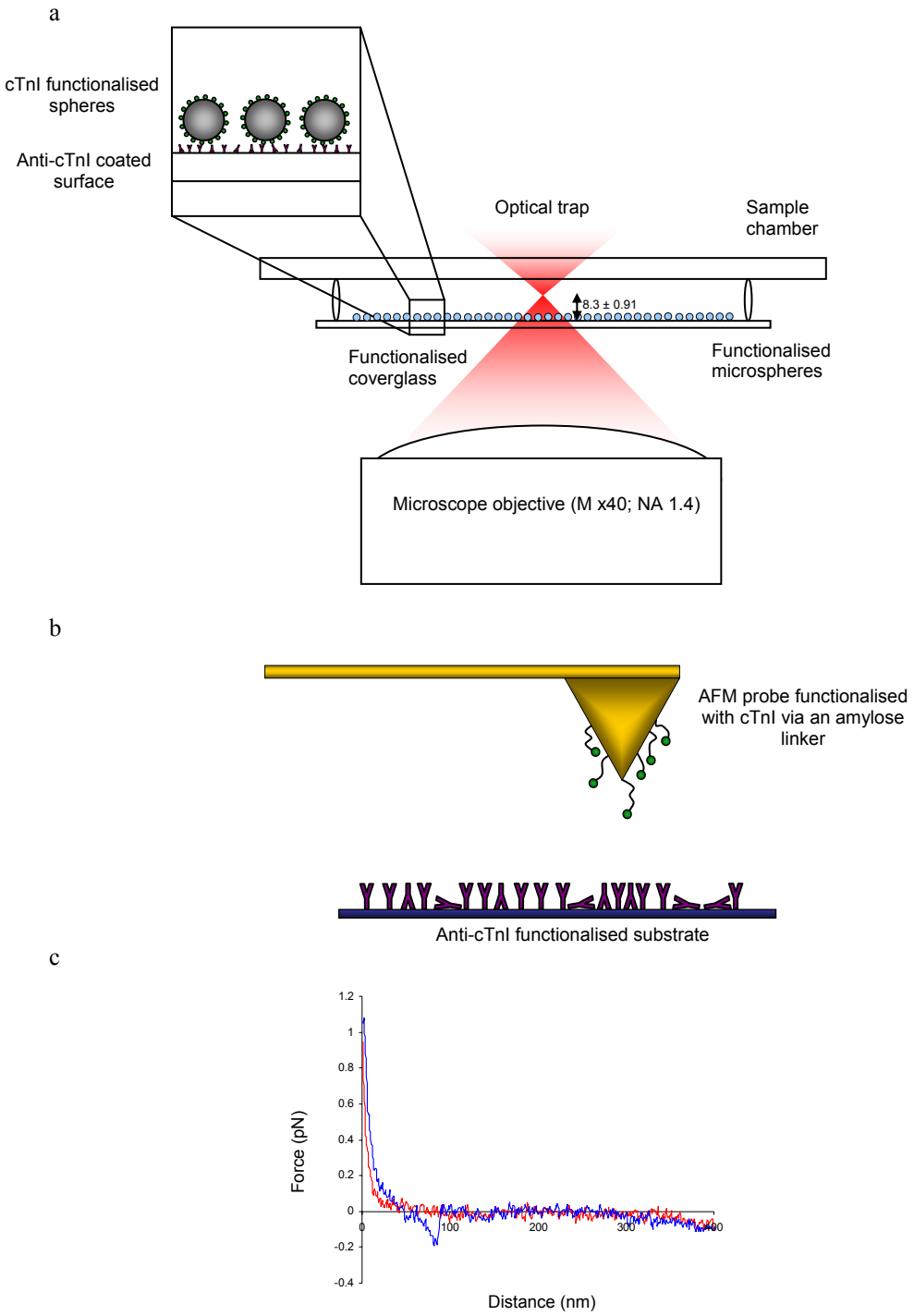

Fig. 5.5 - Schematic of the experimental procedures employed. a) Optical tweezers performed in 100 mM PBS pH 7.4. 50 µL of 0.05 % w/v solution of antigen functionalised polystyrene microspheres were encapsulated in a sample chamber, consisting of an antibody functionalised surface. The microspheres interact with the surface, and the optical focus is positioned 8.3 ± 0.91 µm above the functionalised surface. The laser power was increased until the microsphere jumped from the surface into the optical trap, rupturing the antibody-antigen complex; b) AFM experimental procedure. The AFM probe is functionalised with antigen via a carboxylamylose linker. Measurements are recorded between the probe and an antibody functionalised substrate; c) A typical force-distance profile exhibited between the cTnI probe and anti-cTnI surface, performed in 100 mM PBS at a retract velocity of 1.0 µm s^{-1}.

rupture of the antibody-antigen complex (as previously discussed in chapter 1).

All materials were purchased from Sigma, Poole, UK, unless stated otherwise.

5.2.1 Sample Preparation

The silanisation method (adapted from Vinckier *et al*., 1995, described in detail in chapter 2) was employed for the covalent immobilisation of troponin I antibody (Ortho-Clinical Diagnotics, Bucks, UK) to silicon (Rockwood, Amber Business Centre, Riddings, Derbyshire, UK) and glass for AFM and optical tweezers studies, respectively. Following silanisation the substrates were rinsed in high-purity deionised water and incubated in 0.1 mg mL^{-1} troponin I antibody for 24 h at 2-8 ºC. Prior to force analysis the samples were rinsed in high-purity deionised water to remove any non-covalently bound antibody.

5.2.2 Optical Tweezers Measurements

The optical tweezers instrumentation, described in detail in chapter 3 was employed to perform the force and probability of adhesion measurements described in this chapter. A simple sample chamber consisting of the sample surface (functionalised glass coverslip, thickness 150 ± 10 μm) and a glass slide was employed. A volume of 50 μL of the functionalised 2 μm polystyrene

microspheres (0.05% w/v), were encapsulated within the chamber (fig. 5.5a). Prior to measurements the microspheres were allowed to settle and interact with the surface. The optical trap focus was then positioned at a depth of approximately 8.3 ± 0.9 μm from the sample surface. The escape force method (Ashkin *et al*., 1986 and described in detail in 3.3.2) was employed to calibrate forces acting between the probe and surface.

5.2.2.1 *Microsphere Functionalisation*

Carboxyl-modified polystyrene microspheres were functionalised with human troponin I (Ortho-Clinical Diagnostics, Bucks, UK). A 2.5 % w/v concentration of 2 μm carboxyl-modified polystyrene microspheres were incubated in a 0.04 mg mL^{-1} solution of human troponin I, containing 10 mg mL^{-1} N-ethyl-N'-(dimethylaminopropyl)-carbodiimide (EDC) and 1 mg mL^{-1} N-hydroxysuccinimide (NHS) in PBS (100 mM, pH 8.0), for 2 h at room temperature. The addition of EDC and NHS resulted in the activation of the carboxyl groups present on the polystyrene microspheres, to form *N*-hydroxysuccinimide esters. Through nucleophilic attack the *N*-hydroxysuccinimide esters react with the amine groups of the protein to form covalent bonds (fig. 5.6). This coupling reaction requires uncharged amino groups and therefore favours a high pH (>7). Following incubation, the functionalised microspheres were rinsed in 100 mM PBS, pH 7.4, by performing a series of centrifugations (rpm 13,000 for 30 sec) to remove any reagents and non-covalently bound protein. The microspheres were then

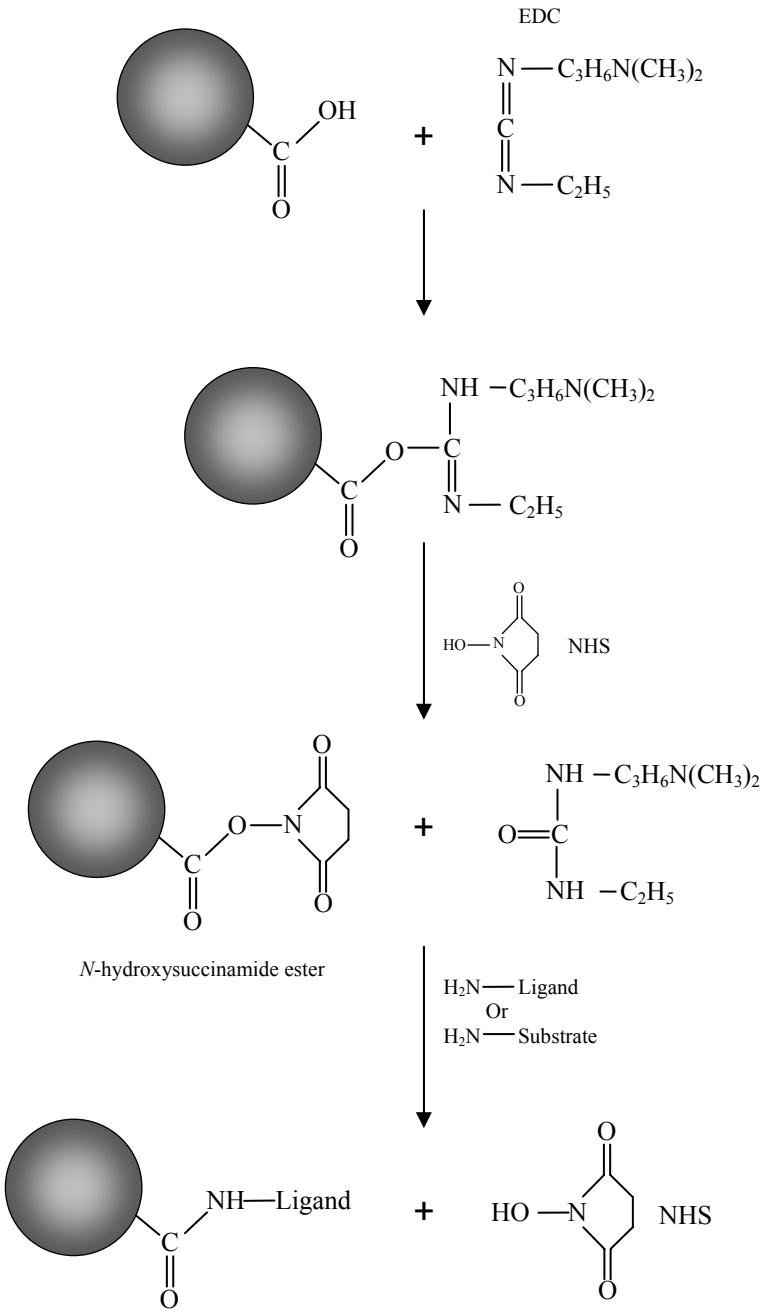

Fig. 5.6 – Scheme for the immobilisation procedure employed for the covalent attachment of proteins via the amine groups to carboxylated microspheres. The carboxy groups are activated with a mixture of N-hydroxysuccinimide (NHS) and N-ethyl-N'-(dimethylaminopropyl)-carbodiimide (EDC) to form *N*-hydroxysuccinimide esters. These esters then react spontaneously with amine groups in the protein to form a covalent attachment.

resuspended in 100 mM PBS, pH 7.4, to produce a final microsphere concentration of 0.05 % w/v.

5.2.2.2 *Probability of Adhesion*

Probability of adhesion measurements were performed using a competitive-binding assay. The probability that the cTnI microsphere would adhere to the anti-cTnI surface was recorded in the presence of the free cTnI antibody over a concentration series of 10^{-15} – 10^{-5} M. The optical focus was positioned approximately 6.3 ± 0.9 μm above individual microspheres and a fixed laser power of 0.69 Amp was applied. Those microspheres which displayed no interaction with the functionalised surface were pulled from the surface into the optical trap at the applied laser power.

The determination of the minimum laser power required to trap a 2 μm microsphere 8.3 ± 0.9 μm from a surface, which demonstrates no interaction with the surface, is outlined in chapter 4 (section 4.2.2.3). However in this particular set of experiments the measurements were performed between two cTnI Mab surfaces in 100 mM PBS, pH 7.4. The minimum laser power determined was 0.69 Amp, which is equivalent to an optical focus power of 2.8 mW and an optical force of <0.015 pN. Those microspheres which required a force greater than 0.015 pN were recorded as demonstrating adhesion, those equal or less than 0.015 pN were recorded as demonstrating no adhesion and thus no interaction with the surface.

These control measurements also demonstrate that the interactions observed in the experimental system between the cTnI MAb surface and the cTnI probe are attributable to the formation of the antibody-antigen complex.

Probability of adhesion measurements over the free MAb concentration series, were re-recorded in the presence of 0.006 mg mL^{-1} heparin, which is the equivalent to 0.95 IU mL^{-1} the therapeutic concentration administered for the treatment of acute myocardial infarction (AMI) (Hirsh *et al*., 1995).

5.2.2.3 *Force Analysis*

Force measurements were recorded for the antibody-antigen interaction in the presence of 0.1 - 0.5 mg mL^{-1} free cTnI MAb. A ramp of power was applied, starting at 0.6 Amp (equivalent to an optical focus power of approximately 2.6 mW) to the point at which the interaction between the cTnI microsphere and the anti-cTnI surface was overcome, and the microsphere was seen to jump into the optical focus. The power required to rupture this interaction was converted to force utilising the escape force calibration method.

Force measurements were re-recorded for the antibody-antigen interaction in the presence of 0.006 mg mL^{-1} heparin and environmental cTnI MAb concentrations of 0.15 mg mL^{-1}, 0.2 mg mL^{-1} and 0.4 mg mL^{-1}.

5.2.3 AFM Measurements

AFM force measurements were performed in liquid environments using instrumentation built and developed in the Laboratory of Biophysics and Surface Analysis (School of Pharmaceutical Sciences, University of Nottingham, U.K.). Raw data was obtained as plots of cantilever deflection signal (nA) versus distance of z-piezo movement (nm). The application of Hookes' Law enabled the conversion of raw data plots to force (nN) versus probe-sample distance (as previously described in Chapter 1). Calibration of cantilever spring constants were performed using the thermal resonance method (Hutter *et al*., 1993, described in chapter 1) and ranged from 0.09 -0.14 Nm^{-1}.

5.2.3.1 *Probe Functionalisation*

V-shaped silicon nitride probes, with a nominal spring constant of 0.12 Nm^{-1}, were chemically modified using the silanisation method, previously described in chapter 2. Subsequent to silanisation using a 4 % v/v solution of 3-APDES in toluene, the probes were rinsed in a series of solvents, propanol, methanol and high-purity deionised water for 1 min, respectively. The cantilever probes were then incubated in a solution of 10 mg mL^{-1} carboxymethylated amylose containing 10 mg mL^{-1} EDC and 1 mg mL^{-1} NHS for 15 min at room temperature. Carboxymethylated amylose is a linear polymer comprising of

glucose residues linked by α-D-1,4-glucosidic bonds (Li *et al*., 1999). The addition of the carboxymethylated amylose to the chemical architecture provides a flexible molecular extension to the probe, thereby reducing steric hindrance experienced by the molecules, which is a common problem when molecules are directly attached to the AFM probe (as previously discussed in chapter 1). Following the attachment of the polymeric linker, the AFM probes were rinsed in 100 mM PBS, pH 7.4, and incubated in 0.04 mg mL^{-1} human cTnI for 2 h at room temperature.

5.2.3.2 *Probability of Adhesion*

The probability that a rupture event was observed, in the retract trace of the force-distance cycle, between the cTnI functionalised probe and the anti-cTnI surface was recorded in the presence and absence of 0.006 mg mL^{-1} heparin.

5.2.3.3 *Force Analysis*

Force measurements were performed between cTnI and the cTnI MAb in a 100 mM PBS pH 7.4 environment, at retract velocities of 1.0 μm s^{-1}, 0.5 μm s^{-1}, 0.1 μm s^{-1}. The effect of 0.006 mg mL^{-1} heparin on the troponin I antibody assay was also studied at these retract velocities.

To ensure that the adhesive interactions observed were specific to the antibody-antigen interaction, the cTnI receptors were blocked by flooding the system

with free cTnI MAbs. This was achieved by incubating the cTnI probe with 0.5 mg mL^{-1} cTnI MAb in 100 mM PBS buffer, pH 7.4 for 1 h at room temperature. Measurements were then re-recorded.

Rupture forces indicative of specific interactions (refer to 2.3.2) were plotted as frequency *versus* force histograms. The histogram peak values were then plotted as a function of logarithm of the retract rate and initial approximations for k_{off} and f_β were derived. Employing these values and utilising Eqn. 1-4 a model force distribution was derived (Evans, 1999) and overlaid onto each histogram, enabling the identification of the most probable rupture force under each condition.

5.3 RESULTS & DISCUSSION

Two types of measurements were performed with optical tweezers and AFM; the first investigates the effect of therapeutic concentrations (0.948 IU mL^{-1}) of heparin on the association of the antibody-antigen complex through adhesion probability studies, and the second explores the effect of heparin on the forced dissociation of the complex.

5.3.1 The effect of heparin on antibody-antigen association

Optical tweezer adhesion probability measurements were performed using competitive binding assay methodology, where the surface immobilised MAbs

compete with free MAbs in the surrounding environment for antigen binding. In these initial studies, the probability of adhesion was measured between a cTnI functionalised microsphere and an anti-cTnI monolayer in the presence of free anti-cTnI over a concentration range of 10^{-15} – 10^{-5} M. In subsequent studies, 0.006 mg mL^{-1} of heparin was added over the free antibody concentration range.

In the absence of heparin and free anti-cTnI the probability of adhesion was observed to be 98 %. The addition of free anti-cTnI into the system resulted in a decrease in this probability of adhesion (fig. 5.7). The application of a 10^{-15} M solution of anti-cTnI resulted in a decrease in probability of adhesion to 97%. A 10 fold increase in antibody concentration led to a further decline in the probability of adhesion to 95 %. This gradual decrease in the probability of adhesion was observed over the complete concentration range studied. The decline became more pronounced with each subsequent 10 fold increase in antibody concentration after 10^{-11} M.

Mammen *et al*., (1996) demonstrated a similar trend in the probability of virus-cell adhesion in the presence of polyvalent inhibitors. With increasing concentrations of inhibitor a sigmoidal decrease in the probability of virus-cell adhesion was observed. This sigmoidal relationship between probability of adhesion and inhibitor concentration is characteristic of a competitive-binding assay, where, at low inhibitor concentrations the number of inhabited binding

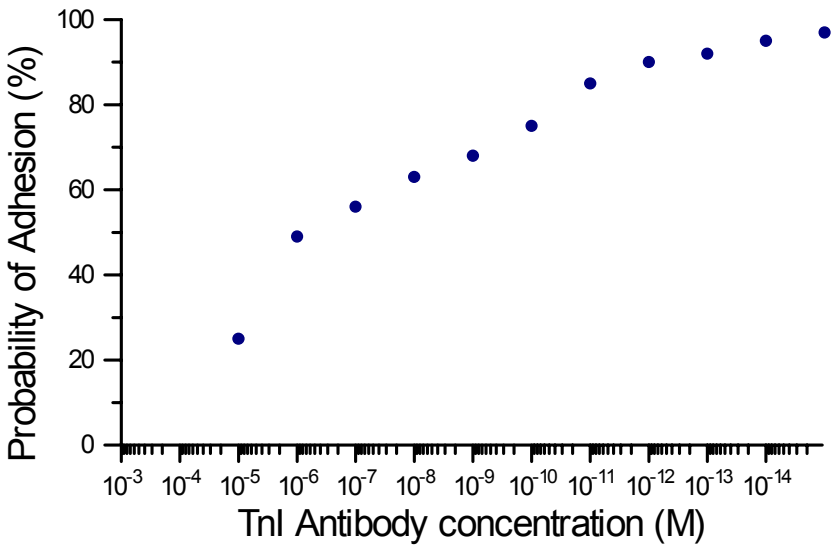

Fig. 5.7 – A plot of the probability of adhesion between the cTnI microsphere and the anti-cTnI surface versus environmental anti-cTnI concentration.

sites are so low that it does not have a significant effect upon the probability of adhesion.

With increasing concentrations the available binding sites are reduced until a point of saturation where the only available binding sites are a result of association-dissociation equilibria, and the probability of adhesion remains constant thereafter. The probability of adhesion measurements recorded between cTnI and anti-cTnI in the presence of 10^{-15}-10^{-5} M anti-cTnI, most likely illustrates the early part of this sigmoidal relationship. However, saturation of the system is not apparent, and it is proposed that if the anti-cTnI concentration was increased beyond 10^{-5} M then saturation would occur, and the probability of adhesion between the cTnI microsphere and the anti-cTnI surface would remain constant.

In the presence of 0.006 mg mL^{-1} heparin a sigmoidal decrease in the probability of adhesion was also observed with a logarithmic increase in free antibody concentration (fig. 5.8). Compared to the relationship observed between probability of adhesion and antibody concentration in the absence of heparin, it is evident that saturation of the system occurs earlier in the presence of heparin. In the absence of heparin, saturation of the system does not occur within the antibody concentration range 10^{-15}-10^{-5} M. However, with the addition of heparin saturation occurs at an antibody concentration of 10^{-10} M.

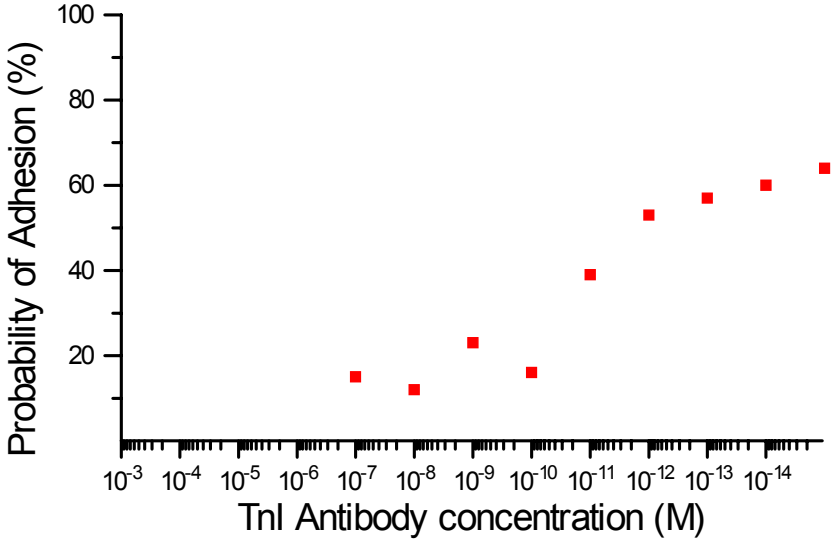

Fig. 5.8 - The probability of adhesion between the probe and surface, in the presence of 0.006 mg mL^{-1} heparin, versus environmental anti-cTnI concentration.

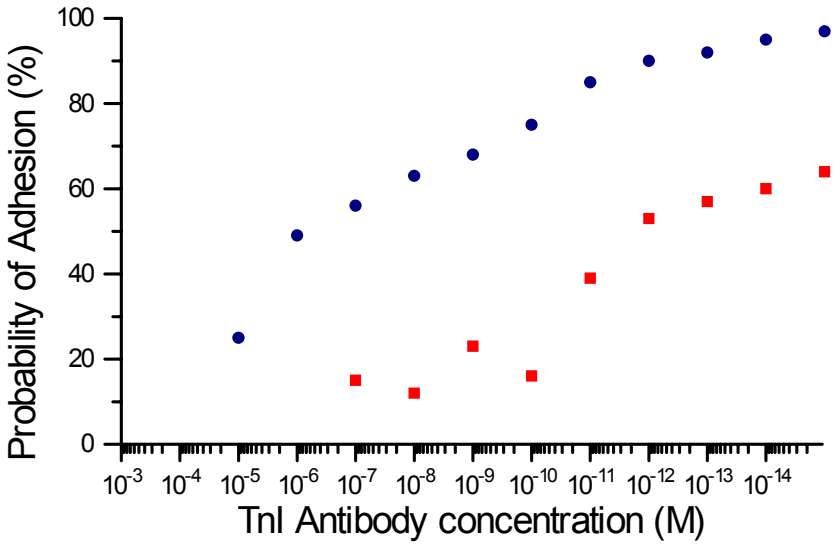

Fig. 5.9 –A comparison of the probability of adhesion in the absence (*blue circles*) and presence of 0.006 mg mL^{-1} heparin (*red squares*).

Furthermore, heparin induces a 38 % decrease in the probability of adhesion between the cTnI microsphere and the anti-cTnI surface (fig. 5.9). A reduction was also observed in the AFM studies, where a 30 % decrease in the probability of adhesion resulted from the addition of heparin. The probability of adhesion experienced between the antibody-antigen complex in the absence of heparin, in the AFM studies, was recorded at 20 %. The addition of heparin resulted in reduction in the probability of adhesion to only 14 %.

This decrease in the probability of adhesion with the addition of heparin suggests that heparin has an inhibitory effect upon the association (k_{on}) of the cTnI-anti-cTnI complex. It is speculated that the binding of heparin to cTnI via electrostatic interactions (Katrukha *et al*., 1999) generates a steric barrier at the surface of the antigen preventing recognition and thus antibody association.

Other groups have also experienced losses in anti-cTnI sensitivity in the presence of heparin (Wu *et al*., 1998; Katrukha *et al*., 1999; Gerhardt *et al*., 2000; Stiegler *et al*., 2000). However, heparin concentrations below 15 IU mL^{-1} have reportedly had no effect on two commercially employed cTnI assays (Wu *et al*., 1998; Katrukha *et al*., 1999). Although, cTnI immunoassay manufactures have also described losses of 19-30 % in concentrations <15 IU mL^{-1} (Wu *et al*., 1998). The ability of the optical tweezers and AFM to detect such low concentrations of heparin (0.98 IU mL^{-1}) and antibodies (1 fM) (optical tweezers) illustrates the application of the techniques as ultrasensitive immunosensors.

5.3.2 The effect of heparin on antibody-antigen dissociation

Initial optical tweezers axial rupture force measurements were performed, again using competitive binding assay methodology, between a cTnI functionalised microsphere and an anti-cTnI monolayer in the presence of free anti-cTnI over a concentration range of 0.67 - 3.33 μM. Subsequent studies investigated the effect of 0.006 mg mL^{-1} heparin on the rupture force experienced between the probe and sample over a free antibody concentration range of 1.0 - 2.67 μM. The AFM was then employed to complement the optical tweezers investigations. Here, rupture force measurements were performed over a range of forced dissociation rates from 1.0 - 0.1 μm s^{-1}, in the absence and presence of 0.006 mg mL^{-1} heparin.

In the absence of free anti-cTnI, the interaction between the cTnI microsphere and the anti-cTnI surface could not be ruptured even at maximum applied optical power of 316 mW (equivalent to 3.52 pN of force) (fig. 5.10a). With the addition of increasing concentrations of free antibody to the surrounding environment a gradual shift in the applied force required to rupture the interaction from 3.52 to 0.015 pN was observed (fig. 5.10a-f). A force of 0.015 pN is equal to the force required to trap a 2 μm polystyrene microsphere (at a chamber depth of 8 μm) which displays no interaction with a surface

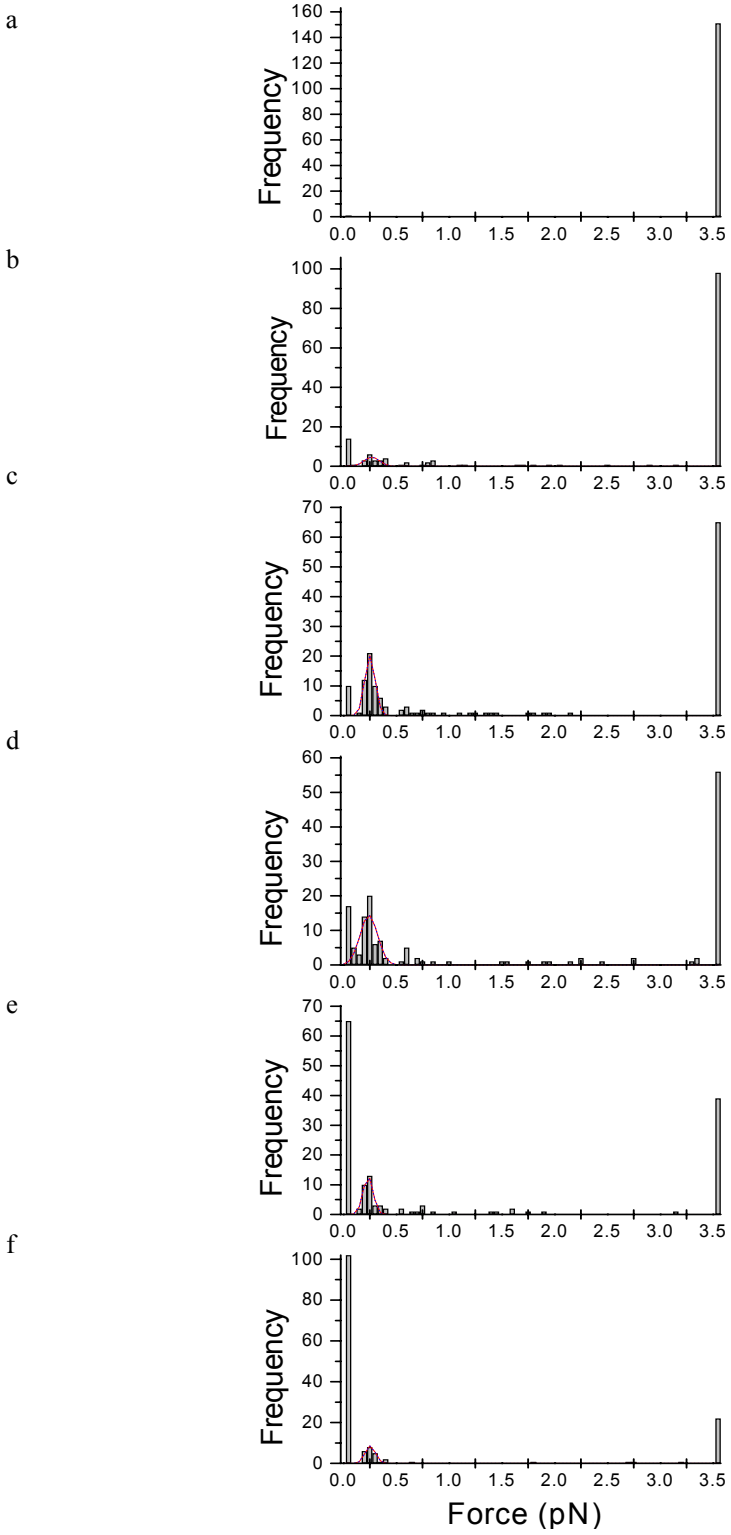

Fig. 5.10 - Frequency distribution histograms of the force required to optically trap single cTnI 2 µm polystyrene microspheres from a anti-cTnI surface. Measurements were performed in increasing environmental concentrations of anti-cTnI; (*a*) No environmental anti-cTnI; (*b*) 0.1 mg mL^{-1} anti-cTnI; (*c*) 0.2 mg mL^{-1}; (*d*) 0.3 mg mL^{-1}; (*e*) 0.4 mg mL^{-1}; (*f*) 0.5 mg mL^{-1}. Superimposed upon the force histograms is a gaussian distribution highlighting the peak force required for rupturing a single interaction between cTnI and anti-cTnI.

(refer to 5.2.1.2). This gradual decrease in rupture force with an increase in free antibody is attributed to the competitive-binding of free antibody to the antigen, resulting in a reduction in the number of available interactions between the cTnI microsphere and the anti-cTnI surface. Hence, a decrease in force is observed.

Furthermore, a force distribution centred at approximately 0.25 pN emerged with an increase in free antibody concentration. Initially appearing at an antibody concentration of 0.1 mg mL^{-1} (fig. 5.10b), the distribution became increasingly prominent up to an antibody concentration of 0.3 mg mL^{-1} (fig. 5.10c-d), and less prominent thereafter, as the number of available binding sites diminished with increasing antibody concentrations to 0.5 mg mL^{-1} (fig. 5.10e-f). As the probability of adhesion diminished with an increase in antibody concentration (as characterised by the shift of force from maximum applied force to the force required to trap an un-interacting microsphere) the peak force distribution remained constant. This would suggest that the force distribution observed may be attributed to the force required to rupture a single cTnI-anti-cTnI bond.

These results concur with previous optical tweezer antibody-antigen investigations (Helmerson *et al*., 1997). Helmerson *et al*., (1997) observed a gradual decrease in laser power required to rupture a BSA coated microsphere from an anti-BSA surface, in the presence of increasing concentrations of environmental BSA. Employing this type of competitive-binding assay

femtomolar concentrations of free antigen were detected, illustrated by a decrease in the trapping power. A decrease in optical power was required with an increase in molar concentration over 5 orders of magnitude up to 10 pM. After which a power of approximately 50 mW was maintained for antigen concentrations of 10 pM-0.1μM. It should be noted that the concentration range investigated in the cTnI-anti-cTnI competitive-binding assay ranged from 0.67 to 3.33 μM. Therefore it is not surprising that a maintained peak force distribution was observed over this concentration range.

The optical tweezers studies performed in the presence of 0.006 mg mL^{-1} heparin also revealed a maintained force distribution over a free antibody concentration range of 0.1 - 2.67 μM (fig. 5.11a-c). Furthermore, this distribution yielded an equivalent peak force (of 0.248 s.d. 0.01 pN) to those observed in the absence of 0.006 mg mL^{-1} heparin (0.252 s.d. 0.01 pN) (refer back to fig. 5.10b-e). Moreover, a comparable shift in force from 3.52 pN to 0.015 pN was also observed with increasing antibody concentrations (fig.5.11a-c).

To confirm that the forces recorded were specific to the interaction between cTnI and anti-cTnI, control measurements were performed between two antibody coated surfaces, an anti-cTnI functionalised polystyrene microsphere and an anti-cTnI functionalised surface (fig. 5.12). The probability of adhesion obtained for the antibody-antigen interaction ranged from 98 % - 25 % (depending upon free antibody concentration).

a

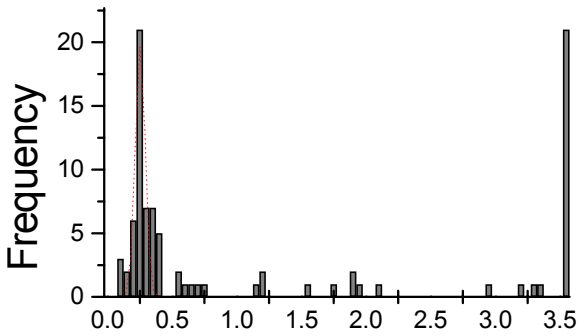

b

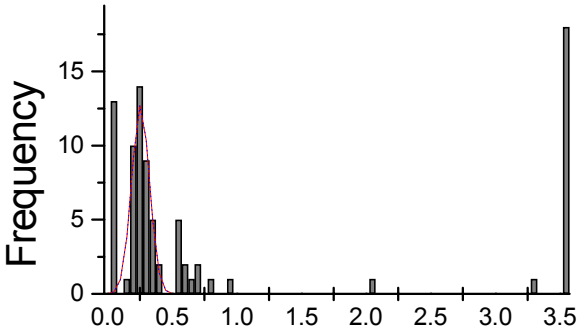

c

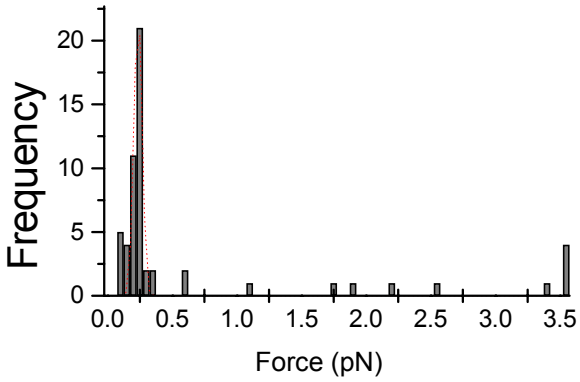

Fig. 5.11 - Frequency distribution histograms of the force required to optically trap single cTnI 2 µm polystyrene microspheres from a anti-cTnI surface in the presence of 0.006 mg mL^{-1} heparin. Measurements were performed in increasing environmental concentrations of anti-cTnI; (*a*) 0.15 mg mL^{-1} anti-cTnI; (*b*) 0.2 mg mL^{-1}; (*c*) 0.4 mg mL^{-1}. Superimposed upon the force histograms is a gaussian distribution highlighting the peak power required for rupturing a single interaction between cTnI and anti-cTnI in the presence of 0.006 mg mL^{-1} heparin.

a

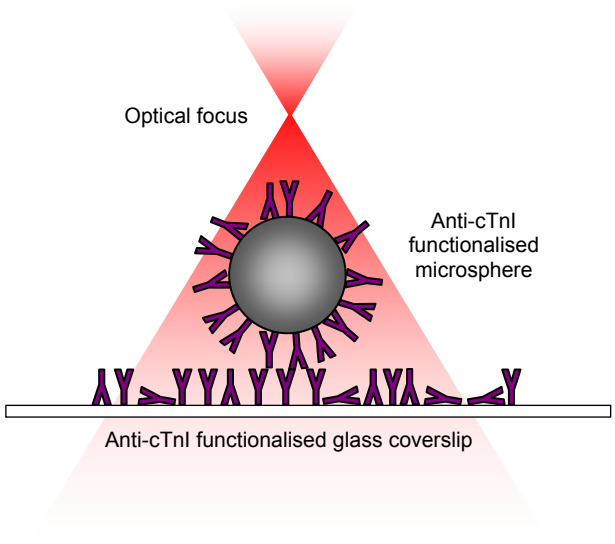

b

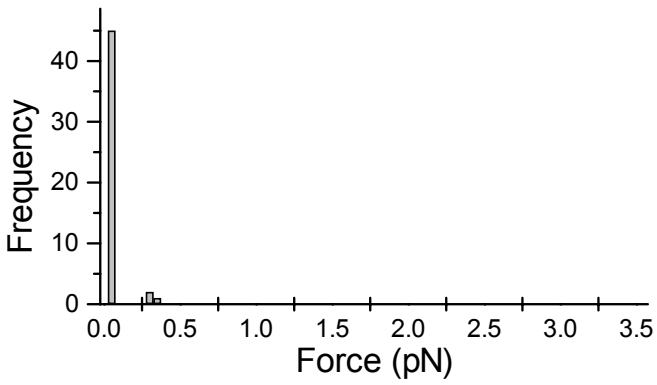

Fig. 5.12 – Control measurements performed between two antibody surfaces. a) A schematic of the control system, where both the 2 µm polystyrene microsphere and the glass substrate are covalently functionalised with anti-cTnI; b) Frequency histogram of the force of interaction between the probe and surface.

Whereas, the probability of adhesion experienced between the two antibody surfaces was only 6 %. This reduced probability of adhesion suggests that the interactions experienced between the antigen probe and the antibody surface are attributable to the forced dissociation of the antibody-antigen complex.

The maintenance of equivalent peak rupture forces in the presence and absence of 0.006 mg mL^{-1} heparin suggests that the heparin does not have an affect upon the forced dissociation of the antibody-antigen complex at the applied load used in these optical tweezers studies.

As a comparison to the above studies and to explore in more detail the effect of heparin upon the dissociation landscape, parallel rupture force experiments were performed with the AFM. Rupture force measurements were initially performed between the cTnI functionalised probe and an anti-cTnI monolayer over a range of mechanical dissociation rates. In later studies 0.006 mg mL^{-1} heparin was added to the surrounding environment.

Analysis of force measurements recorded for the cTnI-anti-cTnI complex over a range of mechanical dissociation rates, revealed a logarithmic relationship between rupture force and dissociation rate. A peak rupture force of 140 s.d. 39 pN was obtained for the unbinding of the antibody-antigen complex at a retract velocity of 1.0 μm s^{-1} (Fig. 5.13a). A decrease in force was experienced with a decrease in velocity. At 0.5 μm s^{-1} a force of 107 s.d. 32 pN was required for

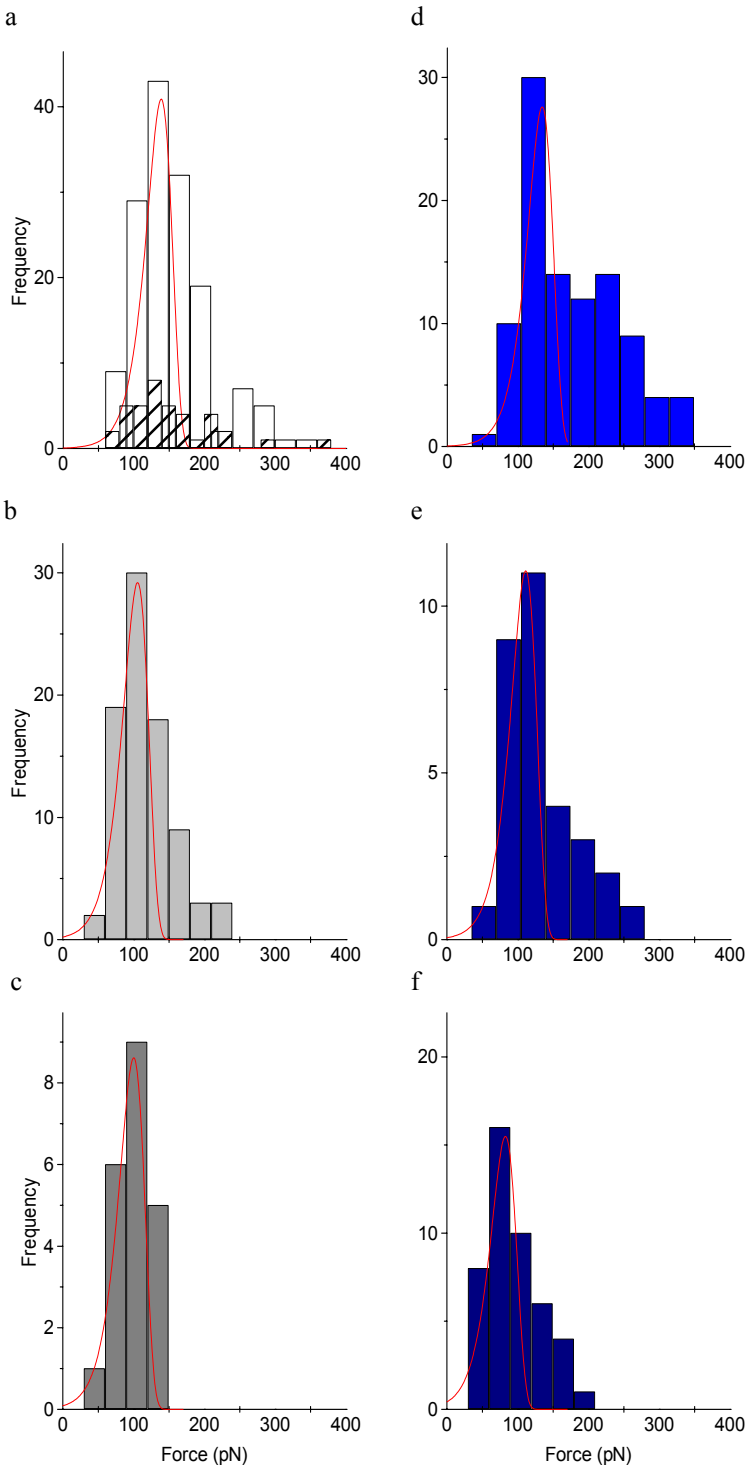

Fig. 5.13 – Frequency distribution histograms of rupture forces performed between the antibody-antigen complex, in 100 mM sodium phosphate buffer. a) *white histogram* depicts the force of interaction between cTnI and anti-cTnI at a retract velocity of 1 µm s^{-1}, the *forward slash histogram* is the control block; b-c) illustrates forced dissociation at rates of 0.5 and 0.1 µm s^{-1}, respectively d-f) frequency distribution of rupture force in the presence of 0.006 mg mL^{-1} heparin, performed at forced dissociation rates of 1.0, 0.5 and 0.1 µm s^{-1}, respectively.

rupture (Fig. 5.13b), and a further decrease in velocity to 0.1 μm s^{-1} lead to a decrease in peak rupture force to 102 s.d. 28 pN, as depicted in figure 5.13c.

A similar relationship was observed in the presence of heparin, producing comparable forces for unbinding to those obtained in the absence of heparin. Peak rupture forces of 135 s.d. 43 pN were obtained at a retract velocity of 1.0 μm s^{-1} (fig. 5.13d), 113 s.d. 33 pN at 0.5 μm s^{-1} (fig. 5.13e), and 84 s.d. 35 pN at 0.1 μm s^{-1} (fig. 5.13f).

The force values obtained for the cTnI-anti-cTnI complex, at a fixed dissociation rate of 1.0 μm s^{-1}, falls within the expected force range of 60 – 244pN for a single antibody-antigen unbinding event (Stuart and Hlady, 1995; Dammer *et al*., 1996; Hinterdorfer *et al*., 1996; Allen *et al*., 1997, 1999; Ros *et al*., 1998).

To confirm that the forces recorded were due to the interaction between cTnI and anti-cTnI, and that the peak rupture forces obtained were the result of single molecular interactions, the cTnI binding sites were blocked through the addition of free anti-cTnI. This resulted in a decrease in probability of a rupture event occurring, from 20 % to 7%. The decrease in the probability of adhesion with a decrease in available binding sites highlights the specificity of the rupture forces experienced in the experimental systems. Furthermore, the probability of specific rupture events for the control study is consistent with

Poisson analysis for single molecular interactions, which suggests that when the probability of observing a rupture event is below 10 %, then 95 % of the rupture events observed are attributable to single molecule unbinding (Evans, 1998). Thus, the low probability of adhesion in the control system and an equivalent peak force (135 s.d. 45 pN at a retract velocity of 1.0 μm s^{-1} (fig. 5.13a *forward slash histogram*)) to the experimental systems also suggests that the forces experienced are mainly due to single molecule unbinding events.

Control measurements were also recorded between an amylose functionalised probe and antibody substrates to verify that the unbinding events observed were that of the antibody-antigen complex and not the amylose linker and the antibody surface. The majority (75%) of measurements displayed no force of interaction between the probe and sample, and of those measurements which displayed an unbinding event the forces exceeded the expected force for an antibody-antigen bond. Furthermore, the force-distance profile of those measurements which displayed an unbinding event were characteristic of non-specific interactions and did not display a molecular extension profile. This demonstrates that the specific unbinding events observed in the experimental systems are attributable to the forced dissociation of the antibody-antigen bond.

The observed decrease in rupture force with retract velocity for the antibody-antigen complex concurs with Evans theorem on bond dissociation dynamics (previously discussed in chapter 1 and 2), which states that the force required

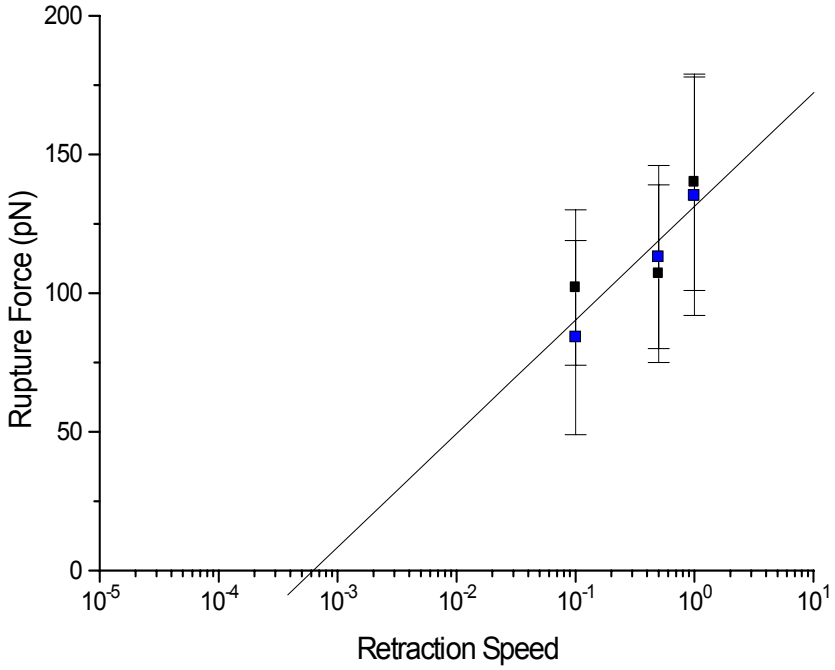

Fig. 5.14 - Representation of rupture forces experienced between cTnI and anti-cTnI *versus* logarithm of retraction speed. *Black square*, cTnI-anti-cTnI complex; *Blue square*, 0.006 mg mL^{-1} Heparin; where, f_β is 18 pN relating to a single energy barrier positioned 2.25 Å from a stable minimum.

to rupture a single molecular interaction is dependent on the timeframe of dissociation.

A plot of the peak rupture forces for the complex in the absence and presence of heparin versus the logarithm of retract velocity produced a single linear regime with a force scale (f_β) of 18 pN (Fig. 5.14). Indicating the presence of a single energy barrier in the dissociation pathway located 2.25 Å from the bound state (using Eqn. 1-3). The maintenance of comparable standard deviations over this linear regime further supports that a single energy barrier is probed over the retraction velocities and environmental conditions studied.

As previously discussed (2.3.2.1) dissociation rate is ordinarily expressed in terms of rate of loading. The employment of a polymeric linker, in this case amylose unfortunately means that the precise rate of loading cannot be identified.

The maintenance of f_β and x_β (barrier location in respect to a stable energy minimum) in the absence and presence of therapeutic concentrations of heparin infers that the dissociation kinetics for the barrier probed remains unaffected, where k_{off} is the intercept of f_β along the x-axis (of a logarithmic plot of force versus rate of loading) at zero force. Thus, heparin does not impede the unbinding of the cTnI-anti-cTnI complex at the transition studied.

These results are commensurate with the force data obtained using optical tweezers, where the force for unbinding of a single cTnI-anti-cTnI complex also appeared unaffected by the presence of heparin. The variation in rupture force between the two force sensing techniques is attributable to differences in the spring constants of the force transducers, and hence the rate of loading. As previously discussed (chapter 1) optical tweezers can apply a wide range of loading, particularly at the lower loading ranges which are not accessible by AFM, in these cases lower forces are required for the rupture of the same receptor-ligand complex. It is speculated that if it were possible to determine the rate of loading in both systems then the linear regime elucidated in the AFM data could be extrapolated to encompass the optical tweezers force data.

5.4 CONCLUSIONS

A therapeutic concentration of heparin, medically administered in response to AMI, has demonstrated an affect upon the binding affinity of the cardiac injury marker troponin to a clinically employed monoclonal antibody. Employing force sensing techniques as ultrasensitive immunoassays, a decrease in the association of the cTnI-anti-cTnI complex was observed, illustrated by a decrease in the probability of adhesion. However, the dissociation kinetics for the single barrier probed in the energy landscape remained unaffected by heparin, demonstrated by the maintenance of f_β, x_β and k_{off}.

These findings suggest that the binding of heparin to the antigen via electrostatic interactions (Katrukha *et al*., 1999) inhibits monoclonal antibody association.

As illustrated here, immunological detection can be an experimental nightmare, with a mine field of influential factors, all of which must be taken into consideration in assay design, to produce a reliable, effective and sensitive immunochemical detection system.

CHAPTER 6

GENERAL CONCLUSIONS

Force spectroscopy has provided a means of directly quantifying the complex interactions that determine the structure and the recognition of biological molecules. The main objective of this research project was to explore the intermolecular forces that govern receptor-ligand interactions at the single molecule level. To achieve this, the complementary force sensing techniques of AFM and optical tweezers were employed in the investigation of single molecule unbinding events between receptor-ligand complexes and their response to changes in the immediate environment.

Until recently intermolecular interactions were investigated at a single rate of loading. However, critical advances in the theoretical interpretation of the force required to induce bond failure, predicts that the force is defined by the rate of loading (Evans & Ritchie, 1997). Thus, forced dissociation of a bond over many orders of loading rate provides a profile of the intermolecular potentials that govern the dissociation pathway. This theorem was employed in empirical investigations of receptor-ligand interactions by the AFM, enabling the elucidation of regions of the energy landscapes of force induced dissociation pathways.

The AFM is already a well-established force sensing technique capable of measuring the intermolecular forces between, or the intramolecular forces within individual biomolecules at a molecular level. In chapter 2, a model drug-enzyme complex was employed to investigate the potential of the AFM to explore the energy landscapes of pharmaceuticals complexed with their target enzymes. Furthermore, the dependence of the intermolecular forces on the immediate environment (van Oss, 1994; Cserháti & Szögyi, 1995) was also addressed.

A single barrier in the energy landscape of the DHFR-MTX complex was elucidated upon the forced mechanical dissociation of the complex along a single unbinding trajectory. The position (at approximately 3 Å from the bound state) and the height of this energy barrier remained unchanged upon the formation of the ternary complex (DHFR-MTX-NADPH).

X-ray crystallography (Bolin, *et al*., 1982) and NMR (Gargargo *et al*., 1998) have previously demonstrated that protonation of a single amino acid residue known to hydrogen bond with methotrexate causes a disruption in bond formation. This perturbation is apparent in the AFM studies, illustrated by a decrease in the force required to rupture the complex.

The application of the AFM as a dynamic force sensing technique has provided an insight into the energy landscape that dictates the DHFR and MTX dissociation process. It has also demonstrated that this window into the energy

landscape is not dictated by cooperative binding between the drug and the cofactor, therefore increasing our understanding of the origins of this cooperativity by reducing the number of potential sources. However, the source of this cooperativity remains elusive and in order to understand it, and the whole recognition process, in greater detail, it will be necessary to perform force measurements over loading rates of many orders of magnitude. Unfortunately, the AFM has a limited range of accessible loading rates and in order to achieve the required range alternative force sensing instrumentation should be considered, for example the BFP and optical tweezers.

The optical tweezers exploits radiation pressure as a transducer of force. The spring constant of the system can be readily increased or decreased by altering the laser power at the optical focus, providing access to a wide range of loading. This ability to rapidly increase, decrease, or terminate the load gives the tweezers the best time-dependent control of forces applied to single molecules (Leckband & Israelachvili, 2001).

For these advantageous traits, chapter 3 details the development and experimental demonstration of an optical trap for employment as a force sensing technique, with general applicability in the study of receptor-ligand interactions.

The single beam optical tweezers model (Ashkin, 1986) forms the foundation of the optical tweezers system, and can be readily adapted to produce a more

sophisticated system. The optical path design employed was an amalgamation of the Ghislian *et al*., (1994) and Visscher *et al*., (1996) optical apparatus. This accounted for sufficient expansion of the beam diameter to achieve strong stable three-dimensional trapping of particles, and manipulation of the optical focus and thus trapped particle in *x*-*y*-*z*.

Calibration of the optical trapping forces provided comparable *Q* values to previously published data employing similar calibration methods (Ghislain *et al*., 1994; Felgner *et al*., 1995). However, the method employed for calibration determines the forces operating at the edge of the trap and not the centre of the trap, and as a result the accuracy provided by the determination of trap stiffness is not accessible (Visscher *et al*., 1996). Thus a beneficial addition to the optical setup would be a position sensitive photodetector. Combined with a photodetector, a piezo-driven *x*-*y*-*z* translation stage will enable the instrumentation to be employed in dynamic force spectroscopy.

The constructed optical tweezers demonstrated the ability and versatility to trap and manipulate a range of particle diameters and particle compositions, from light weight synthetic polymer microspheres to heavy weight silica microspheres to biological cells. The manipulation of individually trapped particles was possible over a translation range of 30 μm in the *x* and *y* axes, and approximately 15 μm in the *z* axis. Furthermore, the application of laser power (where, λ = 1064 nm) to biological samples did not appear to have a detrimental effect upon cell viability, as demonstrated by the motion of bacteria

subsequent to trapping. Chapters 4 and 5 provided a means of determining the effectiveness of the optical trap as a force sensing instrument.

Chapter 4 provides a platform for proof of principle measurements for the constructed optical tweezers apparatus through the investigation of protein adhesion on plasma treated surfaces, in which complementary data was gained from measurements performed by AFM. Initially, the effect of argon plasma on surface chemistry, in particular, hydrophobicity was studied using static contact angle analysis. Contact angles demonstrated that the hydrophobic properties of the polystyrene surfaces decreased with an increase in argon plasma exposure times.

Argon plasma introduces oxygen functionality by producing hydroxyl groups on the surface upon exposure to atmospheric oxygen (Clouet *et al*., 1992). These hydroxyl groups are hydrophilic in nature, and it is therefore not surprising that an increase in argon plasma exposure time resulted in an increase in hydrophilicity.

Leading on from this, optical tweezers and AFM adhesion force and probability of adhesion measurements demonstrated that an increase in surface hydrophilicity induced a decrease in the quantity of HSA protein molecules readily adhered. A reduction in protein adhesion with increase in polymer hydrophilicity has previously shown to be accompanied by a decrease in protein adsorption (McGurk, *et al*., 1999). The increase in resistance to protein

adsorption with an increase in surface exposure to argon plasma is attributed to the formation of a repulsive barrier with an increase in hydroxyl surface coverage.

Although this relationship between surface hydrophobicity and protein adsorption has been known for some time, here it has provided a foundation with which to demonstrate the ability of the optical tweezers to detect and measure intermolecular interactions.

In chapter 5, the intermolecular forces involved in the immuno-detection of marker antigens were investigated using the AFM and optical tweezers as ultrasensitive biosensors. The chapter details the effect of therapeutic concentrations of heparin upon the association and dissociation of the antibody-antigen complex cTnI-anti-cTnI. In the more conventional biosensor techniques, for example immunoassays, such quantities of heparin were undetectable (Wu *et al*., 1998; Katrukha *et al*., 1999). However, due to the ability of the optical tweezers and AFM to measure interactions at a single molecule level, these previously undetectable quantities of heparin, were now detectable.

The complementary techniques of optical tweezers and AFM both detected an inhibitory effect of heparin on the association of the cTnI-anti-cTnI complex. However, the dissociation kinetics, as determined by AFM, for a single energy barrier located 2.25 Å along a single forced dissociation pathway appeared

unaffected by a therapeutic concentration of heparin. Commensurate data was obtained using optical tweezers where the force of unbinding of the antibody-antigen complex remained unchanged by the presence of heparin. In conclusion, it was found in both the AFM and optical tweezers experiments that the presence of heparin clearly causes inhibition of the antibody-antigen association. However, it neither impedes nor facilitates unbinding suggesting that binding is an all or nothing event.

In this thesis the AFM has thus been employed to directly monitor the intermolecular forces governing molecular interactions at a single molecule level, revealing energy barriers along unbinding trajectories. Although currently limited to a narrow region of the force spectrum, these studies revealed that the dominant kinetic impedance in the forced dissociation pathway of the drug–enzyme complex was independent of cooperativity, but not to changes in environmental pH where the force of unbinding decreases with a disruption in bond formation. However, in future studies, investigations of the loading rate dependence upon the dissociation of receptor-ligand complexes should be performed over many orders of magnitude. Furthermore, structural data and molecular dynamics simulations should be employed in conjunction with dynamic force spectroscopy to enable the elucidation of the whole energy landscape, from the bound state to the dissociated state, providing thermodynamic and dissociation rate details over the unbinding process.

The constructed optical tweezers provides an additional force sensing technique to the AFM, capable of measuring intermolecular forces between biomolecules. Furthermore, single molecule investigations of the antibody-antigen complex have revealed the impact of therapeutic concentrations on the association and dissociation of the complex. Although, the current applications of the optical tweezers are limited, the choice of design means that the setup can be readily adapted to accommodate more sophisticated systems.

However, despite the limitations of the current optical setup, the optical tweezers and the AFM have independently provided complementary qualitative data towards the understanding of biomolecular interactions.

REFERENCES

Abadie, J. M. (2001) Can a strategy be developed for more cost-effective ordering of cardiac injury marker assays?. *Clin. Chem.,* **47**, 639.

Allen, S., Davies, J., Davies, M. C., Dawkes, A. C., Roberts, C. J., Sefton, J., Tendler, S. J. B & Williams, P M. (1999) The influence of epitope availability on atomic force microscope studies of antigen-antibody interactions. *Biochem. J*., **341**, 173-178.

Allen, S. (1997a) The study of biomolecular interactions using scanning probe microscopy. *PhD Thesis*. University of Nottingham, Nottingham, UK.

Allen, S., Chen, X., Davies, J., Davies, M. C., Dawkes, A. C., Edwards, J. C., Roberts, C. J., Sefton, J., Tendler, S. J. B. & Williams, P. M. (1997b) Detection of antibody-antigen binding events with the atomic force microscope. *Biochemistry*, **36**, 7457-7463.

Allen, S., Davies, J., Dawkes, A. C., Davies, M. C., Edwards, J. C., Parker, M, C.., Roberts, C, J., Sefton, J., Tendler, S. J. B. & Williams, P. M. (1996) In situ observation of streptavidin–biotin binding on an immunoassay well surface using an atomic force microscope. *FEBS Lett.*, **390**, 161-164.

Amiji, M. & Park, K. (1992) Prevention of protein adsorption and platelet-adhesion on surfaces by PEO-PPO-PEO triblock copolymers. *Biomaterials*, **13**, 682-692.

Andrews, J., Fierke, C. A., Birdsall, B., Ostler, G., Feeney, J., Roberts, G. C. K. & Benkovic, S. J. (1989) A kinetic study of wild-type and mutant dihydrofolate reductases from Lactobacillus casei. *Biochemistry,* **28**, 5743-5750.

Appleman, J. R., Beard, W. A., Delcamp, T. J., Prendergast, N. J., Freisheim, J. H. & Blakely, R. L. (1990) Role of aspartate-27 of dihydrofolate-reductase from *Escherichia coli* in interconversion of active and inactive enzyme conformers and binding NADPH. *J. Biol. Chem.*, **265**, 2740-2748.

Arai, Y., Yasuda, R., Akashi, K., Harada, Y., Miyata, H., Kinosita, K. & Itoh, H. (1999) Tying a molecular knot with optical tweezers. *Nature*, **399**, 446-448.

Ashkin, A. (1992) Forces of a single-beam gradient laser trap on a dielectric sphere in the ray optics regime. *Biophys. J*., **61**, 569-582.

Ashkin, A. & Dziedzic, J. M. (1989) Internal cell manipulation using infrared-laser traps. *Proc. Natl. Acad. Sci. USA*., **86**, 7914-7918.

Ashkin, A. & Dziedzic, J. M. (1987) Optical trapping and manipulation of viruses and bacteria. *Science*, **235**, 1517-1520.

Ashkin, A., Dziedzic, J. M. & Yamane, T. (1987) Optical trapping and manipulation of single cells using infrared-laser beams. *Nature*, **330**, 769-771.

Ashkin, A., Bjorkholm, J. E. & Chu, S. (1986) Caught in a trap. *Nature*, **323**, 585.

Ashkin, A., Dziedzic, J. M., Bjorkholm, J. E. & Chu, S. (1986) Observation of a single-beam gradient force optical trap for dielectric particles. *Opt. Lett*., **11**, 288-290.

Ashkin, A. (1970) Acceleration and trapping of particles by radiation pressure. *Phys. Rev. Lett.*, **24**, 156-159.

Baccanari, D. P., Daluge, S. & King, R. W. (1982) Inhibition of dihydrofolate reductase-effect of reduced nicotinamide adenine dinucleotide phosphate on the selectivity and affinity of diaminobenzlpyrimidines. *Biochemistry*, **21**, 5068-5075.

Baumann, C. G., Bloomfield, V. A., Smith, S. B., Bustamante, C., Wang, M. D., & Block, S. M. (2000) Stretching of single collapsed DNA molecules. *Biophys. J*. **78**, 1965-1978.

Baumgartner, W., Hinterdorfer, P., Ness, W., Raab, A., Vesterweber, D., Schindler, H. & Drenckhahn, D. (2000) Cadherin interaction probed by atomic force microscopy. *Proc. Natl. Acad. Sci. USA*. **97**, 4005-4010.

Bell, G. I. (1978) Models for the specific adhesion of cells to cells. *Science,* **200**, 618-627.

Benmakroha, Y., Zhang, S. & Rolfe, P. (1995) Hemocompatibility of invasive sensors. *Med. Biol. Eng. Comput*., **33**, 811-821.

Bennink, M. L., Scharer, O. D., Kanaar, R., Sakata-Sogawa, K., Schins, J. M., Kanger, J. S., De Grooth, B. G. & Greve, J. (1999) Single-molecule manipulation of double-stranded DNA using optical tweezers: Interaction studies of DNA with RecA andYOYO-1. *Cytometry*, **36**, 200-208.

Berns, M. W., Wright, W. H., Tromberg, B. J., Profeta, G. A., Andrews, J. J. & Walter, R. J. (1989) Use of a laser-induced optical force trap to study chromosome movement on the mitotic spindle. *Proc. Natl. Acad. Sci. USA*., **86**, 4539-4543.

Berry, R. M. & Berg, H, C. (1997) Absence of a barrier to backwards rotation of the bacterial flagellar motor demonstrated with optical tweezers. *Proc. Natl. Acad. Sci. USA.,* **94**, 14433-14437.

Binnig, G., Quate, C. F. & Gerber, C. (1986) Atomic force microscope. *Phys. Rev. Letts.* **56**, 930-933.

Binnig, G., Rohrer, H., Gerber, C. & Weibel, E. (1982) Surface studies by scanning tunneling microscopy. *Phys. Rev. Letts.* **49**, 57-61.

Birdsall, B., Gronenborn, A. M., Hyde, E. I., Clore, G. M., Roberts, G. C. K., Feeney, J. A. & Burgen, A. S. V. (1982) Proton, carbon-13, and phosphorus-31 nuclear magnetic resonance studies of the dihydrofolate reductase-NADP-folate complex: characterization of three coexisting conformational states. *Biochemistry*, **21**, 5831-5838.

Birdsall, B., Burgen, A. S. V. & Roberts, G. C. K. (1980a) Binding of coenzyme analogs to Lactobacillus casei dihydrofolate reductase: binary and ternary complexes. *Biochemistry,* **19**, 3723-3731.

Birdsall, B., Burgen, A. S. V. & Roberts, G. C. K. (1980b) Effects of coenzyme analogs on the binding of p-aminobenzoyl-L-glutamate and 2,4-diaminopyrimidine to Lactobacillus casei dihydrofolate reductase. *Biochemistry*, **19**, 3732-3737.

Birdsall, B., Burgen, A. S. V., Rodrigues de Miranda, J. & Roberts, G. C. K. (1978) Cooperativity in ligand binding to dihydrofolate reductase. *Biochemistry*, **17**, 2102-2110.

Blakely, R. L. (1969) The biochemistry of folic acid related pteridines. North-Holland Publishing Co., Amsterdam.

Block, S. M. (1999) Constructing optical tweezers. *In Cell Biology: A Laboratory Manual*. Spector, D. L., Goldman, R., Leinwand, L. Ed., Cold Spring Harbour Press, vol. II, chapter 7.

Block, S. M., Blair, D. F. & Berg, H. C. (1989) compliance of bacterial flagella measured with optical tweezers. *Nature*, **338**, 514-518.

Bodor, G. S., Porter, S., Landt, Y. & Ladenson, J. H. (1992) Development of monoclonal-antibodies for an assay of cardiac troponin-I and preliminary-results in suspected cases of myocardial-infarction. *Clin. Chem*., **38**, 2203-2214.

Bolin, J. T., Filman, D. J., Matthews, D.A., Hamlin, R. C. & Kraut, J. (1982) Crystal structures of *Escherichia coli* and *Lactobacillus casei* dihydrofolate reductase refined at 1.7 Å resolution. 1. General features and binding of methotrexate. *J. Biol. Chem.,* **257**, 13650-13662.

Bronkhorst, P. J. H., Grimbergen, J., Brakenhoff, G. J., Heethaar, R. M. & Sixma, J. J. (1997) The mechanism of red cell (dis)aggregation investigated by means of direct cell manipulation using multiple optical trapping. *Br. J. Haematol*., **96**, 256-258.

Buer, C. S., Gahagan, K. T., Swartzlander, G. A. & Weathers, P. J. (1998) Insertion of microscopic objects through plant cell walls using laser microsurgery. *Biotechnol. Bioeng*., **60**, 348-355.

Bustamante, C., Smith, S. B., Liphardt, J. & Smith, D. (2000) Single-molecule studies of DNA mechanics. *Curr. Opin. Struc. Biol.,* **10**, 279-285.

Butt, H.-J., Siedle, K., Siefert, K., Fendler, K., Seeger, T., Bamberg, E., Wiesenhorn, A. L., Goldie, K. & Engel, A. (1993) Scan speed limit in atomic force microscopy. *J. Microscopy,* **69**, 75-84.

Bystroff, C. & Kraut, J. (1991) Crystal structure of unliganded Escherichia coli dihydrofolate reductase. Ligand-induced conformational changes and cooperativity in binding. *Biochemistry*, 30, 2227-2239.

Cappella, B. & Dietler, G. (1999) Force-distance curves by atomic force microscopy. *Surf. Sci. Reports*, **34**, 1-104.

Carrion-Vazquez, M., Oberhauser, A. F., Fowler, S. B., Marszalek, P. E., Broedel, S. E.., Clarke, J. & Fernandez, J. M. (1999) Mechanical and chemical unfolding of a single protein: A comparison. *Proc. Natl. Acad. Sci. USA.,* **96**, 3694-3699.

Chan, V., McKenzie, S. E., Surrey, S., Fortina, P. & Graves, D. J. (1998) Effect of hydrophobicity and electrostatics on adsorption and surface diffusion of DNA oligonucleotides at liquid/solid interfaces. *J. Colloid Interface Sci.,* **203**, 197-207.

Cheung, H. T. A., Birdsall, B., Frenkiel, T. A., Chau, D. D. & Feeney, J. (1993) Carbon-13 NMR determination of the tautomeric and ionization states of folate in its complexes with Lactobacillus casei dihydrofolate reductase. *Biochemistry*, **32**, 6846-6854.

Chilkoti, A. & Stayton, P. S. (1995) Molecular origins of the slow streptavidin-biotin dissociation kinetics. *J. Am. Chem. Soc.,* **117**, 10622-10628.

Chu, S. (1991) Laser manipulation of atoms and particles. *Science*, **253**, 861-866.

Clark, D. T. & Dilks, A. (1979) *J. Polym. Sci. Polym. Chem. Ed.,* **17**, 957.

Clausen-Schaumann, H., Seitz, M., Krautbauer, R. & Gaub, H. E. (2000) Force spectroscopy with single biomolecules. *Curr. Opin. Chem. Biol.,* **4**, 524-530.

Cleveland, J. P., Manne, S., Bocek, D. & Hansma, P. K. (1993) A non-destructive method for determining the spring constant of cantilevers for surface force microscopy. *Rev. Sci. Instrum.,* **64**, 403-405.

Clore, G. M., Gronenborn, A. M., Birdsall, B., Feeney, J. & Roberts, G. C. K. (1981) F-19-NMR studies of 3', 5'-Difluoromethotrexate binding to *Lactobacillus casei* dihydrofolate reductase molecular motion and coenzyme induced conformational changes. *Biochem. J.*, **217**, 659-666.

Clouet, F. & Shi, M. K. (1992) Interactions Of Polymer Model Surfaces With Cold-Plasmas - Hexatriacontane As a model molecule of high-density polyethylene and octadecyl octadecanoate as a model of polyester .1. degradation rate versus time and power. *J. Appl. Polym. Sci*., **46**, 1955-1966.

Cocco, L., Groff, J. P., Temple, C., Montgomery, J. A., London, R. E., Matwiyoff, N. A. & Blakley, R. L. (1981) Carbon-13 nuclear magnetic resonance study of protonation of methotrexate and aminopterin bound to dihydrofolate reductase. *Biochemistry,* **20**, 3972-3978.

Colon, J. M., Sarosi, P. G., McGovern, P. G., Ashkin, A., Dziedzic, J. M., Skurnik, J., Weiss, G. & Bonder, E. M. (1992) Controlled micromanipulation of human sperm in three dimensions with an infrared laser optical trap: effect on sperm velocity. *Fertil. Steril.,* **57**, 695-698.

Cserháti, T. & Szögyi, M. (1995) Role of hydrophobic and hydrophilic forces in peptide-protein interaction: New advances. *Peptides,* **1**, 165-173.

Cui, Y. & Bustamante, C. (2000) Pulling a single chromatin fiber reveals the forces that maintain its higher-order structure. *Proc. Natl. Acad. Sci. USA.,* **97**, 127-132.

Dammer, U., Hegner, M., Anselmetti, D., Wagner, P., Dreier, M., Huber, W, & Güntherodt, H.-J. (1996) Specific antigen/antibody interactions measured by force microscopy. *Biophys. J.,* **70**, 2437-2441.

Davies, J., Nunnerley, C. S., Brisley, A. C., Sunderland, R. F., Krüger, P., Knes, R., Paul, A. J. & Hibbert, S. (2000) Argon plasma treatment of polystyrene microtiter wells. Chemical and physical characterisation by contact angle, ToF-SIMS, XPS and STM. *Colliod Surf. A.,* **174**, 287-295.

De Paris, R., Strunz, T., Oroszlan, K., Güntherodt, H. –J. & Hegner, M. (2000) Force spectroscopy and dynamics of the biotin-avidin bond studied by scanning force spectroscopy. *Single Mol.,* **1**, 285-290.

Dewez, J. L., Lhoest, J. B., Detrait, E., Berger, V., Dupont-Gillain, C. C., Vincent, L. M., Schneider, Y. J., Bertrand, P. & Rouxhet, P. G. (1998) Adhesion of mammalian cells to polymer surfaces: from physical chemistry of surfaces to selective adhesion on defined patterns. *Biomaterials*, **19**, 1441-1445.

Dunn, S. M. J. & King, R. W. (1980) Kinetics of ternary complex formation between dihydrofolate reductase, coenzyme, and inhibitors. *Biochemistry,* **19**, 766-773.

Elbert, D. L. & Hubbell, J. A. (1996) Surface treatments of polymers for biocompatibility. *Annu. Rev. Mater. Sci*., **26**, 365-394.

Erie, D. A., Yager, T. D. & Vonhippel, P. H. (1992) The single-nucleotide addition cycle in transcription – A biophysical and biochemical perspective. *Annu. Rev. Biophys. Biomolec. Struct.,* **21**, 379-415.

Evans, E. & Ludwig, F. (2000) Dynamic strengths of molecular anchoring and material cohesion in fluid biomembranes. *J. Phys.: Condens. Matter,* **12,** A315-A320.

Evans, E. (1999) Looking inside molecular bonds at biololical interfaces with dynamic force spectroscopy. *Biophys. Chem.,* **82**, 83-97.

Evans, E. (1998) Energy landscapes of biomolecular adhesion and receptor anchoring at interfaces explored with dynamic force spectroscopy. *Faraday Discuss*, **111**, 1-16.

Evans, E. & Richtie, K. (1997) Dynamic strength of molecular adhesion bonds. *Biophys. J.*, **72**, 1541-1555.

Evans, E., Ritchie, K. & Merkel, R. (1995) Sensitive force technique to probe molecular adhesion and structural linkages at biological interfaces. *Biophys. J.,* **68**, 2580-2587.

Fällman, E. & Axner, O. (1997) Design for fully steerable dual-trap optical tweezers. *Appl. Optics*, **36**, 2107-2113.

Farah, C. S., Miyamoto, C. A., Ramos, C. H. I., Dasilva, A. C. R., Quaggio, R. B., Fujimori, K., Smillie, L. B. & Reinach, F. C. (1994) Structural and regulatory functions of the NH2- and COOH- terminal regions of skeletal-muscle troponin-I. *J. Biol. Chem*., **269**, 5230-5240.

Feeney, J. (2000) NMR studies of ligand binding to dihydrofolate reductase. *Angew. Chem., Int. Ed. Engl.,* **39**, 290-312.

Felgner, H., Muller, O. & Schliwa, M. (1995) Calibration of light forces in optical tweezers. *Appl. Optics*., **34**, 977-982.

Fierke, C. A., Johnson, K. A. & Benkovic, S. J. (1987) Construction and evaluation of the kinetic scheme associated with dihydrofolate reductase from *Escherichia coli*. *Biochemistry,* **26**, 4085-4092.

Finer, J. T., Simmons, R. M. & Spudich, J. A. (1994) Single Myosin Molecule Mechanics - Piconewton Forces And Nanometer Steps. *Nature*, **368**, 113-119.

Florin, E. L., Rief, M., Lehmann, H., Ludwig, M., Dornmair, C., Moy, V. T. & Gaub, H. E. (1995) Sensing specific molecular-interactions with the atomic-force microscope. *Biosens. Bioelectron*., **10**, 895-901.

Florin, E. L., Moy, V. T. & Gaub, H. E. (1994) Adhesion forces between individual ligand-receptor pairs. *Science*, **264**, 415-417.

France, R. M. & Short, R. D. (1998) Plasma treatment of polymers: The effects of energy transfer from an argon plasma on the surface chemistry of polystyrene, and polypropylene. A high-energy resolution X-ray photoelectron spectroscopy study. *Langmuir*, **14**, 4827-4835.

Funatsu, T., Harada, Y., Higuchi, H., Tokunaga, M., Saito, K., Vale, R. & Yanagida, T. (1996) Single molecule imaging of motion and ATPase reaction of motor proteins. *Biophys. J.*, **70**, 1

Futterman, S. (1957) Enzymatic reduction of folic acid and dihydrofolic acid to tretrahydrofolic acid. *J. Biol. Chem.,* **228**, 1031-1038.

Gargaro, A. R., Soteriou, A., Frenkiel, T. A., Bauer, C. J., Birdsall, B., Polshakov, V. L., Barsukov, I. L., Roberts, G. C. K. & Feeney, J. (1998) The solution structure of the complex of *Lactobacillus casei* dihydrofolate reductase with methotrexate. *J. Mol. Biol.,* **277**, 119-134.

Gerhardt, W., Nordin, G., Herbert, A. K., Burzell, B. L., Isaksson, A., Gustavsson, E., Haglund, S., Muller-Bardorff, M. & Katus, H. A. (2000) Troponin T and I assays show decreased concentrations in heparin plasma compared with serum: Lower recoveries in early than in late phases of myocardial injury. *Clin. Chem.,* **46**, 817-821.

Gessner, A., Olbrich, C., Schroder, W., Kayser, O. & Muller, R. H. (2001) The role of plasma proteins in brain targeting: species dependent protein adsorption patterns on brain-specific lipid drug conjugate (LDC) nanoparticles. *Int. J. Pharm.,* **214**, 87-91.

Gessner, A., Waicz, R., Lieske, A., Paulke, B. R., Mader, K. & Muller, R. H. (2000) Nanoparticles with decreasing surface hydrophobicities: Influence on plasma protein adsorption. *Int. J. Pharm.,* **196**, 245-249.

Ghislain, L. P., Switz, N. A. & Webb, W. W. (1994) Measurement of small forces using an optical trap. *Rev. Sci. Instrum*., **65**, 2762-2768.

Gök, E., Kiremitçi, M. & Ateş. I. S. (1994) Protein adsorption on functional hydrophilic polymer beads: role of structural properties and medium conditions. *Reactive Polymers*, **24**, 41-48.

Good, R. J. (1992) Contact-angle, adhesion and wetting - A critical-review. *Abstr. Pap. Am. Chem. Soc.,* **203**, 2

Grange, W., Strunz, T., Schumakovitch, I., Güntherodt, H. –J. & Hegner, M. (2001) Molecular recognition and adhesion of individual DNA strands studied by dynamic force microscopy. *Single Mol.,* **2**, 75-78.

Grant, I. S. & Phillips, W. R. (2001) The elements of physics, Oxford University Press.

Gready, J. E. (1980) Dihydrofolate reductase: Binding of substrates and inhibitors and catalytic mechanism. *Adv. Pharmacol. Chemother.,* **17**, 37-102.

Green, R. J., Davies, J., Davies, M. C., Roberts, C. J. & Tendler, S. J. B. (1997) Surface plasmon resonance for real time in situ analysis of protein adsorption to polymer surfaces. *Biomaterials,* **18**, 405-413.

Grimes, B., Hallick, R., Williams, K., Wells, M., Lapointe, M., Ryan, C. & Wagenheim, M. (2001) The Biology Project. www.biology.arizona.edu.html.

Grubmuller, H., Heymann, B. & Tavan, P. (1996) Ligand binding: Molecular mechanics calculation of the streptavidin biotin rupture force. *Science*, **271**, 997-999.

Guck, J., Ananthakrishnan, R., Mahmood, H., Moon, T. J., Cunningham, C. C. & Kas, J. (2001) The optical stretcher: A novel laser tool to micromanipulate cells. *Biophys. J.,* **81**, 767-784.

Guiliani, I., Bertinchant, J. –P., Granier, C., Laprade, M., Chocron, S. & Toubin, G. (1999) Determination of cardiac troponin I forms in the blood of patients receiving crystalloid or cold blood cardioplegia. *Clin. Chem.,* **45**, 213-222.

Hallawi, E., Chilton, D., Trayer, I. & Cummins, P. (1998) Phosphorylation-specific antibodies for human cardiac troponin I. *Eur. J. Biochem.,* **256**, 535-540.

Hamm, C. W. (1998) Progress in the diagnosis of unstable angina and perspectives for treatment. *Eur. Heart J.,* **19**, N48-N50.

Han, T., Williams, J. M. & Beebe, T. P. (1995) Chemical-bonds studied with functionalized atomic-force microscopy tips. *Anal. Chim. Acta*., **307**, 365-376.

Hansma, H. G., Kim, K. J., Laney, D. E., Garcia, R. A., Argaman, M., Allen, M. J. & Parsons, S. M. (1997) Properties of biomolecules measured from atomic force microscope images: A review. *J. Struct. Biol.*, **119**, 99-108.

Hansma, H. G., Sinsheimer, R. L., Li, M. Q. & Hansma, P. K. (1992) Atomic force microscopy of single-stranded and double-stranded DNA. *Nucleic Acids Res.*, **20**, 3585-3590.

Hecht, E. (1987) Optics. 2nd Ed. Addison-Wesley Publishing Company, Inc.

Hegner, M., Smith, S. B. & Bustamante, C. (1999) Polymerization and mechanical properties of single RecA-DNA filaments. *Proc. Natl. Acad. Sci. USA.,* **96**, 10109-10114.

Helmerson, K., Kishore, R., Phillips, W. D. & Weetall, H. H. (1997) Optical tweezers-based immunosensor detects femtomolar concentrations of antigens. *Clin. Chem*., **43**, 379-383.

Hénon, S., Lenormand, G., Richert, A. & Gallet, F. (1999) A new determination of the shear modulus of the human erythrocyte membrane using optical tweezers. *Biophys. J.,* **76**, 1145-1151.

Heymann, B. & Grubmüller, H. (1999) AN02/DNP-hapten unbinding forces studied by molecular dynamics atomic force microscopy simulations. *Chem. Phys. Lett.,* **303**, 1-9.

Hinterdorfer, P., Kienberger, F., Raab, A., Gruber, H. J., Baumgartner, W., Kada, G., Riener, C., Wielert-Badt, S., Borken, C. & Schindler, H. (2000) Poly (ethylene glycol): An ideal spacer for molecular recognition force microscopy/spectroscopy. *Single Mol.,* **1**, 99-103.

Hinterdorfer, P., Baumgartner, W., Gruber, H. J., Schilcher, K. & Schindler, H. (1996) Detection and localization of individual antibody-antigen recognition events by atomic force microscopy. *Proc. Natl. Acad. Sci. USA*., **93**, 3477-3481.

Hirsh, J., Raschke, R., Warkentin, T. E., Dalen, J. E., Deykin, D. & Poller, L. (1995) Heparin - mechanism of action, pharmacokinetics, dosing considerations, monitoring, efficacy, and safety. *Chest*, **108**, S258-S275.

Hoh, J. H. & Schoenenberger, C. A. (1994) Surface-morphology and mechanical-properties of MDCK monolayers by atomic force microscopy. *J. Cell Sci*., **107**, 1105-1114.

Hoh, J. C., Cleveland, J. P., Prater, C.B., Revel, J. –P. & Hansma, P. K. (1992) Quantized adhesion detected with the atomic force microscope. *J. Am. Chem. Soc.,* **114**, 4917-4919.

Holbrook, J. J., Liljas, A., Steindel, S. J. & Rossman, M. G. (1975) Lactate dehydrogenase. *The Enzymes*, vol. XI, 3rd Ed. Academic Press, NY. pp. 191-292.

Hubbell, J. A. (1995) Biomaterials in tissue engineering. *Bio-Technology*, **13**, 565-576.

Hutter, J. L. & Bechhoefer, J. (1993) Calibration of atomic-force microscope tips. *Rev. Sci. Instrum*., **64**, 1868-1873.

Ikai, A. (1996) STM and AFM of bio/organic molecules and structures. *Surf. Sci. Reports.* **26**, 261-332.

Ingraham, R. H. & Hodges, R. S. (1988) Effects of ca-2+ and subunit interactions on surface accessibility of cysteine residues in cardiac troponin. *Biochemistry*, **27**, 5891-5898.

Israelachvili, J. N. (1991) Intermolecular and Surface Forces*; With Applications to Colloidal and Biological Systems,* Academic Press Inc. (London) LTD.

Israelachvili, J. N. (1985) Intermolecular and Surface Forces*; With Applications to Colloidal and Biological Systems,* Academic Press Inc. (London) LTD.

Israelachvili, J. N. & Adams, G. E. (1978) Measurement of forces between two mica surfaces in aqueous electrolyte solutions in the range 0-100 nm. *J. Chem. Soc. Faraday Trans.,* **74**, 975-1001.

Izrailev, S., Stepaniants, S., Balsera, M., Oono, Y. & Schulten, K. (1997) Molecular dynamics study of unbinding of the avidin-biotin complex. *Biophys. J.*, **72**, 1568-1581.

Jaffe, A. S., Ritter, C., Meltzer, V., Harter, H. & Roberts, R. (1984) Unmasking artifactual increases in creatine-kinase isoenzymes in patients with renal-failure. *J. Lab. Clin. Med.,* **104**, 193-202.

Janshoff, A., Neitzert, M., Oberdorfer, Y. & Fuchs, H. (2000) Force spectroscopy of molecular systems - Single molecule spectroscopy of polymers and biomolecules. *Angew. Chem.-Int. Edit.*, **39**, 3213-3237.

Johnson, J. D., Collins, J. H., Roberts, S. P. & Potter, J. D. (1980) *J. Biol. Chem.,* **255**, 9635-9640.

Katrukha, A., Bereznikova, A., Filatov, V. & Esakova, T. (1999) Biochemical factors influencing measurement of cardiac Troponin I. *Clin. Chem. Lab. Med.*, **37**, 1091-1095.

Katrukha, A. G., Bereznikova, A. V., Filatov, V. L., Esakova, T. V., Kolosova, O. V., Pettersson, K., Lovgren, T., Bulargina, T. V., Trifonov, I. R., Gratsiansky, N. A., Pulkki, K., Voipio-Pulkki, L. M. & Gusev, N. B. (1998) Degradation of cardiac troponin I: implication for reliable immunodetection. *Clin. Chem.*, **44**, 2433-2440.

Katrukha, A. G., Bereznikova, A. V., Esakova, T. V., Pettersson, K., Lovgren, T. & Severina, M. E. (1997) Troponin I is released in bloodstream of patients with acute myocardial infarction not in free form but as complex. *Clin. Chem.*, **43**, 1379-1385.

Katus, H. A., Remppis, A., Neumann, F. J., Scheffold, T., Diederich, K. W., Vinar, G., Noe, A., Matern, G. & Kuebler, W. (1991) Diagnostic efficiency of troponin-T measurements in acute myocardial-infarction. *Circulation*, **83**, 902-912.

Kellermayer, M. S. Z., Smith, S. B., Granzier, H. L. & Bustamante, C. (1997) Folding-unfolding transitions in single titin molecules characterized with laser tweezers. *Science*, **276**, 1112-1116.

Khan, A. (2000) A liquid water model: Density variation from supercooled to superheated states, prediction pf H-bonds, and temperature limits. *J. Phys. Chem.*, **104**, 11268-11274.

Kojima, H., Muto, E., Higuchi, H. & Yanagida, T. (1997) Mechanics of single kinesin molecules measured by optical trapping nanometry. *Biophys. J.*, **73**, 2012-2022.

Kolb, D. A. & Weber, G. (1975) Cooperativity of binding of anilinonaphthalenesulfonate to serum albumin induced by a second ligand. *Biochemistry,* **14**, 4476-4481.

Kramers, H. A. (1940) Brownian motion in a field of force and the diffusion model of chemical reactions. *Physica*, **7**, 284-304.

Krautbauer, R., Pope, L. H., Schrader, T. E., Allen, S. & Gaub, H. E. (2002) Discriminating small molecule DNA binding modes by single molecule force spectroscopy. *FEBS Lett.*, **510**, 154-158.

Krautbauer, R., Allen, S., Tessmer, I., Skinner, G., Pope, L. H., Schrader, T. E., Molloy, J. E., Tendler, S. J. B. & Gaub, H. E. (2001) Single molecule force spectroscopy investigations of DNA-drug interactions. *Abstr. Pap. Am. Chem. Soc.*, **221**, 247

Krautbauer, R. Clausen-Schaumann, H. & Gaub, H. E. (2000) Cisplatin changes the mechanics of single DNA molecules. *Angew. Chem.-Int. Edit*., **39**, 3912

Kuo, S. C. & Sheetz, M. P. (1993) Force of single kinesin molecules measured with optical tweezers. *Science*, **260**, 232-234.

Kuyper, L. F., Roth, B., Baccanari, D.P., Ferone, R., Beddell, C. R., Champness, J. N., Stammers, D. K., Dann, J. G., Norrington, F. E. A., Baker, D. J. & Goodford, P. J. (1982) Receptor based design of dihydrofolate reductase inhibitors - Comparision of crystallographically determined enzyme binding with enzyme affinity in a series of carboxy substituted trimethoprim analogs. *J. Med. Chem.,* **25**, 1120-1122.

Leckband, D. & Israelachvili, J. N. (2001) Intermolecular forces in biology. *Quarterly Rev. Biophys.,* **34**, 105-267.

Leckband, D. (2000) Measuring the forces that control protein interactions. *Annu. Rev. Biophys. Biomolec. Struct*., **29**, 1-26.

Leckband, D., Muller, W., Schmitt, F. J. & Ringsdorf, H. (1995) Molecular mechanisms determining the strength of receptor-mediated intermembrane adhesion. *Biophys. J*., **69**, 1162-1169.

Leckband, D. E., Schmitt, F. –J., Israelachvili, J. N. & Knoll, W. (1994) Direct force measurements of specific and non-specific protein interactions. *Biochemistry*, **15**, 4611-4624.

Leckband, D. & Israelachvili, J. (1993) Molecular-basis of protein function as determined by direct force measurements. *Enzyme Microb. Technol*., **15**, 450-459.

Leckband, D., Virden, J., Kamiyama, Y., Berg, J. & Israelachvili, J. (1992) Molecular mechanism of the stabilization of vesicles bearing terminally anchored polymers. *Abstr. Pap. Am. Chem. Soc*., **203**, 17.

Lee, G. U., Chrisey, L. A. & Colton, R. J. (1994a) Direct measurement of the forces between complementary strands of DNA. *Science*, **266**, 771-773.

Lee, G. U., Kidwell, D. A. & Colton, R. J. (1994b) Sensing discrete streptavidin biotin interactions with atomic-force microscopy. *Langmuir*, **10**, 354-357.

Léger, J. F., Robert, J., Bourdieu, L., Chatenay, D. & Marko, J. F. (1998) RecA binding to a single double-stranded DNA molecule: a possible role of DNA conformational fluctuations. *Proc. Natl. Acad. Sci. USA.,* **95**, 12295-12299.

Lenne, P. F., Raae, A. J., Altmann, S. M., Saraste, M. & Horber, J. K. H. (2000) Stales and transitions during forced unfolding of a single spectrin repeat. *FEBS Lett*., **476**, 124-128.

Lenormand, G., Hénon, S., Richert, A., Simeon, J. & Gallet, F. (2001) Direct measurement of the area expansion and shear moduli of the human red blood cell membrane skeleton. *Biophys. J*., **81**, 43-56.

Li, H., Linke, W. A., Oberhauser, A. F., Carrion-Vazquez, M., Kerkvliet, J. G., Lu, H., Marszalek, P. E. & Fernandez, J. M. (2002) Reverse engineering of the giant muscle protein titin. *Nature*, **418**, 998-1002.

Li, H. B., Rief, M., Oesterhelt, F., Gaub, H. E., Zhang, X. & Shen, J. C. (1999) Single-molecule force spectroscopy on polysaccharides by AFM - nanomechanical fingerprint of alpha-(1,4)-linked polysaccharides. *Chem. Phys. Lett.,* **305**, 197-201.

Li, H., Rief, M., Oesterhelt, F. & Gaub, H. E. (1998) Single-molecule force spectroscopy on xanthan by AFM. *Adv. Mater.*, **3**, 316-319.

Lindsay, S. M., Lyubchenko, Y. L., Tao, N. J., Li, Y. Q., Oden, P. I., Derose, J. A. & Pan, J. (1993) Scanning-tunneling-microscopy and atomic-force microscopy studies of biomaterials at a liquid-solid interface. *J. Vac. Sci. Technol. A-Vac. Surf. Films*, **11**, 808-815.

Liu, J. & Hlady, V. (1996) Chemical pattern on silica surface prepared by UV irradiation of 3-mercaptopropyltriethoxy silane layer: surface characterization and fibrinogen adsorption. *Colloids Surf. B*., **8**, 25-37.

Lo, Y. –S., Zhu, Y. –J. & Beebe. T. P (2001) Loading-rate dependence of individual ligand-receptor bond-rupture forces studied by atomic force microscopy. *Langmuir*, **17**, 3741-3748.

Lomas, M. (2000) *PhD Thesis*. University of Nottingham, Nottingham, UK.

Lu, H. & Schulten, K. (1999) Steered molecular dynamics simulation of conformational changes of immunoglobulin domain I27 interpret atomic force microscopy observation. *Chem. Phys.,* **247**, 141-153.

Lu, H., Isralewitz, B., Krammer, A., Vogel, V. & Schulten, K. (1998) Unfolding of titin immunoglobulin domains by steered molecular dynamics simulation. *Biophys. J.,* **75**, 662-671.

Macgeoch, C., Barton, P. J. R., Vallins, W. J., Bhavsar, P. & Spurr, N. K. (1991) The human cardiac troponin-i locus - assignment to chromosome. *Hum. Genet*., **88**, 101-104.

Magonov, S. N. & Whangbo, M. H. (1996) *In* Surface Analysis with STM and AFM. VCH Publisher, New York. Chapter 3, Scanning probe microscopes. pp 21-49.

Maier, B., Bensimon, D. & Croquette, V. (2000) Replication by single DNA polymerase of stretched single-stranded DNA. *Proc. Natl. Acad. Sci. USA.,* **97**, 12002-12007.

Mammen, M., Helmerson, K., Kishore, R., Choi, S. K., Phillips, W. D. & Whitesides, G. M. (1996) Optically controlled collisions of biological objects to evaluate potent polyvalent inhibitors of virus-cell adhesion. *Chem. Biol.,* **3**, 757-763.

Margosiak, S. A., Appleman, J. R., Santi, D. V. & Blakely, R. L. (1993) Dihydrofolate reductase from pathogenic fungus *pneumocystis carinii* - Catalytic properties and interaction with folates. *Arch. Biochem. Biophys.*, **305**, 499-508.

Marszalek, P. E., Lu, H., Li, H. B., Carrion-Vazquez, M., Oberhauser, A. F., Schulten, K. & Fernandez, J. M. (1999) Mechanical unfolding intermediates in titin modules. *Nature*, **402**, 100-103.

Martin, A. L., Davies, M. C., Rackstraw, B. J., Roberts, C. J., Stolnik, S., Tendler, S. J. B. & Williams, P. M. (2000) Observation of DNA-polymer condensate formation in real time at a molecular level. *FEBS Lett*., **480**, 106-112.

Matthews, D. A., Bolin, J T., Burridge, J. M., Filman, D. J., Volz, K. W., Kaufman, B. T., Beddell, C. R., Champness, J. N., Stammers, D. K. & Kraut, J. (1985a) Refined crystal structures of *Escherichia coli* and chicken liver dihydrofolate reductase containing bound trimethoprim. *J. Biol. Chem.,* **260**, 381-391.

Matthews, D. A., Bolin, J T., Burridge, J. M., Filman, D. J., Volz, K. W. & Kraut, J. (1985b) Dihydrofolate reductase the stereochemistry of inhibitor selectivity. *J. Biol. Chem.,* **260**, 392-399.

Matthews, D. A., Alden, R. A., Freer, S. T., Xuong, N. & Kraut, J. (1979) Dihydrofolate reductase from *Lactobacillus casei*: Stereochemistry of NADPH binding. *J. Biol. Chem.,* **254**, 4144-4151.

Matthews, D. A., Alden, R. A., Bolin, J. T., Filman, D. J., Freer, S., Hamlin, R., Hol, W. G. J., Kisliuk, R. L., Pastore, E. J., Plante, T., Xuong, N. & Kraut, J. (1978) *J. Biol. Chem.*, **253**, 6946-6954.

McGurk, S. L., Green, R. J., Sanders, G. H. W., Davies, M. C., Roberts, C. J., Tendler, S. J. B. & Williams, P. M. (1999) Molecular interactions of biomolecules with surface-engineered interfaces using atomic force microscopy and surface plasmon resonance. *Langmuir*, **15**, 5136-5140.

Mehta, A. D., Rief, M., Spudich, J. A., Smith, D. A. & Simmons, R. M. (1999) Single-molecule biomechanics with optical methods. *Science*, **283**, 1689-1695.

Merkel, R. (2001) Force spectroscopy on single passive biomolecules and single biomolecular bonds. *Phys. Rep.-Rev. Sec. Phys. Lett*., **346**, 344-385.

Merkel, R., Nassoy, P., Leug, A., Ritchie, K. & Evans, E. (1999) Energy landscapes of receptor-ligand bonds explored with dynamic force spectroscopy. *Nature*, **397**, 50-53.

Molloy, J. E., Veigel, C. & Knight, A. (1999) Single molecule mechanics of acto-myosin using optical tweezers. *J. Gen. Physiol*., **114**, 18-20.

Molloy, J. E., Burns, J. E., Kendrickjones, J., Tregear, R. T. & White, D. C. S. (1995) Movement and force produced by a single myosin head. *Nature*, **378**, 209-212.

Momose, Y., Tamura, Y., Ogino, M., Okazaki, S. & Hirayama, M. (1992) Chemical-reactivity between teflon surfaces subjected to argon plasma treatment and atmospheric oxygen. *J. Vac. Sci. Technol. A-Vac. Surf. Films,* **10**, 229-238.

Moranja, N., Clark, D. & Tal, R. (2001) Biochemical and immunological properties of human cardiac troponin I fragments. *Biotech. Appl. Biochem.,* **33**, 107-115.

Moranja, N. (1998) Degradation of human cardiac troponin I after myocardial infarction. *Biotech. Appl. Biochem.,* **28**, 105-111.

Morrison, J. F. & Stone, S. R. (1988) Mechanism of the reaction catalyzed by dihydrofolate reductase from Escherichia coli: pH and deuterium isotope effects with NADPH as the variable substrate. *Biochemistry*, **27**, 5499-5506.

Moy, V. T., Florin, E. L. & Gaub, H. E. (1994) Intermolecular forces and energies between ligands and receptors. *Science*, **266**, 257-259.

Muncaster. (1988) A-level physics. 3rd Ed. Cheltenham:Thornes.

Murakami, T., Kuroda S. & Osawa, Z. (1998) Dynamics of polymeric solid surfaces treated by oxygen plasma: Plasma-induced increases in surface molecular mobility of polystyrene. *J. Colloid Interface Sci.,* **200**, 192-194.

Neish, C. S., Martin, I. L., Henderson, R. M. & Edwardson, J. M. (2002) Direct visualization of ligand-protein interactions using atomic force microscopy. *Br. J. Pharmacol*., **135**, 1943-1950.

Nosanchuk, J. S. (1999) False increases of troponin I attributable to incomplete separation of serum. *Clin. Chem*., **45**, 714.

Oberhauser, A. F., Marszalek, P. E., Erickson, H. P. & Fernandez, J. M. (1998) The molecular elasticity of extracellular matrix protein tenascin. *Nature*, **393**, 181-185.

Oesterhelt, F., Oesterhelt, D., Pfeiffer, M., Engel, A., Gaub, H. E. & Müller, D. J. (2000) Unfolding pathways of individual bacteriorhodopsins. *Science*, **288**, 143-146.

Otting, F. & Heunnekins, F. M. (1972) *Arch. Biochem. Biophys.,* **152**, 429-431.

Perkins, J. P. & Bertino, J. R. (1966) Dihydrofolate Reductase from the L1210R Murine Lymphoma. Fluorometric Measurements of the Interaction of the Enzyme with Coenzymes, Substrates, and Inhibitors. *Biochemistry*, **5**, 1005-1012.

Polshakov, V. I., Birdsall, B., Frenkiel, T. A., Gargaro, A. R. & Feeney, J. (1999) Structure and dynamics in solution of the complex of *Lactobacillus casei* dihydrofolate reductase with the new lipophilic antifolate drug trimetrexate. *Protein Sci.,* **8**, 1-15.

Radmacher, M., Rotsch, C., Fritz, M., Kacher, C. M., Hofmann, U., Gaub, H. E. & Hansma, P. K. (1996) Measuring the elastic properties of bio-polymers and living cells with the atomic force microscope. *Abstr. Pap. Am. Chem. Soc*., **212**, 324.

Radmacher, M., Cleveland, J. P., Fritz, M., Hansma, H. G. & Hansma, P. K. (1994) Mapping interaction forces with the atomic-force microscope. *Biophys. J*., **66**, 2159-2165.

Reyes, V. M., Sawaya, M. R., Brown, K. A. & Kraut, J. (1995) Isomorphous Crystal Structures of Escherichia coli Dihydrofolate Reductase Complexed with Folate, 5-Deazafolate, and 5,10-Dideazatetrahydrofolate: Mechanistic Implications. *Biochemistry*, **34**, 2710-2723.

Rief, M., Clausen-Schaumann, H. & Gaub, H. E. (1999a) Sequence dependent mechanics of single DNA-molecules. *Nature struc. Biol.,* **6**, 346-349.

Rief, M., Pascual, J., Saraste, M. & Gaub, H. E. (1999b) Single molecule force spectroscopy of spectrin repeats: low unfolding forces in helix bundles. *J. Mol. Biol.,* **286**, 553-561.

Rief, M., Gautel, F., Oesterhelt, F., Fernandez, J. M. & Gaub, H. E. (1997) Reversible unfolding of individual titin immunoglobulin domains by AFM. *Science*, **276**, 1109-1112.

Roberts, G. C. K., Feeney, J., Burgen, A. S. V., Yuferov, V., Dann, J. G. & Bjur, R. A. (1974) Nuclear magnetic resonance studies of the binding of substrate analogs and coenzyme to dihydrofolate reductase from *Lactobacillus casei*. *Biochemistry*, **13**, 5351-5357.

Ros, R., Schwesinger, F., Anselmetti, D., Kubon, M., Schäfer, R., Plückthun, A & Tiefenauer, L. (1998) Antigen binding forces of individually addressed singl-chain Fv antibody molecules. *Proc. Natl. Acad. Sci. USA.*, **95**, 7402-7405.

Rugar, D. & Hansma, P .K. (1990) Atomic force microscopy. *Physics today*, **43**, 23-30.

Sakata-Sogawa, K., Kurachi, M., Sogawa, K., Fujii-Kuriyama, Y. & Tashiro, H. (1998) Direct measurement of DNA molecular length in solution using optical tweezers: detection of looping due to binding protein interactions. *Eur. Biophys. J. Biophys. Lett*., **27**, 55-61.

Sawaya, M. R. & Kraut, J.(1997) Loop and Subdomain Movements in the Mechanism of *Escherichia coli* Dihydrofolate Reductase: Crystallographic Evidence. *Biochemistry*, **36**, 586-603.

Schirra, H. J., Scanlon, M. J., Lee, M. C. S., Anderson, M. A. & Craik, D. J. (2001) The Solution Structure of C1-T1, a Two-Domain Proteinase Inhibitor Derived from a Circular Precursor Protein from Nicotiana Alata. *J.Mol.Biol.,* **306**, 69.

Schmidt, TH., Hinterdorfer, P. & Schindler, H. (1999) Microscopy for recognition of individual biomolecules. *Microscopy Res. Tech.,* **44**, 339-346.

Schneider, J., Dufrene, Y. F., Barger, W. R. & Lee G. U. (2000) Atomic force microscope image contrast mechanisms on supported lipid bilayers. *Biophys. J.,* **79**, 1107-1118.

Schwesinger, F., Ros, R., Strunz, T., Anselmetti, D., Güntherodt, H. –J., Honegger, A., Jermutus, L., Tiefenauer, L. & Plückthun, A. (2000) Unbinding forces of single antibody-antigen complexes correlate with their thermal dissociation rates. *Proc. Natl. Acad. Sci. USA.,* **97**, 9972-9977.

Segura, R., Varela, E., Marti, R., Vidal, E., Gonzalez, C. & Figueras, J. (1999) Comparison of three assays for cardiac troponin I measurement: effect of chelating agents. *Clin. Chem. Lab. Med.,* **37**, 457.

Shivashankar, G. V. & Libchaber, A. (1997) Single DNA molecule grafting and manipulation using a combined atomic force microscope and an optical tweezer. *Appl. Phys. Lett.,* **71**, 3727-3729.

Shao, Z. & Yang, J. (1995) Progress in high resolution atomic force microscopy in biology. *Quarterly Rev. Biophys.,* **28**, 195-251.

Sigal, G. B., Mrksich, M. & Whitesides, G. M. (1998) Effect of Surface Wettability on the Adsorption of Proteins and Detergents. *J. Am. Chem. Soc.,* **120**, 3464-3473.

Simson, D. A., Strigl, M., Hohenadl, M. & Merkel, R. (1999) Statistical breakage of single protein A-IgG bonds reveals crossover from spontaneous to force-induced bond dissociation. *Phys. Rev. Lett.,* **83**, 652-655.

Smith, S. P., Bhalotra, S. R., Brody, A. L., Brown, B. L., Boyda, E. K. & Prentiss, M. (1999) Inexpensive optical tweezers for undergraduate laboratories. *Am. J. Phys*., **67**, 26-35.

Smith, S. B., Cui, Y. & Bustamante, C. (1996) Overstretching B-DNA: The elastic response of individual double-stranded and single-stranded DNA molecules. *Science*, **271**, 795-799.

Smith, S. B., Finzi, L. & Bustamante, C. (1992) Direct mechanical measurements of the elasticity of single DNA-molecules by using magnetic beads. *Science*, **258**, 1122-1126.

Solaro, R. J. (1986) Protein phosphorylation and the cardiac myofilaments. In: Protein phosphorylation in the heart muscle. Boca Raton, CRC Press Inc., pp. 129-156.

Steubing, R. W., Cheng, S., Wright, W. H., Numajiri, Y. & Berns, M. W. (1991) Laser-induced cell-fusion in combination with optical tweezers - the laser cell-fusion trap. *Cytometry*, **12**, 505-510.

Stevens, M. M., Allen, S., Chan, W. C., Davies, M. C., Roberts, C. J., Tendler, S. J. B. & Williams, P. M. (2000) Probing protein-peptide-protein molecular architecture by atomic force microscopy and surface plasmon resonance. *The Analyst*, **125**, 245-250.

Stiegler, H., Fischer, Y., Vazquez-Jimenez, J. F., Graf, J., Filzmaier, K., Fausten, B., Janssens, U., Gressner, A. M. & Kunz, D. (2000) Lower cardiac troponin T and I results in heparin-plasma than in serum. *Clin. Chem.,* **46**, 1338-1344.

Stone, S. R. & Morrison, J. F. (1984) Catalytic mechanism of the dihydrofolate reductase reaction as determined by pH studies. *Biochemistry*, **23**, 2753-2758.

Stout, A. L. (2001) Detection and characterization of individual intermolecular bonds using optical tweezers. *Biophys. J.,* **80**, 2976-2986.

Strigl, M., Simson, D. A., Kacher, C. M. & Merkel, R. (1999) Force-induced dissociation of single protein A-IgG bonds. *Langmuir*, **15**, 7316-7324.

Strunz, T., Oroszlan, K., Schäfer, R. & Güntherodt, H. -J. (1999) Dynamic force spectroscopy of single DNA molecules. *Proc. Natl. Acad. Sci. USA.,* **96**, 11277-11282.

Stuart, J. K. & Hlady, V. (1995) Effects of discrete protein-surface interactions in scanning force microscopy. *Langmuir*, **11**, 1368-1374.

Subramanian, S. & Kaufman, B. T. (1978) *Proc. Natl. Acad. Sci. USA.,* **75**, 3201-3205.

Svoboda, K. & Block, S. M. (1994) Biological application of optical forces. *Ann. Rev. Biophys. Biomol. Struct.,* **23**, 247-285.

Svoboda, K., Schmidt, C. F., Schnapp, B. J. & Block, S. M. (1993) Direct observation of kinesin stepping by optical trapping interferometry. *Nature*, **365**, 721-727.

Tabata, Y. & Ikada, Y. (1990) Phagocytosis of polymer microspheres by macrophages. *Adv. Polym. Sci*., **94**, 107-141.

Tabor, D. & Winterton, F. R. S. (1969) *Proc. R. Soc. London, A.,* **312**, 435.

Tadir, Y., Wright, W. H., Vafa, O., Ord, T., Asch, R. H. & Berns, M. W. (1990) Force generated by human sperm correlated to velocity and determined using a laser generated optical trap. *Fertil. Steril.,* **53,** 944-947.

Tadir, Y., Wright, W. H., Vafa, O., Ord, T., Asch, R. H. & Berns, M. W. (1989) Micromanipulation of sperm by a laser generated optical trap. *Fertil. Steril.,* **52**, 870-873.

Tao, N. J., Lindsay, S. M. & Lees, S. (1992) Measuring the microelastic properties of biological material. *Biophys. J.,* **63**, 1165-1168.

Tashiro, H., Uchida, M. & Satomaeda, M. (1993) 3-Dimensional cell manipulator by means of optical trapping for the specification of cell-to-cell adhesion. *Opt. Eng*., **32**, 2812-2817.

Tessmer, I. (2002) In preparation. *PhD Thesis*. University of Nottingham, Nottingham, UK.

Theorell, H. & Yonetani, Y. (1963) Liver alcohol dehydrogenase–DPN–pyrazole complex: a model of the ternary intermediate in the enzyme reaction. *Biochem. Z.,* **338**, 537–553.

Thillet, J., Adams, J. A. & Benkovic, S. J. (1990) The kinetic mechanism of wild-type and mutant mouse dihydrofolate reductases. *Biochemistry*, **29**, 5195-5202.

Thomson, N. H., Collin, I., Davies, M. C., Palin, K., Parkins, D., Roberts, C. J., Tendler, S. J. B. & Williams, P. M. (2000) Atomic force microscopy of cationic liposomes. *Langmuir*, **16**, 4813-4818.

Thundat, T., Zheng, X. –Y., Shrap, D., Allison, D. P., Warmack, R. J., Joy, D. C. & Ferrell, T. L. (1992) Calibration of atomic force microscope tips using biomolecules. *Scanning Microscopy,* **6**, 903-910.

Trask, R. V. & Billadello, J. J. (1990) Tissue-specific distribution and developmental regulation of M-creatine and B-creatine kinase messenger-RNAs. *Biochim. Biophys. Acta.,* **1049**, 182-188.

Tripet, B., VanEyk, J. & Hodges, R. S. (1997) Specific interactions of the central region of Troponin I with the N-domain of Troponin C. *Biophys. J*., **72**, WP205.

Tsai, H. A., Chen, C. H. & Lee, W. C. (2001) Influence of surface hydrophobic groups on the adsorption of proteins onto nonporous polymeric particles with immobilized metal ions. *Colloid Interface Sci.,* **240**. 379-383.

Tskhovrebova, L., Trinick, J., Sleep, J. A. & Simmons, R. M. (1997) Elasticity and unfolding of single molecules of the giant muscle protein titin. *Nature*, **387**, 308-312.

Tsung, S. H. (1981) Several conditions causing elevation of serum CK-MB and CK-BB. *Am. J. Clin. Pathol*., **75**, 711-715.

Vallins, W. J., Brand, N. J., Dabhade, N., Butlerbrowne, G., Yacoub, M. H. & Barton, P. J. R. (1990) Molecular-cloning of human cardiac troponin-I using polymerase chain-reaction. *Febs Lett.*, **270**, 57-61.

van Oss, C. J. (1997) Hydrophobicity and hydrophilicity of biosurfaces. *Curr. Opin. Coll. Interface Sci.,* **2**, 503-512.

van Oss, C. J. (1994) *In* Immunochemistry. (van Oss, C. J. & van Regenmortel, M. H. V., Eds.) Marcel Dekker: New York. *Chapter 23, Nature of specific ligand-receptor bonds, in particular the antigen-antibody bond*. pp 581-614.

Veigel, C., Bartoo, M. L., White, D. C. S., Sparrow, J. C. & Molloy, J. E. (1998) The stiffness of rabbit skeletal actomyosin cross-bridges determined with an optical tweezers transducer. *Biophys. J*., **75**, 1424-1438.

Verma, C. S., Fischer, S., Caves, L. S.D., Roberts, G. C. K. & Hubbard, R. E. (1996) Calculation of the reaction pathway for the aromatic ring flip in methotrexate complexed to dihydrofolate reductase. *J. Phys. Chem.,* **100**, 2510-2518.

Vinckier, A., Heyvaert, I., D'Hoore, A., McKittrick, T., van Haesendonck, C., Engelborghs, Y. & Hellemans, L. (1995) Immobilizing and imaging microtubules by atomic force microscopy. *Ultramicroscopy*, **57**, 337-343.

Visscher, K., Schnitzer, M. J. & Block, S. M. (1999) Single kinesin molecules studied with a molecular force clamp. *Nature*, **400**, 184-189.

Visscher, K., Gross, S. P. & Block, S. M. (1996) Construction of multiple-beam optical traps with nanometer-resolution position sensing. *IEEE J. Selec. Top. Quantum Electronics,* **2**, 1066-1076.

Voet, D. & Voet, J. G. (1995) Biochemistry, 2nd Ed. New York: John Wiley & Sons.

Wagner, T. L., Schessler, H. M., Liotta, L. A. & Day, A. R. (2001) On the interaction of cardiac troponin I (cTNI) and heparin. A possible solution. *Clin. Chem.,* **47**, 696.

Wang, M. D., Schnitzer, M. J., Landick, R., Gelles, J. & Block, S. M. (1998) Force and velocity measured for single molecules of RNA polymerase. *Science*, **282**, 897-901.

Wang, M. D., Yin, H., Landick, R., Gelles, J. & Block, S. M. (1997) Stretching DNA with optical tweezers. *Biophys. J.,* **72**, 1335-1346.

Weber, P. C., Ohlendorfer, D. H., Wendoloski, J. J. & Salemme, F. R. (1989) Structural origins of the high-affinity biotin binding to streptavidin. *Science*, **243**, 85-88.

Weisenhorn, A. L., Hansma, P. K., Albretch, T. R. & Quate, C. F. (1989) Forces in AFM, in air and water. *Appl. Phys. Letts.,* **54**, 2651-2653.

Wertz, C. F. & Santore, M. M. (2001) Effect of surface hydrophobicity on adsorption and relaxation kinetics of albumin and fibrinogen: Single-species and competitive behaviour. *Langmuir*, **17**, 3006-3016.

Wilchek, M. & Bayer, E. A. (1990) *In* avidin-biotin technology. (Wilchek, M. & Bayer, E. A., Eds.) Methods in Enzymology Series No. 184, Academic Press, Inc.: New York. Pp. 5-13 & 49-67.

Willemsen, O. H., Snel, M. M., Kuipers, L., Figdor, C. G., Greve, J. & De Grooth, B. G. (1999) A physical approach to reduce nonspecific adhesion in molecular recognition atomic force microscopy. *Biophys. J.,* **76**, 716-724.

Williams, J. W. & Morrison, J. F. (1981) Chemical mechanism of the reaction catalyzed by dihydrofolate reductase from *Streptococcus faecium*: pH studies and chemical modification. *Biochemistry,* **20**, 6024-6029.

Williams, J. W., Morrison, J. F. & Duggleby, R. G. (1979) Methotrexate, a high-affinity pseudosubstrate of dihydrofolate reductase. *Biochemistry,* **18**, 2567-2573.

Williams, P. M. & Evans, E. (2002) In Preparation.

Williams, P .M., Moore, A., Stevens, M. M., Allen, S., Davies, M. C., Roberts, C. J. & Tendler, S. J. B. (2000) On the dynamic behaviour of the forces dissociation of ligand-receptor pairs. *J. Chem. Soc. Perkin Trans.* **2***,* 5-8.

Woronick, C. L. (1963) *Acta. Chem. Scand.*, **17**, 1789.

Wright, W. H., Sonek, G. J. & Berns, M. W. (1994) Parametric study of the forces on microspheres held by optical tweezers. *Appl. Optics*, **33**, 1735-1748.

Wu, A. H. B., Apple, F. S., Gibler, B. W., Jesse, R. L., Warshaw, M. M. & Valdes, R. (1999) National academy of clinical biochemistry standards of laboratory practice: recommendations for the use of cardiac markers in coronary artery diseases. *Clin. Chem.,* **45**, 1104-1121.

Wu, A. H. B., Feng, Y. J., Moore, R., Apple, F. S., McPherson, P. H., Buechler, K. F. & Bodor, G. (1998) Characterization of cardiac troponin subunit release into serum after acute myocardial infarction and comparison of assays for troponin T and I. *Clin. Chem*., **44**, 1198-1208.

Yang, Z. H., Galloway, J. A. & Yu, H. U. (1999) Protein interactions with poly(ethylene glycol) self-assembled monolayers on glass substrates: Diffusion and adsorption. *Langmuir*, **15**, 8405-8411.

Yin, H., Wang, M. D., Svoboda, K., Landick, R., Block, S. M. & Gelles, J. (1995) Transcription against an applied force. *Science*, **270**, 1653-1657.

Yuan, S., Szakalasgratzl, G., Ziats, N. P., Jacobsen, D. W., Kottkemarchant, K. & Marchant, R. E. (1993) Immobilization of high-affinity heparin oligosaccharides to radiofrequency plasma-modified polyethylene. *J. Biomed. Mat. Res.,* **27**, 811-819.

Yuan, C., Chan, A., Kolb, P. & Moy, V. T. (2000) Energy landscape of streptavidin-biotin complexes measured by atomic force microscopy. *Biochemistry*, **39**, 10219-10223.

Zahn, M., Renken, J. & Seeger, S. (1999) Fluorimetric multiparameter cell assay at the single cell level fabricated by optical tweezers. *FEBS Lett*., **443**, 337-340.

ACKNOWLEDGEMENTS

Many thanks to my supervisors Prof Saul Tendler, Prof Martyn Davies, Dr Stephanie Allen, Dr Clive Roberts and Dr Phil Williams. Funding was gratefully received from the University of Nottingham and Ortho-Clinical Diagnostics, without which this thesis would not exist.

A special thanks to a dear friend, Lisa, for the coffee, the gossip, and the laughs. Thanks to the rest of the gang, Nicola, Billy, Eoin, and Claire.

Craig I couldn't have done it without you sweetheart…Thanks. And Boston, thank you for being such a precious little boy. You've been so patient and understanding for what must feel like a life time…but now my darling son, my time is all yours.

Mum I did it…not that you ever thought I wouldn't. Thanks for supporting me throughout my education, always being there for me during each and every examination crisis from the of age 5 to 27.